MULTIPLE BEAM LASER DIODE ADDITIVE MANUFACTURING FOR METAL PARTS

Andrew Timothy Payne

Sidney Sussex College

University of Cambridge

A thesis submitted for the degree of

Doctor of Philosophy

July 2017

Declaration

This dissertation is my own work and has not been conducted in collaboration with others. This dissertation is not similar to any other body of work that I have submitted or will be submitting for a degree, diploma or any other qualification at another university. This dissertation meets the requirements of the word limit and figure limits, having a total word count of 49266 words and 112 figures respectively.

Andrew Payne

28th July 2017

Abstract

Fibre laser based powder bed fusion has become the dominant commercial additive manufacturing technology for producing fully dense metal parts. This technology is difficult to scale up for build volume and build rate. Continuing advances in semiconductor technology have produced single emitter laser diodes with outputs of many tens of Watts and diode stacks that can output hundreds of Watts. These powers now make laser diodes effective for metal based additive manufacturing which when configured in a raster scanned multi beam array allow for scaling of build volume and rate.

A multiple laser diode powder bed fusion additive manufacturing platform has been developed along with the firmware and software to enable the automated building of multiple layer objects. An 'expose-move-expose' strategy was employed for energy delivery; the multiple beam array is stationary whilst the diodes are on. The influence of powder layer thickness, exposure power, exposure time and the temporal and spatial positioning of exposures were investigated by the use of custom software analysis tools. Five scanning strategies were developed and characterised for the creation of layered objects.

The higher absorptivity and lower thermal conductivity of powders when compared to bulk material produced an independence of melt volume from power for a given pulse energy in deep powder. Conversely the melt volume produced for a given pulse energy in a substrate without powder was proportional to the power used. The melt volume produced from a thin layer of powder on a substrate was also found to be proportional to power but the extent of powder denudation, whilst proportional to pulse energy, was independent from power.

For a given pulse energy per exposure when creating lines of melt balls the greatest line sharpness and a lowest surface roughness were achieved with a small powder layer thickness, a high exposure power, a low spot pitch, a temporal delay of 400 ms and a square exposure profile. Single layers build in deep powder using the vertical scanning strategies (numbers one and two) showed the greatest consolidation but as layer thicknesses were between 400 and 1000 microns the relative density was no better than that of the un-fused powder.

It is concluded that the intensity of the diode lasers used in this research, 2400 W/mm^2 from 42 W focussed into a 150 μm diameter spot, is insufficient for building high density parts. This intensity did not produce sufficient melting of the substrate to enable efficient wetting of the melted powder. Consequently, the tendency for balling within the melt produced features within the re-solidified material that were hundreds of microns high. These features required commensurate powder layer thickness to allow uninterrupted passage of the powder wiper. The density of parts was compromised by the large layer thickness needed with 61 % being the highest density achieved. Further study would benefit from using laser diodes with an output power greater than 40 W.

Acknowledgements

I would like to thank my supervisor Prof. Bill O'Neill for his confidence and guidance through the process of creating this thesis. Without his grand vision and his ability to charm financial backers this project, and many others, would not have been conducted within the Centre for Industrial Photonics.

A large debt of gratitude is owed to Dr Martin Sparkes for his willingness to proof read this thesis and his honest evaluations, incisive criticism and rare but precious praise throughout my three plus years spent on this work. All other members of the CIP have contributed to make the group a fun and enjoyable place to work but particular thanks must be given to Dr Andrew Cockburn, Dr David Hopkinson and Dr Krste Pankovski who all unreservedly gave me time and knowledge according to my needs.

The EPSRC made it all possible by funding this research. Similarly IPG for supplying the laser diodes and repairing them on the strength of the results of two month's work after I pushed them beyond their safe working limits.

I need to thank Megan Ruddlesden for the beer that she bought me in exchange for a mention in my thesis.

I would also like to thank my undergraduate lecturer Dr George Dobre for without his appraisal I would not have thought myself worthy of a place at Cambridge.

Turning the clock back further, my gratitude to Shannon Molver is beyond measure. The last ten years in academic training are as a result of her initial and continuing struggle to help me make the best of myself.

Back to the present; thank you Victoria for your support, proof reading prowess and gentle persistent encouragement to make me finish the task when it seemed to be difficult.

Finally, thanks and apology to my parents; the former for equipping me with an enquiring mind and the latter for making you wait so long.

Table of Contents

List of Figures

List of Tables

Chapter 1

Introduction

1.1 The development of additive manufacturing

The first commercial additive manufacturing (AM) machine was produced by 3D Systems in 1987 [1] and based upon Charles Hull's 1986 patent for a "method for production of three-dimensional shapes by stereolithography" [2]. It used photo-sensitive monomers that could be polymerised by laser light and was used to produce prototype parts for form and fit studies or as visualisation tools. Selective laser sintering (SLS) was commercialised by the DTM Corporation five years later and in 1993 they produced a process called "RapidTool" that could produce metal parts [3, p. 227]. It used a laser to selectively sinter plastic coated metal powders creating a fragile 'green' part. Further processing steps included burning off the plastic and sintering the metal powder in an oven ('brown' part) followed by infiltration with a lower melting point metal such as copper to produce a fully dense part.

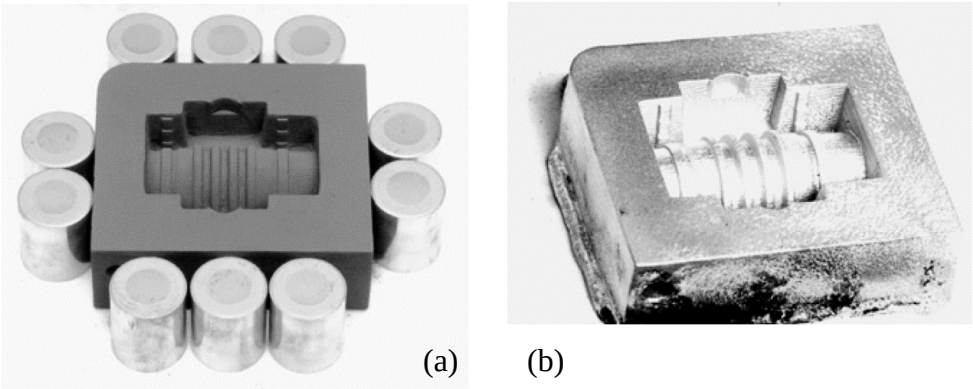

Figure 1 The RapidTool process, (a) brown part with copper cylinders before infiltration. (b) After infiltration.

Since then advances in laser power and beam quality, mainly provided by fibre laser technology, have taken metal powder based AM from a sintering process to a full melting process. Selective Laser Melting (SLM) technology is now capable of creating dense parts from high temperature melting point materials such as tungsten or tantalum [4][5] and is capable of creating functional parts for diverse industries such as aerospace, dentistry, fashion and prosthetics [6].

1.2 Research motivation

As the areas where AM can be applied continue to grow, build rate and cost are limiting its application. The specific AM technology that is the focus of this research is a variant of laser based Powder Bed Fusion (PBF) technology in which an energy source is used to selectively melt a bed of powdered material layer by layer in order to create a solid 3D object.

There are two elements of the PBF process that contribute to the total manufacturing time: the time to prepare the powder layer and the time to selectively melt the layer. Layer preparation is not considered in detail within the following work. Melting time can be reduced by increasing the energy deposition rate within the selective melting phase. There are two ways of doing this:

a) use a more powerful laser,
b) use several lasers.

The first approach is relatively easy to implement in that the overall design of the machine remains unchanged. However, some material properties such as thermal conductivity or thermal diffusivity have a temporal component, so whilst scanning a 1000 W laser beam at 1000 m/s delivers the same energy to a given point as a 1 W laser scanned at 1 m/s the effects upon the material, such as temperature rise, differ. As a result of this time dependence, each material has a range of effective processing parameters imposing both a minimum and maximum limit of useful power thus constraining the build rate achievable with a single laser.

The second approach of using several lasers presents problems in keeping the laser beams in focus over the surface of the powder bed. A commonly employed method of scanning a laser beam is the galvo-scanner, but an uncorrected galvo-scanner will produce a spherical field of focus and a planar field of focus is required by the process. One of two solutions can be used to compensate for this inherent spherical shape: adjust focus between the laser and the galvo-

scanner or adjust focus between the galvo-scanner and the powder bed. The first case requires the use of a motorised focussing element that is synchronised to the orientation of the galvo-scanner but is not commercially favoured for metal systems due to its high cost despite being available for systems up to 4 kW [7]. The second solution utilises a passive optical element whose focal length is dependent upon the angle of the incoming beam called an f-theta lens. This element can limit power handling but due to its lower cost, greater reliability and simplicity it is the favoured commercial solution. The geometry of the f-theta lens is such that it is optimised for a single point source and so every galvo-scanned beam in a multiple beam system would require its own f-theta lens. This restricts the degree of overlap that each beam's footprint has over the powder bed surface. Commercial systems that use multiple galvo-scanned beams such as Concept Laser's X line 2000 R [8] arrive at an increased build rate by increasing the volume that can be built but at the rate defined by the material and the power of the lasers. This does not allow for a small item that does not span the multiple beams' footprints to be built any faster nor lead to a cost reduction of the machine itself.

Almost any method of increasing build rate is likely to find some commercial application. Similarly any method of reducing the cost of the technology is also likely to be welcomed. This work aspires to both these ends.

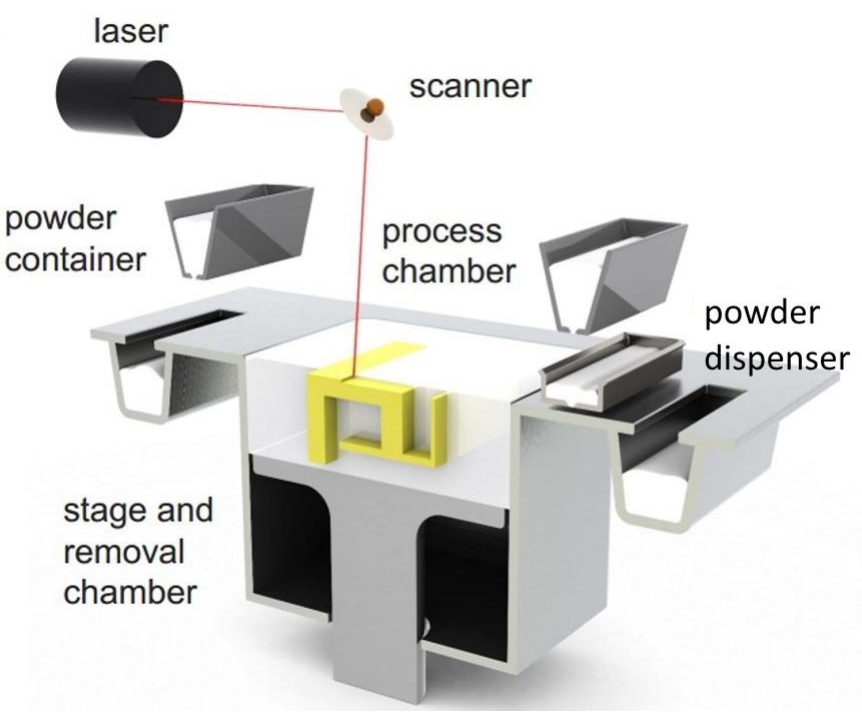

Figure 2 Illustration of powder bed fusion technology. [9]

1.3 Research aim

Given the desire to improve PBF technology build rates and that a single beam PBF system has a material dependent maximum build rate that cannot be overcome it is logical to consider how to configure a multiple beam system. A multiple beam system based solely upon galvo-scanning technology is limited in its scalability; the number of beams that can be employed within a given build envelope is restricted by the size of the galvo-scanners. Alternatively a gantry-based parallel beam system is more flexible and could be scaled to tens or even thousands of beams within the build environment. Considering the simplest implementation of a system with a linear array of beams the width of the powder bed would require a single pass of the beams per layer. A two dimensional array of beams would just require movement sufficient to cover the gaps between the beams effectively resulting in a multi-kW stamping system with a build rate limited by the powder handling mechanism.

Given the potential advantages of scalability the following research objective has been identified:

Investigate the feasibility, limitations and potential of using multiple beams for powder bed fusion fabrication.

This objective will be further refined into specific research questions after the literature review.

1.4 Thesis outline

1.4.1 Chapter 2 – Review

This chapter answers the questions: What is AM? How does it work? Why is it important? By which methods can metal parts be made? The case for using PBF is given along with some of the problems inherent in the process and review of scanning strategies is given. The research questions are presented within the context of the review.

1.4.2 Chapter 3 – Experimental system

This chapter covers the construction and development of the photonic system used for this research. The sub-components are described and their integration is detailed along with the communication methods and protocols.

1.4.3 Chapter 4 – Single spot processing

The technology developed within this research can be likened to that of dot matrix printing in that the optical head from which the multiple beams emerge is utilized in an 'expose-move-expose' approach. As such, single exposures to laser radiation are the fundamental building blocks and their effects upon substrate and powder are explored here.

1.4.4 Chapter 5 – Manufacture of lines

The sequential placement of melt spots to create melt beads is examined and the acquisition and preparation of data are detailed along with qualitative analysis of process parameters.

1.4.5 Chapter 6 – Multiple layer building

The placement of lines within the context of 2D scanning strategies is demonstrated by building single-layer rectangular ribbons in a thin layer of powder on a substrate or in deep powder. The builds are qualified by thickness, consolidation and relative density. Multiple layer cuboids are built and density measured.

1.4.6 Chapter 7 – Conclusions and future work

The results of chapters 4-6 are revisited and evaluated within the context of the research question and aims. Improvements to process and hardware are presented and future work suggested.

Chapter 2

Additive manufacturing

2.1 Introduction

The objective of this research is to develop a multiple beam powder bed fusion additive manufacturing system using laser diodes. This chapter will examine three of the conceptual components of that objective. Firstly, what is AM and why it is useful? Secondly, an explanation of the different types of AM is presented along with a section of the problems attendant on the PBF process. Thirdly, a multiple beam system is contextualised by examining the scanning strategies currently used by single beam systems and the current and previous incarnations of multiple beam machines.

2.2 What is additive manufacturing

The definition of additive manufacturing given by the American Society for Testing and Materials is:

"The process of joining materials to make parts from 3D model data, usually layer upon layer, as opposed to subtractive manufacturing and formative manufacturing methodologies." [10]

The key part of this definition is *"from 3D model data".* This eliminates a lasagne from being considered as an additively manufactured product despite being made to a predetermined pattern by the successive addition of material layers. Additive manufacturing is more than this; it is a process whereby the precise location of each volume of individual material is predetermined

by 3D model data followed by the accurate placement of said volumes during construction. This typically happens in a layer-wise manner to allow access to the interior during construction.

2.3 Why is additive manufacturing important

The release from the need for specific tooling has made AM an important step in product development. When using conventional processes that require, for example, a mould, the total development cost of the mould has to be absorbed by the number of parts that it produces. These costs can run to tens of thousands of dollars [11] and limit production to large volume runs in order to dilute the cost of the mould. When using AM technologies there are no tooling costs. Depending on the size of the part, a machine's build volume can contain many parts all of which can be different. Therefore single custom specification parts can be commercially viable as is evidenced by the growing use of AM for the creation of hearing aid shells [12]. Furthermore, by eliminating the creation of specialist tooling, lead times are reduced and prototype design can be rapidly cycled from concept to production part by allowing an earlier detection of fit or form errors.

Another significant advantage of AM is the freedom of design conferred by building using sequential layers. Geometrically complex shapes can be built just as easily as simple cubes. A complex honeycomb structure, for example, can be built more quickly than a solid cube because less material has to be added or fused to create the shape. This can offer a financial advantage over conventional techniques where the part would be difficult and therefore costly to make.

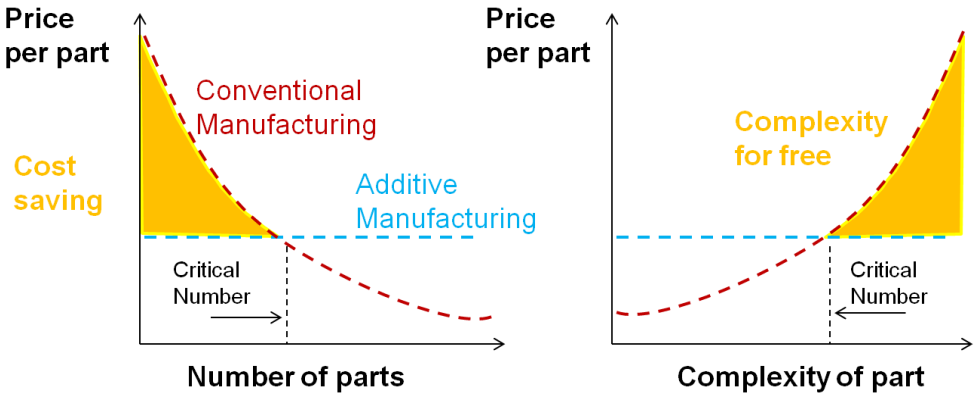

Figure 3 AM can offer cost savings when the required number of parts is low or the part complexity is high.

2.4 Types of additive manufacturing

In autumn 2009, as a result of the growing confusion within AM's nomenclature, the American Society for Testing and Materials convened the F42 committee to standardise some of the terminology [13]. A result of the committee's work was the subdivision of all AM technologies into seven basic types. A brief outline of each follows:

2.4.1 Vat Photopolymerisation

This technology uses photo-curable liquid monomer that is selectively solidified by exposure to a laser beam [3][14]. This technology was used in the first commercially available AM machine, the SLA-1 from 3D Systems Inc in 1988 [1], and the process was named stereolithography. In its original form a build platform is just submerged in a vat of liquid monomer and a UV laser beam is scanned across the surface of the liquid polymerising the monomer where required. When the layer is complete the build platform is lowered and a squeegee-like recoating blade is passed over the surface to ensure that the previously solidified layer is covered in liquid and the process is repeated [15]. Not all embodiments of this technology build from the surface down; EnvisionTec's Perfactory range [16] project the polymerising light through a window in the bottom of the vat and pull the part upwards out of the vat as it is being built.

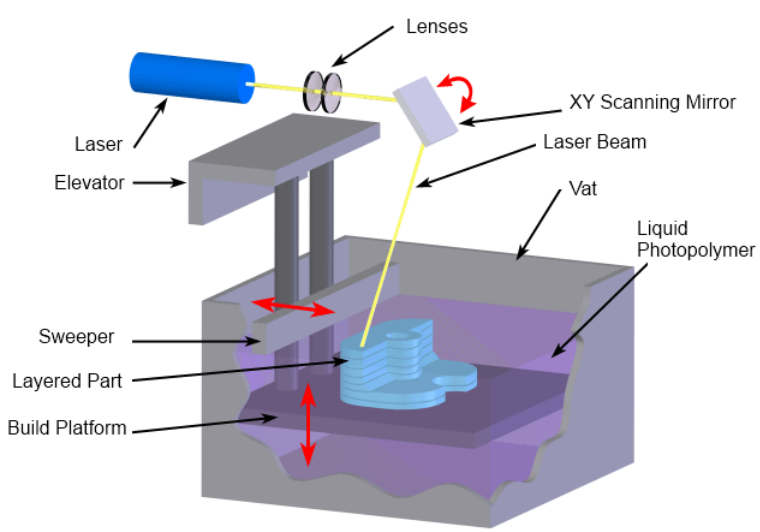

Figure 4 Illustration of the vat photopolymerisation process. [17]

Vat photopolymerisation can produce parts with a relatively high build rate: 500 cc/hour with 50 µm layer thickness for a Rapid Shape S60 [18] or with two photon curing a build resolution of hundreds of nanometres is possible [19]. However, the material choice is limited to photo-curable monomers and only single-colour parts can be produced although several individual colours are available [20]. It can be expensive to fill the vat to start with but any un-polymerised material can be re-used. Support structures are needed when producing overhanging parts to eliminate part sag. These structures must be removed in the post-processing steps which also involve washing away any uncured polymer together with a final curing in a UV oven [21] or a thermal curing [22].

2.4.2 Binder Jetting

This is a powder-bed-based technology where an inkjet-style printer head traverses the build chamber selectively depositing a binding liquid. After each layer has been fused by the binder, the build chamber and the powder bed that it contains is lowered, a re-layering roller or blade spreads a new layer of powder and the process repeats [23]. The unbound powder serves to support the part as it is built so no support structures are required and any un-fused powder can be recycled. This is a relatively quick process with build rates of 47 litres/hour using 400 µm thick layers for a Voxeljet VX2000 [24] and can produce coloured parts if coloured binder is used, such as a Projet 4500 from 3D systems [25].

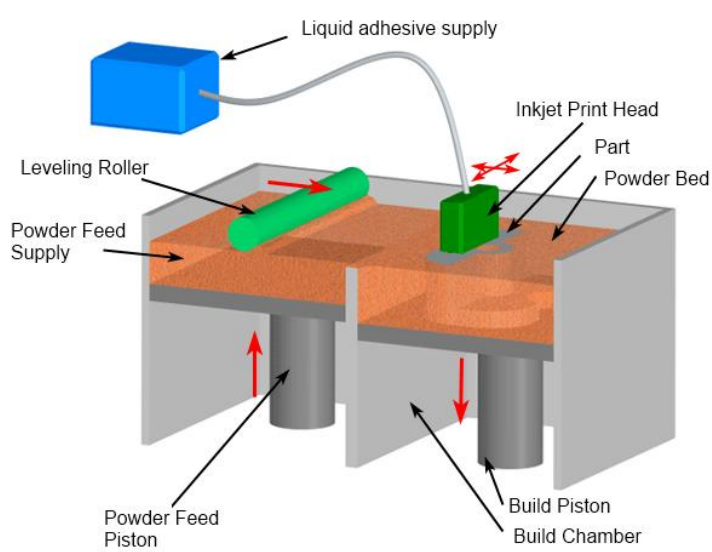

Figure 5 Illustration of the binder jetting process. [26]

The surface finish from binder jetting is not as good as from vat polymerisation due to a certain amount of un-fused powder adhering to the part. However, an advantage of this technology is that any material that can be powdered can be used [3]. Metal parts can be created with this technology although to create fully dense parts requires several post-processing steps such as burning off the binder and sintering the powder together in a furnace and then infiltrating the part with a lower melting point metal.

One of the main industrial uses for this technology is using foundry sand to create cores and moulds for casting metal parts. The S-Max Furan [27] from ExOne is built for this purpose and has a 1.8 x 1.0 x 0.7 m build envelope and with a layer thickness of 0.28 mm can build at 60 litres/hour.

2.4.3 Material Jetting

Material jetting technology uses an ink jet style printer head that is translated across the build platform whilst depositing material. This is similar to binder jetting but here it is the build material itself that is jetted whereas in binder jetting the build material is pre-placed in the powder bed. The jetted material is in a liquid droplet form and is hardened by either cooling or UV curing [3][23]. In between each deposition phase a milling stage can be employed to machine the top surface planar before the build platform is lowered and the next deposition phase occurs. Using this technology, overhanging parts require support but since the machines can have many printer nozzles depositing materials with a variety of structural qualities or colours a specific support material can be added as part of the build. Support materials have been developed from water-soluble gels to minimise time spent in post processing the parts. A wide variety of plastic materials can be used in this technology even within the same build to create multi material parts [28]. Due to the small droplet size used and the additional milling stages this technology can deliver very high resolution parts: A Max^2 machine from Solidscape can produce parts to 5000 dpi in X and Y and 8000 dpi in Z [29]. This can also be a relatively quick process with build speeds of 2.7 litres/hour for a Projet 660 Pro from 3D systems that has 1520 jets [30].

Due to the high resolutions possible using this technology it can be used in creating wax investment casts for jewellery patterns. The ability to print simultaneously in many colours and materials has led to this technology being used for realistic product prototyping.

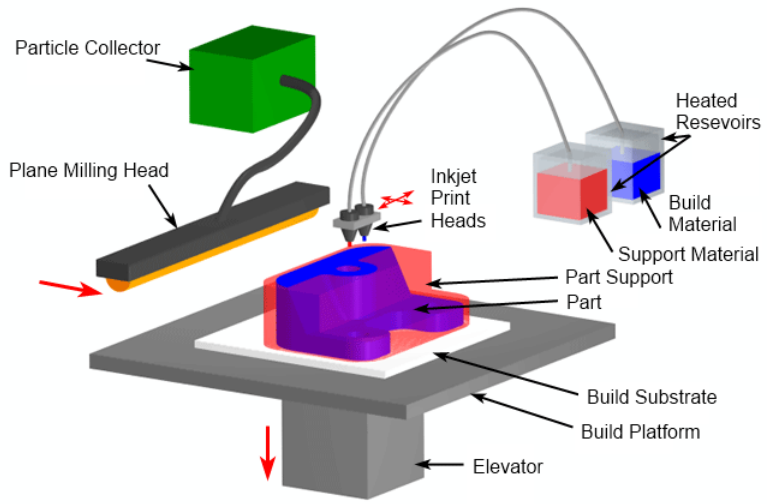

Figure 6 Illustration of the material jetting process. [31]

2.4.4 Material Extrusion

Material extrusion technology uses filaments of plastic that are fed through a heated extrusion head which scans the build area, selectively depositing material that sets by cooling [32]. After each layer is deposited either the build platform moves down or the extrusion head moves up by a layer thickness and the process is repeated. This technology is similar to material jetting, however the key difference is that the build material is extruded under pressure from the building nozzle rather than jetted [3]. Build material and support material where needed are typically thermo-setting plastics, thus limiting the choice of materials but allowing a wide range of individual colours to exist. The build rates for this technology are defined by the diameter of the extrusion nozzle. Typical nozzle diameters are between 0.3 and 0.5 mm [33][34] and so the resolution of the parts is relatively poor. 3DP's Workbench machine has a large build volume of 1 m x 1 m x 0.5 m and comes with a 0.6 mm nozzle as standard but a 2.5 mm diameter nozzle is available to achieve the build rate of over 900 cc/hour necessary to produce such large parts in a reasonable time [35]. This technology can be made cheaply and is the choice of the hobbyist with models currently selling for as little as $200 for a QU-BD OneUp 3D printer [36]. The cheaper hobbyist machines tend to use only one build material and so models are a single colour, but professional machines have many extrusion heads and can print in multiple colours such as 9 for a Dimension 1200 from Stratasys [37].

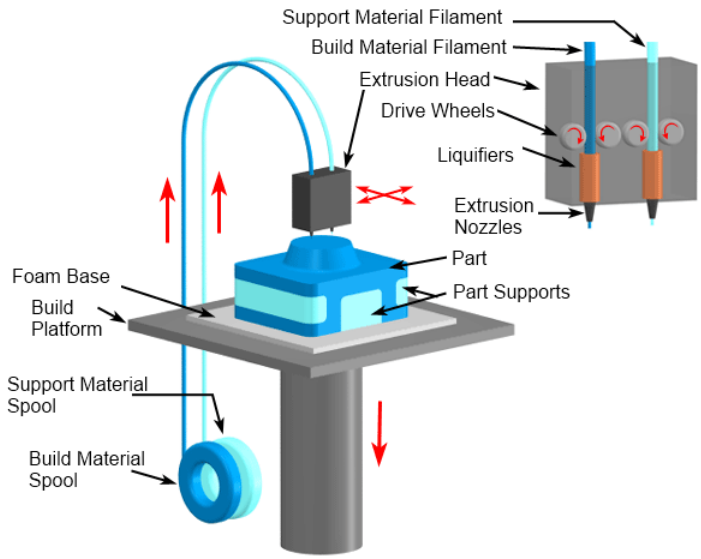

Figure 7 Illustration of the material extrusion process. [38]

2.4.5 Sheet lamination

The sheet lamination process involves stacking, fusing and shaping successive sheets of material [39]. After each layer is cut the build platform lowers and the next sheet is drawn into position. Each layer can be cut to shape by knife, laser or milling machine [40][41][3] and as a consequence the technologies are quite different if they use, for example, paper cut with a knife or metal ribbons machined by a CNC mill. Unlike the other AM technologies all waste material is scrap using this process; it is either milled away in the case of metal ribbons or is left behind as a support material for paper parts but diced to enable easy part removal from the build volume.

Fabrisonic's metal consolidation process uses no adhesive but ultrasonically welds the sheets together under high pressure [42]. These machines use a milling head to cut the sheets to shape and tend to have a large workshop footprint. Although due to the low temperature build process, plastic sensors can be built into metal devices and a wide variety of dissimilar metals can be welded together creating graded materials [43].

Paper based machines can use sheets with pre applied adhesive [39] or plain sheets with adhesive that is selectively deposited [40]. Full colour parts can be produced with this technology if the machine is equipped with a colour print head such as the Mcor Iris [44] and the build material is cheap. However, the use of parts created from paper is limited to demonstration

models. The build rate for the Mcor Iris is given as 25 mm/hour producing a build rate of over 1500 cc/hour if a brick of A4 dimensions was printed. In practice the build rate is less than this depending upon what percentage of the A4 sheets is used for the build object.

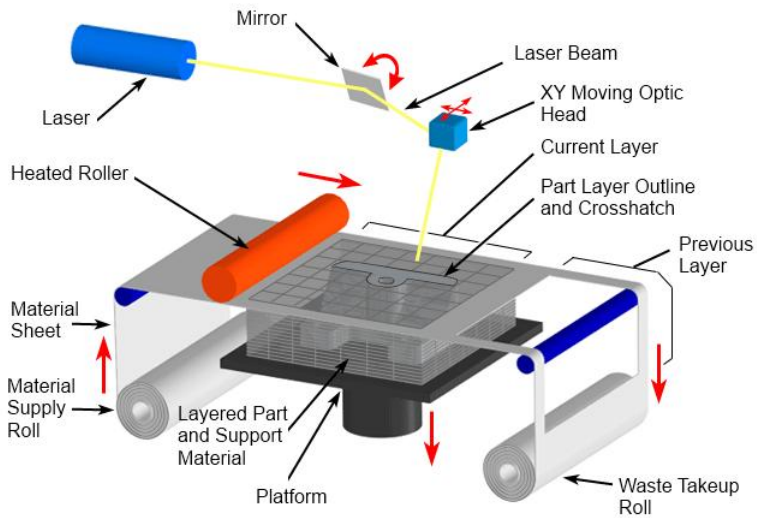

Figure 8 Illustration of the sheet lamination process. [45]

2.4.6 Directed energy deposition

This technology uses focussed thermal energy to fuse materials by melting as the material is being deposited [46]. The build head is typically articulated to move in five axes relative to the work piece allowing these processes to build more freely in space and to break from the layer by layer approach common to all other AM varieties. Various forms of this technology exist such as e-beam and wire stock used by Sciaky's 'Electron Beam Additive Manufacturing' (EBAM) or laser and powder blown through a nozzle used by Beam's 'Construction Laser Additive Directe' (CLAD). In either type of system the resolution and surface finish is relatively poor. However, deposition rates can be high, for example up to 20 lbs/hour for Sciaky's EBAM process [47] which equates to ~1000 cc/hour depending upon material. An advantage of the blown powder variant is if two or more separate powder supply streams are used then functionally graded parts can be created, as is possible using an Optomec MR7 [48].

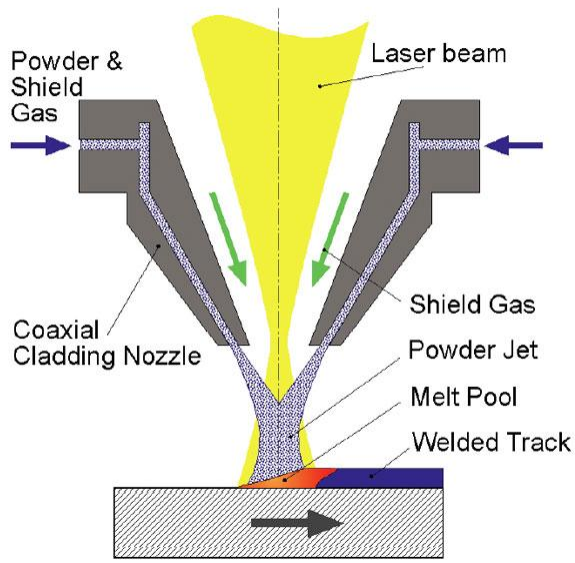

Figure 9 Illustration of the directed energy deposition process. [49]

Due to the poor surface finish and the need for subsequent machining this technology is used in creating near net shape components from materials such as tool steels which are difficult to machine [50], or in applying a hard wearing cladding such as tungsten carbide in order to prolong tool lifetime [51]. Also, as the deposition process is not constrained within a parallel layering format it is possible to use this technology to repair parts such as the replacement of a broken gear tooth, albeit with subsequent machining [52].

2.4.7 Powder bed fusion

Powder bed fusion technology is similar to binder jetting technology in that the build material is preplaced in a powder bed, but this technology uses an energy beam to sinter or melt the powder grains together. Once a layer has been selectively fused the powder bed is lowered, another layer of powder is spread, the process repeats, and parts can be supported by the un-fused powder. However, due to the thermal stresses involved the parts are usually anchored to the build platform to prevent buckling [53]. As with vat photopolymerisation it can be costly to fill the machine at first as material sufficient for the entire build envelope is required. However, any unused material may be recycled. A wide range of materials can be used with this technology including plastics, ceramics and metals [54][55][56].

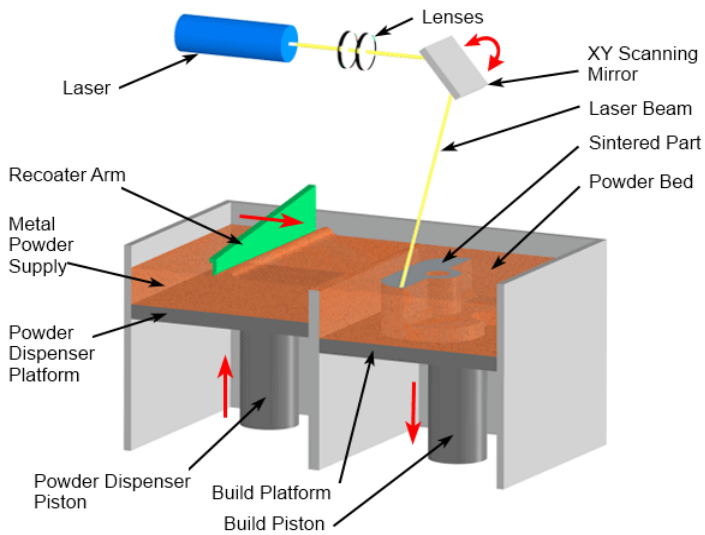

Figure 10 Illustration of the powder bed fusion process. [57]

The first commercial PBF machine capable of creating parts using metal powder was DTM's 'Sinterstation 2000' released in 1993. This machine was designed for sintering plastic parts but could use a material called 'RapidSteel 2.0' which comprised metal grains coated in polymer. In operation the CO_2 laser only melted the polymer coating sintering the grains together into a 'green' part. Subsequently the part was baked in an oven to burn off the polymer and to sinter the metal grains thereby creating a 'brown' part. To create a dense metal part this 'brown' part was then vacuum infiltrated with a lower melting point metal such as copper [3, p. 227]. The recommended process parameters for 'RapidSteel 2.0' were: laser power = 20 W, scan speed = 1524 mm/s, scan spacing 75 µm and layer thickness = 75 µm and could build at 29 cc/hour [58]. However this build rate was for green parts and the lengthy post processing steps would decrease the build rate significantly for finished parts.

In the subsequent 25 years the constituent technologies of PBF (the laser, the computer and powder feedstock manufacturing) have advanced and reduced in price leading to a proliferation of PBF machines for a wide range of applications. The sizes of parts now made with metal based powder bed fusion technology range from millimetres for dentistry and jewellery to hundreds of millimetres for the automotive and aerospace industries. As a consequence machines have been produced with a commensurate range of build volumes. Table 1 gives the specifications of the smallest and largest machines produced by seven of the leading PBF machine producers together with an intermediate example.

Table 1 PBF machine specifications taken from manufacturer's data sheets

	Power (W)	**Scan speed** (m/s)	**Spot size** (µm)	**Build rate** (cc/hour)	**Build volume** (L)	**Machine volume** (m^3)
Arcam						
Q10	3000	8000	140	~	7.2	5.7
Q20	3000	8000	140	~	37	9.2
A2	3000	8000	250	80	15	3.7
SLM Solutions						
SLM 125	400	10	70-100	25	2.0	3.1
SLM 280	2 x 700	10	80-115	88	29	8.4
SLM 500	4 x 700	10	80-115	171	51	39
Renishaw						
AM 250	200	~	70	20	19	~
AM 400	400	~	70	~	19	~
RenAM 500Q	4 x 500	~	80 to 500	150	22	5.7
Realizer						
SLM 50	120	~	~	~	0.2	0.3
SLM 125	400	~	~	20	3.1	2.0
SLM 300i	1000	~	~	~	27	3.7
EOS						
M80	100	7	30	~	0.5	~
EOSINT M 290	400	7	100	~	20	7.1
EOS M 400-4	4 x 400	7	100	100	64	16
3D Systems						
ProX DMP 100	50	~	~	~	1.0	1.8
ProX DMP 200	300	~	~	~	2.5	3.5
ProX DMP 300	500	~	~	~	32	12
Concept Laser						
Mlab Cusing R	100	7	50	1 to 5	0.6	1.6
M1 Cusing	400	7	50	2 to 15	16	8.1
X Line 2000R	2 x 1000	7	100 to 500	120	160	69

The majority of commercially available metal based PBF machines use a laser as the energy source but a Swedish company, Arcam, uses an e-beam and magnetic deflection coils.

Due to the absence of mirrors and optical elements, high powers (3 kW) can be delivered and coupled with fast scan rates that are able to create multiple melt pools a build rate of 80 cc/hour is possible [59]. However, the disadvantages of using an e-beam are that a vacuum is needed within the processing environment and that with a minimum beam diameter of 140 μm, compared to a typical laser system's minimum beam diameter of 70 μm, the resolution and surface finish is poorer than that of laser based systems [60].

Using the more commonly adopted laser technology much smaller beam diameters can be achieved, such as 30 μm for an EOS M80 and build rates of up to 150 cc/hour can be obtained with Renishaw's RenAM 500Q [61]. The higher build rates given in Table 1 are all achieved in multiple beam systems where either two or four fibre lasers scan individual halves or quarters of the powder bed with some footprint overlap; that is 50 mm for an EOS M400-4 [62]. Improvements in productivity can also gained by employing a bi-directional powder recoating system, EOS (Electro Optical Systems) and 3D systems, or the dual build modules of the Xline 2000R from Concept Laser [8]. In this case there are two modules that can be automatically swapped at the end of a build so that the time for part removal and powder refilling can be eliminated from the production chain. Improvements in build quality by reducing residual stresses within the parts are now achieved by the use of a heated base plate, up to 550 °C for a SLM 280 from SLM Solutions. Powder handling is potentially hazardous and many machines now have an integrated powder recycling system such as Realizer's SLM 300i and Renishaw's RenAM 500Q or a modular powder loading unit such as Concept Laser's MLAB Cusing 200R to minimise this risk and to make refilling easier.

The high resolutions possible with small focal spots and build rates achievable with multiple beam systems have led to market domination for the production of additively manufactured metal parts using powder bed fusion technology [63].

2.4.8 Comparison of additive manufacturing technologies

The versatility of AM technology is such that any AM machine can produce almost any part. However all technologies are not equal, especially in the choice of build material, and each has its own sphere of useful application. Table 2 gives a generalised overview of each of the seven previously detailed technologies' attributes.

Table 2 Comparison of additive manufacturing techniques [64].

Type	Vat Polymerisation	Binder Jetting	Material Jetting	Material Extrusion	Sheet Lamination	Directed Energy Deposition	Powder Bed Fusion
Material type	Liquid (Photopolymer)	Powder	Liquid (Photopolymer, wax)	Solid (Filaments)	Solid (Sheets)	Powder (Metal) Solid (Wire)	Powder (Metal, Polymer, Ceramic)
Materials	Thermoplastics (Elastomers)	Ferrous metals such as Stainless steel; Non-ferrous metals such as Bronze; Elastomers; Composites; Ceramics	Thermoplastics such as Acrylic (Elastomers)	Thermoplastics such as ABS, Polycarbonate, and Polyphenylsulfone; Elastomers	Thermoplastics such as PVC; Paper; Composites (Ferrous metals; Non-ferrous metals; Ceramics)	Ferrous metals such as Steel alloys, Stainless steel, Tool steel; Non-ferrous metals such as Aluminum, Bronze, Cobalt-chrome, Titanium;	Ferrous metals such as Steel alloys, Stainless steel, Tool steel; Non-ferrous metals such as Aluminum, Bronze, Cobalt-chrome, Titanium; Ceramics. Thermoplastics such as Nylon, Polyamide, and Polystyrene; Elastomers; Composites
Minimum feature size	0.10	0.20	0.15	0.13	0.20	0.75	0.13
Minimum layer thickness	0.03	0.05	0.02	0.13	0.05	N/A	0.03
Tolerance	0.13	0.10	0.03	0.13	0.10	0.25	0.25
Surface finish	Smooth	Rough	Smooth	Rough	Rough	Rough	Average
Build speed	Average	Very Fast	Fast	Slow	Fast	Very Fast	Fast
Applications	Form/fit testing, Functional testing, Rapid tooling patterns, Snap fits, Very detailed parts, Presentation models, High heat applications	Concept models, Limited functional testing, Architectural & landscape models, Color industrial design models, Consumer goods & packaging	Form/fit testing, Very detailed parts, Rapid tooling patterns, Presentation models, Jewelry and fine items	Form/fit testing, Functional testing, Rapid tooling patterns, Small detailed parts, Presentation models, Patient and food applications, High heat applications	Form/fit testing, Less detailed parts, Rapid tooling patterns	Repair of worn components, Modification of tooling for re-use, High heat applications, Aerospace parts	Form/fit testing, Functional testing, Rapid tooling, High heat applications, Medical implants, Aerospace parts

2.4.9 Suitability of techniques for metallic part creation

All seven of the previously described varieties of AM can in some way be used to make metal or metal-included parts. The only technology not capable of making fully metallic parts is that of vat photopolymerisation although this technology has been used to create electrically conductive parts by the addition of a metallic powder to a photopolymer followed by a post processing sintering stage [65]. Of the remaining six technologies only binder jetting requires the use of non-metallic build materials, namely the binder. However, binder jetting technology can be used to make fully metallic parts after the binder has been burned off [3, p. 227] but lengthy post-processing has limited its current commercial application for metal parts.

Material extrusion technology has been used by Ladd *et al*. to produce free standing structures using a low melting point alloy of gallium and indium [66] and metal material jetting technology has been explored for low melting point metals such as tin based solder [67], zinc [68] and aluminium[69]. However to directly make single material high melting point metallic parts either sheet lamination, powder bed fusion or directed energy deposition is required.

2.5 Build problems

Powder bed fusion is a complicated process involving absorption of energy, heat transfer, phase change and densification, fluid flow, evaporation, solidification and chemical reactions [70]. If the processing conditions/parameters are not carefully balanced and controlled during processing, defects such as porosity, balling, buckling and de-lamination can occur, which can affect part density, microstructure and geometrical accuracy.

2.5.1 Balling / porosity

Porosity is characterised by the presence of voids within the bulk of the final part which subsequently reduce density and part strength. Balling is characterised by the fragmentation of melted material into disconnected balls when scanning. Both porosity and balling have similar causes and in some ways porosity can be considered to be symptomatic of the onset of balling [71].

The two main factors that influence the tendency for balling are insufficient wetting to the previously consolidated layer and the tendency of metals in the liquid phase to have high

surface tension and low viscosity [72]. To avoid balling requires the correct balance of power and scanning speed and each material has its own processing window [73][74].

Balling occurs when the molten material does not wet to the lower layers and surface tension causes spheres to form [75] or when high scan speeds create long melt pools that are unstable and break up due to Rayleigh instabilities. Rayleigh instability breaks up the melt cylinder to minimise surface energy when the length to diameter ratio exceeds ~3 [72]. The minimum time to break can be expressed as Eqation (1) where γ_{LV} = surface tension, ρ = density and r = radius of melt cylinder [76].

$$t_{break} = \left(0.3433 \cdot \sqrt{\frac{\gamma_{LV}}{\rho r^3}}\right)^{-1} \tag{2.1}$$

This means that balling is a time-dependent process and if solidification can occur quickly then the tendency for balling can be reduced [75]. However the breakup time for a Fe melt bead with diameter 0.4 mm is 0.5 ms which is much less than the solidifying time [76], so wetting to the previous layer is important to minimise balling [77]. Wetting can be improved by the presence of certain alloying metals that lower surface tension such as the addition of P to Fe [77] or by the reduction of oxygen within the processing environment [78].

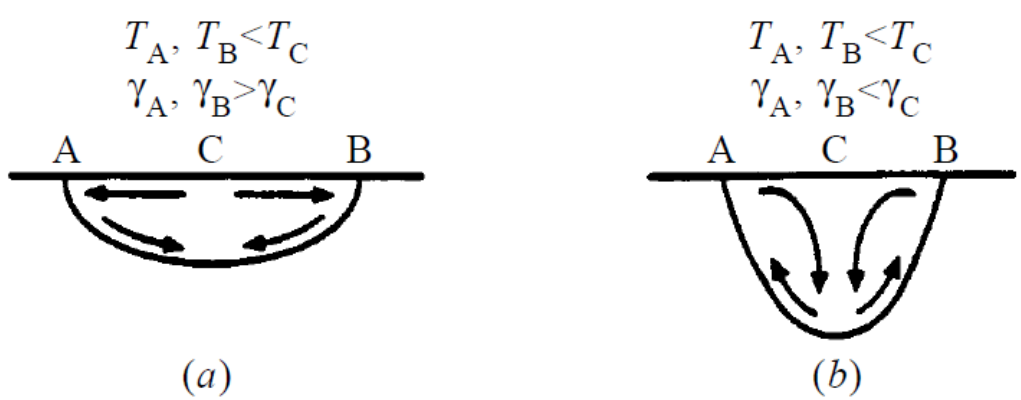

Figure 11 (a) Outward flow of convection currents caused by negative surface tension gradient. (b) Inward flow of convection currents caused by positive surface tension gradient. [80]

The presence of surface tension gradients within the melt pool can be another cause of balling as they cause Marangoni flow [79]. The presence of this flow is enough to influence the

circulatory direction of convection currents within the melt pool [80]. The direction of the Marangoni flow is dictated by the sign of the surface tension gradient and is shown in Figure 11 [80]. The majority of metals have a negative surface tension gradient but the presence of oxygen can change the sign of the surface tension gradient and thus the direction of the convection currents [81]. An outward flow tends to aid wetting whereas an inward flow tends to promote balling.

2.5.2 Warpage / buckling

Buckling and warping are characterised by geometrical distortions to the intended form of the part [82]. These distortions are caused by thermal stresses introduced by differential cooling. A difference in the cooling rate between the top and bottom of the part exists on account of the localised rapid heating caused by the laser followed by rapid cooling of the top surface and the relatively slow conduction through the part [83]. This is exacerbated by the addition of relatively cool powder during the re-layering phase and the cool inert atmospheric gas [84]. Thus both material properties and processing parameters affect the thermally induced stresses in the final part [77].

The buckling mechanism is caused by the thermal expansion of a heated surface which results in elastic and plastic deformations of the top layer. Upon cooling the elastic deformations relax but the plastic deformations remain, resulting in residual stress [77]. These stresses accumulate layer by layer and if the rate of cooling can be lowered for each layer then the final total stress can be reduced. This can be achieved by the use of a heated base plate [85] or pre-heating the powder bed and supply powder [53]. Rescanning is reported to relieve stress and thus reduce part curl [86]. A study of thermal stress by Osakada and Shiomi showed that rescanning reduced stress in nickel alloy parts by 55 % [87]. Also a scanning strategy that divides a large area into several smaller areas can help to minimise thermal stress [75].

As well as reducing the geometrical quality of the part, buckling can also cause the build to fail if the powder re-layering mechanism fouls a protruding corner of the part and dislodges it in the powder bed [75]. To avoid this and help with stress containment parts are usually anchored down to the substrate during build [77].

2.5.3 De-lamination

De-lamination is characterised by cracks and gaps between the horizontal layers of a part. Insufficient inter-layer consolidation and thermal stresses are the primary causes of de-lamination. The thermal stresses involved in de-lamination are the same as for buckling and their causes have been covered in the previous section.

Layer thickness has a significant effect upon inter-layer consolidation. When powder is selectively melted in a PBF process the incident energy must not only be sufficient to melt the current layer of powder but must also melt part of any previously consolidated layers.. The slower energy transfer associated with a thick layer leads to a larger heat-affected zone which in turn increases stress and the tendency for de-lamination. Therefore thinner layers tend to produce a greater degree of interlayer bonding [88].

The degree of wetting between melt and previously consolidated material affects inter-layer consolidation and is detrimentally affected by the presence of oxides on the surface of the melt or substrate thus the previous layer must be sufficiently re-melted to break down and remove any oxide layer to provide a clean surface for the new melt [89].

2.6 Scanning strategies

Parts created by the powder bed fusion form of additive manufacturing are built layer by layer. To build a part each successive layer must be fully melted, solidified and bonded to the layer beneath over the area that corresponds to the intersection of a slicing plane and the 3D computer model of the part to be created.

As yet there is no method for stamping a layer in one exposure for metal based powder bed fusion as is possible in vat polymerisation and exemplified by Cubital's Solid ground curing technology [3, p. 105]. In this case stamping is achieved by exposure of the photopolymer by a UV flash lamp through an appropriate mask [90]. Single exposure stamping has not been developed for metal based powder bed fusion due to the high level of energy needed to fuse a large area of metal powder and the limited power handling capabilities of the existing technologies that could facilitate the stamping process, such as spatial light modulators. At the time of writing, 41 W/cm^2 is a high average output power from a Hamamatsu SLM [91]. To calculate the effects of illuminating a 316L sample with this intensity the heat transfer equations can be used.

The heat transfer equations have analytical solutions for some special cases. One of those is for temperature change for a semi infinite medium under uniform illumination [92]

$$\Delta T(z,t) = \frac{2H}{k}\sqrt{\alpha t}\ \ ierfc\left[\frac{z}{2\sqrt{\alpha t}}\right] \tag{2.2}$$

where T = temperature, z = distance from the surface, t = time, H = incident intensity , k = thermal conductivity, α = thermal diffusivity.

The temperature rise at the surface can be obtained by setting *z=0* and given that

$$ierfc(0) = \frac{1}{\sqrt{\pi}} \tag{2.3}$$

this gives

$$\Delta T(0,t) = \frac{2H}{k}\sqrt{\frac{\alpha t}{\pi}} \tag{2.4}$$

rearranging for *t* yields

$$t = \frac{\pi}{\alpha}\left(\frac{k\Delta T(0,t)}{2H}\right)^2 \tag{2.5}$$

then using median values for *k* and α and melting temperature from Appendix A α = 5e-06 m^2/s, k = 25 W/m/K, ΔT = 1400 °K and H = 41 W/m^2. This gives a time to raise the surface temperature of a semi infinite block of SS 316 from room temperature to its melting temperature of ~1100s. As a result, a typical SLM configuration uses a condensed energy source such as a focused laser or e-beam spot that is swept across the bed in a given pattern at a given speed to achieve the desired selective melting.

2.6.1 What is a scanning strategy

A distinction can be made between the build strategy and the scanning strategy. The build strategy will control such variables as the specific material, the powder particles size distribution and part orientation within the powder bed. The scanning strategy will control the laser power,

the speed at which the spot or spots are moved and the patterns used to cover the surface of the bed. The layer thickness will be considered as part of the scanning strategy in this report as it has bearing upon the speed at which the laser should be scanned and the power to be used.

Energy density

The use of single or multiple spots formed by focused energy beams requires that the spots are scanned across the layer to selectively melt the layer where needed. The simplest method is to raster scan the spot in parallel lines across the surface at a speed sufficient to melt the layer thickness of powder and to partly melt the pre-consolidated layer beneath. This simple strategy is the backbone of many of today's successful strategies but it has become optimized and adapted to improve its efficiency according to the particular chosen success metric. Some of the metrics by which researchers have judged the effectiveness of their proposed scanning strategies include density/lack of porosity [56], surface roughness [93], microstructure [75], residual stress [94], lack of cracking [95] and mechanical properties such as hardness [96] and Young's modulus [97].

Aside from the pattern of scanning, the key parameters to a scanning strategy are the power of the energy beam, the scanning speed, the spacing between successive scan lines and the thickness of the powder layer. All these parameters affect the temporal and spatial energy distribution throughout the building process. Various researchers have combined these parameters into energy density measurements to allow for parameter-set comparison. They are set out below.

Linear energy density

In a study using W-Cu powder, Gu and Shen [98] define a linear energy density parameter as a means of assessing the combined effect of power and scanning speed, which they consider to be the most important parameters for controlling powder melting. In single layer building trials they establish that a linear energy density of 13-19 J/mm yields the highest density samples but place limits upon the variation of scan speed.

$$Linear\ energy\ density = \frac{P}{v} \qquad \begin{array}{l} P = power \\ v = scanning\ speed \end{array}$$

In a sequence of single layer, single track experiments using Inox 904L powder, Yadroitsev *et al*. [99] observe that for a constant *P/v* ratio the quality of the tracks produced is constant across a range of powers. However they also note from multi-layer builds that the difference in track width due to different scanning speeds decreases with an increasing number of layers. This last observation, and Gu and Shen's observation that the linear energy density metric is only valid between certain bounds of scanning speed, suggests that this metric is of limited use for scanning strategy definition. Niu and Chang have observed that a low power and slow scan speed can give the same energy density as a high power and high speed, but with a high scan speed the material has a faster cooling rate and so the tendency for balling (as balling is a time dependent process) can be reduced [100].

Area energy density

In a single layer study using a WC-Co powder mix, Maeda and Childs [101] defined an area-based energy density parameter and found that the density of the sample and the thickness of the sintered layer increased with energy density. However, of the three ways to increase energy density (increase power, decrease scan speed or decrease scan spacing), they argue that firstly the power should be as high as possible to increase local energy density. Then secondly to decrease the scan speed rather than the scan spacing as the powder cools between scans.

$$Area\ energy\ density = \frac{P}{vd} \qquad \begin{array}{l} P = power \\ v = scanning\ speed \\ d = hatch\ spacing \end{array}$$

Kruth *et al*. [102] in a study using an iron-based powder mix also use a similar area based energy density metric. They do not draw any conclusions from its use but use it to expedite the exploration of parameter space. In their trials they also keep the power at full and vary the scan speed and scan spacing whilst keeping the energy density to between 4 and 6 J/mm^2.

Volumetric energy density

A volumetric energy density is proposed by Simchi and Pohl [56] in their study using iron powder. They justify the use of this metric by arguing that the density of the final part is the average of the densities of each sintered track and therefore the total energy input *per* volume

directly affects the final part density. This is verified by their evidence of increased density as a function of energy density.

$$Volumetric\ energy\ density = \frac{P}{vdh} \qquad \begin{array}{ll} P = power & d = hatch\ spacing \\ v = scanning\ speed & h = layer\ thickness \end{array}$$

In a study of the microstructure of Ti-6Al-4V, Thijs *et al*. [103] define a volumetric energy density and observe a correlation between Vickers microhardness and the applied energy density. Also using Ti-6Al-4V, Vandenbroucke and Kruth [104] establish that fractional part density increases with increasing volumetric energy density.

2.6.2 Research based scanning strategies

The following sections detail some of the adaptations made to the simple raster scan including bi-directional raster [105], spiral [86], perimeter then fill [88] and random islands [106].

Uni-directional / bi-directional

The simplest scanning strategy is that of parallel tracks. Subsequent parallel tracks can be created in a constant direction, termed 'uni-directional', or in alternate directions, termed 'bi-directional'.

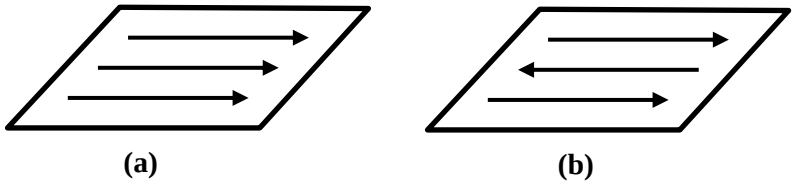

Figure 12 Linear scan patterns. (a) Uni-directional. (b) Bi-directional.

In a study using Ti6Al4V, Kruth *et al*. [106] compared uni-directional and bi-directional scanning, which they term 'zig-zag'. They found that the relative density of the samples was higher for the bi-directional scanning strategy using the same values for power, scanning speed and hatch spacing. However, they give no explanation for this effect.

Yasa *et al*. [105] performed a series of trials investigating the effect of processing parameters upon edge height and established that the uni-directional scanning strategy is inferior

to the bi-directional in that it tends to produce a higher edge to the sample at the trailing end of beam travel which can cause interference between the re-layering mechanism and the part.

Alternating layer direction

An improvement to part quality can be achieved by alternating the scanning direction between the X direction and the Y direction for successive layers of the build. Thijs *et al*. [103] compared uni-directional, bi-directional and alternating layers and also found that uni-directional yielded the least dense samples whereas alternating layers gave the highest density samples for the same scan parameters. They give no reason for the bi-directional strategy being better than the uni-directional but they suggest that the alternating layer strategy is best because "the risk for having un-melted zones between adjacent scan tracks is lower" [103].

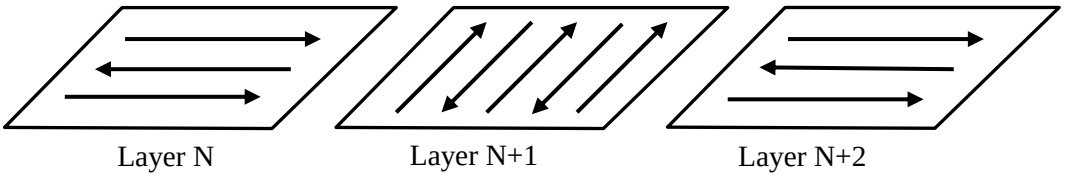

Figure 13 Alternating layer direction scanning strategy.

A two-layer sequence where the angle of rotation between the layers is 90 degrees is the most common alternating layer strategy. However, it is quite possible to have three or more layer sequences with other angles of rotation. In a study performed by Manfredi *et al*. [88] a three-layer sequence with 67 degree rotation between layers is successfully used, but as the results are not compared to a 90 degree strategy no comparison can be made.

Spiral scanning

A typical spiral strategy is shown in Figure 14 where it can be seen that 'concentric' may be a better description but this term has not been used in the research literature. Two versions of this scanning strategy are possible: those of outward or inward progression.

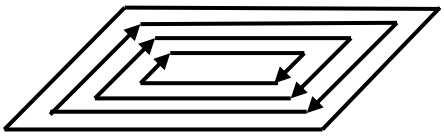

Figure 14 Spiral scanning strategy.

Dai and Shaw [107] compared an outward spiral pattern with a bi-directional pattern and as a result of finite element modelling concluded that an outward spiral pattern was the better scan pattern for reducing part distortion. As an opposing scan test example, Fateri *et al*. [86] built sample cuboids with silver powder and used the surface deformation as a metric to judge an inward spiral pattern to be worse than a bi-directional pattern. To compare these studies place the bi-directional scanning strategy between the outward and inward spiral strategies with the outward being the best and the inward being the worst.

Nickel *et al*. varied scanning pattern and calculated substrate distortion by the use of finite element models which they subsequently validated experimentally [108]. They created single layer squares with a simple raster, an outward spiral and an inward spiral pattern. They establish that the inward spiral pattern produces the lower and most uniform stresses and postulate that the last line to be scanned produces the greatest stresses. Consequently the inward spiral is effective because the final lines are the shortest. This is in opposition to the previous conclusions of Fateri *et al*. and Dai and Shaw however this is possibly because the studies are quite different. Dai and Shaw only model the heating of a plate, Fateri *et al*. build 10 mm high cubes and measure surface undulations and Nickel *et al*. measure substrate deformation from a single layer of blown powder deposition.

Re-melting

Re-melting or re-scanning is a technique employed in some scanning strategies to create parts with enhanced qualities. However the quality improvements that this technique confers come at the cost of increased build time.

Re-melting is used in the previous section's knit-scan strategy to increase part density. Kruth *et al*. [106] also improved part density with re-scanning in trials using stainless steel 316L powder. They show that re-melting reduced porosity from 0.77 % to 0.032 % in the best case which incorporated three re-melting passes *per* layer. Kruth *et al*. also demonstrate an order of magnitude improvement in top layer surface roughness by the application of re-scanning.

Re-melting can also have the effect of reducing thermal stresses. Wu *et al*. [75] use a re-melting scheme that is applied perpendicular to the layer's melting vectors to reduce buckling and Osakada and Shiomi [87] in a study using a nickel based alloy found that re-melting could reduce tensile stress by 55 %.

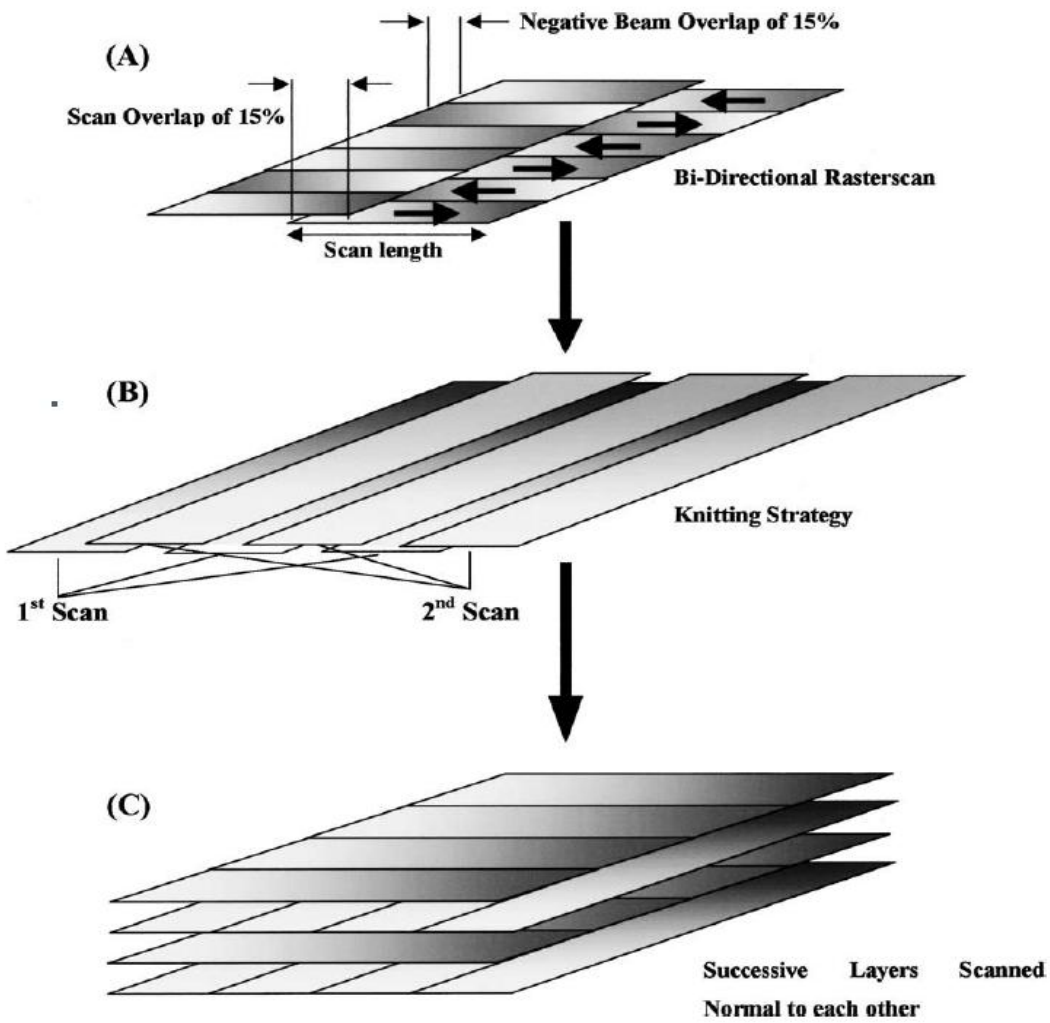

Figure 15 A complex knit scan strategy: Schematic (A) shows the bi-directional raster scan strategy with changing beam direction and beam overlap, schematic (B) shows the knitting strategy of the scan-units, and (C) how layers are scanned normal to each other to reduce porosity. [78]

Knit scan strategy

A complex scan and knit strategy has been developed by Morgan *et al* that results in densities of >99 % for stainless steel 316L [78] Figure 15. It involved raster scanning short vectors with a negative 15 % overlap between them to create scan units. All the odd numbered scan units were placed first then these scan units were then knitted together by the even numbered scan units with a positive 15 % overlap. A re-layering operation without height change was applied between the odd and even scan unit applications. Each successive layer was scanned

normal to the previous and each layer had a re-melting phase applied to release any trapped gases.

2.6.3 Commercial scanning strategies

The makers of commercial powder bed fusion systems tend to regard their scanning strategies as trade secrets and so it is difficult to obtain details directly from the companies. The majority of literature which does exist in the public domain is as a result of academic research using commercial systems.

The EOS M270 Xtended has been used by several researchers who have documented some of its scanning strategy details [93][88]. In this particular model, EOS have adopted a contour-fill-contour approach to scanning. Each layer is processed as follows: first the contour is scanned using a beam offset value so that the dimensions of the part are as desired, secondly, the interior is filled with bi-directional hatching; finally the contour is traced again with a specific beam offset to enhance dimensional accuracy. Each layer is processed in the same way but there is the option to rotate the direction of the fill scanning between each subsequent layer. In a study conducted by Manfredi *et al*. a rotation of 67 degrees between each layer is used [88]. Each layer is also subject to subdivision into areas labelled 'in-skin', 'up-skin' and 'down-skin' and these are given separate scanning parameters for power, scan speed and hatch spacing. All three 'skin' types are bi-directionally raster scanned. 'In-skin' or core is defined as that part of the layer that has or will have adjacent consolidated powder in the layer above and in the layer below. 'Down-skin' is that part of the layer that has unconsolidated powder in the layer below but consolidated powder in the layer above. 'Up-skin' has consolidated powder below and unconsolidated powder above. 'Down-skin' scanning parameters are used for two-layer thicknesses and 'up-skin' scanning parameters are used for three layers to improve surface quality.

Table 3 EOS scanning parameters. [93]

	Scan Speed (mm/s)	Power (W)	Hatching distance (mm)
In-Skin (core)	800	195	0.17
Up-Skin (3 layers)	1000	195	0.2
Down-Skin (2 layers)	900	190	0.1
Contour	900	80	X

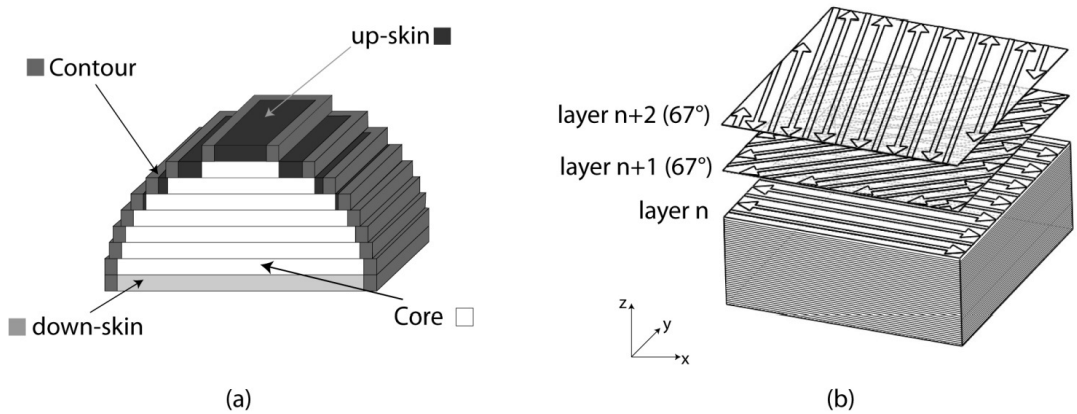

Figure 16 An EOS scanning strategy. (a) Illustration of part sections. (b) Optional layer rotation. [88]

The scanning strategy used in the MCP Realizer 250 is also a contour-and-fill strategy. The filling is bi-directional with the scanning direction alternating with each layer [109]. The strategy starts the scanning at the front left corner of the build chamber and works towards the back. The first layer is scanned in the X direction, the second is scanned in the Y direction and subsequently alternates direction.

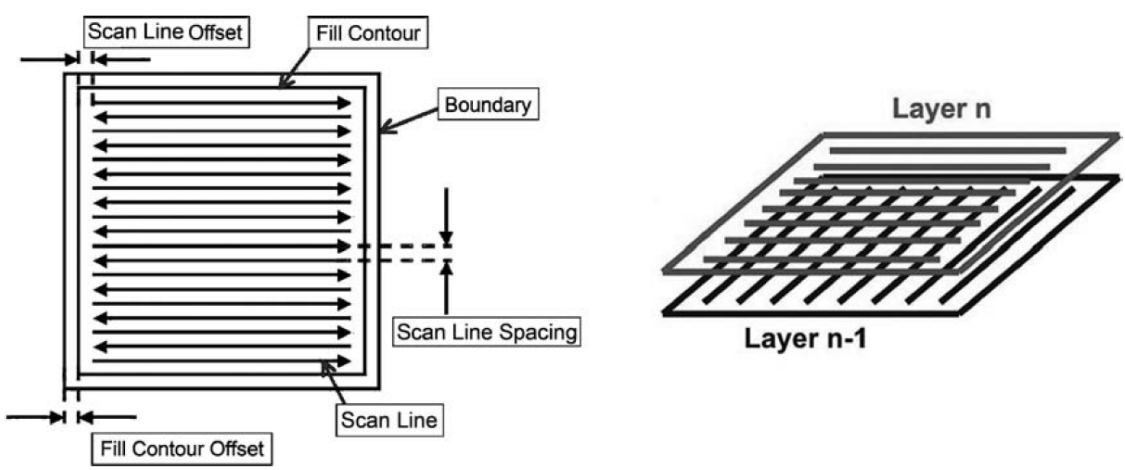

Figure 17 MCP Realizer scanning strategy. [109]

Machines produced by Concept Laser use a patented scanning strategy based upon a random island principle [110]. This is implemented in the M2 and M3 and the details of the scanning strategy have been documented by several researchers [95][111][112]. The random island scanning strategy involves dividing the area to be scanned into a 5 mm square grid that is typically aligned at 45 degrees to the direction of re-layering. However, Kruth *et al*. experimented with 15º and 45º and found 45ºto give the greatest stress reduction [106].

Each square is bi-directionally raster scanned with a user-definable hatch spacing and scan speed. The individual squares are scanned in a random order to help minimise thermal stress by distributing the heating. Once the hatching is complete the contour is scanned. To prevent any artefacts of the 'checkerboard' pattern propagating vertically throughout the build the origin of the 'checkerboard' pattern is successively shifted by 1 mm in X and Y between each layer.

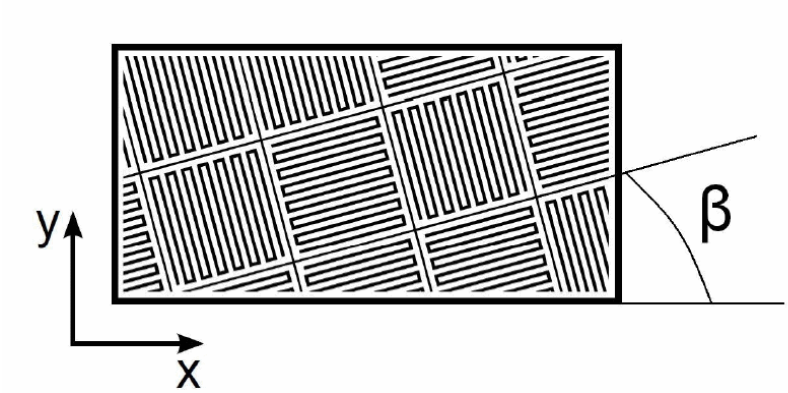

Figure 18 Concept Laser random island scanning showing bi-directionally scanned squares at an angle β to the re-layering direction. [106]

2.6.4 Multiple beam scanning strategies

All the previously described scanning strategies have been employed by equipment using a single energy beam. However, these strategies all lend themselves to being employed in multiple beam machines but with modification to allow for scan overlap. Current multiple beam systems include SLM solutions' SLM500 [113] that can have up to four fibre lasers fitted and Arcam's range of e-beam machines [114] which can use up to 100 beam spots, although these spots are created by time-sharing the output of a single electron gun [115]. These two technologies are in principle the same in that the beams' trajectories can be arbitrarily and

independently chosen to suit the demands of the scanning strategy: the laser beams by the use of galvo-scanning mirrors and the e-beams by the use of deflection coils.

However, there is an alternative approach to the delivery of multiple beams that involves linearly scanning an array of parallel beams across the powder bed. In 1996 Marutani and Kamitani proposed a vat polymerisation apparatus where the output of a UV flash lamp was channelled down five optical fibres fitted with individual shutters [116]. The five optical fibres formed a one by five array of light sources that was focussed onto the surface of the photopolymer by a single lens and was successful in producing some simple parts.

In 1999, whilst working for the NTT Data Corporation, Mahito Arai patented an apparatus that used an array of many fibre-coupled LEDs fitted with gradient index lenses for use in stereolithography [117]. The LEDs could be coupled in several one-dimensional arrays with offsets between them so that the spots created could be placed upon a finer pitch grid than the spacing between the fibres.

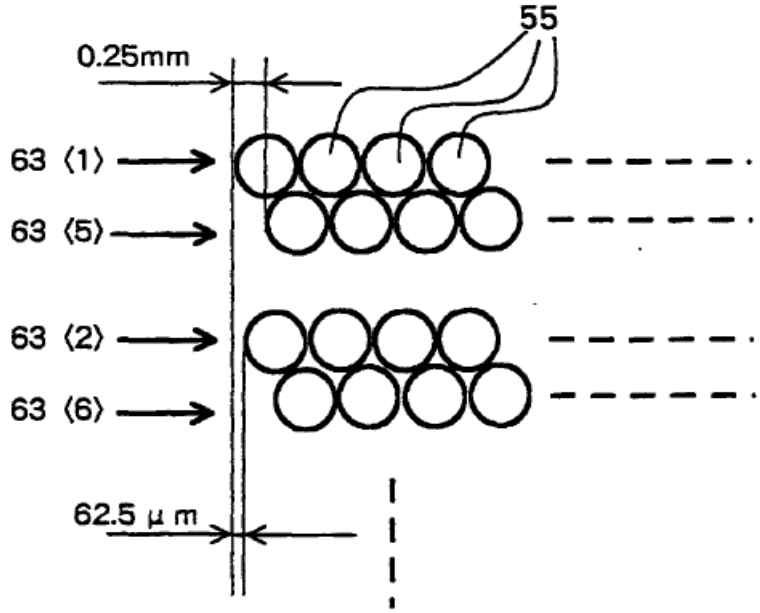

Figure 19 Four one dimensional arrays of fibres (63) aligned horizontally to the page. Each horizontal array has a different offset. The scanning direction is vertical to the page. [117]

Using a variant of this technology Loose *et al*. designed and used a system comprising 1024 LEDs mounted in a one dimensional array that was linearly scanned across a 1024 x 1024 pixel build area [118], [119]. The system suffered high coupling losses from LED to fibre but

was effective. They concluded that improvements to the accuracy and repeatability were needed but that the system had potential as a high speed, low cost building system. It is assumed that since this technology no longer exists the system did not gain popularity as a result of the development of micro-mirror arrays that have allowed the entire layer to be polymerised in one exposure [120].

2.7 Energy sources

In current commercial PBF systems the energy source is either laser or electron beam based. Electron beam sources are in the minority with only the Swedish company Arcam utilising them. Two advantages of using an electron beam source are that a high power can be delivered, up to 3.5 kW, and that the beam steering mechanism (deflector coils) have no mass thus the beam's position can be altered sufficiently swiftly that multiple melt pools can be maintained simultaneously [115]. However the use of an electron beam source confers several disadvantages: the electron charge puts limits on the minimum focal spot diameter, 140 μm for a Q20 and the build must be conducted in a high vacuum [121].

The majority of commercial PBF machines use a laser as the energy source with fibre lasers being the preferred energy sources by the industry leaders such as Renishaw, Concept Laser, EOS, 3D Systems ReaLizer and SLM solutions for several reasons: compact size, wavelength suitable for processing metals, high beam quality permitting a small focal spot (70 μm for a AM250 [122]) and the point of delivery being easily separated from the device by virtue of the fibre. However there is growing interest in the use of laser diodes for PBF systems given that a single broad stripe laser diode is capable of producing tens of Watts [123] and multiple diode packages are capable of delivering hundreds of Watts [124]. They are also attractive solutions due to their low cost and the greater efficiency at which their shorter wavelengths are absorbed by metals [125, p. 27] despite having a lower beam quality [126]. In 2014 the Fraunhofer ILT produced a multiple diode laser prototype at the EuroMold expo [127] although details of its operation have not been given and in 2016 Sheffield university had success in using a linear array of 19 overlapping beams to fuse low melting point metals [126].

2.8 Research questions

Given the suitability of laser diodes as an energy source for the PBF process and the availability of an IPG packaging marker device that contained seven 60 W laser diodes it was decided to use this device as the energy source for the experimental multiple parallel beam PBF system.

Consequently the research questions have been framed as:

1) *How will the poor beam quality of laser diodes affect the PBF process?*
2) *How much power is required of the laser diodes given the poor beam quality?*
3) *How do multiple beams interact and how does this affect the effectiveness of a multiple beam scanning strategy?*
4) *What is the optimum scanning strategy for multiple beam delivery when focusing on part density?*

Chapter 3

Experimental system

3.1 Introduction

The fundamental building block of the technology developed during this research is the 'melt ball'. This chapter will describe the process of creating a melt ball from software through hardware and into existence and as such is an explanation of the final state of the photonic system developed for the purpose of this research. Within this work the term 'melt ball' is used to describe the resultant cooled material that was melted by exposure to laser radiation regardless of its actual shape.

To track the creation of a melt ball through this system the path can be usefully subdivided into these five steps:

1. System overview.
2. Generation of build instruction file.
3. Instruction-file processing and hardware control. (Appendix A)
4. System hardware.
5. Material properties and photon absorption.

3.2 System overview

An overview of the system will be given to contextualise the subsequent sections which give more detail about the individual components and their operation. This overview has two parts: a description of the system's sub-components and a brief description of operation.

System sub-components

(1) A personal computer (PC) that runs the software that controls the position of the X, Y and Z movement stages and sets/reads the state of the input/output ports of the axis controllers.

(2) A three axis gantry movement system manufactured by Aerotech Inc.

(3) Custom built and programmed microcontroller circuitry that interprets signals sent from (1) and that controls (4) and (5).

(4) A packaging marker system comprising seven 60 W laser diodes manufactured by IPG photonics.

(5) Custom-built powder-handling unit.

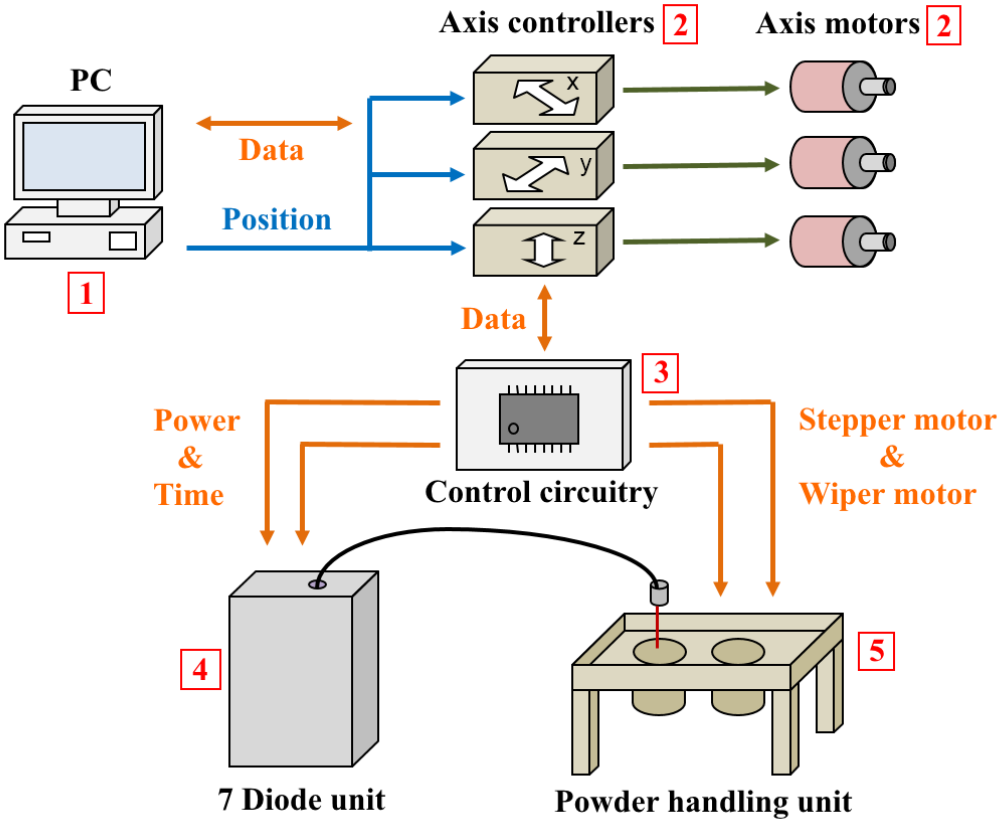

Figure 20 The flow of control signals between the five sub components of the system.

Brief description of operation

The parameters that define the melt balls for any given build are all calculated in advance and recorded in a build instruction file. This file is read by proprietary Aerotech software running on the Lab PC (1). Positional commands are then sent to the three axes motors (2) to ready the system for the creation of a melt ball. The Aerotech software also sends the desired exposure time, exposure power and temporal pulse profile number to the microcontroller (3). The microcontroller waits until it receives the 'fire' command then sends two types of signal to the marker unit (4). The first is an analogue 'exposure power' voltage, common to all seven diodes and the second is a timed 'enable' pulse or pulses for all seven diodes. These are individually adressable so that one to seven diodes can expose simultaneously. Alternatively, if a 'relayer' command is sent from the PC to the microcontroller then the microcontroller sends and receives signals to and from the powder handling unit (5). When a 'relayer' is triggered the microcontroller sends signals to the stepper motors that control the height of the 'build' and 'supply' pistons and to the DC motor that controls the movement of the powder wiper.

3.3 Instruction file generation

Several scripts and functions were written in Matlab to produce build files from a number of start points, which can be divided into three categories:

1) To produce a parameter sweep or experimental pattern of some kind.
2) To produce a layer from an image file stored in a format such as Joint Photographic Experts Group (JPEG) or Portable Network Graphics (PNG).
3) To produce a file from a 3D Computer Aided Design (CAD) model saved in the Standard Tessellation Language (STL) format.

3.3.1 Source for build instructions

The three conceptual sources for the creation of melt balls are considered here. Each handles the user's requirements in different ways but each ends up adding entries to a list in the same format.

Parameter sweep

This is the simplest source for build file instruction creation. In this case the Matlab script contains several 'FOR-NEXT' loops that increment position and define the exposure time,

exposure power and the temporal pulse shape of the exposure. The tool path or scanning pattern is defined by the order of the instructions.

Image

In this mode a JPEG or other image type is taken as the source of melt ball locations on a square grid. The image is loaded into memory then if it is a colour image the three colour planes are combined to a single plane. This grey scale image is then transformed to a binary image using a user-definable threshold. From this binary image either the ones or zeros can be used as the grid locations where a melt ball needs to be placed. A tool path is then created from the 'on' pixels within the image based upon the desired scanning strategy, spot pitch, and ribbon overlap.

This particular mode of operation can be used for producing prismatic objects from a repetition of the build layer, or to perform ribbon-based parameter sweeps by using a simple N x M rectangular image of 'on' pixels.

Figure 21 A PNG image, top, used to create a 261 x 64 pixel build file for the melted example.

STL file

In this case a lattice of points is generated that spans the 3D model and is used to produce a sequence of planar slices through the model, each of which can be treated as a bitmap image as previously described. The steps for this algorithm are as follows:

1. Load model into memory.
2. Establish X,Y,Z limits of model.

3. Create 3D lattice of points that span model from predefined unit cube size.
4. For each point within lattice ask: 'Is this point within the STL model?'
5. From lattice of yes/no points generate sequence of horizontal slices as bit planes that can be processed by the previous JPEG processing scripts.

The STL file format encodes a three dimensional object by defining its surface as a patchwork of triangular faces: for example, a square-based pyramid would be defined by six triangular faces, two for the base and one for each face that shares a vertex at the apex Figure 22 (a). Also shown in Figure 22 (a) is a planar grid of points at the 6th level of a 10 x 10 x 10 lattice where it is possible to see that 16 of the 100 points that comprise the layer are within the pyramid and as a consequence 84 are without. To print that particular layer only the middle four by four points of the ten by ten layer need melting, as is shown on the right of Figure 22.

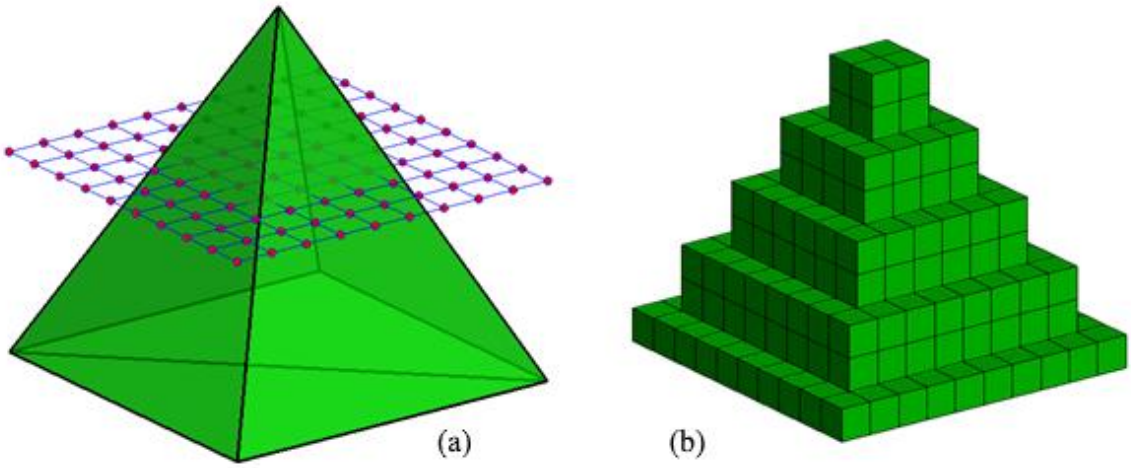

Figure 22 (a) Solid square based pyramid defined by six triangular facets with a 10 by 10 grid of points shown intersecting the pyramid at a level of 0.67 pyramid height. (b) Unit cubes centred on the 340 points of the 10 x 10 x 10 lattice that fall within or on the surface of the square based pyramid.

The method used to establish whether a point is inside the shape has been outlined in a University of Texas electromagnetics lecture [128] using the following steps:

1. From the point in question find the nearest vertex.
2. Consider in turn each of the faces that incorporate that vertex.
3. Calculate which side of each plane defined by each face the point in question is.
4. Only if the point is on the 'inside' side of all the faces is it inside the solid.

Steps 1, 2 and 4 are trivial to perform. However, to perform step 3 and to differentiate between the sides of a plane a surface normal is required. STL files define solids by a surface mesh of triangular facets. The convention for the listing order of the vertices for each triangle is the right hand thumb rule. The outward-pointing surface normal can be constructed for any triangular facet by taking the cross product of two of the edge vectors:

$$\overrightarrow{(P3-P1)} \times \overrightarrow{(P2-P1)}\ or\ \overrightarrow{(P1-P2)} \times \overrightarrow{(P3-P2)}\ or\ \overrightarrow{(P2-P3)} \times \overrightarrow{(P1-P3)}$$

where $P1$, $P2$ and $P3$ are the vertex points of the facet in the right hand rule order.

To establish which side of a plane a given point is, the dot product is calculated between the outward-pointing surface normal and the vector defined by $\overrightarrow{P-P_{plane}}$ where P is the point in question and P_{plane} is any point on the plane such as the centroid of the face in question. The sign of this dot product indicates whether the angle between the two vectors is greater or less than 90º and thus which side of the plane the point in question is.

- Dot product > 0 angle < 90 point on outside of plane
- Dot product = 0 angle = 90 point on plane and regarded as inside object
- Dot product < 0 angle > 90 point on inside of plane

3.3.2 Scanning strategies

Once the number and locations of the melt balls required for the build are decided and a bit map created then the order of placement and exposure parameters need to be defined to create the build instruction file. Five scanning strategies were developed for this purpose and comprise an exposure strategy and a movement strategy

Exposure strategy

A pulsed expose-move-expose strategy was chosen for use within this research. In operation this means that the diode array is moved to a given position, the diodes activated whilst stationary, then the array is moved to the next position and activated again. Figure 23 shows the delivery of light from the fibres to the powder bed. There were three reasons for this choice. The first was based upon a potential process improvement, the second upon the symmetry of the build, and the third upon a limitation of the system. Regarding a potential process improvement, a significant problem within the powder bed fusion process using metals is the balling phenomenon. One of the contributory factors to this effect is that of capillary breakup due to

Rayleigh instabilities within a melt bead if the length to width ratio exceeds three. It was therefore considered useful to remove the potential for capillary breakup with a pulsed exposure-move-expose strategy. With regards to the symmetry of the build, the prototype system was not designed with the ability to alter the orientation of the diode array relative to the build chamber during processing. This dictated that the direction of scanning would be constant during any given build. If lines of melt were created in Constant Wave (CW) mode they would all be parallel throughout the entire build without the ability to alter angle between layers. Consequently to remove any directional bias and to take Concept Laser's random island strategy to the limit a strategy based upon individual melt spots was conceived. With regards to the system limitation, the communication time between various parts of the system limited how fast the system could process information, making in process adjustment of power levels impractical. Subsequent to system commissioning, the software cycle time to read and process an instruction from file was found to be ~70 ms. With reference to other research using stainless steel powder Table 4 and considering a scan speed of 50 mm/s, then a 70 ms delay would be equivalent to 3.5 mm of travel between build commands which would lead to an unacceptable build resolution. With all three points considered it was decided to utilise an expose–move–expose strategy.

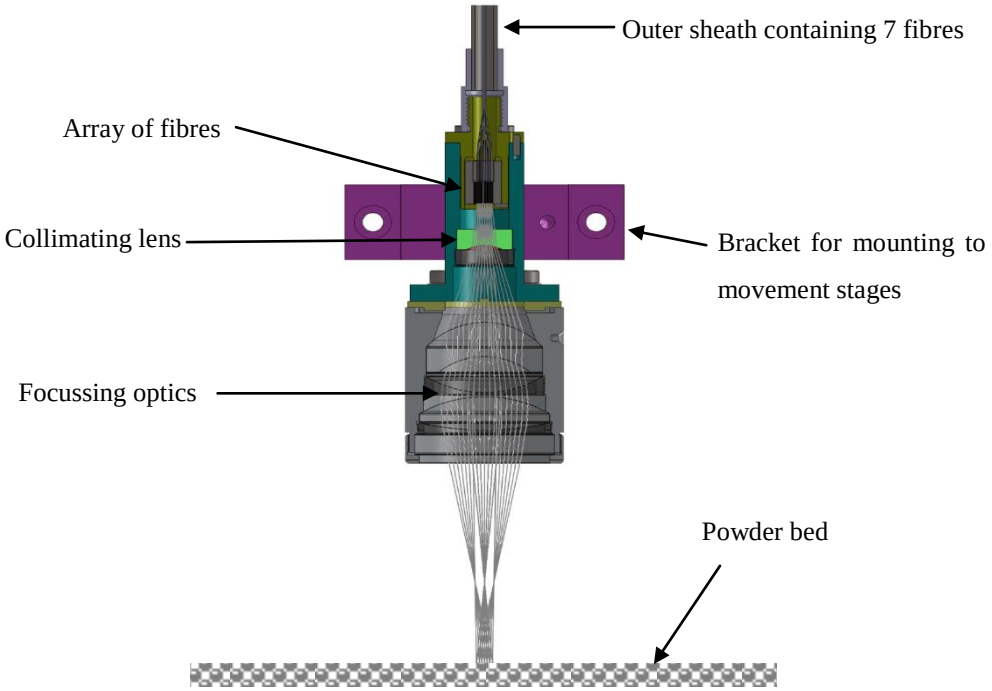

Figure 23 Sectional view through array optics.

Table 4 Powers and scan speeds used in research using stainless steel powders.

Material	Power (W)	Scan speed (mm/s)	Layer thickness (µm)	Reference
316L	87	150	75	[109]
316L	105	360	30	[105]
316L	150	600	35	[129]
316L	75	50	100	[94]

Movement strategy

This research uses an IPG 7-diode packaging marker. This marker unit comprises seven 60 W laser diodes that are coupled by co-bundled optical fibres to an optical head. The configuration of the fibres within the head is fixed as a one by seven array of 110 µm fibres on a 0.5 mm pitch. When focussed on the bed this translates to a one by seven array of spots on a 600 µm pitch. Given that the individual melt balls created by each exposure will be less than 600 µm then a strategy to place more balls in the space between is required to produce consolidated material.

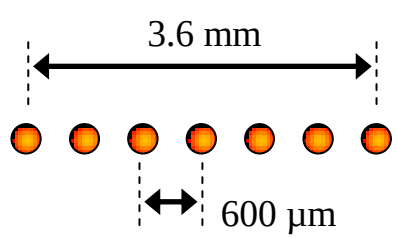

Figure 24 Geometry of laser diode spots when focussed upon the powder bed

A triangular or square grid could be used as the basis for filling in the 600 µm gaps of the diode array but due to the ease of storing and manipulating a square array this was chosen. Utilising this square grid an efficient filling-in strategy uses an integer amount (n) of equidistant fill positions. This strategy leads to grid pitches of 600/n µm. Examples for $n = 1,2\ and\ 3$ giving grid pitches of 600, 300 and 200 µm are shown in Figure 25

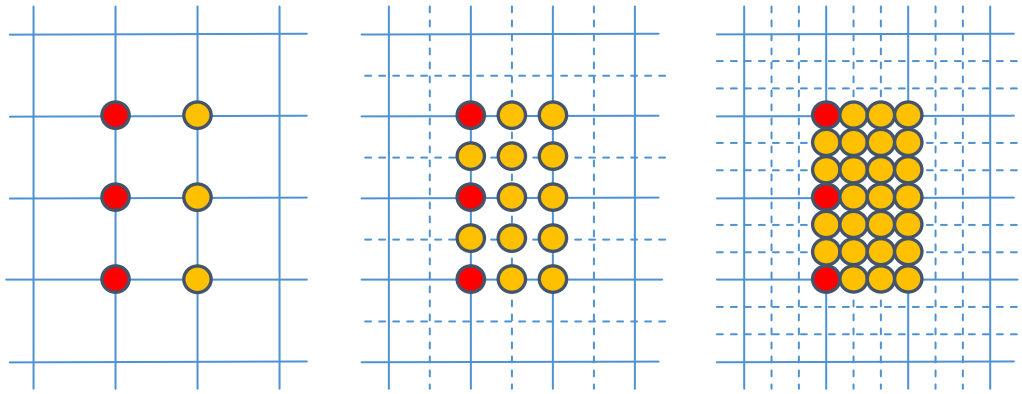

Figure 25 Grid pitches for n=1, 2 and 3(see text). Red spots show 600 µm pitch produced by optical head. Yellow spots show the fill-in spots required to build a 1200 x 600 µm rectangle. Left to right: grid pitches of 600, 300 and 200 µm.

Based upon the square grid previously described, five scanning strategies have been developed for calculating the path of the optical head over the powder bed Figure 26. These strategies fall into three basic types: vertical, horizontal and diagonal with the vertical and horizontal types having uni-directional and bi-directional variants.

To create a layer of arbitrary dimensions the scanning strategies of Figure 26 are used to create many parallel ribbons of melt balls. These ribbons can be of any length orthogonal to the long axis of the spot array but are just short of 420 µm in width. The actual width depends upon the grid spacing.

$$width = 600\left(7 - \frac{1}{n}\right)\mu m$$

The construction of a 2.6 x 6.0 mm rectangle is shown in Figure 27. In this example n=3 giving a grid spacing of 200 µm. The first ribbon (red and orange) is built full height (with n=3 full height = 4.0 mm) and 2.6 mm long. The second ribbon (blue and green) is added with an overlap (in this case 2 balls) to ensure consolidation and an appropriate height (2.2 mm) to achieve the desired final height.

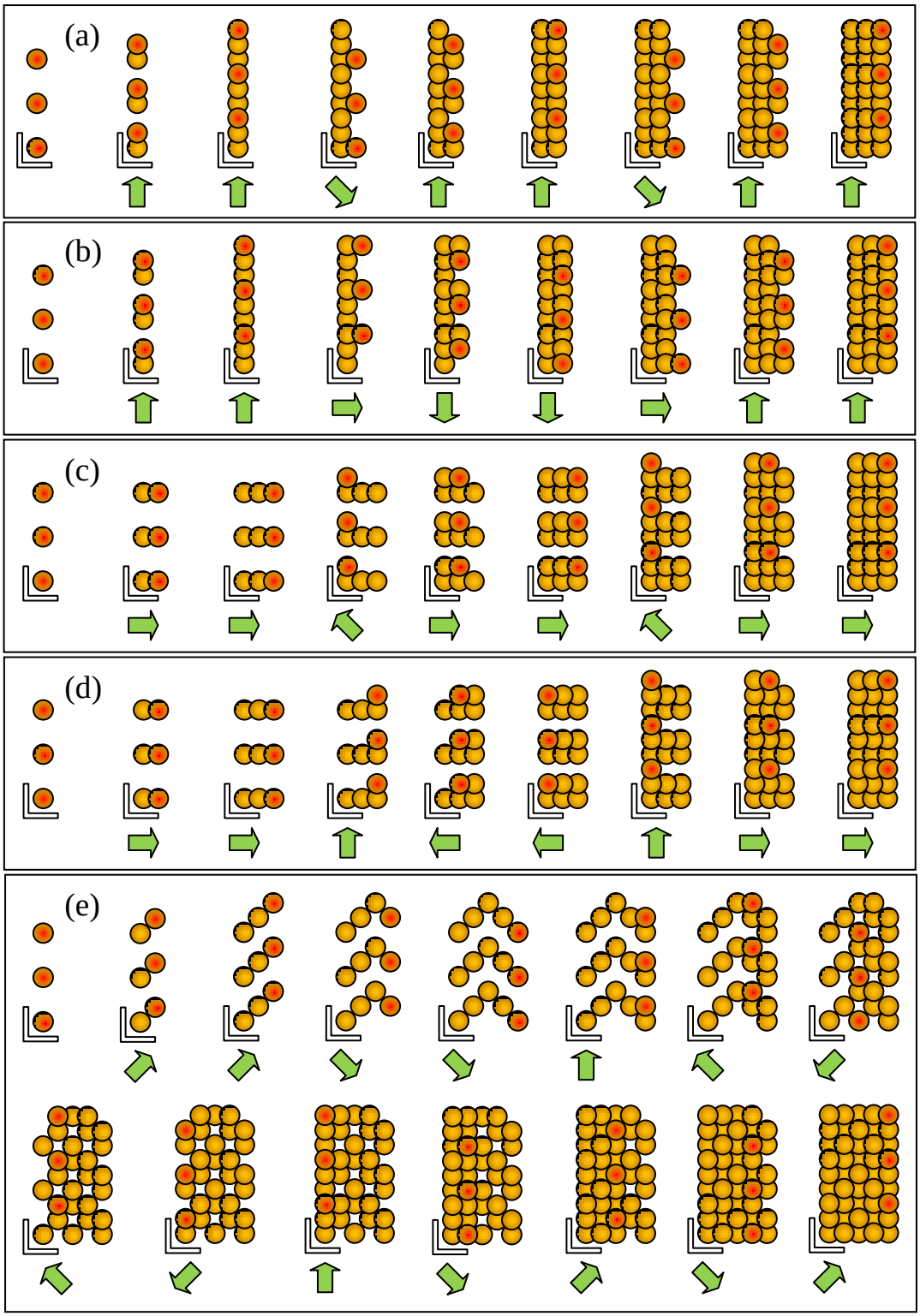

Figure 26 Five scanning strategies: (a) Vertical (uni-directional). (b) Vertical (bi-directional). (c) Horizontal (uni-directional). (d) Horizontal (bi-directional). (e) Diagonal. Red spots = currently added. Yellow = existing.

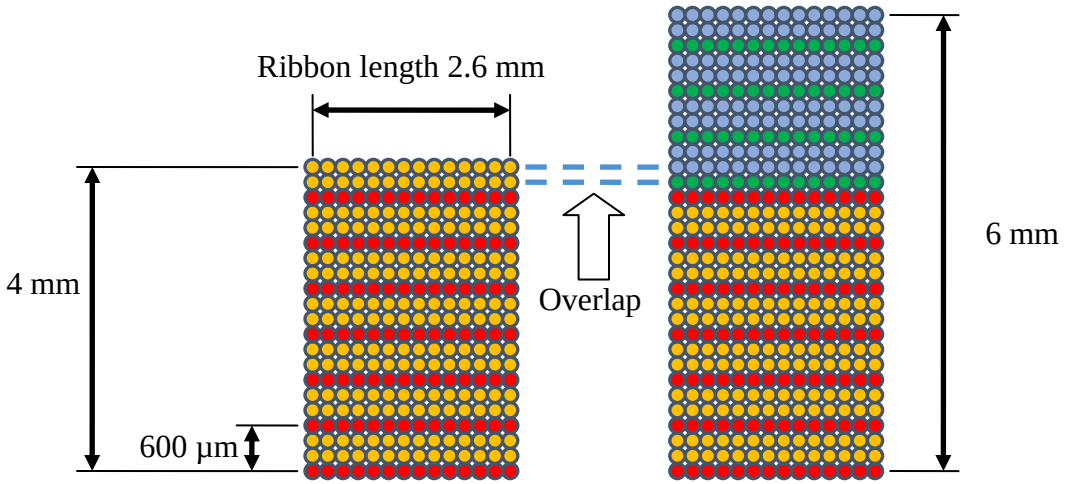

Figure 27 Example construction of a 2.6 x 6.0 mm rectangle with a grid pitch of 200 µm. A full height ribbon is built first, red and orange. Then an appropriate height second ribbon is overlapped with the first.

Using this method of merging ribbons any size layer can be accommodated. To create shapes other than rectangles melt balls are omitted from/ added to the grid in rather the same way that an image is made of pixels. Using this analogy the individual layer slices used for building objects are stored as bitmaps.

3.3.3 Tool path generation

There are three parameters available for the build file generation algorithm that affect the tool path: scanning strategy number, spot pitch, and ribbon overlap. Other parameters used in generating the build instruction file are exposure power, exposure time, and pulse shape number. Although these are applied to each entry on the list they do not affect the actual tool path. It would be possible to make the exposure parameters vary with the position of melt ball (top, side, bottom or interior of object) but within this research they were left as global settings.

The steps involved in creating the tool path are:

- From the given spot pitch and ribbon overlap calculate how many ribbons will be needed.
- Start in the bottom left corner of the bitmap with ribbon 1.
- Increment through the ribbons and for each ribbon, step through the positions of the optical head according to the given scanning strategy number.
- At each position interrogate the bit map to establish how many diodes require activating.
- Add line to build instruction file as long as at least one diode is used.

An example of tool path generation is illustrated in Figure 28. In this example the bit map is three pixels in X and seven pixels in Y and the pixels that require melting are coloured blue. The example diode array is three high and the spot pitch has been chosen to be half the diode pitch to produce a short example file. As a result of the size of this diode array and this spot pitch each ribbon can be up to six pixels high. To span the example seven-high bit map with a ribbon overlap of two requires a six-high ribbon followed by a three-high ribbon.

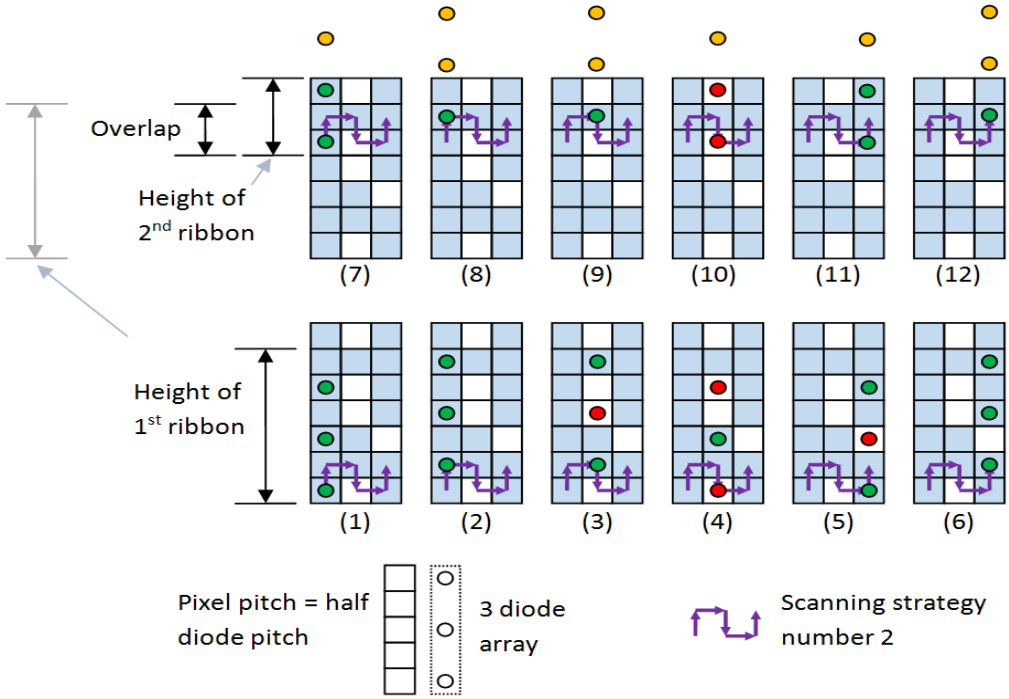

Figure 28 Tool path generation for a 3 by 7 layer using an array of 3 diodes. The pixel pitch is half the diode pitch and the desired shape is indicated by the blue squares.

Starting with diode number one in the bottom left hand corner the diode array is moved according to the chosen scanning strategy through the length of the ribbon then repeated from the origin of the second ribbon. At each position the desired state of the diodes is decided. In the example image the steps are numbered one to twelve and the diode states are shown as green for on, red for off, and yellow for not used and therefore off. These are summarised in Table 5.

Table 5 The tool path generated from Figure 28 showing the required states of the diodes at the listed coordinates.

Step number	1	2	3	4	5	6	7	8	9	10	11	12
X	1	1	2	2	3	3	1	1	2	2	3	3
Y	1	2	2	1	1	2	5	6	6	5	5	6
Diode 3	1	1	1	0	1	1	0	0	0	0	0	0
Diode 2	1	1	0	1	0	1	1	0	0	0	1	0
Diode 1	1	1	1	0	1	1	1	1	1	0	1	1

3.4 System hardware

The hardware components of the system detailed here are the movement stages, the powder handling unit, the laser diode control and the laser diodes. Details of the microcontroller circuitry and its operation are given in Appendix A

3.4.1 Movement stages

The relative movement of the diodes and powder bed was provided by an Aerotech gantry system model number ALS20000 with an accuracy of ±18 μm in Y and ±24 μm in X and driven by Ndrive-HPE controllers manufactured by Aerotech. The proprietary Aerotech software (Nview) that controlled the positions of the movement stages was used to run the build instruction reader program that sequentially extracted the X, Y and Z values from the build instruction file and set the movement stage positions accordingly.

3.4.2 Powder handling unit

The powder-handling unit was custom built for the purpose of this research. It comprised two cylinders, one for powder supply and one for building within. This design is used in many commercially available machines such as EOS's EOSINT M250 [130] and is considered simpler than the three cylinder variant used by the DTM (Desk Top Manufacturing) corporation's Sinterstation range of machines [3]. Three cylinders are used in this case to increase build rates by removing the time for the wiper to return to its home position. However, for this research the two cylinder design was preferred for simplicity. The maximum build envelope for this design was 70 mm high and 100 mm diameter.

The positions of the pistons within the cylinders were controlled by four phase linear stepper motors driven in normal full wave mode and giving a step resolution of 25 μm. When they were not in use the coils were de-energised to limit current consumption. This was possible as the pistons had sufficient sliding friction to stop the ingress of powder so that the braking effect of energised coils was unnecessary.

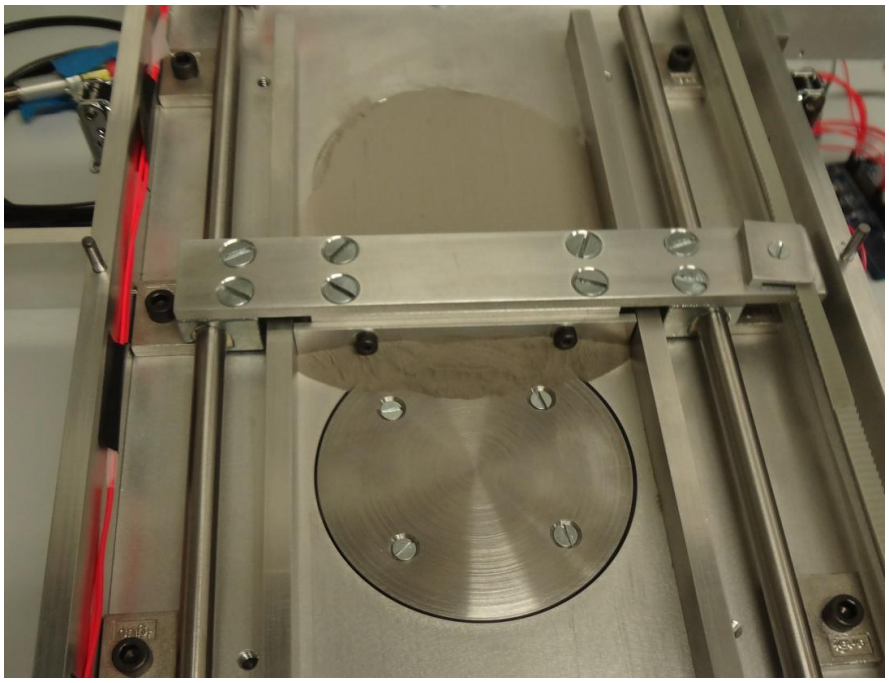

Figure 29 The first powder layering operation at the halfway point.

A new powder layer was created by the movement of a replaceable wiper blade attached to a carriage that moved on linear bearings. The wiper was moved by a DC motor, whose speed was controlled by PWM signals generated by the dsPIC and whose movement was constrained by two limit switches.

The entirety of the powder manipulation system was enclosed within a vacuum chamber for atmospheric control and a trial to establish the effects of oxygen and the efficiency of the vacuum process was performed. Five ribbons were built in deep powder using strategy number one on a grid pitch of 150 μm. The first ribbon was built in the normal planetary atmosphere. The second was built after one pump-down and re-fill with nitrogen phase and the third, fourth and fifth ribbons were built after two, three and four pump-down and re-fill cycles respectively Figure 30.

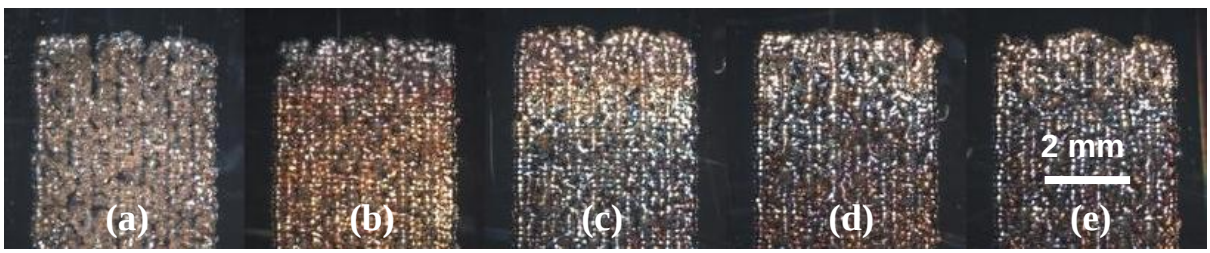

Figure 30 Effects of successive vacuum-down and re-fill with nitrogen cycles upon a ribbon build. Left to right, 0, 1, 2, 3 and 4 cycles.

The ribbon built with the normal atmospheric oxygen content showed signs of significant oxidization by its matt brown appearance, Figure 30(a) however the photograph appears less brown than its neighbour due to the matt finish. The ribbon built after a single vacuum-down and back-fill cycle was less matt but still significantly orange in colour Figure 30(b). There was little to distinguish the ribbons built after two, three and four pump-down and back-fill cycles. However the start of the ribbon (top) showed more colouration at two pump-down cycles than for three. As a result 3 pump-down cycles were subsequently used to prepare the powder for processing. The vacuum pump used was an Edwards E2M5 capable of a maximum vacuum of $1x10^{-3}$ mbar. The pressure gauge used had a scale resolution of 10 mbar and in practice leaving the vacuum pump for seven minutes would result in a reading of <10 mbar. This equates to a reduction of oxygen percentage by two orders of magnitude for each vacuum and nitrogen refill

cycle. Consequently the three cycle approach should reduce the atmospheric oxygen level by six orders of magnitude to approximately 0.2 ppm.

3.4.3 Control of laser diodes

The marker unit supplied by IPG photonics was developed as a packaging marker system for the addition of best before dates as appears on perishable items. As such it was configured to be controlled by software running on an external PC. A printing operation entailed the PC sending a character string *via* USB to the marker unit which would then sequentially fire the diodes in a pre-set order corresponding to each character in the sequence using a given exposure time and at given time intervals corresponding to how fast the item to be marked was passing in front of the marker head. For this research full control of when and which diodes were fired and for how long was required, thus the marker unit's internal control system was overridden and replaced by external control.

The IPG 7-diode marker unit comprised four modules: a high current power supply incorporating safety interlocking, an 'off the shelf' Dymotion KFLOP microcontroller-based controller board, a diode control module incorporating thermal management, and some interfacing circuitry. To be able to control the laser diodes with an external microcontroller, eight communication lines to the diode control module were disconnected and attached to external interface circuitry buffered by opto-isolators to produce a robust control system. The eight communication lines correspond to seven digital 'enable' signals for individually addressing each diode and one common analogue 'power' level signal. An earth was also needed but this line was left connected. When designing the opto-isolator circuitry the Dymotion KFLOP board was used as a pattern. The KFLOPs power rails and logic levels are 3.3 V and the digital to analogue circuitry for the laser diode power level signal had been bypassed with a jumper to give a digital 3.3 or 0 V only. As a consequence the new external opto-isolator circuitry was designed to run on and produce 3.3 V signal levels and a 12-bit DAC was added so that the analogue 'power' signal could be varied in sub-millivolt increments between 0 and 3.3 V.

There were two possible methods for triggering the laser diodes for a given exposure time shown as Method 1 and Method 2 in Table 6. Each method allowed individual diode control by selection of the appropriate 'enable' bits but the second method also allowed for temporal pulse shaping by varying the power level during exposure. The response of one of the laser diodes to

each control method was captured by using a photodiode (Thorlabs DET10A) and Figure 31 shows these responses in relation to the corresponding electronic signals fed to the diode control module. After capture the photodiode's response was multiplied by an arbitrary factor of 275 to allow comparison of the signals. From the top two graphs of Figure 31 it can be deduced that there was some slower circuitry on the diode control module's 'power' input than the 'enable' input. This is some suspected analogue to digital circuitry. When using control method two to produce the square, ramp up, and ramp down power signals the photodiode response showed a glitch as the enable signal was set to high. This was particularly noticeable in the ramp up case but the square case also had a similar glitch, albeit masked by the rapid rise in the laser diode's output. The glitch was less noticeable in the ramp down case. The difference between the start of the ramp down and square cases suggests that the end of the previous pulse affects the beginning of the current pulse as all the images of Figure 31 were captured from within a train of many pulses to get a stable representation of the laser diode's output within a 50 % duty cycle. It is assumed that there is some retention of charge within the power level control circuitry to improve the rise time response of the laser diodes which is dumped though the laser diode when the enable pin is set. As a result of this the external microcontroller was programmed to use method one so that the laser diode output pulse shape most resembled a square pulse, although control method two was used for some trials detailed in section 5.3.5

Table 6 Proposed diode switching methods.

Method 1	**Method 2**
1) Set analogue power level	1) Turn on enable bits
2) Turn on enable bits	2) Set analogue power level
3) Wait for exposure time	3) Wait for exposure time and adjust level
4) Turn off enable bits	4) Set power level to zero
5) Set power level to zero	5) Turn off enable bits

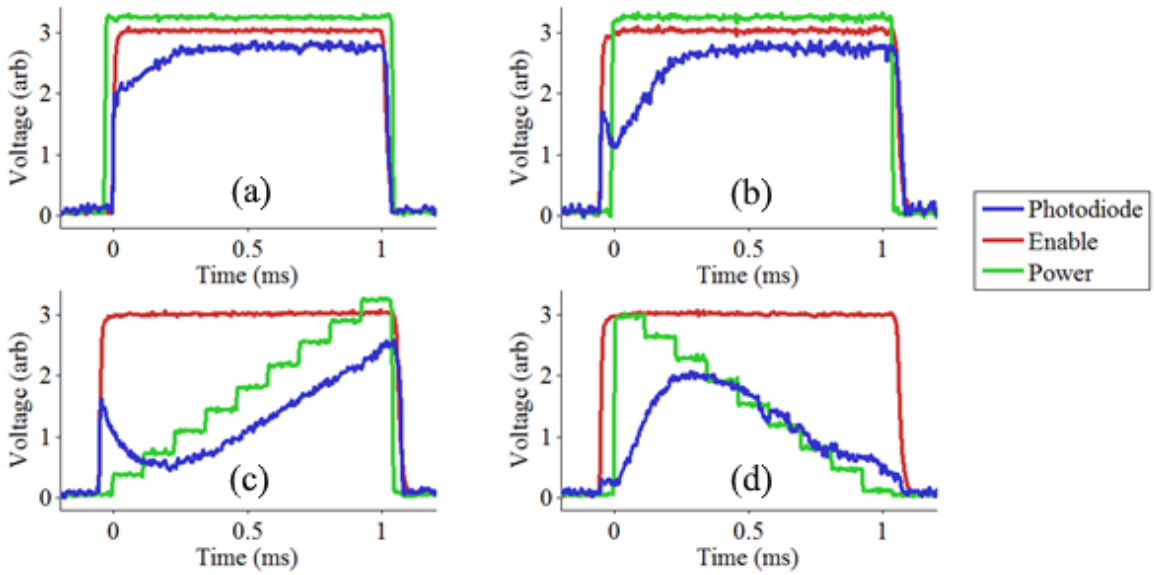

Figure 31 A comparison of the diode-laser's response to varied control signals. (a) Switching method 1. All three other images are using method 2 but with: (b) square, (c) ramp up and (d) ramp down profiles. Diode-laser output was measured by a DET10A photodiode and its output arbitrarily scaled.

3.4.4 Laser diode characteristics

The laser diodes present within the IPG 7-diode packaging marker system are IPG PLD 60s which have a centre wavelength of 974 nm, a Full Width Half Maximum (FWHM) of 5 nm and are capable of delivering 60 W [131]. A Fieldmaster GS with a 1000LM head, manufactured by Coherenet Ltd, was used to measure the CW output powers of the seven laser diodes, and the results of this test are shown in Table 7. The average laser diode power of 41.4 W is ~2/3 of the specified max output power. The reason for this deficit is suspected to be IPG's use of an off-the-shelf microcontroller running 3.3 V logic connected to one of their diode control modules working on 5 V logic levels. It is not known whether the IPG diode control module can stand 5 V logic and thus, from fear of damaging the unit, the custom control circuitry, described earlier, was left using 3.3 V. As a consequence, the work herein was done with a maximum of 39-44 W of power.

Table 7 Experimentally measured CW output power of the seven laser diodes within the IPG marker unit.

Diode No	1	2	3	4	5	6	7
Output power (W)	44	42	41	39	41	41	42

Along with the already measured output power the beam profile was measured so that the spot size, beam quality, and energy distribution profile could be calculated. This was done by the use of a translated slit and a deconvolution procedure.

Beam profile measurement

In order to automate the process and to optimise accuracy of slit movement XYZ Aerotech stages were used and the equipment set up as follows:

- The optical head from which the beams emanate was attached to the Z stage.
- An Ophir 30A thermal head was also attached to the Z stage and positioned such that the incident beam from the laser diode was central to the detector and that the detector was ~100 mm from the optical head
- An adjustable slit was mounted upon an adjustable height platform attached to the XY stage.

With this arrangement, adjusting the position of the Z stage altered the distance of the slit relative to the optical head. Keeping the distance from the optical head to the sensor constant and adjusting the XY stage created the movement of the slit through the beam Figure 32.

The distance of the thermal head from the optical head was chosen to be 100 mm to a) allow unobstructed movement of the adjustable slit through the beam path and b) minimise the power density incident upon the thermal head whilst capturing the entirety of the beam. This was checked by moving the thermal head relative to the optical head and an 8 mm movement was found to be sufficient to move the head from 90 % of max power through max power and back down to 90 % of max power. Given that the aperture of the thermal head is 17 mm it can be inferred that at this standoff the beam diameter is >9 mm. The literature for the Ophir 30A thermal head gives a maximum average power density of 25 kW/cm^2. The power density from

40 W over 5 mm radius gives ~51 W/cm^2 which is over two orders of magnitude less and therefore assumed to be within safe working limits.

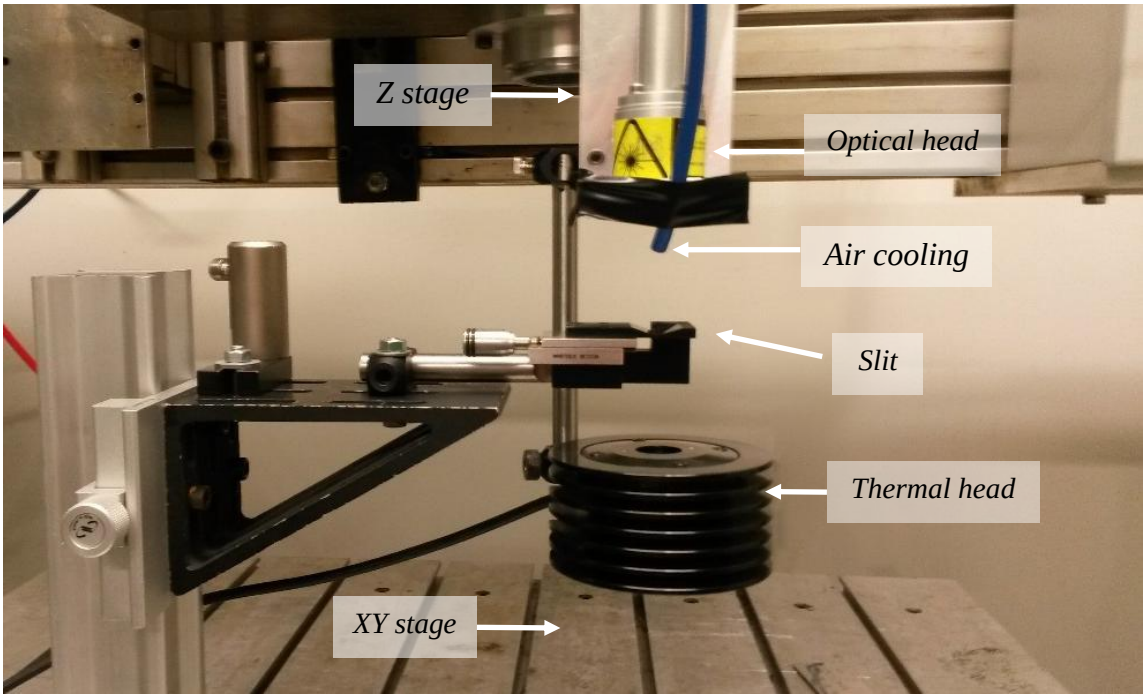

Figure 32 Experimental setup. Adjustable slit attached to the XY stage and the optical head and power meter head attached to the Z stage.

To lower the risk of damage to the slit and to lower the thermal stress upon the laser diode throughout the ninety minute experiment, the laser diode was operated at a 39 % duty cycle which resulted in a power meter reading of 15.76 W with no slit present. The duty cycle period was 43 ms and the response time of the Ophir 30A thermal head is quoted by the manufacturers as 0.8 s consequently the cycle time was negligible and the average power would be recorded by the system.

The slit width was set to ~50 µm and checked using a microscope to be 51 ± 1 µm. To create the beam's transverse irradiance distribution the slit was moved through the beam in 10 µm increments and power readings taken at each position. The transverse irradiance distribution was captured throughout a 5 mm range of Z positions along the beam Figure 33.

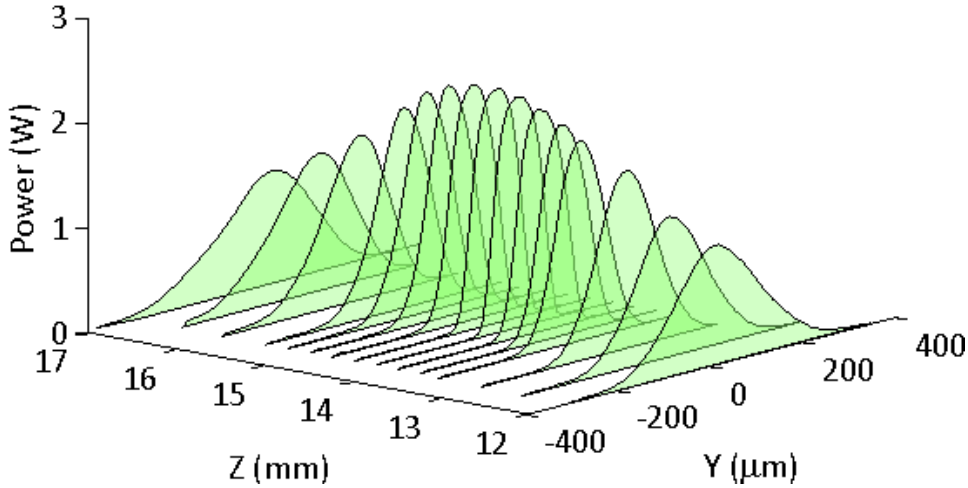

Figure 33 Evolution of transverse irradiance profile with position (Z) along beam.

The beam radius at each Z position was found by the second moment method. This gives the beam diameter as four times the standard deviation of the transverse irradiance distribution. Where standard deviation is given by [132]

$$\sigma_x{}^2 = \frac{\iint (x-\bar{x})^2 I(x,y,z)\, dxdy}{\iint I(x,y,z) dxdy} \tag{3.1}$$

The beam radius was plotted as a function of Z position along the beam and a curve of the form Eq. 3.2 [133] was fitted by least squares to establish the appropriate beam parameters.

$$W_z = W_0 \left\{ 1 + \frac{(z-z_0)^2}{z_r{}^2} \right\}^{1/2} \tag{3.2}$$

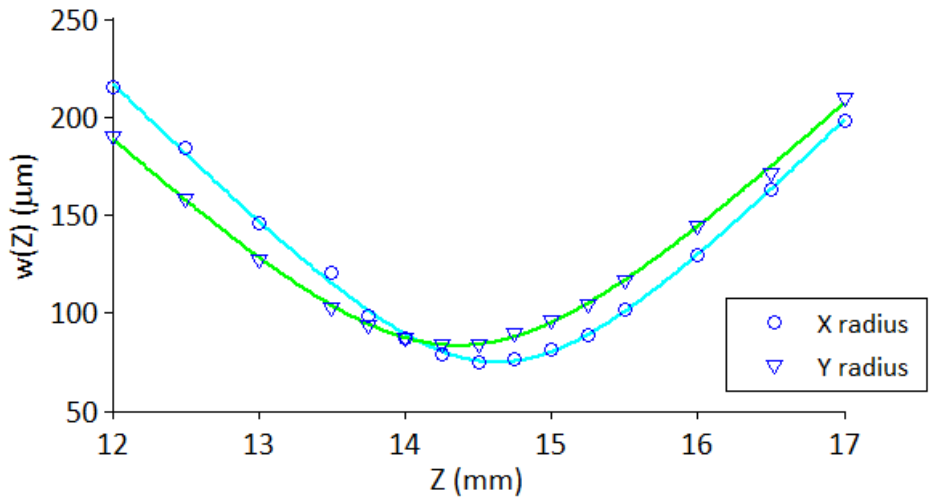

Figure 34 Second moment beam radius as a function of Z position along beam for both X and Y sections.

Table 8. X and Y section beam parameters extracted from curve fits Figure 34.

	Z_{0s} (mm)	W_{0s} (µm)	Z_{rs} (mm)	M_s^2
X sections	14.63	75	0.96	18.7
Y sections	14.36	83	1.16	19.3

The beam parameters extracted from the curves of Figure 34 are shown in Table 8. These parameters have been given the subscript 's' as they are uncorrected for slit width. These results can be corrected for slit width by applying the transforms of equations 3.3 [134] and Zr can be calculated by the application of equation 3.4 [133]. These corrected values are given in Table 9.

$$z_0 = z_{0s},\ \ {w_0}^2 = {w_{0s}}^2 - s^2/3,\ \ M^2 = {M_s}^2\, w_0/w_{0s} \tag{3.3}$$

$$z_r = \frac{\pi {W_0}^2}{\lambda M^2} \tag{3.4}$$

Table 9. X and Y section beam parameters corrected for slit width.

	Z_0 (mm)	W_0 (µm)	Z_r (mm)	M^2
X sections	14.63	72	0.93	18.0
Y sections	14.36	78	1.07	18.1

The difference in Z_0 values between the X and Y sections would normally suggest astigmatism. However in order to change the orientation of the slit for X and Y sectioning it had to be physically relocated. A relative Z position check was performed but it is possible that some of the 0.27 mm difference resulted from the relocation and not astigmatism. The difference in W_0 and Zr values suggests an elliptical beam profile. The appearance of eccentricity could be introduced into the results if the experimental geometry was at fault but to account for it all would require the axis of the beam to be ~22° away from perpendicular to the plane of the XY stage. This degree of tilt would be noticeable without measurement and thus it is proposed that cumulative experimental error accounts for some eccentricity and some can be attributed to the beam.

Beam profile deconvolution

When creating a transverse irradiance profile by the use of a translated slit, all data so collected are integrations of irradiance over the area of the slit. This means that the profile created by the slit method is not necessarily the actual beam profile unless the beam profile is a Gaussian. The Gaussian is the only case in which the form of the profile created by a translated slit has the same form as that of the beam profile. Figure 35 shows the transverse irradiation profile created by orientating the slit parallel to the X axis and moving it through the beam in the Y direction. Error bars are given at ±3 % according to the accuracy of the Ophir 30A power meter used to collect the data and a Gaussian is fitted by the least squares method. It can be seen from the Gaussian fit that the transverse irradiance profile deviates from the Gaussian form by having a broader top and a narrower bottom. This suggested that an attempt should be made to reconstruct the actual beam profile from the slit profile data.

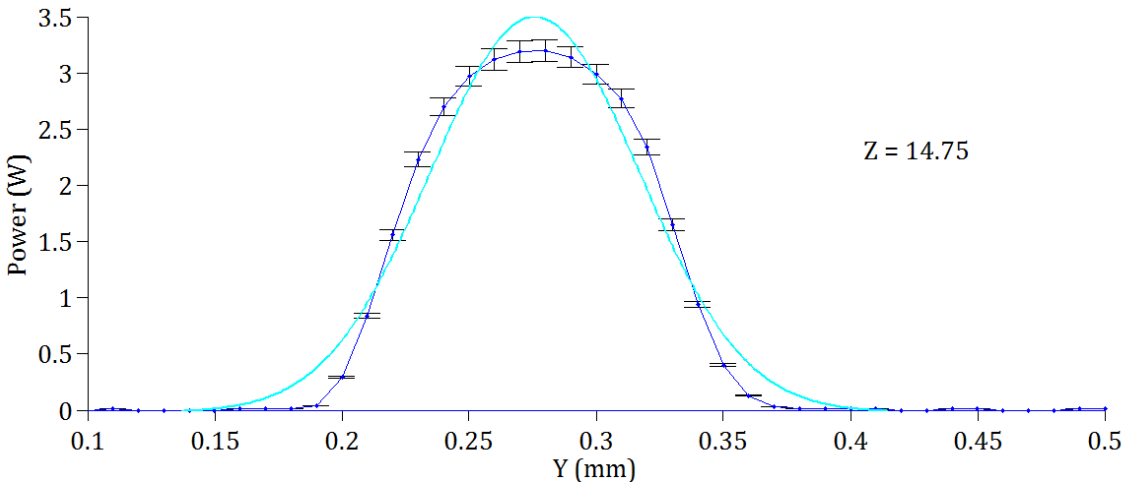

Figure 35 Transverse irradiance profile captured by translated 50 µm slit at or near focus. Cyan line is best-fit Gaussian.

There is some similarity between the translated slit method of beam profiling and that of Computed Tomography (CT) scanning and so one of the reconstruction techniques used in CT scanning was employed to reconstruct the beam profile. The method used was the inverse radon transformation which is based upon Fourier domain analysis and iterative reconstruction [135]. The Matlab image processing toolbox contains functions for the Radon transformation and was used to process the data. The Radon transformation of a 2D object, in the CT context, is a one-dimensional array containing the intensities produced by parallel beams of X-rays passing through the object and is thus an integration of attenuation over the area defined by the width of the pixels in the sensor and the thickness of the sample. This is an analogue of the translated slit method of beam profiling. Conversely, the inverse Radon transformation attempts to recover the 2D object from a sequence of 1D projections. The more 1D projections from different angles used the more accurate is the reconstruction. However, in this case there are only two sections available to recover the beam profile, the X and Y sections. These two sections were used as projections at 0, 90, 180 and 270 degrees with the X profile at 0 degrees, its mirror at 180 degrees, the Y profile at 90 degrees and its mirror at 270 degrees. In order to arrive at a smooth reconstruction the profiles at one degree increments between these fixed sections were produced by linear interpolation of the difference between the known sections. The reconstructed beam profile is shown in Figure 36 and orthogonal sections shown in Figure 37 where the fibre core

size has been added for comparison. The flattened top of the distribution agrees with the notion that the optics will image the end of the fibre at the workpiece.

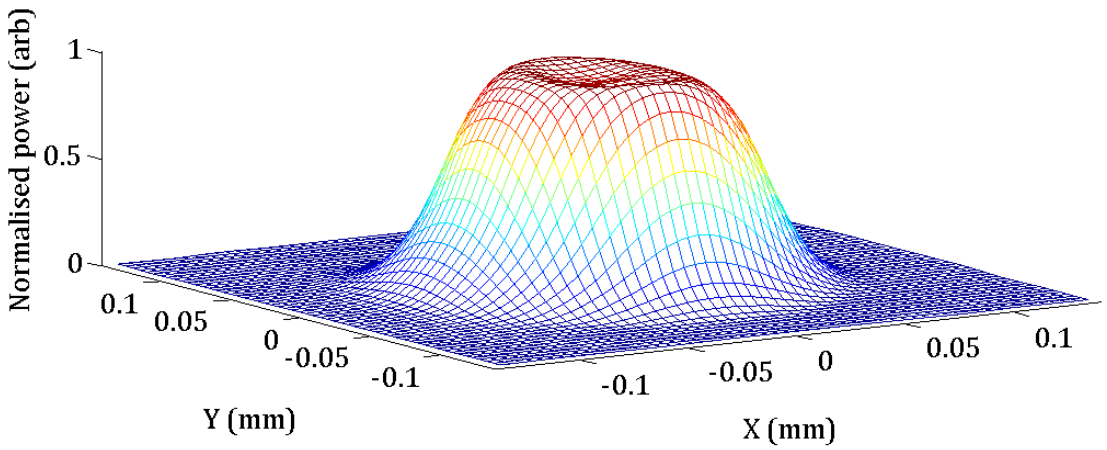

Figure 36 Beam profile recovered by inverse Radon transformation of the transverse irradiance profiles.

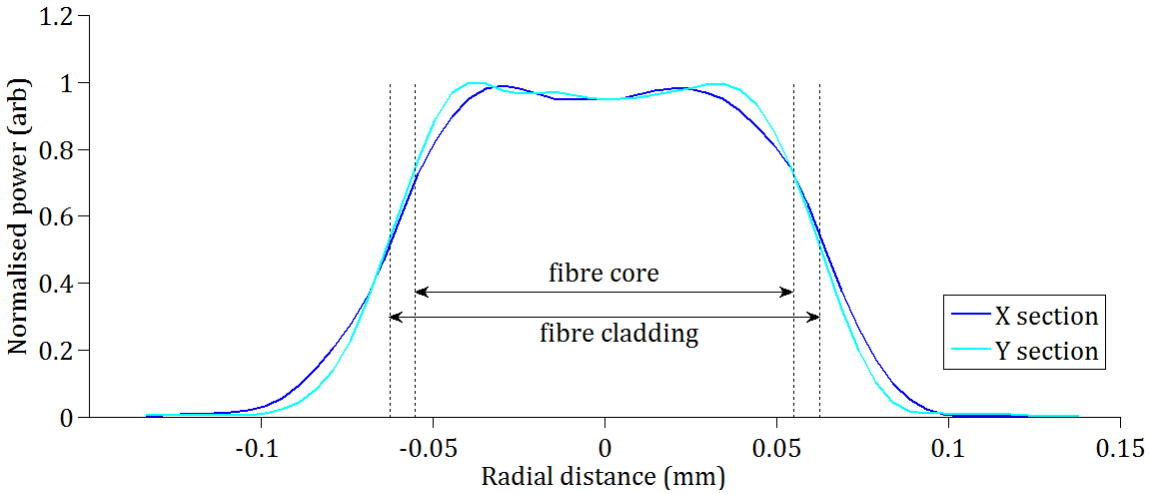

Figure 37 Sections through the beam profile of Figure 36.

3.5 Material properties and photon absorption

The pre-placed stainless steel powder is heated beyond melting point by the incident photon flux then left to cool to form the melt ball. This section provides an explanation of the melting process and some of the more relevant material properties that affect the process.

3.5.1 Material interaction

Energy incident upon a material surface is reflected, absorbed, or transmitted in various degrees dependent upon the material in question, the surface roughness, and the wavelength of the radiation. Conservation of energy gives the relationship that can be expressed by:

$$I_0 = I_T + I_A + I_R \tag{3.5}$$

where I is the intensity of radiation and the subscripts 0, T, A and R correspond to incident, transmitted, absorbed and reflected respectively. The method of energy exchange between photons and bulk material is through the medium of electrons.

In the case of metals the sea of free electrons, that give rise to high thermal and electrical conductivities, offer a vast number of unfilled energy levels above the Fermi energy that allow for efficient photon absorption and re-radiation within the visible and infra-red.

In the case of metals the sea of free electrons that give rise to high thermal and electrical conductivities also gives rise to high reflectivity. This reflectivity increases with increasing wavelength and can approach near unity for a CO_2 laser emitting at 10.6 μm [136, p. 90]. Metals have a vast number of unfilled energy levels above the Fermi energy that allow for efficient photon absorption within the visible and infra-red. This leads to high values of the absorption coefficient, typically $5 \times 10^5\ cm^{-1}$for metals in the visible spectrum [137]. With reference to the Beer Lambert law Equation 3.6 this means that 63 % of the incident photons are absorbed within ~20 nm of the surface.

$$E = E_0 exp(-az) \tag{3.6}$$

where a is the absorbtion coefficient and z is distance. An electron promoted to a higher energy level by photon absorption will gain energy inversely proportional to the wavelength of the incident photon defined by:

$$\Delta E = \frac{hc}{\lambda} \tag{3.7}$$

where h is Planck's constant, c is the speed of light and λ is the wavelength of the photon. Electrons can only occupy these elevated states for a short period of time before they return to the Fermi level and release the stored energy. The majority of this energy is in the form of photons, hence the high reflectivity, but some will decay *via* phonon release which leads to heating.

Once light energy has been absorbed in the skin of the metal, conduction is required to transfer the energy away from the surface and into the bulk so that temperature rise and phase transitions can occur. Thermal conduction and other material properties necessary for characterising this process are presented in Appendix B along with material data for SS 304 (substrate) and SS 316 (powder) stainless steels.

3.6 Summary

An overview of the experimental system has detailed the system's sub-components and how they have been configured to interact.

The first step in a melt ball's path to existence was given as the creation of a text file comprising a list of build instructions. The compilation of this list from a bit map of desired exposure sites and various scanning parameters was detailed and a description of the file format given. The second step comprised reading the instruction file, controlling the hardware (movement stages, laser diodes and powder handling unit), and transferring data between a PC and the custom microcontroller circuitry for which the communication protocol has been described. The third step was the generation and delivery of photons. The laser diodes used in this research have been characterised for output power and spatial intensity profile. A review of relevant thermal properties and their temperature dependence has been presented.

Chapter 4

Single spot processing

4.1 Introduction

The technology developed for this research can be compared to that of dot matrix printing. The employment of an 'expose-move-expose' strategy has resulted in the delivery of laser energy whilst the laser head is stationary relative to the powder bed. Using this strategy, 3D shapes could be built in a powder bed by the successive creation of individual melt pools/balls rather by the creation of a continuous melt bead as is typical in commercially available machines. The individual melt ball is therefore the fundamental building unit for more complex structures. Consequently this chapter will detail the experiments concerned with the effects of single isolated exposures. The process of creating a melt ball will be characterized as follows:

1. On substrate without powder.
2. On substrate with a thin powder layer.
3. In deep powder without substrate.

The effects of exposure time, exposure power, and powder depth upon the melt ball will be established by 3D scanning with an interferometer, microscope photography and sectioning samples.

4.2 Single exposures on substrate

Two experiments were performed exposing a substrate without powder. The first was a focus-finding exercise. The second was to give a baseline measurement of the extent of melting both of horizontal spread across the surface of the substrate and vertical penetration into the

substrate. A finite element model was developed, verified with experimental data and used to predict the effects of altering the focal spot size.

4.2.1 Focus finding

Focus finding was performed by the following procedure. A one-millimetre thick plate of stainless steel grade 304 was affixed to a powder handling mechanism piston top plate and ground flat with P180 grit silicon carbide abrasive paper. The piston top plate was then fitted into place within the powder handling machine and adjusted by sprung levelling screws. The orientation of the substrate was measured by the use of a dial gauge attached to the optical head support bracket and was adjusted such that the maximum variation from corner to corner of the substrate was less than 20 μm (Figure 38).

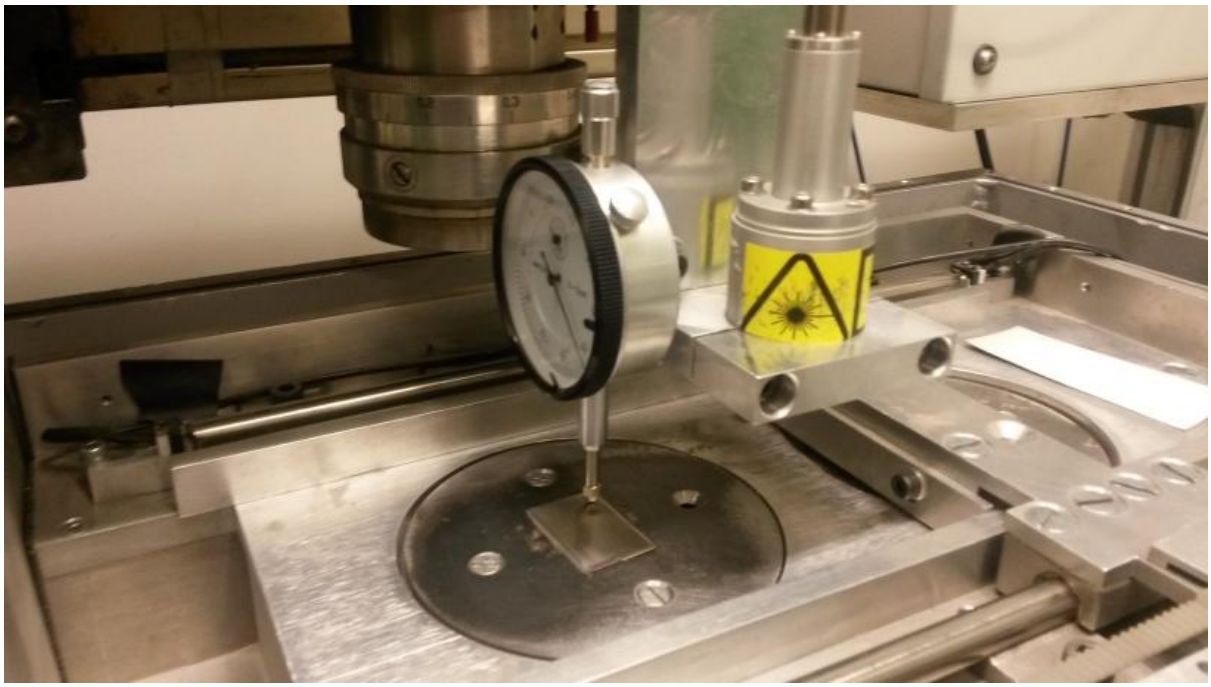

Figure 38 Levelling of the substrate.

To find focus the varied parameters were the standoff distance of the optical head from the substrate, exposure time and exposure power. Seven exposure times were used for each of three power levels Table 10. The three power levels used were 100 %, 75 % and 50 % which equated to 42, 32 and 21 W. The exposure times were adjusted inversely proportional to the power level so that the energies delivered in each sequence of exposures for a given power was

commensurate with the other sequences. Three spots were created with each exposure time/power combination and the diameters of the resultant melt spots were measured with optical microscope software.

Table 10 Exposure times in milliseconds.

Laser power	Pulse energy (mJ)						
	32	42	84	126	210	420	630
42 W	0.75	1.00	2.00	3.00	5.00	10.0	15.0
32 W	1.00	1.31	2.63	3.94	6.56	13.1	19.7
21 W	1.50	2.00	4.00	6.00	10.0	20.0	30.0

The three spots shown in Figure 39 were created with powers of 42, 32 and 21 W at focus or at Z = 1.50 mm for the Aerotech gantry stage which equates to a standoff distance of 49.59 mm between the bottom of the optical head and the surface of the substrate. The diameter of the spot can be seen to decrease with decreasing power although the brown heat affected zone has become darker and larger so that the overall diameter of the heat affected zone is approximately constant.

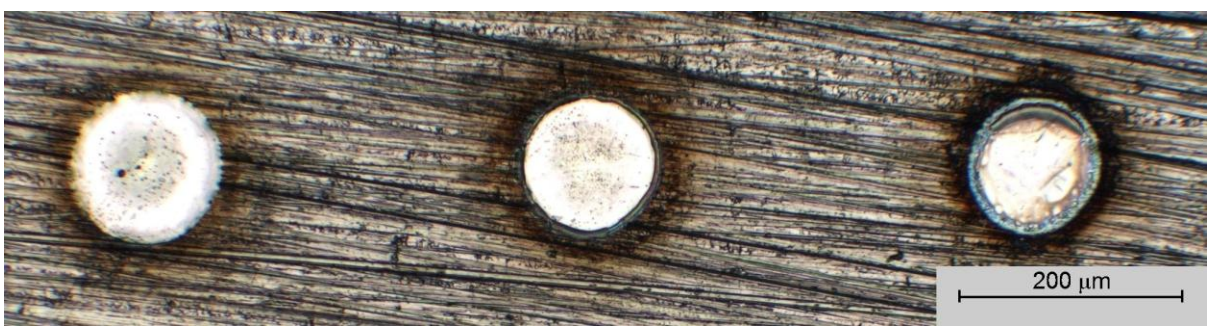

Figure 39 Melt spots created on 304 stainless steel at focus with powers of 42, 32 and 21 W from left to right with a pulse energy of 420 mJ for each exposure.

The spot diameter as a function of focal distance was plotted for the seven pulse energies using 42 W of power (Figure 40). The sequences of melt spots produced with the lower powers showed similar trends to that of the 42 W sequence but had greater variation and more missing data points away from the focal position. Consequently the trends were less clear and therefore the data are not shown. It can be seen in Figure 40 that at low pulse energies there is a maximum

in spot size at Z = 49.59 mm and at higher pulse energies there is a local minimum at Z = 49.59 mm.

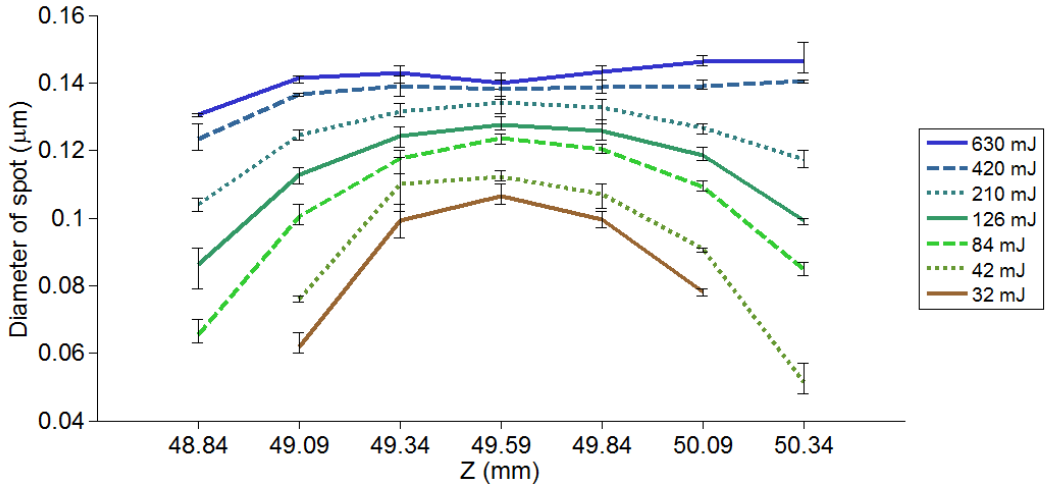

Figure 40 Diameter of melted spot on substrate as a function of focal distance.

At low pulse energies the maximum is an indication of beam focus as this is where the beam has a sufficiently high energy density to overcome the conduction of heat into the bulk of the substrate and to melt more material. At higher pulse energies the local minimum is also an indication of focus as this is where the beam diameter is smallest and thus yields a smaller molten spot Figure 41. The derivation of the standoff distance between the optical head and the substrate from the Z stage value involves the sum of three measurements that are ±10 µm that add in quadrature, so the focal length can be given as 49.59 ± 0.02 mm.

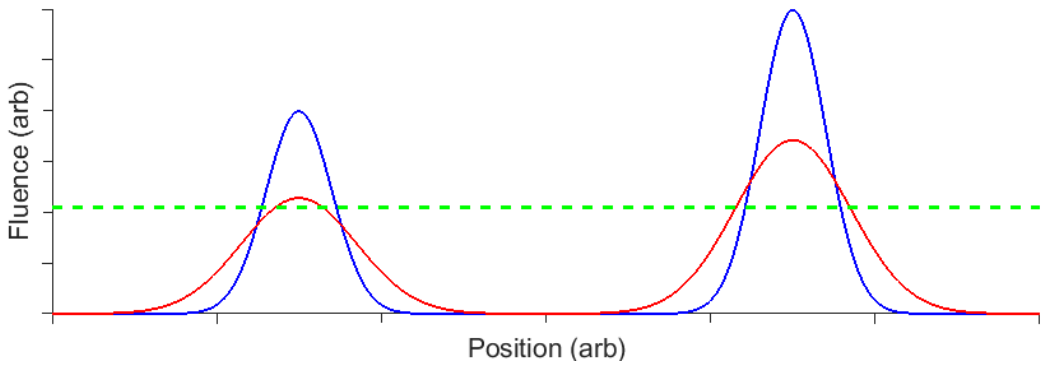

Figure 41 Two pairs of Gaussians. Each overlapped pair has equal pulse energy. Blue = in focus, red = de-focussed, green line indicates melting threshold. Left hand, lower pulse energy case shows larger melt at focus. Right hand, higher pulse energy shows smaller melt at focus.

4.2.2 Substrate melting

In order to establish the degree of melt penetration into the substrate in the absence of powder, lines of melt spots were created with a range of power levels and pulse lengths. The sample was first photographed using an optical microscope then sectioned, mounted, polished and etched with Marbles agent to reveal the extent of melt penetration. A line of spots was used because of the difficulty in sectioning and polishing a sample so that the section plane would be within the 50 μm necessary to intersect usefully with a single melt spot. Twenty seven lines of spots were created using three powers, 42, 32 and 21 W, and nine exposure times from 0.25 to 15 ms Table 11.

Table 11 Exposure times in milliseconds.

Laser power	Pulse energy (mJ)								
	11	**21**	**32**	**42**	**84**	**126**	**210**	**420**	**630**
42 W	0.25	0.50	0.75	1.00	2.00	3.00	5.00	10.0	15.0
32 W	0.34	0.66	1.00	1.31	2.63	3.94	6.56	13.1	19.7
21 W	0.50	1.00	1.50	2.00	4.00	6.00	10.0	20.0	30.0

The exposure times were sufficient to cover the range of no melting to significant melting. Figure 42 shows one such line of spots created with 1 ms exposures to 42 W of power and Figure 43 shows the transverse section obtained by sectioning orthogonally to the line of spot placement. The location of the section plane can create significant variation in the observed width of the melt pool (red lines Figure 42) and as a consequence variation between the observed sectional depth and the maximum depth of the melt pool. However, the location of the section plane can be calculated from the observed sectional width and the actual maximum width and thus an estimation of the maximum depth of the melt pool can be made.

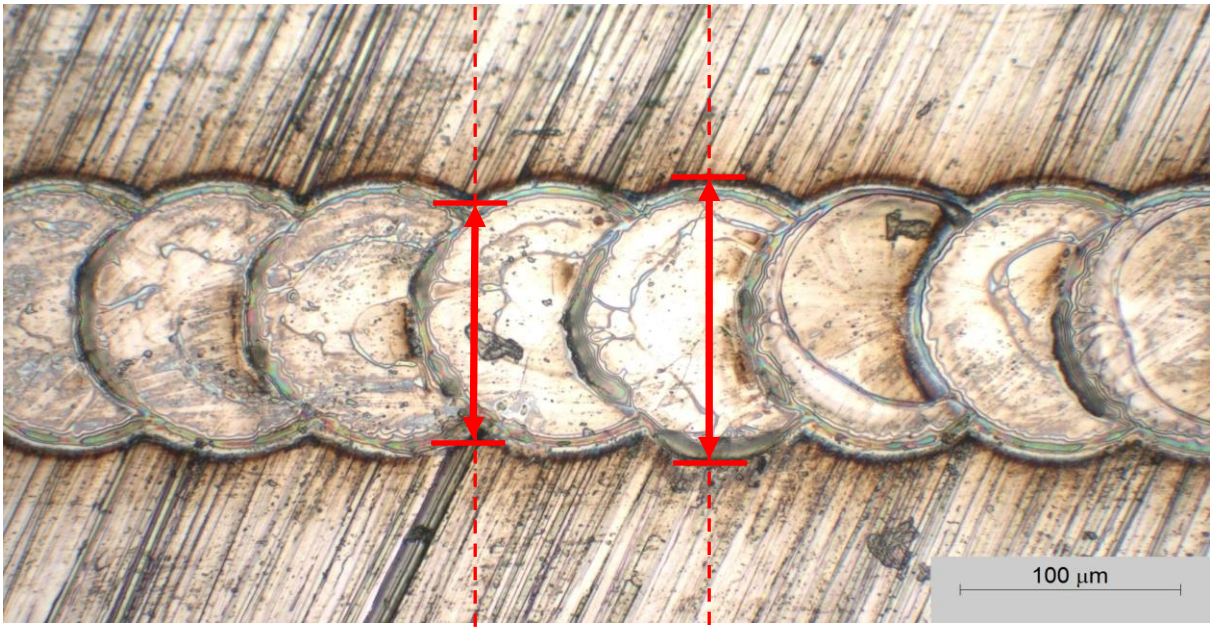

Figure 42 Melt spots in stainless steel 304 substrate on 75 μm pitch created by 1 ms exposures to 42 W of diode laser power. The red arrows illustrate the variation in melt pool width that would manifest in a transversal section plane located at the positions of the dashed lines.

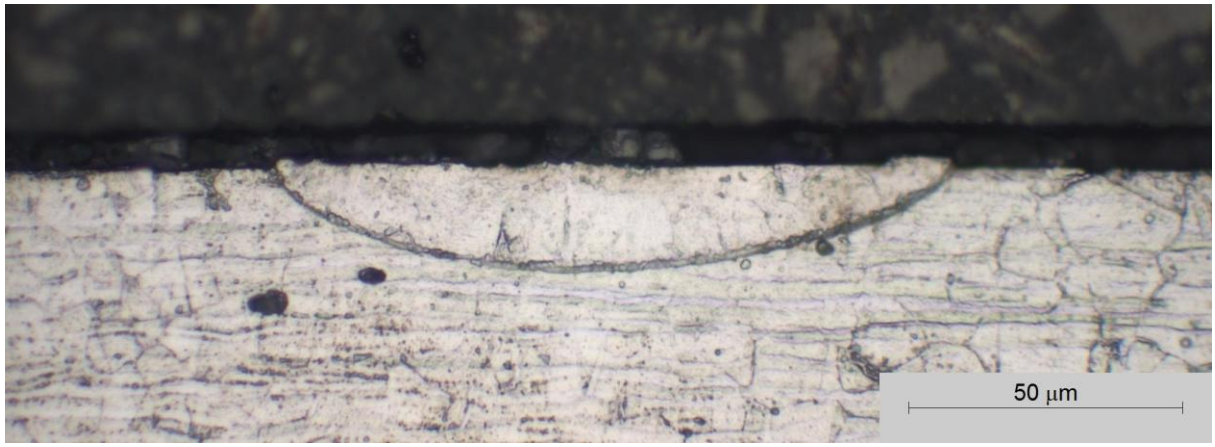

Figure 43 Transversal section through the line of spots of Figure 42. The exact location of the section is unknown but can be inferred from comparison between width and the variation illustrated in Figure 42.

To establish the maximum melt pool depth from a section plane not located at the maximum depth position the following method was used. It assumes that the melt pool has the profile of a spherical cap within the range of energies used. Although this assumption is unlikely

to be 100 % accurate the approximation is close, Figure 44 and considered more valuable than assuming a linear proportionality between melt pool width and depth or making no attempt to correct the data. With respect to Figure 45 the problem can be defined as: *what is Depth_2 given the measured Depth_1, Width_1 and Width_2?* Depth_1 and Width_1 are taken directly from the transverse section and Width_2 is taken from the microscope images of the substrate surface as in Figure 42.

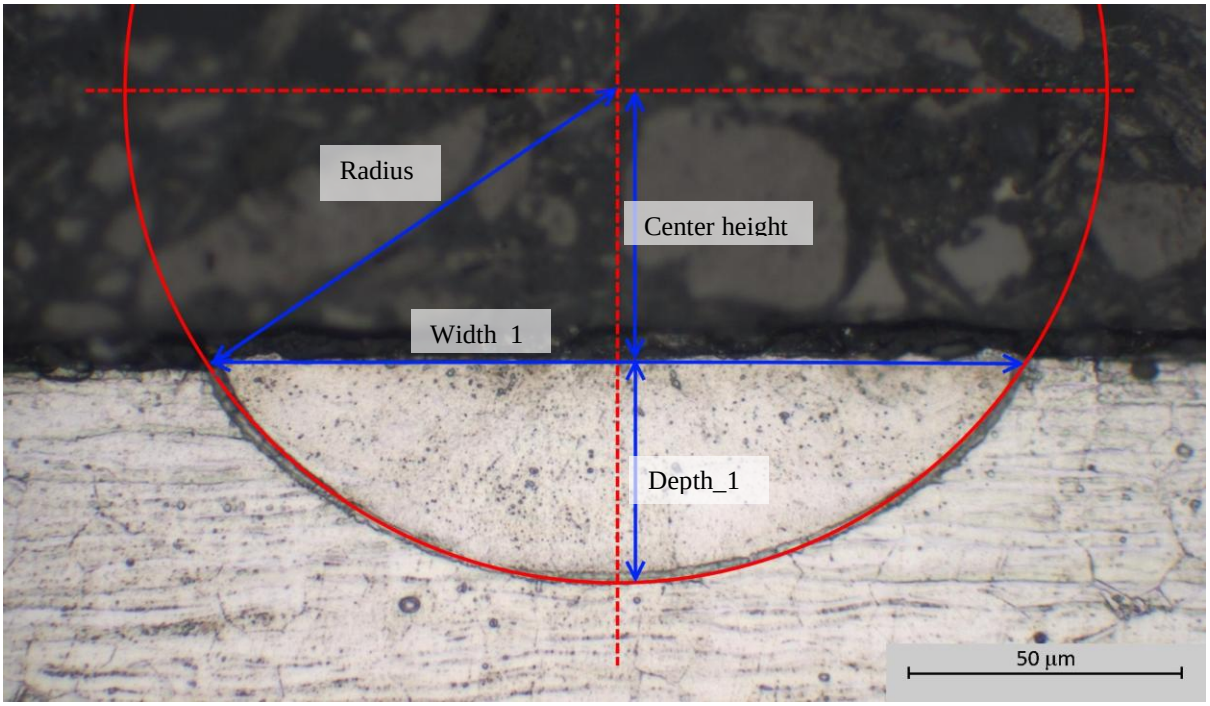

Figure 44 Section through a melt spot created by 10 ms exposure to 32 W showing the assumed circular geometry.

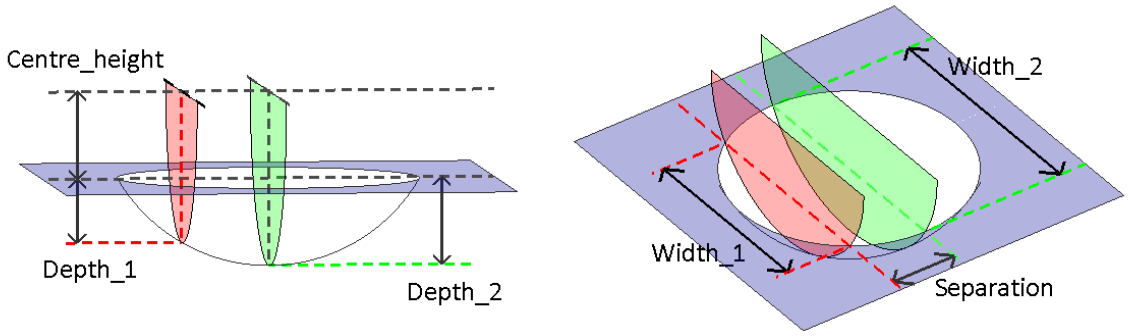

Figure 45 illustration of the melt pool depth problem. Red semi-circular plane = location at which section is taken. Green semi-circular plane = location of maximum depth and width.

The first step is to calculate the centre height, which is the height above the substrate of the centre of the sphere that defines the spherical cap. Given Depth_1 and Width_1 and the assumption of a circular profile, the application of Pythagoras' theorem and reference to Figure 44 gives

$$(Centre\_height + Depth\_1)^2 = \left(\frac{Width\_1}{2}\right)^2 + (Centre\_height)^2 \tag{4.1}$$

which gives

$$Centre\ height = \frac{(Width\_1/2)^2 - (Depth\_1)^2}{2 \times Depth\_1} \tag{4.2}$$

also by the application of Pythagoras' theorem and reference to Figure 45

$$Separation^2 = \left(\frac{Width\_2}{2}\right)^2 - \left(\frac{Width\_1}{2}\right)^2 \tag{4.3}$$

and

$$(Centre\_height + Depth\_2)^2 = Separation^2 + (Centre\_height + Depth\_1)^2 \tag{4.4}$$

therefore

$$Depth\_2 = \sqrt{Separation^2 + (Centre\_height + Depth\_1)^2} - Centre\_height \tag{4.5}$$

This method of correction has been applied to the measured penetration data, and the effects of pulse energy upon melt pool depth and width are shown in Figure 46. There is a threshold energy density below which the thermal energy is conducted away from the irradiated area before it raises the temperature to above melting. This is between 10 and 21 mJ *per* pulse at 42 W and between 21 and 42 mJ *per* pulse at 21 W for the given energy distribution within the focal spot Figure 46. Above this threshold the depth and width of the melt pool both increase with pulse energy until the width stabilises at approximately the beam diameter. Given that the powers were kept constant during each sequence of melt spots Figure 46 can be regarded as showing the temporal evolution of the melt pool's dimensions, although the horizontal time scale for each of the three curves will be different. At the maximum pulse length used in these experiments the rate of increase of the melt pool width has reduced significantly. This yields a ~160 μm diameter for 42 W which is close to the measured second moment beam diameter of ~150 μm whereas the rate-of-depth increase had not stabilised.

For a given pulse energy both the depth and width of the melt pool formed are greater when using a higher power. This is as a result of the decreased losses into the bulk caused by conduction [138]. This is evidenced in Figure 46 where a depth increase of ~50 % and a width increase of ~10 % occur with a doubling of the applied power for a given pulse energy.

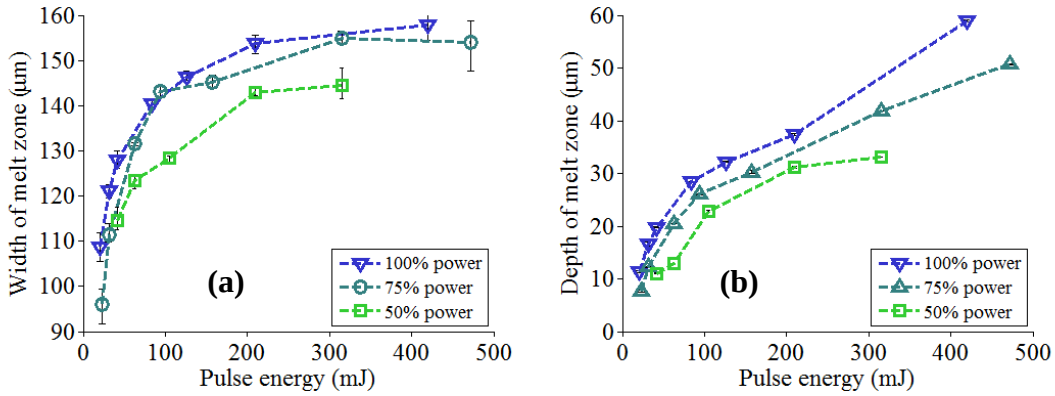

Figure 46 Substrate melt dimensions as a function of pulse energy for three powers. (a) melt pool width. (b) melt pool depth

4.2.3 Finite difference model

A finite difference thermal model was constructed in order to model the effects of power and spot size upon the dimensions of a melt pool created in a solid substrate. Proprietary software such as Fluent or Comsol could have been used but it was thought that a better understanding of the thermal principles would be achieved if the model was written from scratch using Matlab and that the time investment to master either would be similar.

The starting point was to investigate the suitability of a simple 1D conductivity model and whether this could match the results previously obtained by experimentation. As this did not agree with the measured data a 3D model was developed

1D model

The 1D conductivity model is a much-studied problem and analytical solutions exist for some specific cases. Two potentially useful cases were:

Semi-infinite medium with constant parameters and uniform illumination [139]

$$\Delta T(z,t) = \frac{2H}{k}\sqrt{\alpha t}\, ierfc\left[\frac{z}{2\sqrt{\alpha t}}\right] \tag{4.6}$$

Semi-infinite medium with constant parameters and uniform illumination of a spot with given radius [139]

$$\Delta T(z,t) = \frac{2H}{k}\sqrt{\alpha t}\left\{ierfc\left[\frac{z}{2\sqrt{\alpha t}}\right] - ierfc\left[\frac{\sqrt{z^2+a^2}}{2\sqrt{\alpha t}}\right]\right\} \tag{4.7}$$

Where H = I(1-R), I = Intensity, R = reflectivity, k = conductivity and α = diffusivity and

$$ierfc(x) = \frac{e^{-x^2}}{\sqrt{\pi}} - x[1 - \mathrm{erf}\,(x)] \tag{4.8}$$

$$\mathrm{erf}(x) = \frac{2}{\sqrt{\pi}}\int_0^x e^{-\xi^2} d\xi \tag{4.9}$$

However these analytical solutions do not incorporate the phase change from solid to liquid so they are only useful up to the melt point of the material. Therefore, it was decided to create a finite difference 1D conduction model in Matlab where phase change could be added, and to use the analytical solutions to verify the model's sub melting point behaviour.

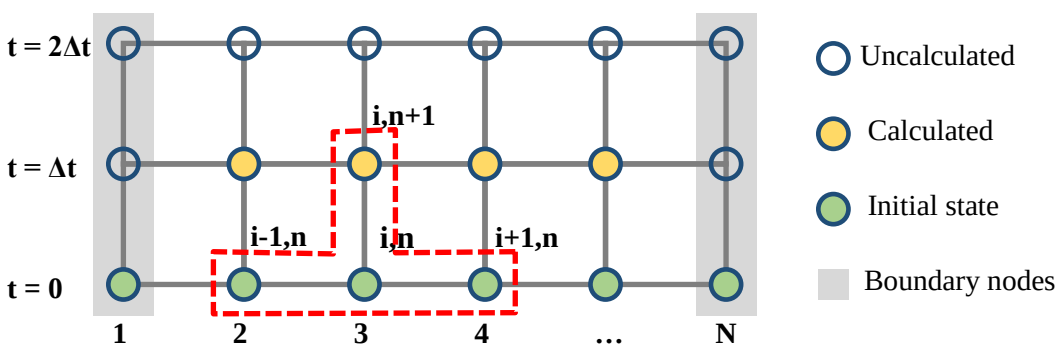

Figure 47 Grid of nodes representing a 1D conduction model in X with time evolution in Y showing, in yellow, the nodes that can be calculated using Equation 4.13 from the initial state (green). The red outline illustrates the nodes connected by Equation 4.13.The state of the 1st and Nth nodes are defined by the problem's boundary conditions.

In a finite difference model the continuous medium is approximated by a series of discrete points or volumes and the differential equations governing its evolution are approximated by finite difference equations. In one dimension the conduction equation is

$$\frac{\partial^2 T}{\partial x^2} = \frac{1}{\alpha}\frac{\partial T}{\partial t} \tag{4.10}$$

With reference to the nodal notation of Figure 47, the approximation of the time-dependent single differential term of Equation 4.10 calculated with a forward difference becomes

$$\frac{\partial T}{\partial t} \approx \frac{T_i^{n+1} - T_i^n}{t^{n+1} - t^n} = \frac{T_i^{n+1} - T_i^n}{\Delta t} \tag{4.11}$$

and the spatial double differential term of Equation 4.10 calculated with a central difference becomes

$$\frac{\partial T}{\partial x^2} \approx \frac{\frac{T_{i+1}^n - T_i^n}{\Delta x} - \frac{T_i^n - T_{i-1}^n}{\Delta x}}{\Delta x} = \frac{T_{i+1}^n - 2T_i^n + T_{i-1}^n}{\Delta x^2} \tag{4.12}$$

Thus, after substituting equations 4.11 and 4.12 into Equation 4.10 the temperature of node i after time Δt can be expressed as

$$T_i^{n+1} = T_i^n + \frac{\alpha \Delta t}{\Delta x^2}(T_{i+1}^n - 2T_i^n + T_{i-1}^n) \tag{4.13}$$

Using this equation and knowledge of the initial state of all nodes in the model it is possible to calculate the state of all nodes at the next time interval except the first and last nodes Figure 47. The states of the first and last nodes are arrived at by the application of boundary conditions which in this case are:

At x=L the boundary condition is

$$A\frac{\partial T}{\partial x} = 0 \tag{4.14}$$

The finite difference approximation using backward difference is

$$kA\frac{T_N^{n+1} - T_{N-1}^{n+1}}{\Delta x} = 0 \tag{4.15}$$

Which gives the expression

$$T_N^{n+1} = T_{N-1}^{n+1} \tag{4.16}$$

where N is number of spatial nodes in simulation.

At x=0 the boundary energy balance can be expressed as

$$Energy\ in = energy\ used\ for\ heating + energy\ out$$

$$Q_{laser} = \rho CA\frac{\partial T}{\partial t}dx - kA\frac{\partial T}{\partial x} \tag{4.17}$$

The finite difference approximation using forward differences becomes

$$\frac{Q_{laser}}{A} = \rho C\left(\frac{T_1^{n+1} - T_1^n}{\Delta t}\right)dx - k\left(\frac{T_2^{n+1} - T_1^{n+1}}{\Delta x}\right) \tag{4.18}$$

Which gives the expression

$$T_1^{n+1} = \frac{\frac{\alpha\Delta t\Delta x}{k}H + (\Delta x)^2 T_1^n + \alpha\Delta t T_2^{n+1}}{(\Delta x)^2 + \alpha\Delta t} \tag{4.19}$$

For verification of numerical method the output of this finite difference model was then compared to the analytical solution of Equation 4.7. Figure 48 demonstrates convergence towards the analytical solution with decreasing time and distance steps within the finite difference model. The non-temperature dependent material parameters used for the model are

shown in Table 12. The energy density was equivalent to 30 W into a spot of radius 100 µm. The thermal diffusivity was calculated by the application of Equation 4.20.

$$\alpha = \frac{k}{\rho C_p} \tag{4.20}$$

Table 12 Properties of stainless steel 316L [140, p. 72]

Property	Symbol	Value	Units	Value	Units
Density	ρ	0.29	lb/in^3	8030	kg/m^3
Specific heat	C_p	0.12	Btu/lb/ºF	502	J/kg/ºK
Thermal conductivity	k	112.8	Btu $in/ft^2/hr/ºF$	15.80	W/m/ºK
	Calculated thermal diffusivity			**3.92e-6**	**m^2/s**

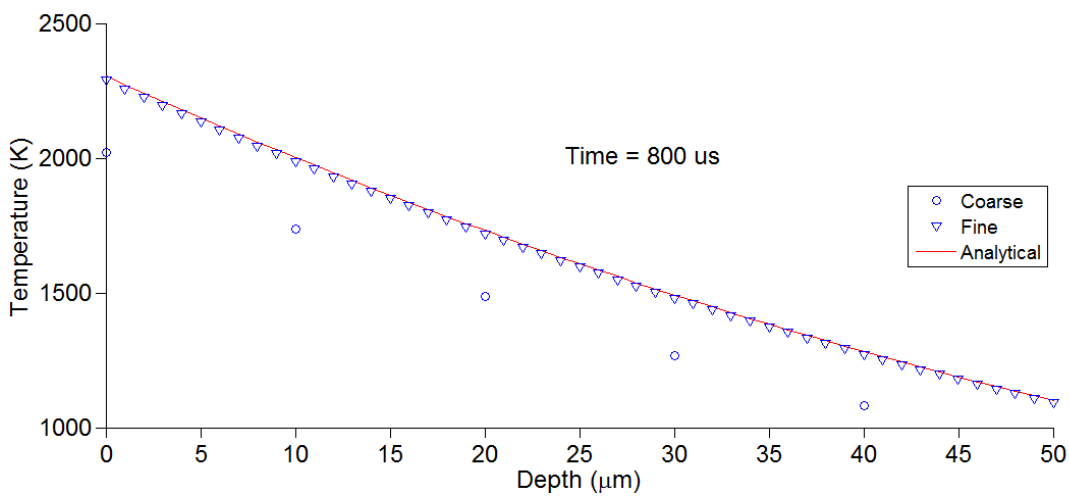

Figure 48 Two outputs from the 1D finite difference model compared to the analytical solution showing convergence with smaller iteration steps. For coarse and fine models the dt and dx values respectively are dt = 1 µs, dx = 10 µm and dt = 0.1 µs, dx = 1 µm.

To model the phase change at each node the accumulated latent heat method was used [141]. This method calls for both the temperature and the accumulated latent heat to be stored for

each node in the model. Once the temperature of any node exceeds the melting temperature then the energy available for melting is

$$\Delta Qaccumulated_i = \rho C_p^{mushy}\left(T_i^{n+1} - T_f\right) \tag{4.21}$$

where $T_f = melting\ temperature$ and the specific heat capacity in the semi-molten node is calculated from the solid and liquid specific heat capacities

$$C_p^{mushy} = (1 - f_{i-1})C_p^{solid} + f_{i-1}C_p^{liquid} \tag{4.22}$$

using the molten fraction of the node

$$Molten\ fraction = f_i = \frac{Qaccumulated_i}{\rho L_f} \tag{4.23}$$

where $L_f = latent\ heat\ of\ fusion.$

Once the accumulated latent heat has been updated the temperature of the node is set to the melting temperature and the next iteration is performed. If the accumulated latent heat is greater than the latent heat of fusion the temperature of the node is allowed to rise above the melting temperature.

$$T_i^{n+1} = T_f + \frac{Qaccumulated_i - \rho L_f}{\rho C_p^{liquid}} \tag{4.24}$$

After this the temperature rise for the node is calculated in the same way as below the melting point but using the liquid specific heat capacity. An example of the inclusion of phase change within the model is shown in Figure 49 which was created with the same material and power parameters as Figure 48. In the absence of knowledge, the liquid specific heat capacity was set to the solid specific heat capacity.

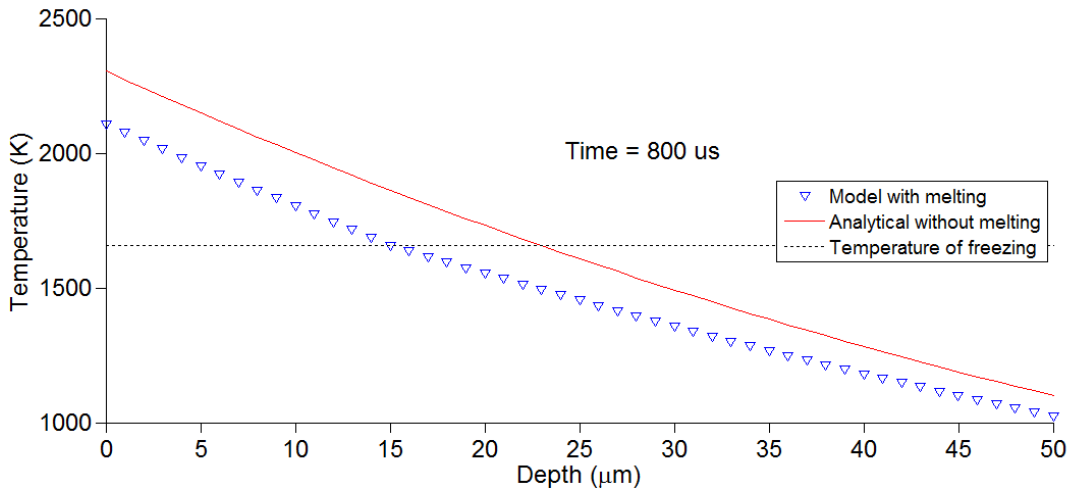

Figure 49 Output of finite difference model with phase change compared to the analytical model without melting. The change in gradient of the finite difference curve at the melting temperature indicates the effect of the latent heat of fusion.

This model was then used to plot the melt depth as a function of time to compare with existing experimentally measured data Figure 50. The theoretical melt depth is approximately five times that of the measured melt depth and the near linear form of the curve produced by this model doesn't agree with the logarithmic form of the experimental data. This suggests that ignoring lateral heat transfer by using a 1D model cannot approximate the real data.

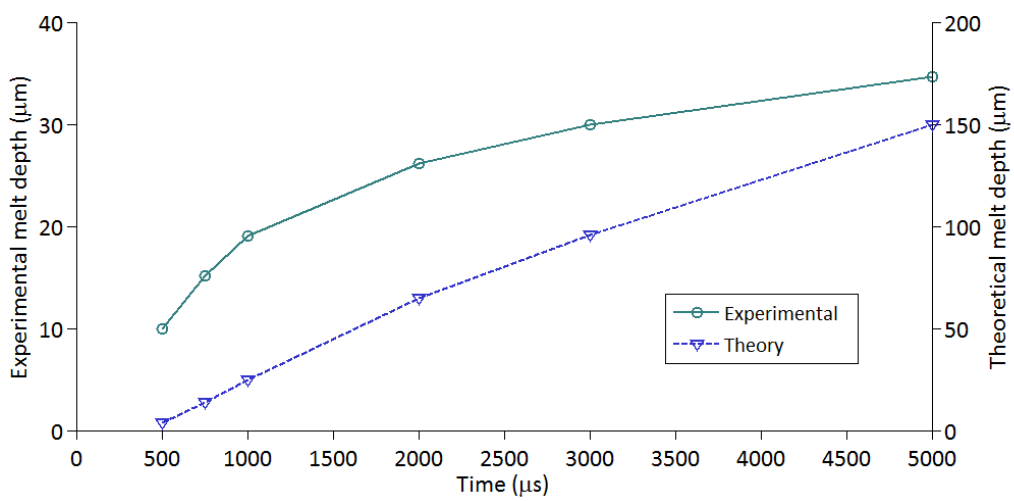

Figure 50 Melt pool depth within 316L substrate when illuminated with 30 W into a spot of ~100 μm radius.

3D model

As the model mechanics are the same it was therefore decided to extend the 1D model to three dimensions in an effort to model the experimentally obtained data more accurately. At the same time temperature dependant variables and a more sophisticated surface model incorporating radiative and convective losses were added.

The model volume is defined as follows: It has a unit cell of dimensions dx, dy, dz and spans –Lx/2 to Lx/2, -Ly/2 to Ly/2 and 0 to Lz with N_x, N_y and N_z cells in the X, Y and Z directions respectively. The laser illumination is normally incident upon the Z=0 plane.

In three dimensions the conduction equation becomes

$$\frac{\partial T}{\partial x^2}+\frac{\partial^2 T}{\partial y^2}+\frac{\partial^2 T}{\partial z^2}=\frac{1}{\alpha}\frac{\partial T}{\partial t} \tag{4.25}$$

Thus for 1<i<N, 1<j<N and 1<k<N the temperature of node I,j,k after time Δt can be expressed as

$$T_{i,j,k}^{n+1}=T_{i,j,k}^{n}+\alpha\Delta t\left[\frac{T_{i+1,j,k}^{n}-2T_{i,j,k}^{n}+T_{i-1,j,k}^{n}}{\Delta x^2}+\frac{T_{i,j+1,k}^{n}-2T_{i,j,k}^{n}+T_{i,j-1,k}^{n}}{\Delta y^2}+\frac{T_{i,j,k+1}^{n}-2T_{i,j,k}^{n}+T_{i,j,k+1}^{n}}{\Delta z^2}\right] \tag{4.26}$$

The nodes that cannot have their temperature after time Δt calculated with the above equation all belong to the six faces of the total cuboidal volume of the model. To assist in generating the temperatures of these nodes they can be usefully segregated according to whether they belong to a) a face, b) an edge or c) a corner of the total cuboidal volume of the model.

Boundary conditions:

The boundary condition for the face z = 0 is

$$H=\rho C\frac{\partial T}{\partial t}dz-k\frac{\partial^2 T}{\partial x^2}dz-k\frac{\partial^2 T}{\partial y^2}dz-k\frac{\partial T}{\partial z} \tag{4.27}$$

where

$$H=\frac{Q_{laser}}{dxdy}-\sigma\varepsilon\left(T^4-T_0^4\right)-h(T-T_0) \tag{4.28}$$

$where\ \sigma = Stephan\ Boltzman\ constant,\ \varepsilon = emissivity,\ T_0 = ambient\ temperature$ and $h = heat\ transfer\ coefficient$ which gives the expression

$$T_{i,j,k}^{n+1} = \frac{\frac{\alpha \Delta t \Delta z}{k} H + term1 + term2 + \Delta z^2 T_{i,j,k}^{n} + \alpha \Delta t T_{i,j,k+1}^{n+1}}{\Delta z^2 + \alpha \Delta t} \tag{4.29}$$

where

$$term1 = \alpha \Delta t \Delta z^2 \frac{T_{i+1,j,k}^{n} - 2T_{i,j,k}^{n} + T_{i-1,j,k}^{n}}{\Delta x^2} \tag{4.30}$$

$$term2 = \alpha \Delta t \Delta z^2 \frac{T_{i,j+1,k}^{n} - 2T_{i,j,k}^{n} + T_{i,j-1,k}^{n}}{\Delta y^2} \tag{4.31}$$

The boundary condition for the face z = Lz is

$$kA \frac{\partial T}{\partial z} = 0 \tag{4.32}$$

which gives the expression

$$T_{i,j,N_z}^{n+1} = T_{i,j,N_z-1}^{n+1} \tag{4.33}$$

The boundary condition for the face and two edges where x = -Lx/2 and the face and two edges where x = Lx/2 is

$$kA \frac{\partial T}{\partial x} = 0 \tag{4.34}$$

which gives the expressions

$$T_{1,j,k}^{n+1} = T_{2,j,k}^{n+1} \quad and \quad T_{N_x,j,k}^{n+1} = T_{N_x-1,j,k}^{n+1} \tag{4.35}$$

The boundary condition for the face and two edges where y = -Ly/2 and the face and two edges where y = Ly/2 is

$$kA\frac{\partial T}{\partial y} = 0 \tag{4.36}$$

which gives the expressions

$$T_{i,1,k}^{n+1} = T_{i,2,k}^{n+1} \quad and \quad T_{i,N_y,k}^{n+1} = T_{i,N_y-1,k}^{n+1} \tag{4.37}$$

The boundary conditions for the eight corners and four edges aligned to the z axis are

$$kA\frac{\partial T}{\partial x} = 0 \quad and \quad kA\frac{\partial T}{\partial y} = 0 \tag{4.38}$$

which gives the expressions

$$\begin{gathered} T_{1,N_y,k}^{n+1} = T_{2,N_y-1,k}^{n+1} \quad and \quad T_{N_x,N_y,k}^{n+1} = T_{N_x-1,N_y-1,k}^{n+1} \\ T_{1,1,k}^{n+1} = T_{2,2,k}^{n+1} \quad and \quad T_{N_x,1,k}^{n+1} = T_{N_x-1,2,k}^{n+1} \end{gathered} \tag{4.39}$$

Results

The 3D model previously described was used to generate the temporal evolution of melt pool depth and width data for a stainless steel 316L sample when exposed to the laser radiation used in Chapter 4. The dimensions of the model were 0.8 x 0.8 x 0.5 mm with an elemental unit cell of 5 x 5 x 5 μm and a time step of 0.5 μs. The energy profile of the laser radiation is that derived from translated slit data and scaled such that the sum of each elemental area's power comes to the 42 W that the diode laser had previously been measured to produce. The temperature dependent material parameters have been given in Appendix A Only the reflectivity of the solid and liquid phases was adjusted until a good agreement with reality was reached. The model was then used to illustrate the effects of changing the intensity of the illumination by changing the radius of the laser spot using scale factors of 20 % smaller and larger for the power distribution.

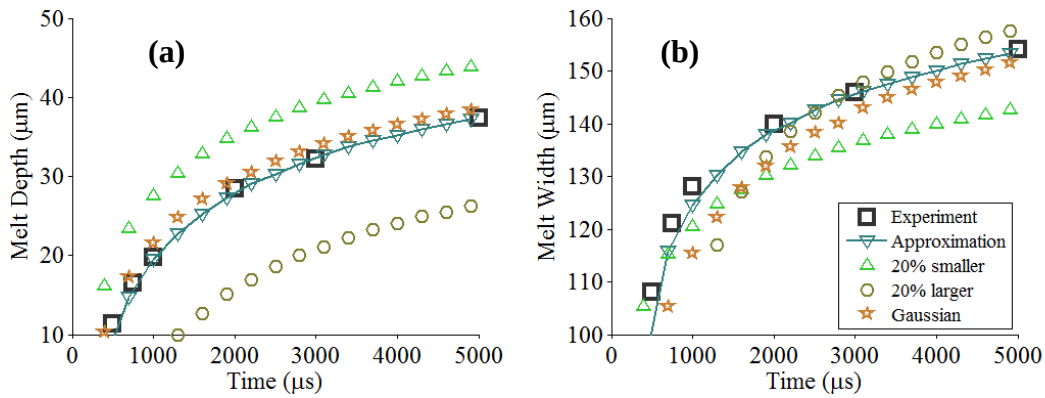

Figure 51 The experimental data for 100 % power from Figure 46 overlaid with four finite difference model results. 1) Approximation: closest results to reality. 2), 3) and 4) using the parameters of 1) but with a beam diameter that is 20 % smaller and larger or a Gaussian beam profile of same second moment diameter and total power.

Table 13 Finite element model melt pool dimension changes from altering the laser beam energy distribution.

Beam diameter	Mean Intensity	Change in melt depth	Change in melt diameter
20 % smaller	+56 %	+18 %	-7 %
20 % larger	-69 %	-30 %	+3 %
Gaussian with equivalent diameter	0 %	+3 %	-1 %

The finite difference model shows that an increase in intensity of 56 % caused by reducing the beam diameter by 20 % whilst keeping the power level constant increases the penetration of the melt by 18 % after 5 ms at the expense of decreasing the diameter by 7 %. Decreasing the intensity by 69 % by increasing the beam diameter by 20 % causes a 30 % drop in penetration for a 3 % gain in diameter. A Gaussian power distribution with the same second moment beam radius normalised to the same total power was also used to show the effect that could be achieved by using a laser with a higher beam quality, M^2=1. This demonstrates that a 3 % increase in penetration is achieved for the same power.

These results illustrate that melt penetration is more sensitive to the intensity of the energy source than the diameter of the melt pool is. To be able to build high density parts

requires that the previously consolidated material is re-melted to remove the oxide layer therefore working in focus and with the highest power (42 W) for a given pulse energy are important considerations.

4.3 Single exposures in single layer of powder

Experiments were performed to assess the effects of single exposures upon a layer of powder on a substrate. The powder used was 316L stainless steel, supplied by Sandvik Osprey, with a size distribution of between 5 and 53 μm and the substrate was 304 stainless steel ground planar with P180 grit wet and dry paper. Within this experiment melt balls were created using a single laser diode at three power levels of 42, 32 and 21 W. Eight pulse energies were used for each power level. Each run of different pulse energies was repeated three times in two powder layer thicknesses of 100 and 50 μm for a total of 144 individual exposures. The resultant melt balls were photographed and scanned with a Veeco interferometer to extract melt volume and melt feature height.

Many of the melt features that appeared as a result of this experiment had the appearance of semi-ellipsoids and their volume was calculated by

$$Volume = \frac{2}{3}\pi abh \tag{4.40}$$

where a = minor radius, b = major radius and h = height. Where there were small spherical features remaining stuck to the substrate or the main melt ball these were ignored if they were less than 50 μm in diameter as these could be the powder grains sintered to the substrate. If they were larger they would be the result of melting and thus included in the total of volume melted and modelled as spheres or cylinders depending upon approximate shape. The protrusions of Figure 52 are assumed to be caused by grains of material being brought into the melt by gas flow induced by thermal gradients and metal vapour ejection. These grains can join the melt as it is cooling down but if there is insufficient time before solidification to minimise the surface energy then the protrusions remain.

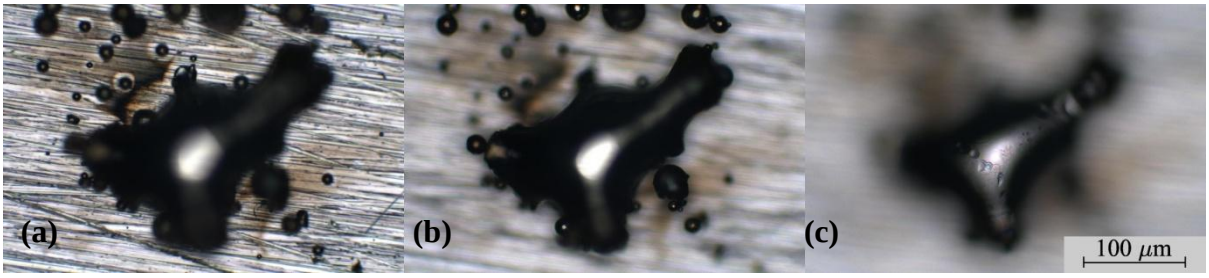

Figure 52 Images of a melt ball produced by 6 ms exposure at 21 W in 50 μm powder layer on SS 304 substrate. The three parts of the image taken at different focal positions show the overall shape in which grains of material have joined the melt as it was cooling down thereby forming protrusions.

The measured heights and calculated volumes are shown in Figure 53 and Figure 54. There is an increase in both height and volume of the melt balls when using a deeper powder layer for any of the three power levels or pulse energies. This is to be expected as there is more powder available to melt for the energy supplied. However, this trend will stabilise at a maximum regardless of any further layer thickness increase once the layer is sufficiently thick as the incident energy can no longer penetrate the powder as far as the substrate. There is also a trend for the height and volume of the melt ball to increase with power level for a given pulse energy and powder layer thickness. This is a result of less thermal energy being dissipated from the site of the incident laser beam primarily by conduction through the substrate [142].

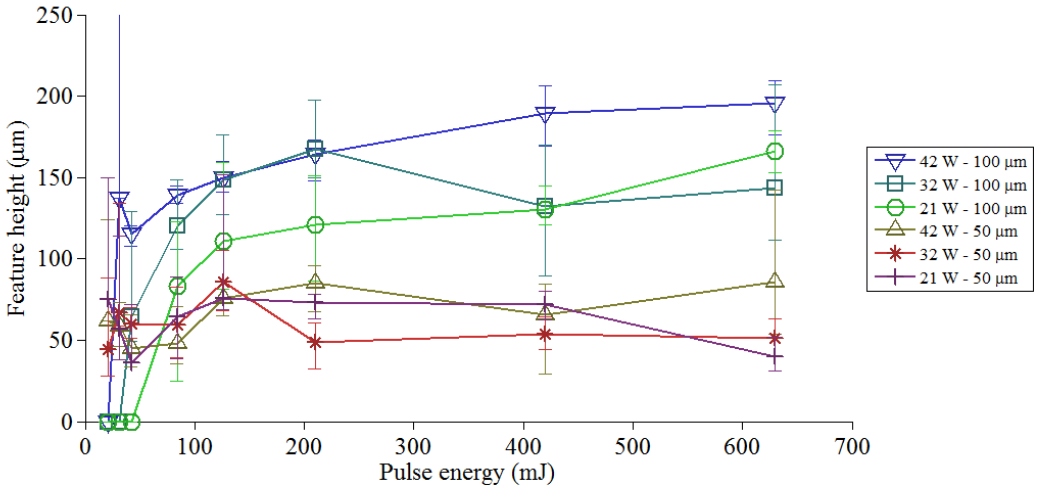

Figure 53 Maximum height of melt ball as a function of pulse energy for three power levels and two powder layer thicknesses.

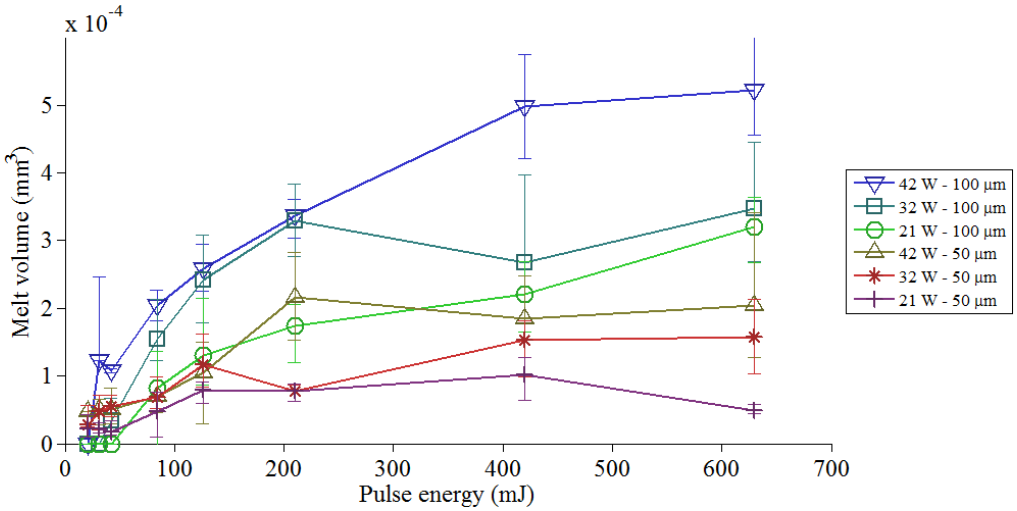

Figure 54 Calculated melt volume of melt ball and features asd a function of pulse energy for three power levels and two layer thicknesses.

One of the unwelcome effects of laser powder bed interaction is that of powder denudation. This manifests as a region of little or no powder around the solidified melt. A significant factor in its creation is that of localised gas flow caused by the ejection of metal vapour. This gas flow entrains neighbouring particles that can either be drawn into the melt or be expelled upwards [143].

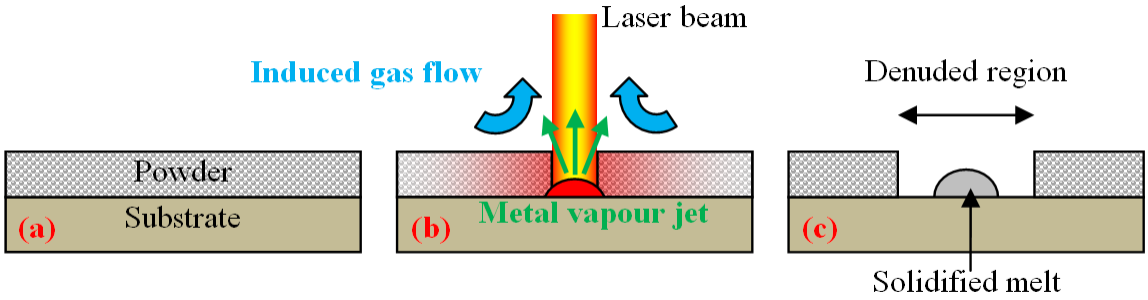

Figure 55 Illustration of powder denudation by a laser beam.(a) Initial state of powder layer. (b) Evaporated metal vapour induces gas flow that entrains nearby grains. (c) Solidified material within a region denuded of powder.

The denudation diameter around each exposure was calculated to compare with the volume of melt. This was achieved by using 3D scan data of the balls *in situ* in the powder layer that are generated by a Veeco white light interferometer. An example of such a point cloud is

shown in Figure 56 along with illustrations of the steps used to calculate the denudation width. Using Matlab and starting with a 3D scan of the melt balls in powder a threshold height was applied to create a binary image such that all points below 10 µm were coloured white and all missing data points and those above 10 µm were coloured black. Next the binary image was loaded into an image manipulation program (Paint.net) and the black areas that corresponded to melt balls were removed by hand. This method is can be subjective but it was performed with reference to the Veeco scan data and microscope photographs to act as aids. The adjusted binary image was then processed by the use of Matlab to generate a profile of the total number of white squares within each column which gives a measure of the amount of missing powder along the line of the sequence of melt balls. The profile was then smoothed with a moving average filter to reduce noise and interrogated at each of the eight spot positions for the width of denudation at those points. However, the maximum width of the denuded zone rarely occurred at the exact position that the balls were created at so an algorithm was developed to search the profile either side of the expected position for the top of a peak. This peak-search algorithm had a width of 150 µm to localise its search and in the absence of a peak it would default to the value at the expected position.

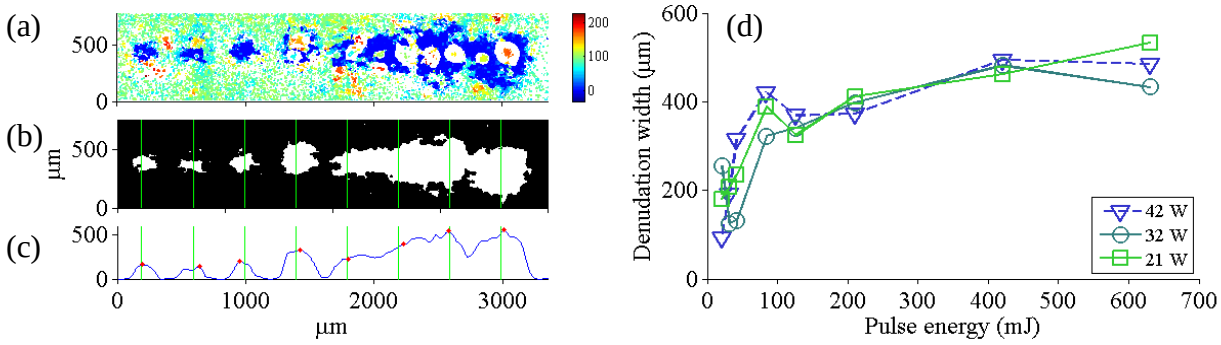

Figure 56 Denudation of powder by single exposures. (a) Point cloud scan of eight exposures of increasing time (left to right) using 21 W into a 100 µm powder layer. (b) Binary image of top scan using a 30 µm threshold height and after having the melt balls removed from the image by hand. (c) Total of white points in each column of left middle, green lines indicate position of exposures. (d) Mean denudation width from three runs for three exposure powers.

The mean denudation width as a function of pulse energy for three exposure powers is shown in Figure 56 (d) where there is little difference in denudation width for each exposure

power for a given pulse energy. This is at odds with the increase in melt ball volume displayed in Figure 54 and requires explanation. To assist with this the total volume of denuded powder was calculated for each of the nine runs of eight exposures with varied pulse energy. The total was used because, with reference to Figure 56 (b) it can be seen that the 400 μm pitch of the exposure placement allowed overlap between each denudation zone which makes it difficult to isolate the exact denudation for each exposure. However the total will be valid in comparison with the total volume of melt balls produced. The total volume was calculated by summing the total number of white pixels in each binary image, Figure 56 (b), multiplied by the appropriate pixel scale factor then multiplying by the thickness of the layer and the relative density of the powder. The relative density was calculated to be 57 ± 2 % from simple volume and weight measurements. The mean values for the three duplications of each sequence are given in Table 14 where it can be seen that there is less than 3 % difference between the values. Although the volume of powder material displaced by each run of exposures is similar there is a significant difference in the percentage of material left affixed to the substrate when the powder was brushed off and subsequently scanned. In conclusion material is leaving the immediate interaction zone either as powder or as smaller melt balls that do not wet to the substrate. Simonelli *et al* propose that vapour pressure caused by the vaporisation of material is enough to expel droplets of molten material away from the interaction zone [144]. However, another significant factor for explaining the material deficit would be balling of the melt as a result of insufficient or no wetting to the substrate. When this balling is combined with the vapour pressure effect this can lead to the movement of entire melt balls. Insufficient wetting is more prevalent when using lower exposure powers as evidenced by the lower percentage of denuded powder converted into melt ball volume adhering to the substrate (Table 14).

Table 14 Volumes of melt balls and denuded material.

Power level	42 W	32 W	21 W
Mean Volume melt balls (x 10^6 μm^3)	19.7	13.6	9.30
Volume of denuded material at 57 % relative density (x 10^6 μm^3)	41.8	42.9	42.5
Percentage of denuded volume adhering to substrate	47	32	22

4.4 Single exposures in deep powder

The Scanning Electron Microscope (SEM) image (Figure 57) of melt balls created with 9 ms exposures to 42 W into deep powder shows that the resultant melt balls are approximately spherical due the cooling material attempting to minimise surface energy and being supported by un-melted powder grains. Subsequent melt ball volume calculations will approximate the balls as spheres for convenience. The melt balls have many powder grains adhering to their surface. The lower left melt ball of Figure 57 has one part of its surface without and one part with adherent powder grains. It is proposed that the part of the surface without adherent powder grains is the upper surface that was directly exposed to the incident radiation and that the part with the adherent grains is the lower part of the melt ball that was in contact with the non-melted powder as it solidified.

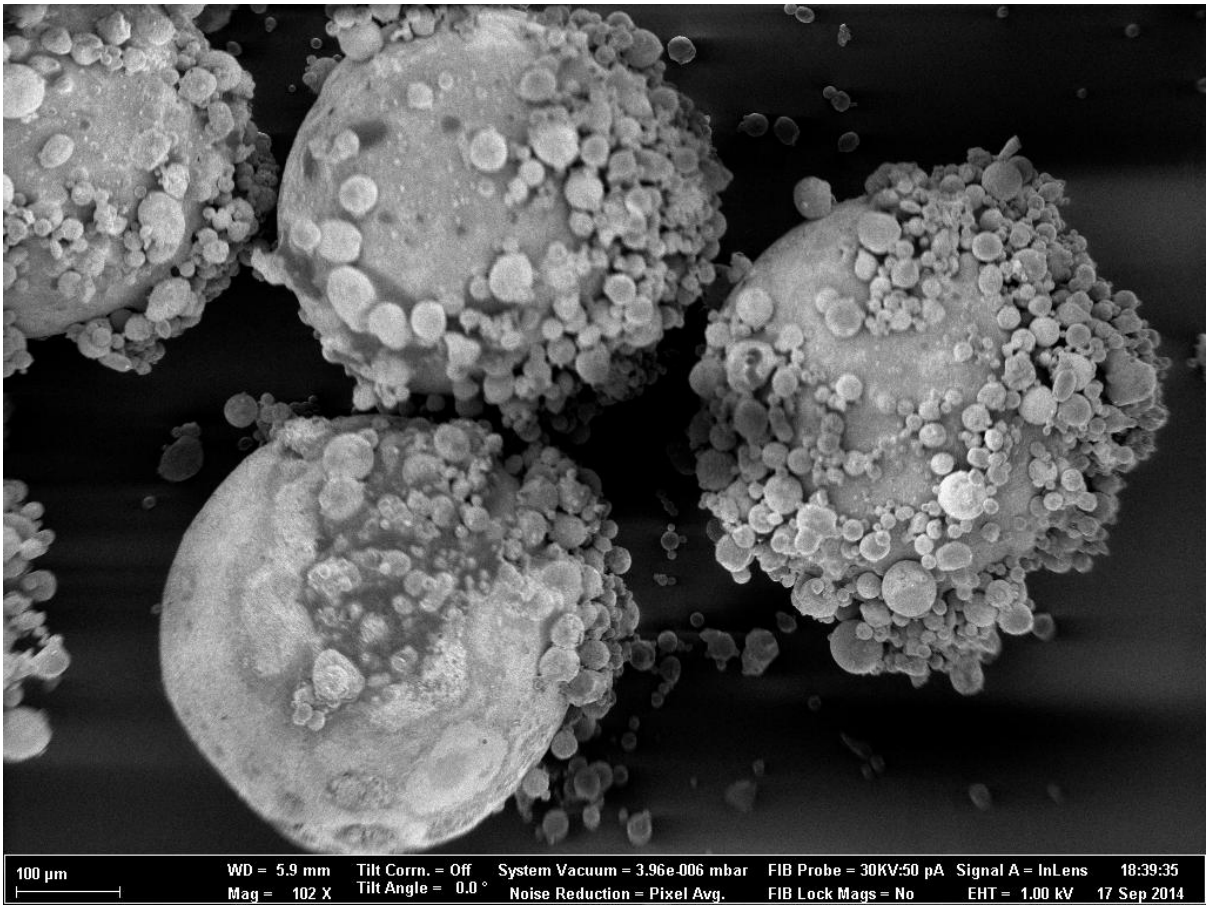

Figure 57 SEM image of melt balls created in deep powder by 9 ms exposure to 42 W.

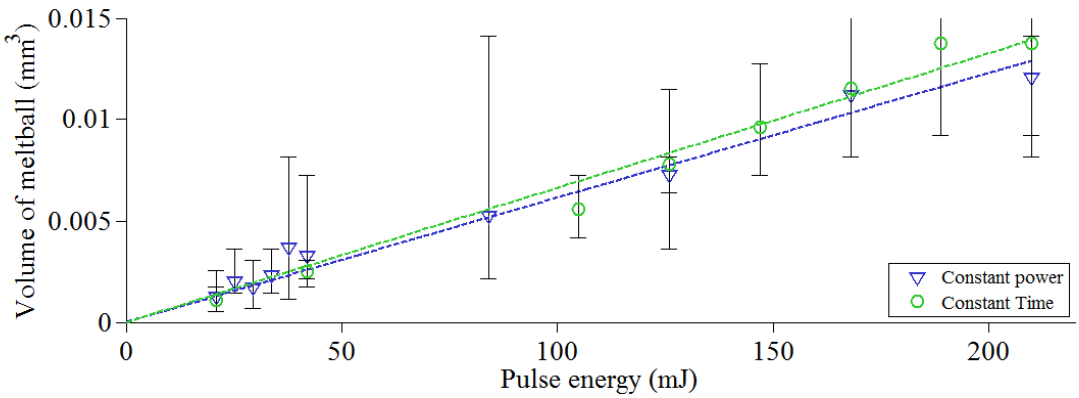

Figure 58 Volumes of melt balls created in a deep layer of 316L powder. Pulse energy altered in two ways: (1) Time: exposure power was kept constant at 42 W and the exposure time was varied down from 5 ms to 0.4 ms or (2) Power: Exposure time was kept constant at 5 ms and exposure power was varied down from 42 W to 3.3 W.

To establish the effects of exposure power upon melt ball size two series of melt balls were created using the same range of pulse energies. In the first series the power was kept constant at 42 W and the exposure time varied and in the second series the exposure time was kept constant and the exposure power varied. In both cases the range of pulse energies used was 21 to 210 mJ and the 210 mJ exposure was produced by a 5 ms exposure to 42 W. Twenty one melt balls were created at each exposure time and power combination which were sized with an optical microscope and their volumes calculated by approximation as spheres. The resultant volumes are shown in Figure 58 where first order polynomials have been fitted by least squares and forced to pass through the origin yielding gradients of 0.061 and 0.066 mm^3/J for the data produced using constant power and constant time respectively. Both fits have a 97 % R squared value suggesting that there is a linear correlation between the energy supplied and the volume of the melt ball produced within the experimental interval. The 8 % variation in gradient would indicate that it makes little difference if one exposes at full power for half the time or half power for full time. This contradicts the results obtained when melting the substrate without any powder present, (section 4.2.2). This is thought to be due to the difference in absorbance and thermal conductivity between the powdered and bulk forms of the material.

The absorbance of a powder is far greater than that of a flat substrate because the incident light that is not absorbed directly is reflected off the sides of the grains and further into the

powder to be subsequently absorbed. An estimation of powder absorbance is made by Streek *et al* as: [145]

$$\lim_{z\to\infty} A_{powder} \approx \sqrt[3]{A_{bulk}} \tag{4.41}$$

The thermal conductivity of a powder material is less than of solid because there are only point contacts between the particles. Therefore the thermal conductivity is governed largely by the thermal conductivity of the interstitial air and the radiative transfer from one grain to another. This is demonstrated by this approximation used by Li *et al*. [146]

$$\frac{k_p}{k_g} = \left(1-\sqrt{\beta}\right)\left(1+(1-\beta)\frac{k_r}{k_g}\right) + \sqrt{\beta}\left(\frac{2}{1-\frac{k_g}{k_s}}\left(\frac{1}{1-\frac{k_g}{k_s}} ln\left(\frac{k_s}{k_g}\right)-1\right)+\frac{k_r}{k_g}\right) \tag{4.42}$$

where k_p = conductivity of powder, k_s= conductivity of solid, k_g= conductivity of air β = relative density and k_r=radiation coefficient which is expressed as

$$k_r = 4F\sigma T_p^2 D_p \tag{4.43}$$

Where σ is the Stephan-Boltzmann constant, T_p = temperature of the particles, D_p = mean diameter of the particles and F is the apparent coefficient. This is a potentially unwieldy expression and requires the determination of an apparent coefficient with units of Kelvin. However, a variation of two orders of magnitude for $k_s$within equation 4.2 gives less than 1 % variation in the value of k_p which is in agreement with the assertion of Gusarov *et al* [147] who state that the thermal conductivity of a powder is essentially independent of the material and governed by the thermal conductivity of the gas. Gusarov *et al* also suggest that for un-compacted 10-50 μm powders the thermal conductivity is in the range 0.1 to 0.2 W/m/K rising to 0.3 W/m/K at melting point because the thermal conductivity of air increases with temperature. This is verified by Rombouts *et al*'s work in calculating the thermal conductivity of 316L power to range between 0.156 and 0.186 W/m/K and for copper powder to range between 0.078 and 0.19 W/m/K for various particle size distributions and packing fractions.

Given that the thermal conductivity of the 316L powder used in this research is likely to be ~0.2 W/m/K [148] a crude estimate of the powder's absorption coefficient can be made by regarding the thermal losses to conduction as negligible and calculating the energy necessary to heat a ball from room temperature to melting point as well as change its phase from solid to liquid. From the mean of the gradients of Figure 58 a 210 mJ exposure would create a ball of volume 0.014 mm^3 or 1.4e-8 m^3. To heat this amount of 316L from room temperature and to just melt it would require 120 mJ. This energy difference can yield an estimate of the minimum absorption coefficient for the 316L powder used as 120/210 = 57 %.

4.5 Summary

Figure 59 shows the melting ratio for the four cases detailed within this chapter that all use the full 42 W of power available. Melting ratio is a concept borrowed from the study of welding and is defined as the energy required to just heat and melt the affected volume of material compared to the energy supplied. The energy losses to conduction, convection, and radiation are included within this quantity so it can never be 100 % and for a bulk material the maximum has been reported as 48 % [149]. With respect to Figure 59 the energy losses are greatest with no powder and they decrease with increasing powder depth until an efficiency of 40-50 % is achieved with the very small conductive losses into deep powder. However, because of the difficulties in trying to section a sample through a feature ~100 μm in size, the penetration of the melt into the substrate for the 50 and 100 μm powder thickness cases is not included so these two cases will actually have a higher efficiency than shown. Within the experimental range of energies used there does not appear to be a common trend for melting ratio to change with pulse energy. The cases of just substrate and 100 μm powder layer show a small decrease in efficiency with pulse energy and the other two cases show an increase with pulse energy. This near independence from pulse energy would suggest that the thermal losses are in linear proportion to applied pulse energy and so from the perspective of an energy budget it makes little difference which pulse energies are employed to build objects using this technology.

When building 3D objects in a layer wise fashion each new layer must re-melt a portion of the previous layers in order to achieve a high density and to minimise the potential for de-lamination. Section 4.2 demonstrated that the power density or brightness of the laser affects the penetration of the melt pool more than the width and that the width of the melt pool is largely

affected by the size of the focal spot. Therefore, for a given pulse energy, it seems preferable to use the diodes at full power to achieve a higher penetration of the substrate. Furthermore, a higher power decreased the chances of insufficient wetting at low pulse energies which are required to limit the height of the resultant melt balls and the extent of denudation, both of which increase with pulse energy.

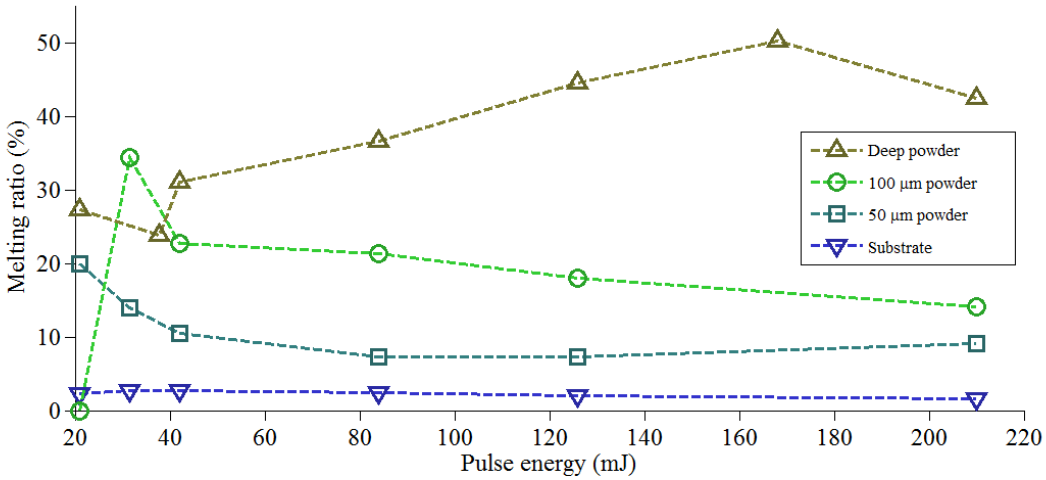

Figure 59 Ratio of energy required to just melt affected material to energy supplied for various powder layer thicknesses.

Chapter 5

Line building

5.1 Introduction

The previous chapter dealt with the creation of single melt balls as the fundamental building block used by this technology. This chapter will detail the creation of lines as the next step towards building 3D objects. Lines are created by the sequential addition of single melt balls into a linear structure. The variables of exposure power, exposure time, and layer thickness pertinent to single melt ball creation are expanded to include the spatial and temporal distance between individual spots and some simple pulse shaping. The qualities required from a 'good' line are: evenness of profile, the lack of high features that could intermit the passage of the powder wiper on a re-layer operation and good penetration of the melt into the previous layer or substrate.

5.2 Data acquisition

To return 3D profile information about the lines of melt spots vertical profiles were obtained by using a Veeco white light interferometer. The raw scan data produced by the Veeco are in the form of a two-dimensional array (corresponding to X and Y) containing the Z coordinates of the sample scanned. The data have an arbitrary zero level and will be tilted if the scanning head of the Veeco is not perpendicular to a given planar feature within the sample. The proprietary Veeco software has many post-processing options for filtering, tilt compensation, and measurement. However, for the samples created in this work the proprietary algorithms were insufficient and more robust solutions were created using Matlab. An outline of the proprietary

software's limitations and the methods used to overcome these limitations for each of the three stages follows.

5.2.1 Filtering

The Veeco interferometer projects light onto the sample to be measured and uses the intensity of the interference between the original and reflected light to calculate distance. The melt bead samples that required profiling were created on a planar substrate and comprise rounded features. The substrate and the tops of the rounded features reflect enough light for the interferometer to return good data. However, the sides of the rounded features are oblique to the interferometer's beam path and reflect little or nothing back to the interferometer, which causes missing data and increased noise.

The median filter within the proprietary software is effective at removing noise and the size of the filter's kernel can be set to 3, 5, 7 or 9 pixels wide. In general a large kernel will reject more noise than a small kernel but a large kernel will blur the good data more than a small kernel. In practice the kernel size should be set to suit the level of noise. The problem encountered using the proprietary median filter on the melt bead scans results from the amount of missing data within the scans. Even using the proprietary filter with its largest kernel some noise was unaffected as it was surrounded by a region of missing data greater in width than half the kernel size.

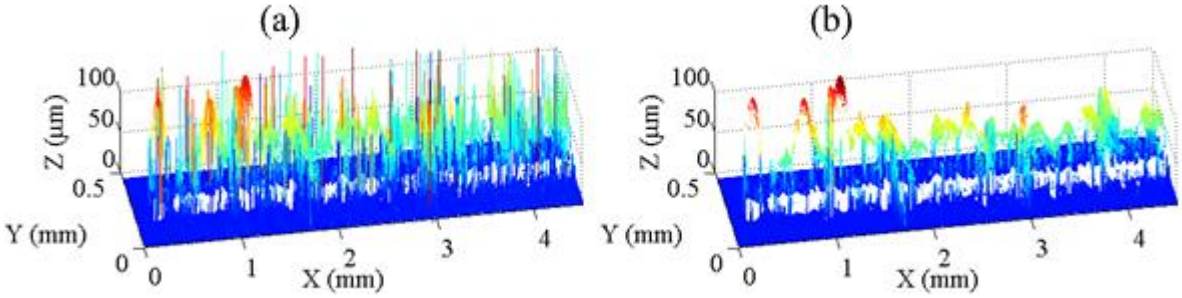

Figure 60 The effect of the adaptive median filter on a scan of a melt bead.
(a) Unfiltered. (b) Filtered.

Therefore a median filter was created that adapted the size of its kernel to the surrounding data which allowed sparse data to be filtered while not blurring dense data unnecessarily. In operation, for every non-missing point in the dataset the algorithm starts with a kernel size of

three and increases the size until there are at least a given number of non-missing data points encompassed by the kernel up to a given maximum kernel size. In practice the minimum number of non-missing data points was set to six. This would allow a pair of missing data points to be processed within a kernel size of three but three missing points together would require a kernel size of five or more.

The filter as described above has the effect of adjusting the value of a data point to suit those of its surroundings even if that data point is purely noise. Given that a point may be spurious it was considered sensible to remove some data that were outliers than to methodically adjust their values to a more believable level. Consequently two data removal conditions were introduced into the filter algorithm:

1) If the size of the kernel reaches the given maximum value without finding the chosen amount of non-missing data points and the amount of non-missing data points is two or less.
2) If the unfiltered value of a point is greater than a given threshold amount more than the filtered value.

Condition 1) was introduced to remove isolated data points that had no neighbouring data points to give context to the validity of the data. The maximum size of the kernel for this condition was set to 19. This value was chosen empirically so that an isolated group of up to six good data points on the top of a rounded feature would not be influenced by data points on the substrate if they were surrounded by a ring of missing points of width nine.

Condition 2) was introduced to remove non-isolated data points that were significantly different in value to their neighbours. The threshold value for this condition was empirically chosen to be 50 μm.

5.2.2 Tilt correction

The proprietary Veeco software has plane fitting functionality which puts a best fit plane through the entire data set by least squares fitting. If the sample in question has a strong planar content with a small feature upon it then this simple fitting is usually adequate. Where this is not the case there is the option to restrict the data used for the fitting calculation to either within or without an area or areas of the sample. This is useful for samples where the planar content is easily segregated but it requires user input to define the planar content which slows down the

process. For samples such as Figure 61 where the planar content is not easy to segregate then the proprietary software is inappropriate.

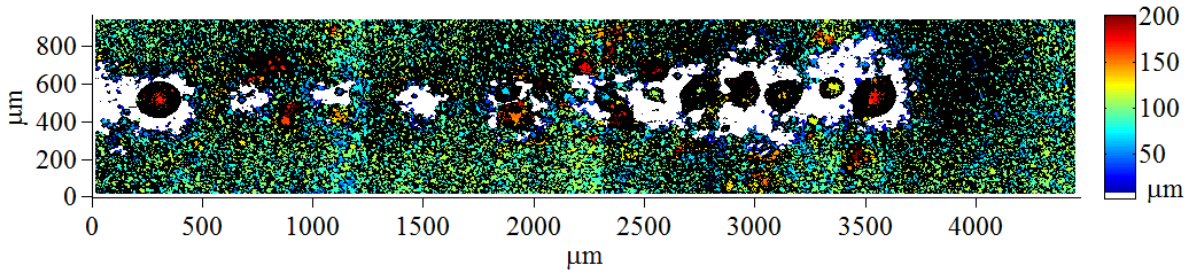

Figure 61 A plan view scan of melt balls within a layer of powder. The sample has been tilt corrected to show the substrate clearly. Black = missing data, white = all points below 5 µm.

A Matlab solution was sought that would enable operating without user input for each sample so that fast-batch processing could be achieved. The approach taken was to assume that the planar content within the point cloud would have a small tilt angle as a result of the user attempting to null the fringes on the substrate when setting up the interferometer, and that the other content from the melt balls would be spread over a range of heights. Therefore, if a histogram of the height values within the scan was produced the planar content would produce a broad peak within the histogram due to the tilt. Then if only the data points that comprised the peak in the histogram were used for plane fitting the goal of segregating the points corresponding to the planar content would be achieved.

In practice a moving average filter with a small kernel (width = 5) was applied to the histogram data to assist with locating the centre of the peak corresponding to the planar content. The peak was identified as the maximum value and the width of the peak was defined by the closest instance of a value less than one third of the peak's value on either side of the peak. Only the data points corresponding to the defined peak were then employed to fit a plane to using least squares. Subsequently the coefficients of the fitted plane were used to apply a transformation to the point cloud to remove the tilt and to centre the planar content on the zero level in Z. To increase robustness the algorithm was run multiple times until the percentage change to the current height of the histogram peak was less than 1 %. An example of the process is given in Figure 62 where the initial data set has had over 20 µm of extra tilt added to illustrate two steps of the process.

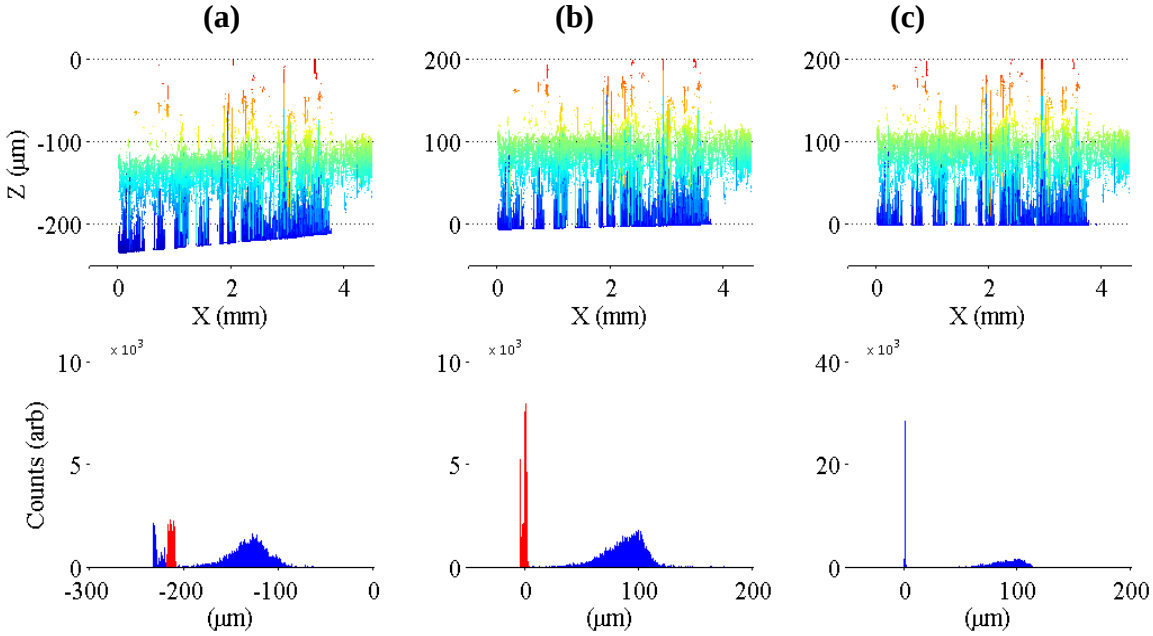

Figure 62 Two applications of tilt correction. Upper images: side views of the data from Figure 61. Lower images: histograms of Z data corresponding to the side view above. The red sections of histogram data are those that are used for plane fitting to produce the view and histogram in the next column to the right. (a) Original data. (b) Data after one application of the filter. (c) Data after two applications of the filter. Note the change of vertical scale in the final histogram where the tilt compensation has been optimized.

5.2.3 Measurement

Some of the metrics subsequently used to qualify samples within this chapter are roughness measurements such as Ra and Rq. These measurements can be applied with equal relevance to a 2D section and a 3D surface, however the data sets produced by the Veeco interferometer have many missing data points. The missing points resulting from a surface that is oblique to the interferometers beam path will occur predominantly in between the sample's high points and the substrate. The consequence is a correlation between height and the likelihood of missing data so a 3D analysis of the sample's present data points will impart a bias which rules out the usefulness of 3D analysis. Therefore a method of 2D analysis was developed and is described here.

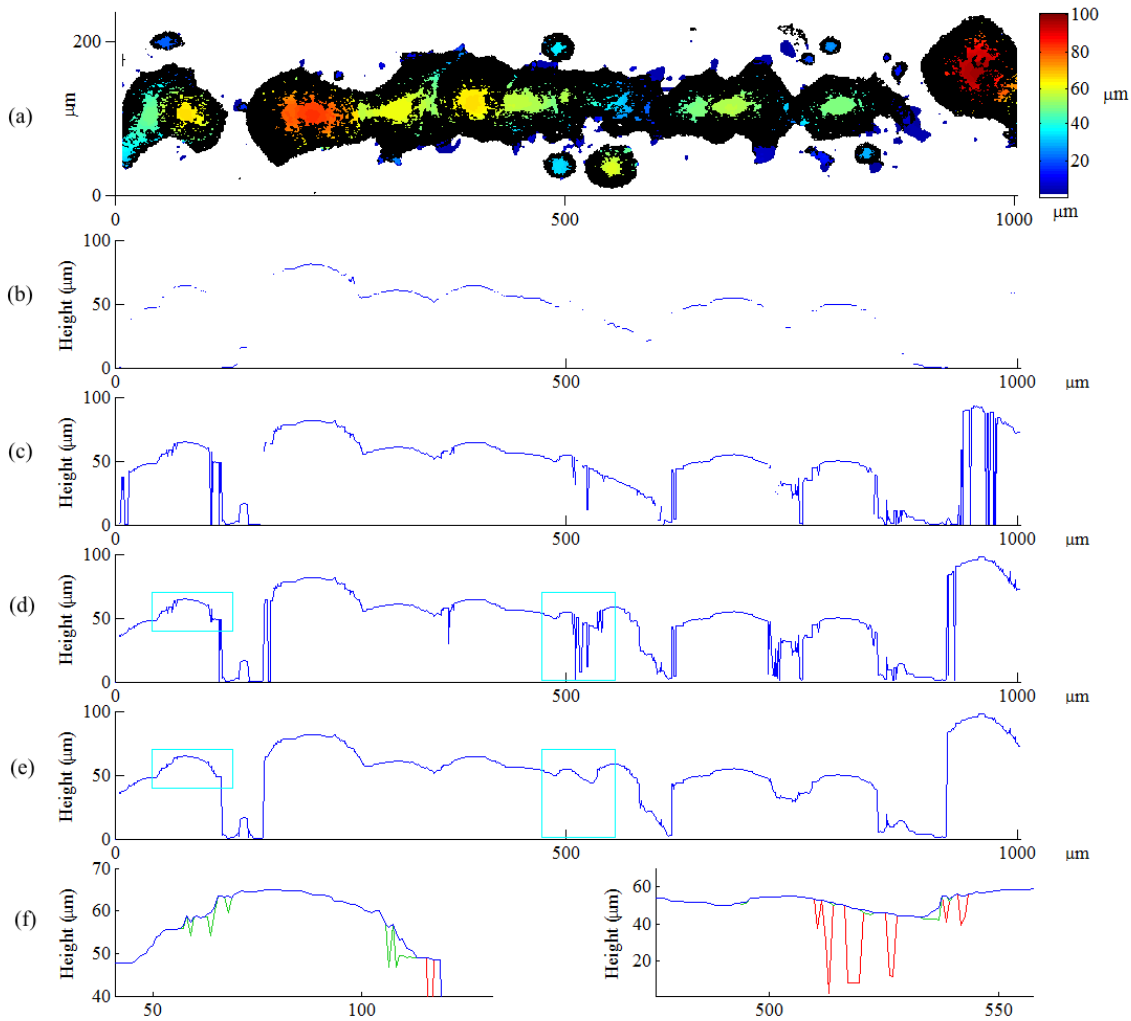

Figure 63 Profile generation. (a) Plan view of a section of a melt line, Black =missing data, white = below 3 µm. (b) Data points on centre line of melt line, many missing data points. (c) maximum values of data points in 60 µm wide central strip, fewer missing points. (d) Profile created by projection of maximum values across entire width of sample, no missing points but some erroneous points. (e) Profile after application of filter. (f) Enlarged sections corresponding to the two cyan boxes shown in views d and e showing the points that are adjusted by two settings of the filter shown as green and red.

Since the samples produced for this chapter were lines of melted material the linear profile was required for analysis. Simply to take the data on the centre line of the scan was insufficient as this included many missing data points Figure 63 (b). To improve this method strips central to the melt bead were utilised to generate profiles by projection; that is, for every x

coordinate take the maximum Z value from all Y coordinates within strips. The effect of this for a 60 μm wide strip is shown in Figure 63 (c) where it can be seen that there is still some missing data. The method arrived at and subsequently used was to generate the profile by maximum projection across the whole sample. The advantage of this method is that the resulting section has no missing data points (albeit by inserting the flanking substrate level where there is no central value) and thus the roughness can be calculated without having to justify missing out particular points from the calculation. The potential disadvantage of this method is that the profile of the central melt track is obscured if there are any higher points in any flanking splatter, as is the case in this example. At approximately 550 μm in X there is a yellow blob below the main melt track Figure 63 (a). The inclusion of this feature can be seen in the difference between Figure 63 (c) and Figure 63 (d). However, the height of splatter is significant in determining whether the powder wiper will foul on the melted material. Its presence can be seen as undesirable so it was considered useful to have these features included within the quality metrics derived from these profiles.

The method of producing profiles by projection across the entire width of the sample avoids missing data by the inclusion of substrate values where there is no data from the melted material present. However this is still a form of missing data and if one assumes that the section of the melt track is likely to vary smoothly then it is obvious to the human eye that there are still some erroneous points Figure 63 (d) where the smooth curve is notched. Consequently a filter algorithm was designed to identify some of these cases and insert estimated values so that roughness calculations would not be affected by these erroneous values.

The filter identifies points that require alteration within notches that are below the average level of the curve on both sides of the point in question by more than a given amount. To make the filter behave as desired four parameters were introduced and their usages are explained within the following process steps:

1) Each point in the profile is considered in turn.
2) From the particular point under consideration two neighbourhoods are defined. The first comprises all points to the left of the point under consideration within a given ‘Width’ distance of this point. The second is the same but to the right.

3) Each of the two neighbourhoods is individually refined by the exclusion of points whose values are less than the maximum value within the neighbourhood minus the 'Range' value.
4) Each of the two refined neighbourhoods has a centre of mass assigned to it Figure 64 (b). The X and Y values of each centre of mass are defined as the mean X and Y coordinate respectively.
5) The point under consideration is checked for suitability of replacement. Two conditions must be met Figure 64 (c).
6) The difference between the Y coordinates of the left and right centres of mass must be within a given 'Step' value.
7) The difference between the Y coordinate of the mean of the centres of mass and the point under consideration's Y coordinate must be greater than a given 'Depth' value.
8) If both the previous conditions are met then the point under consideration has its Y coordinate replaced by linear interpolation between the two refined centres of mass Figure 64 (d).

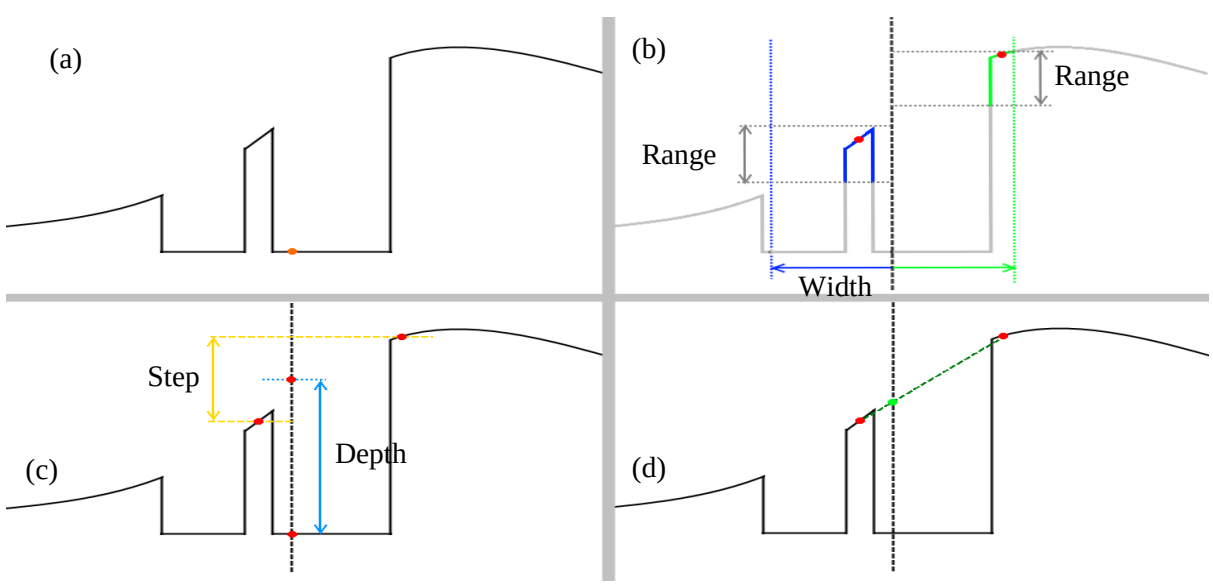

Figure 64 Working details of the notch filling filter. (a) Smooth curve with two notches. Red spot = point to apply filter. (b) Apply limits to define data to use to generate the centers of mass = red spots. (c) Thresholds used to determine suitability of point in question. (d) Creation of new value by linear interpolation.

In operation the 'Width' parameter allows tuning of the maximum width of the features that could be considered as notches and needs to be kept low to avoid adjusting good data within a naturally concave feature. The Range value should also be kept low as a high value negates its purpose. The purpose of the range value is to exclude data within another nearby notch. The Step value allows for filling notches within a slope where the mean value on each side may be significantly different. If this value is too high then the filter will adjust data at the foot of step changes. This may seem useful given that step changes are unlikely to be natural features of the melt line and more likely to be as a result of missing data, but without useful context on both sides it was considered better not to adjust the values. The Depth value affects how deep the feature needs to be before it is considered a notch. If this value is too low depressions that are not notches get filled in. In the enlarged views of Figure 63 (f) the effects of two different filter settings are shown. The features shown in red were removed with a narrow filter that required the depth to be more than 10 μm but allowed a Step difference of 30 μm, and the green features were removed with a narrow Width and a Depth of 1 μm tempered by a small Step value of 10 μm. It can also be seen from these two examples that the filter does not affect the majority of the data.

5.2.4 Line sharpness

The inconsistent wetting of melt balls within a line affects the width and the height of the melt line and whilst the height of the line can be analysed by the profile generation previously described 5.2.3 a method of quantifying the evenness of the width of the line was also required. This width quality metric should give an indication of the evenness of width, be detrimentally affected by the irregular splatter and be insensitive to the actual width of the line. This was achieved in the following way:

Firstly, a binary image was created from the 3D scan of the line by the use of a height threshold; every point above 5 μm was considered to be part of the line Figure 65 (a). Secondly, the sum of all black pixels (that correspond to the melt line) in each row of the image was calculated and an example is plotted as a graph in Figure 65 (b). This does not give the mean profile of the line but is effectively a histogram of how many points are not substrate. If the line in question had perfectly straight edges then this curve would have a rectangular shape. Thus the gradient of the histogram curve gives an indication of the swiftness of the transition from

substrate to melt line. Thirdly, the differential of the black pixel histogram was taken which shows peaks at the edges of the melt line Figure 65 (c). The absolute value of the differential was used to make both peaks positive and because the differential operation is sensitive to noise the histogram was smoothed by a moving average filter prior to differentiation. The height and narrowness of the peaks in the differential graph both give an indication of the swiftness of the transition from substrate to melt line so the line width quality metric was defined as the mean of the peaks' height divided by Full Width Half Maximum (FWHM) for both edges of the line. The mean width of the melt line was also a useful property for comparative purposes and this was defined as the FWHM of the black pixel curve Figure 65 (b).

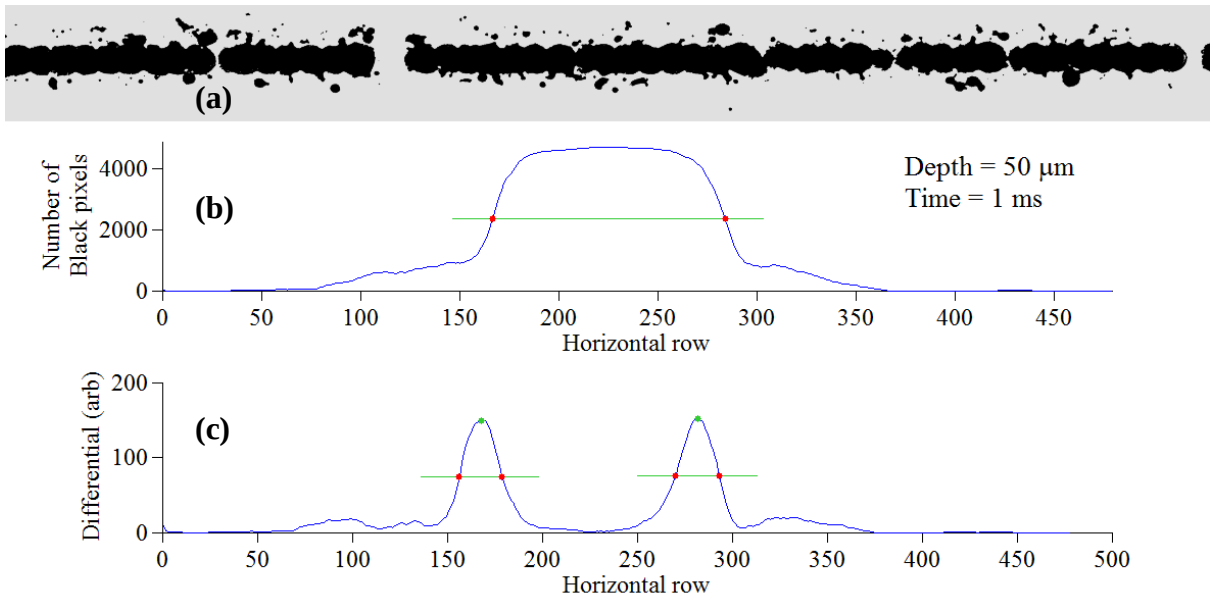

Figure 65 Line sharpness derivation. (a) Binary image of a melt line created with 42 mJ pulses on a 75 µm pitch into 50 µm 316L powder, grey <= 5 µm, black > 5 µm high. (b) Nnumber of black pixels in each row of the top image with red spots marking the 50 % of maximum levels. (c) Absolute value of differential of middle graph showing FWHM of peaks.

5.3 Single line building

Using a conventional PBF system that comprises a laser beam steered by a galvo-scanning mirror, the usual machine parameters varied within a build quality study would be scanning speed, laser power, and layer thickness [150]. The technology developed within this research whereby single melt balls are created at given locations with an optical head that is

static during laser exposure means that the concept of scanning speed is difficult to quantify for comparative purposes. The parameters available using this technology are: laser power, exposure time, pitch of ball placement, the time between successive balls, the temporal pulse shape of delivered energy, and the powder layer thickness. The terms melt line and melt bead are to be considered synonymous.

In the following sections the quality of the melt lines will be judged by their evenness of profile in both height and width and also in some cases by the degree of penetration into the substrate. The mean height and width are presented by way of an indication of how much material has been melted rather than as a quality metric. In all cases the powdered material is stainless steel 316L and the substrate is stainless steel 304.

5.3.1 Effects of powder thickness

In the following experimental investigation of the effects of powder thickness upon melt bead quality, the variation in thickness was achieved by the use of a tapered powder layer Figure 66. Each melt line was placed parallel to and 5 mm from the previous line in a 10 μm/mm taper yielding depths of 50, 100, 150, 200 and 250 μm. Melt beads 3 mm long were produced by the creation of melt spots on a 75 μm pitch with three exposure times (1, 5 and 10 ms) using 42 W of power. The resultant melt beads were scanned with a Veeco interferometer to obtain height profiles then sectioned, polished and etched to reveal the extent of melt penetration into the substrate.

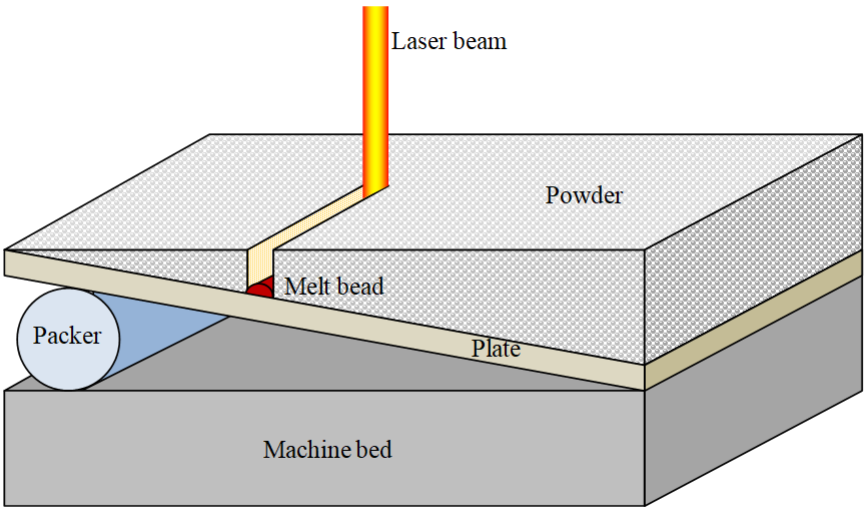

Figure 66 Tapered powder layer created by the placement of a packer underneath the substrate.

Figure 67 shows the height profiles of lines created with 42 mJ pulses in a range of powder depths. Here it can be seen that for the same exposure settings the height of the lines increases with powder depth. This trend is quantified in Figure 68 (a) along with data from other lines created with higher pulse energies of 210 and 420 mJ. The lines created using 210 mJ pulses gives the lowest mean line height for all powder depths except 50 µm. With a 50 µm powder layer all three pulse energies are sufficient to melt the powder and enough of the substrate for good wetting. At greater powder depths the energy of the 42 mJ pulses is sufficient to melt the powder but insufficient to melt the substrate so the melt balls adhere poorly to the substrate leaving melt balls that sit high with little contact area with the substrate. The higher energy pulses, 210 and 420 mJ, have energy sufficient to melt the substrate and induce good wetting however the 420 mJ pulses produce greater gas flow and entrain more surrounding particles thus creating a higher mean melt bead height. The Ra roughness variation in melt bead height also increases with powder depth in a similar way to the mean height suggesting that the Ra roughness scales with mean height.

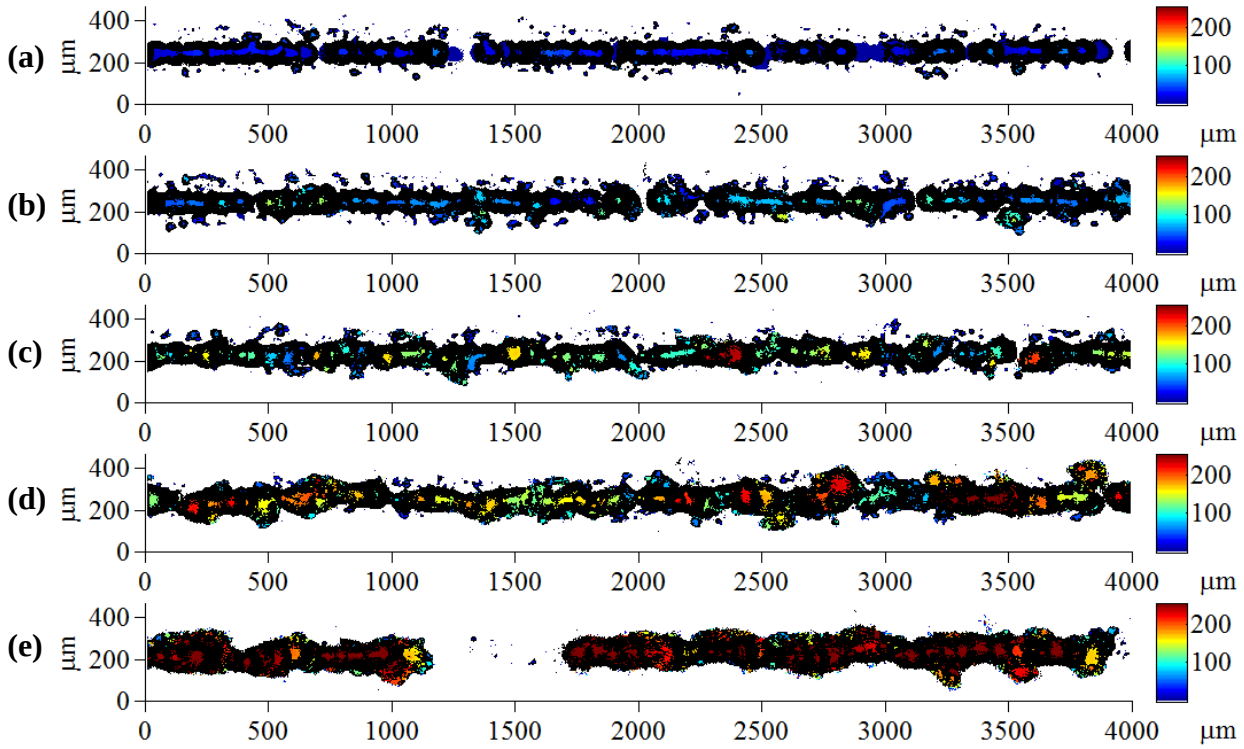

Figure 67 Height profiles of melt lines created by 42 mJ exposures on a 75 µm spot pitch in various powder layer thicknesses. (a) to (e): 50, 100, 150, 200 and 250 µm.

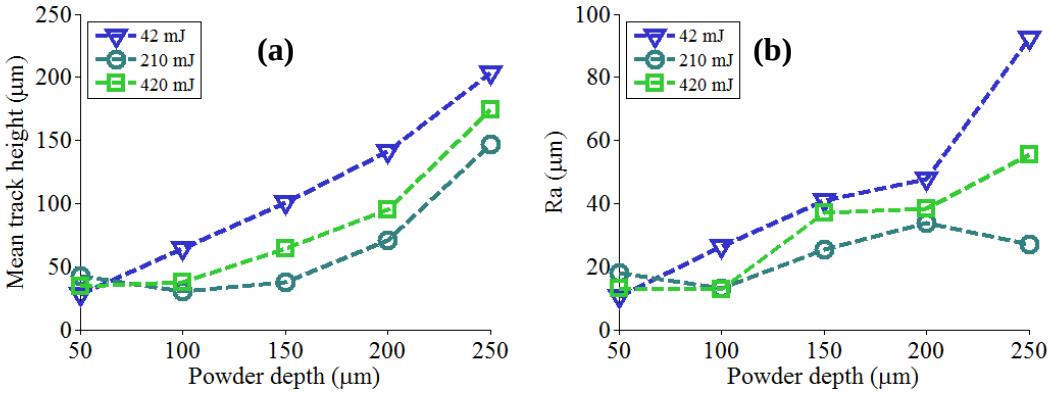

Figure 68 Mean melt bead height and Ra roughness as a function of powder depth for a range of pulse energies.

The binary images of the melt lines (Figure 69) clearly show an increase in melt line width with increasing powder depth across the range of pulse energies used. Moreover there is an increase in melt line width with pulse energy and also an increase in the amount of splatter adhering to the substrate.

Figure 69 Binary images for line sharpness calculation created from melt lines using various pulse energies and power thicknesses. Left to right 42, 210 & 420 mJ pulse energy. Top to bottom 50, 100, 150, 200 and 250 µm layer thickness.

Figure 70 shows graphs of line sharpness and width where the observed trend for increasing width with powder depth and pulse energy is quantified. Increasing the powder thickness from 50 to 250 µm has the effect of increasing the line width by ~55 % regardless of pulse energy. The sharpness of the melt line decreases with increasing powder thickness. The lines built using 210 mJ exposures are the sharpest over all powder thicknesses except 50 µm where the line built using 42 mJ exposures is the sharpest.

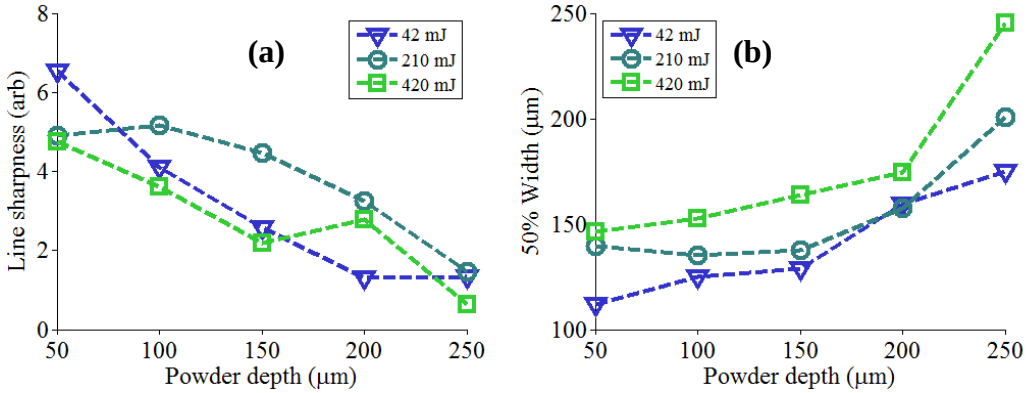

Figure 70 Line sharpness and line width as a function of powder depth for the three pulse energies used.

The cross sections of Figure 71 show three types of melt line with substrate penetration. Figure 71 (a) shows a small volume of melted powder where the penetration of melt into the substrate is approximately the same as the height of the bead, thus having a wetting angle of greater than 90°. Figure 71 (b) shows a melt bead with a larger height than that of the substrate penetration but still a good level of penetration. Figure 71 (c) shows a large volume of melted material resulting in little or no substrate penetration.

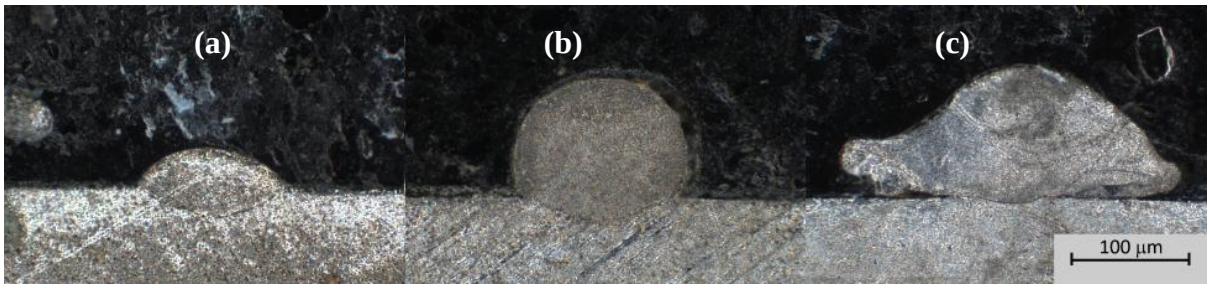

Figure 71 Sections through melt lines created with 210 mJ exposures on 75 µm spot pitch in various powder thicknesses. (a) to (c) 50, 150 and 250 µm powder thickness.

The mean depth and width of the substrate melt penetration from three cross sections for each melt bead are shown in Figure 72. A trend can be seen whereby both the depth and width of melt penetration increases with pulse energy and decreases with powder thickness. The degree of substrate penetration caused by building with the higher pulse energies appears to be independent of powder thickness until the thickness exceeds 200 µm. At this point the melt

penetration diminishes rapidly. There is little difference between the depths created by 210 and 420 mJ exposures, however the depth of penetration is significantly less for the 42 mJ pulses.

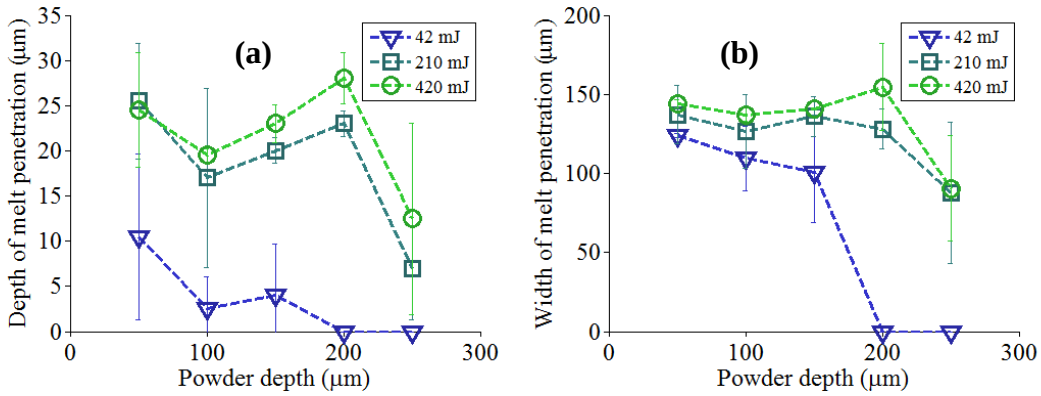

Figure 72 Depth and width of melt penetration into substrate as a function of powder thickness for various pulse energies.

An increase in powder thickness enlarges the volume of powder that is melted and consolidated into the melt bead produced by a given energy density through an expansion of both the mean height and width of the melt beads. This increase in volume of consolidated powder comes at the expense of melt penetration into the substrate. It ultimately leads to no substrate melting when the powder thickness passes a threshold amount dependent upon energy density. In this case the situation effectively becomes that of a deep powder bed with no substrate present.

The sharpest and smallest Ra roughness lines were created in 50 μm of powder by 42 and 210 mJ exposures on a 75 μm pitch which equates to linear energy densities of 560 and 2800 J/m. In a layer thickness study by Yadroitsev and Smurov [142] using stainless steel 316L powder and a 50 W fibre laser they give the upper and lower limits of scanning speed for continuous melt beads as 0.08-0.20 m/s or 625-250 J/m. This range encompasses the 560 J/m used here to good effect but excludes the lines produced using 2800 J/m. This difference in energy requirements will be partly due to the increased conduction losses concomitant with a expose-move-expose scanning strategy but largely due to the difference in focal spot size between the systems. The fibre laser used by Yadroitsev and Smurov has a spot diameter of 70 μm resulting in a mean intensity of 13 $kWmm^{-2}$ whereas the laser diodes used in this work have a 150 μm diameter spot yielding a mean intensity of 2.4 $kWmm^{-2}$.

5.3.2 Effects of power

To study the effects of exposure power 16 melt beads were created using four exposure powers and four pulse energies. The powers were adjusted through the values of 40, 60, 80 and 100 % of the maximum output of diode 1's 42 W, yielding powers of 17, 25, 34 and 42 W. The exposure times used with 42 W were 1, 2, 3 and 5 ms and scaled accordingly for the lower power settings so that the energy *per* pulse was equivalent. A spot pitch of 75 µm and a 50 µm powder layer were used for all melt beads.

It is apparent from Figure 73 that despite the same energy *per* pulse the lines created using 40 % power are significantly less continuous than those created using 100 % power. The melt bead is broken in many places, leaving a series of disconnected islands of melt for all pulse energies. The mean bead height and Ra roughness are shown in Figure 74. The mean track height can be seen to increase with pulse energy but it is largely independent of pulse power across the range of powers and pulse energies used. The variation in bead height given by the Ra roughness shows a decrease trend with increasing power and an increase trend with pulse energy.

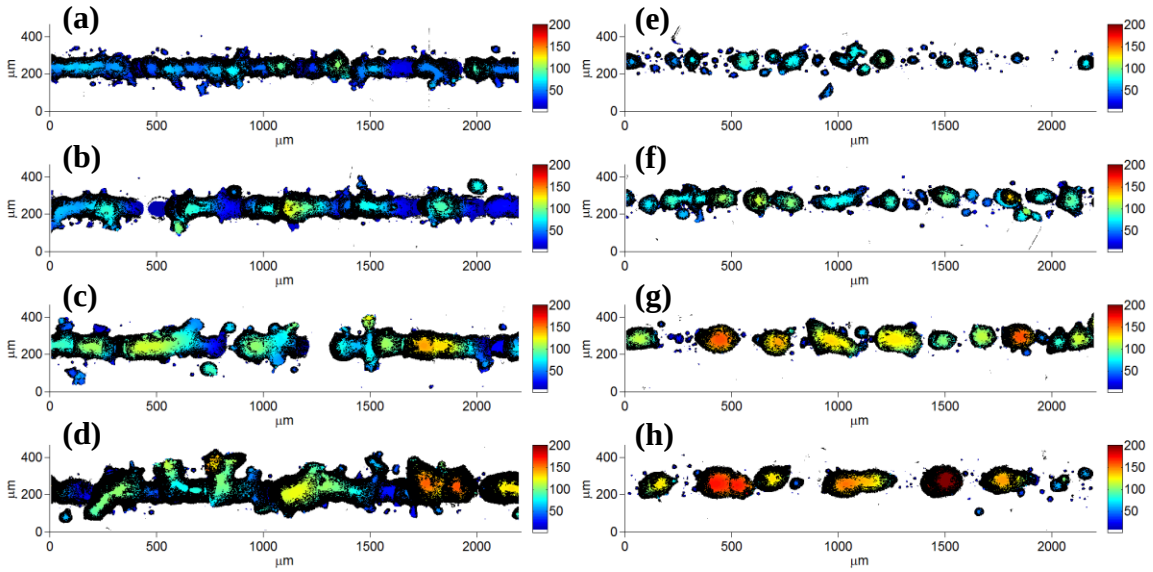

Figure 73 Height profiles of melt lines created in ~50 µm of 316L powder. Left column: 100 % power. Right column: 40 % power. Top to bottom energy per pulse 42, 84, 126 and 210 mJ.

The binary images of Figure 75 for all 16 melt beads show that decreasing power decreases the bead width and leads to breakup of the melt bead when the power reaches 17 W, although the signs of break up are evident at 25 W. Figure 76 quantifies these observations and

clearly shows the width increasing with power and with pulse energy. The line sharpness also increases with power, but contrary to width decreases with pulse energy.

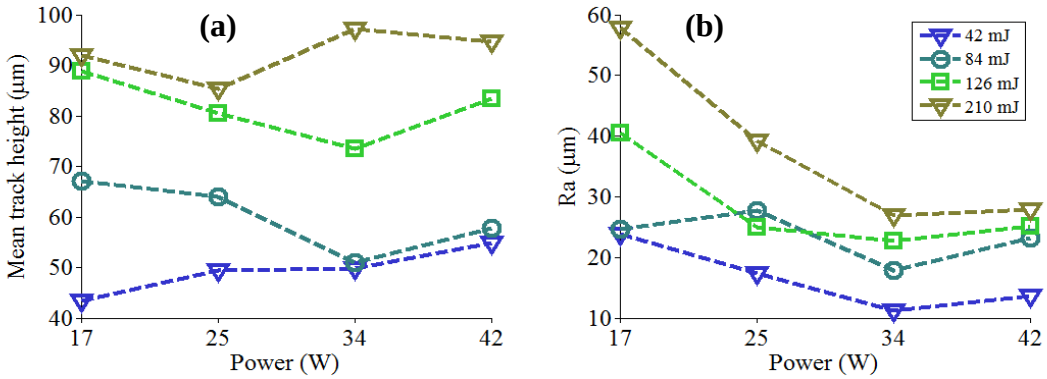

Figure 74 Mean melt bead height and Ra roughness as a function of exposure power for a range of pulse energies.

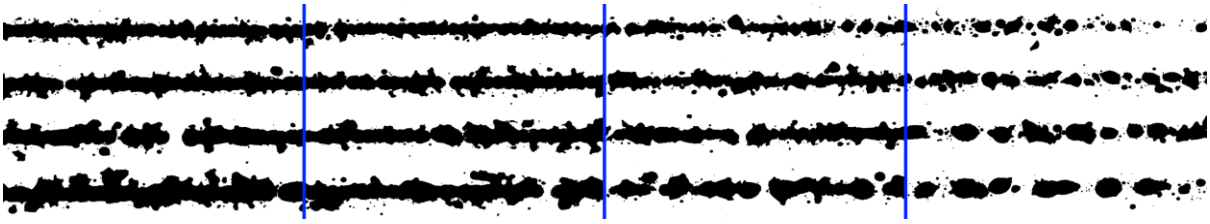

Figure 75 Binary images for line sharpness calculation created from melt lines using various exposure powers and pulse energies. Left to right: exposure powers of 42, 34, 25 and 17 W. Top to bottom: pulse energies of 42, 84, 126 and 210 mJ.

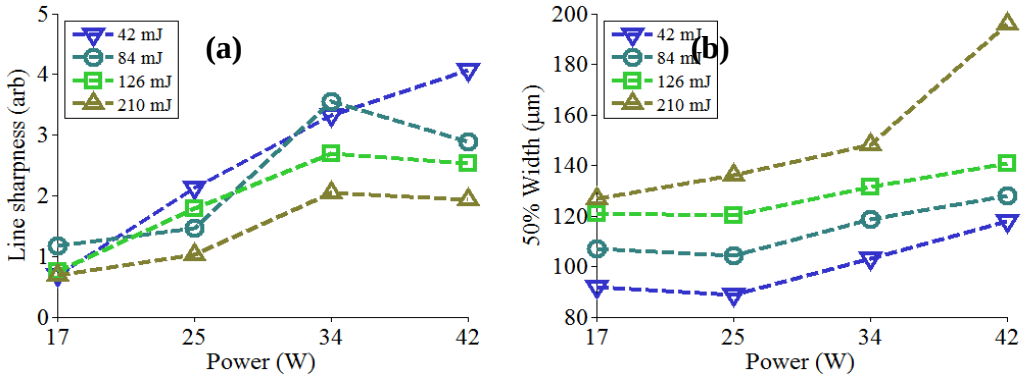

Figure 76 Line sharpness and line width as a function of power for the four pulse energies used.

Figure 77 shows four sections of melt beads all produced using 126 mJ pulses but using different pulse powers. The examples showing the greatest melt penetration into the substrate for

each exposure power have been chosen for this montage. The substrate was cut up so that each of the melt beads was sectioned three times along its length. However, sometimes the section plane would intersect the melt bead where there was a gap in the bead, especially for the beads built using 17 W of power which produced many gaps. Consequently there was too much missing data from the melt lines produced with 17 W to include in Figure 78.

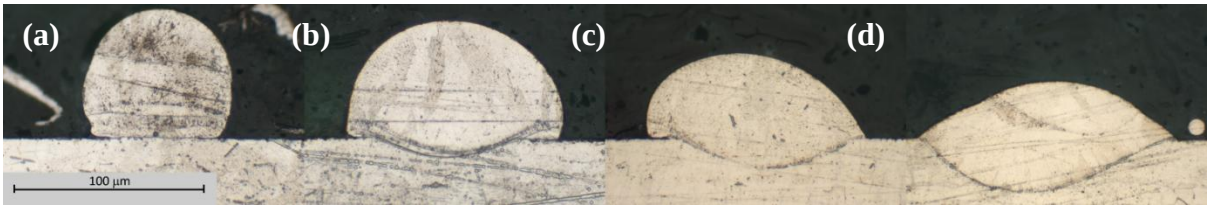

Figure 77 Melt bead sections created using 126 mJ exposures. (a) to (d) power = 17, 25, 34 and 42 W.

The depth and width of the substrate penetration is shown in Figure 78 where it can be seen that both depth and width of the melted substrate increase with exposure power and pulse energy. The lack of substrate penetration when using low exposure powers removes the stabilizing effect of wetting to the substrate on the powder melt and increases the tendency for balling [151]. In a power/scanning speed study using 50 µm layer of 316L powder Yadroitsev *et al* [152] found that increasing the exposure power from 25 to 50 W increased the range of scanning speeds that gave continuous tracks with penetration into the substrate, but that at 12.5 W only a broken track of isolated droplets was possible.

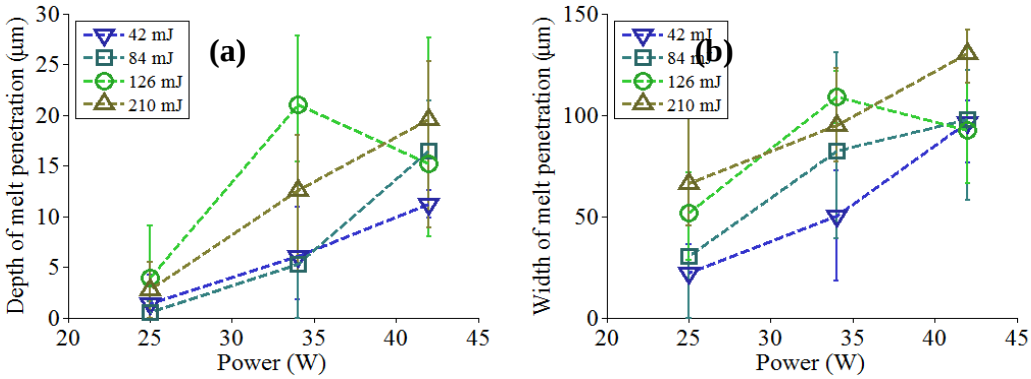

Figure 78 Depth and width of melt penetration into substrate as a function of power used for various exposure times.

5.3.3 *Effects of spot pitch*

To evaluate the effects of spot pitch upon melt bead quality melt lines were created using three spot pitches and six pulse energies. The spot pitches chosen for this study were approximately half the focal spot diameter to allow good overlap between the individual exposures and that the 600 µm pitch of the seven diode's focal spots was evenly divisible by the spot pitches. This led to spot pitches of 67, 75 and 86 µm being used. The exposure power was kept at 100 % or 42 W throughout and the depth of powder was 50 µm.

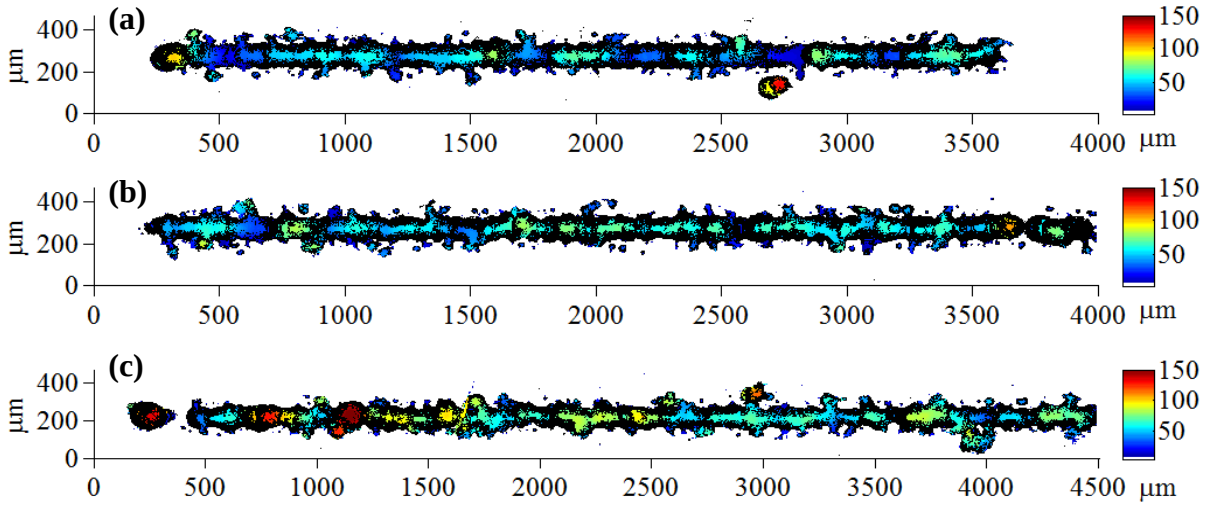

Figure 79 Height maps of melt beads created using 50 exposures of 42 mJ from 42 W exposure power in a 50 µm powder layer. Top to bottom: spot pitches of 67, 75 and 86 µm.

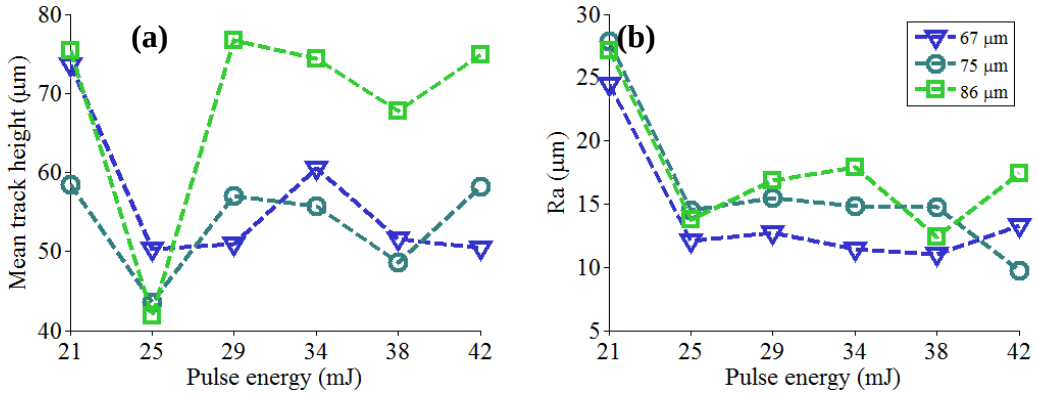

Figure 80 Mean melt bead height and Ra roughness as a function of pulse energy for three spot pitches.

Figure 80 shows the mean bead height and Ra roughness values for the line profiles generated from the melt beads. Barring an exceptional case at 25 mJ *per* pulse, the mean height of the melt beads produced using a spot pitch of 86 µm yields beads that are approximately 40 % higher than those produced with the smaller spot pitches. Decreasing the spot pitch of the melt lines has the effect of increasing the linear energy density and several researchers have reported upon the effects of this [98][153] demonstrating that too high or low a value results in a breakup of the lines' consistency. However the Ra roughness of the lines produced here is sensitive to spot pitch but insensitive to pulse energy so it is not the increased energy density that has improved the evenness of the melt beads. The dependency of the line sharpness upon decreasing spot pitch suggests that the positions of the individual melt exposures are contained within the shape of the melt line Figure 81. If the line is considered as a sequence of overlapping hemispheres then the amplitude of both the vertical and horizontal undulations is diminished by decreasing the pitch of the hemispheres[154].

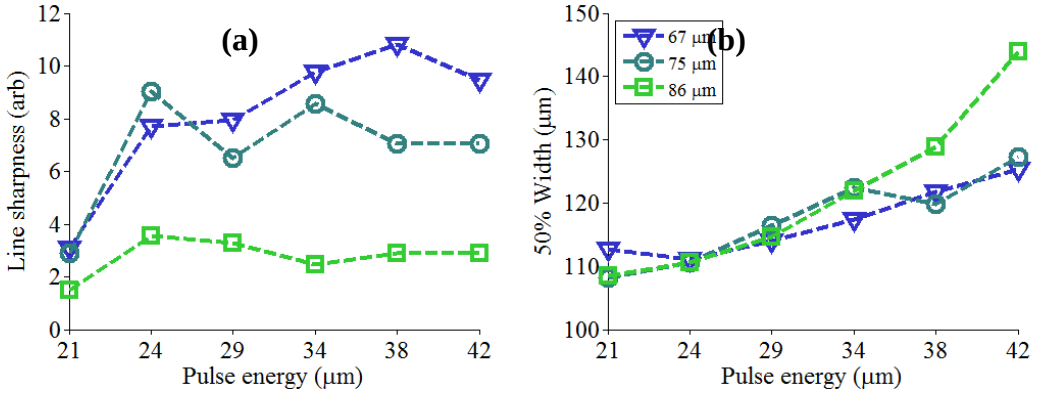

Figure 81 Line sharpness and line width as a function of pulse energy for three spot pitches.

5.3.4 Effects of temporal delay

The previous section described the effects of altering the spatial positioning of the individual melt balls within a line. This section will deal with varying the temporal spacing of the melt balls. A series of melt lines were built using three pulse energies and five inter-spot delays ranging up to 800 ms. Each delay was applied after each exposure and before movement to the next spot location. All of the lines were built using 42 W and a spot pitch of 75 µm in 50 µm powder thickness.

The delay time within this experiment is not the time between exposures but the extra time between exposures on top of the software and hardware limits imposed by the system. The software loop time to read the next line from the build instruction file, process the information, and set the appropriate I/O bits for communication with other sub components is 69.9 ms. The time to move the stages depends upon grid pitch but for a 75 µm step this is 62.3 ms. This gives a minimum time of 132 ms between successive spots to which is added the extra delay as specified.

Figure 82 shows the height profiles of five melt lines demonstrating that the mean height and variation in height decreases with the introduction of a processing delay. The lines produced with the shorter delays of 100 and 200 ms show this reduction in the second half of their extent (the building direction was from left to right) whereas in the first half there is still some large fluctuation of height. The higher delays of 400 and 800 ms show this reduction along their entire length. Figure 83 quantitatively shows the reduction in mean height and Ra roughness with increasing delay for three pulse energies. The trend is consistent across the three pulse energies and for both the mean height and Ra roughness. The minimum mean height and roughness is produced using a process delay of 400 ms.

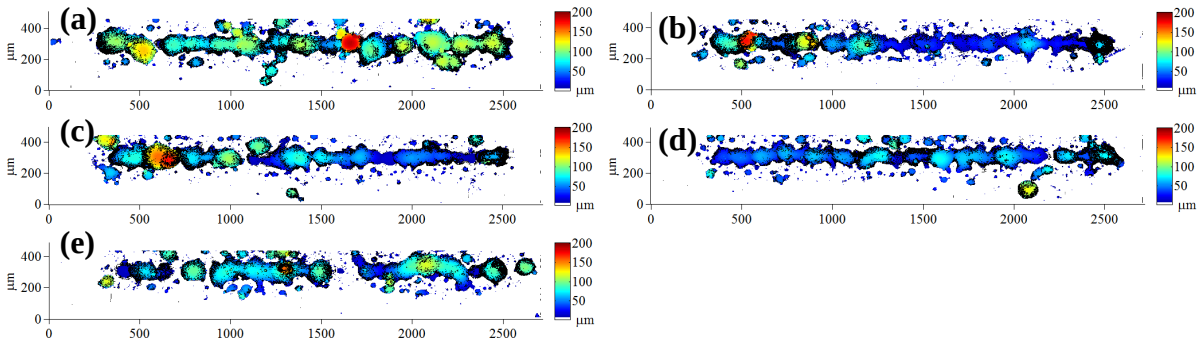

Figure 82 Height maps of melt beads created using 30 exposures of 42 W exposure power in a 50 µm powder layer with varying delay. (a) to (e) delays of 0, 100, 200, 400 and 800 ms.

The line sharpness shown in Figure 84 (a) is the highest for the lines produced using a 400 ms delay except when using the lower pulse energy of 25 mJ where a delay of 0 or 100 ms gives the sharpest line. However, a delay of 800 ms causes the least sharp line across all three pulse energies. The width of the melt lines, Figure 84 (b) shows no clear trend for the influence of process delay but the lines created using the 400 ms delay have, on average, the lowest width.

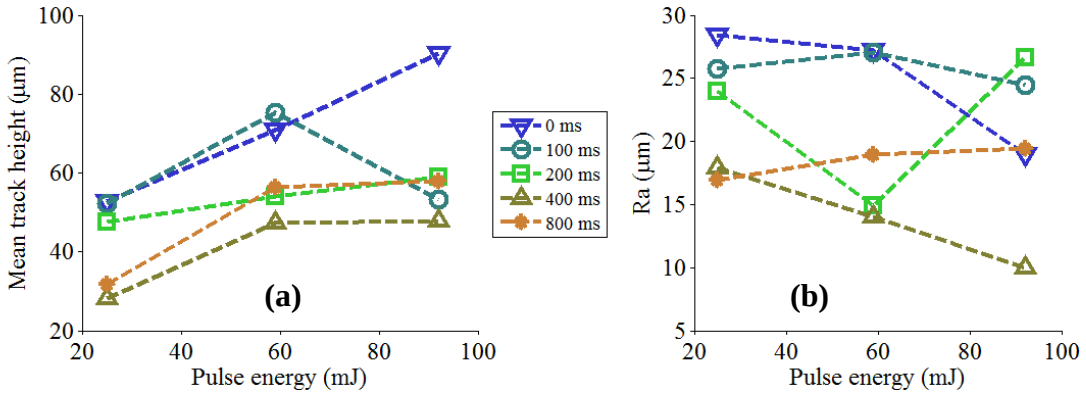

Figure 83 Mean melt bead height and Ra roughness as a function of pulse energy for five time delays.

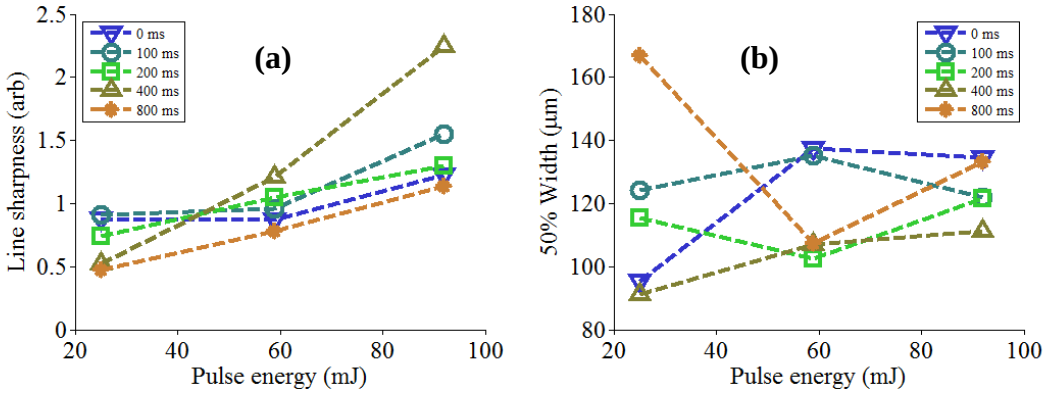

Figure 84 Line sharpness and line width as a function of pulse energy for five time delays.

Incorporating a process delay between each melt spot aggravates the difficulty in comparing the linear energy density of this technology with that of galvo-scanning a CW laser because linear density is unchanged by the inclusion of a delay. However the delay does have an effect upon the melt line as evidenced in the dimensions of the melt lines. It is the conductive losses that cause the effective change in energy density and are the mechanism by which the line roughness is altered. When a delay is added between spot placements the previous melt pool loses more heat to conduction thus lowering the peak temperature achieved with the next exposure. This lower temperature will produce less metal vapour and thus lower the induced gas flow calming the process and producing more consistent melting.

5.3.5 *Effects of temporal pulse shape*

The effect of temporal pulse shape is explored here. For this purpose melt beads were created using three pulse shapes and four pulse energies. The three pulse shapes used were simple linear profiles of square, ramp up, and ramp down. In order to keep the same pulse energy to allow comparison the temporal length of the square pulse shape was half that of the ramp profiles. The pulse energies ranged from 42 to 210 mJ and all lines were created using 42 W, 75 µm spot pitch and 50 µm powder thickness.

Figure 85 shows the effect of pulse shape upon melt line height, and from this figure there is little to distinguish the lines created using square or ramp up pulse shapes. However, there is an obvious breakup of the melt bead when using a ramp down profile.

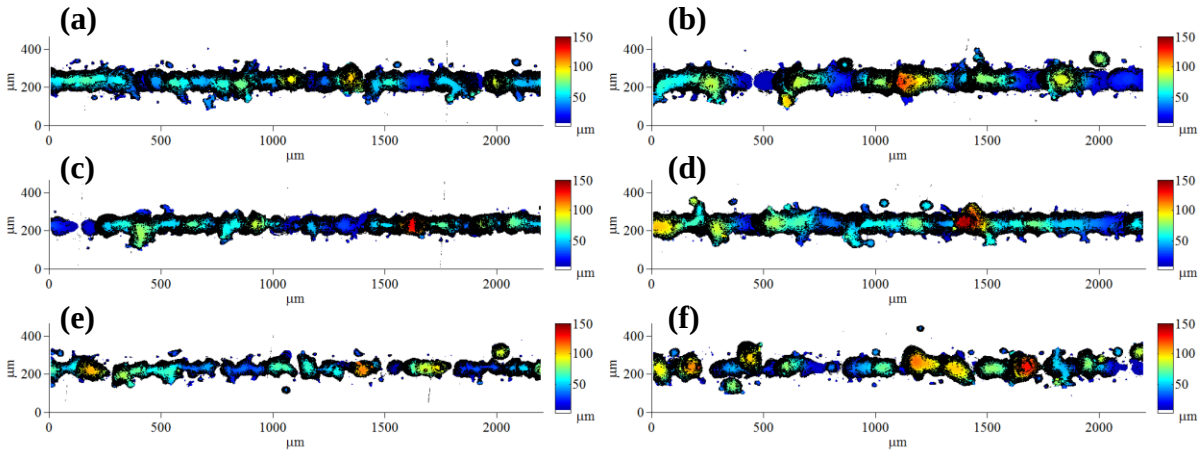

Figure 85 Melt bead height profiles. Top to bottom = Pulse shape: Square, ramp up and ramp down. Left to right = pulse energy: 42 and 126 mJ.

Figure 86 shows that the ramp down profile produces a higher mean bead height and Ra roughness than the ramp up profile across all of the exposure times used. The lines produced by the square pulse profile are generally lower in mean height and Ra roughness than the ramp down profile but there is less of a distinction in effects when compared to the lines produced with the ramp up profile.

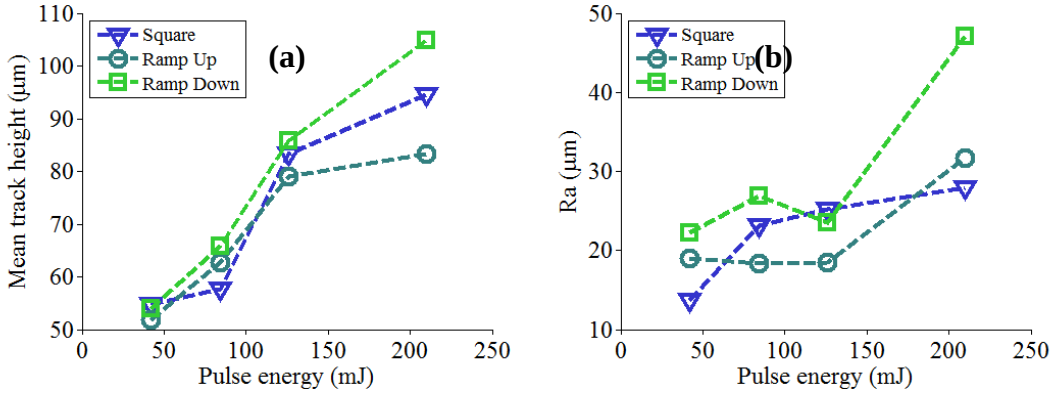

Figure 86 Mean melt bead height and Ra roughness as a function of pulse energy for three pulse shapes.

Figure 87 shows that the line sharpness and line width have a clearer dependency upon pulse shape than the mean height and Ra roughness. For all the pulse energies used in this study the ramp up pulse profile produces lines that are both sharper and wider than those produced by the use of a ramp down profile. The sharpness of the lines produced by both of the ramp profiles seem to stay constant with pulse energy. However the lines produced with the square profile decrease in sharpness with increasing pulse energy from the sharpest to the least sharp of the lines. The width of the melt beads is greatest when using a square pulse profile and has the highest rate of increase with pulse energy. The widths of the lines produced by using both ramp profiles increase more slowly with increasing pulse energy and the ramp down profile consistently gives the narrowest melt line for a given pulse energy.

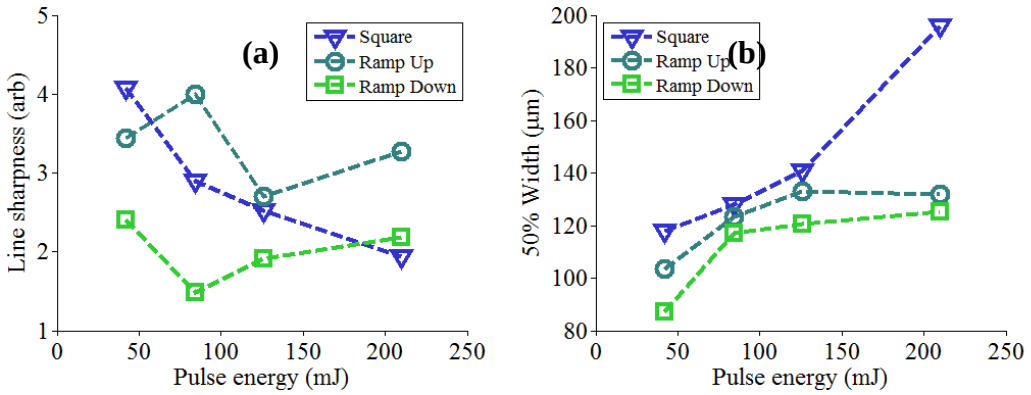

Figure 87 Line sharpness and line width as a function of pulse energy for three pulse shapes.

The ramp down profile generates a melt pool sooner than that of the ramp up profile due to high initial power. The subsequent ramping down draws more material into the melt increasing its volume. The larger melt pool will have greater thermal gradients and variations in surface tension making the balling effect more prominent and increasing surface roughness. The increased tendency for balling is manifest in the height-to-width ratio where a more upright melt bead is created when using a ramp down profile Figure 88. The ramp up profile creates a later melt pool than the ramp down and square profiles with consequently less material, lower mean temperature, and higher viscosity. This higher viscosity and the rapid cooling created by the steep end to the pulse shape create the sharper line widths and lower Ra roughness observed. The square pulse shape is half the duration of the ramps to keep the pulse energy constant, thus less energy is lost to conduction effects. At low pulse energies the smaller melt pool and the rapid cooling serve to create the low Ra roughness and high line sharpness of the ramp up profile. At high pulse energies, since less energy is lost to conduction, there is a higher melt pool temperature resulting in lower viscosity and greater Marangoni flow which produces higher Ra roughness and lower line sharpness.

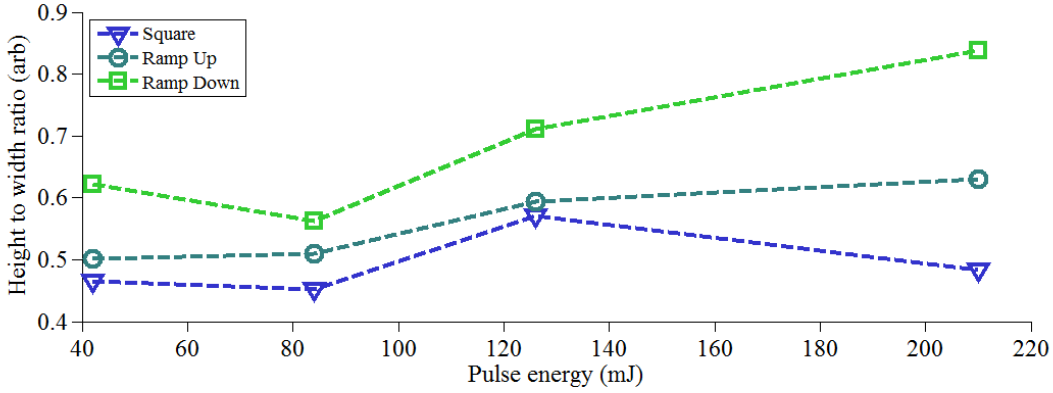

Figure 88 Aspect ratio of melt lines built with three pulse shapes.

5.4 Melt height

There are many high points within the melt lines presented in this chapter where the material, as a result of balling, has solidified at heights greater than that of the powder layer thickness. This makes a powder refill without height change impossible as the passage of the powder wiper would be intermitted.

A high intensity source quickly melts powder and substrate leading to good wetting and a smaller heat-affected zone which pulls in less powder, decreases denudation, and lowers the tendency for balling. A process map study by Childs *et al* [155] using M2 tool steel illustrates this concept, whereby they found that halving the focal spot diameter increased the range of scan speeds that produced continuous beads and reduced the tendency for line break up and balling. A sectioned melt line created using exposures to 25 W is shown in Figure 89 (b) where the lack of substrate melting (and thus wetting) has caused the volume of re-solidifying material to ball up whilst wetted to the melted top surface of the previous melt ball thereby increasing the height of the line. The melt line dimensions from the power trials of Section 5.3.2 are expressed in Figure 89 (a) as a height-to-width ratio where the effect of increasing the laser intensity by increasing power within a fixed focal spot can be seen to lower the aspect ratio which is favourable for producing melt beads with features lower than the original depth of powder. The laser diodes used within this research are ~42 W with a focal spot diameter of ~150 μm yielding a mean intensity of ~2400 W/mm^2. This intensity is well below that used by other researchers in studies upon stainless steel powders (Table 15). The study by Dadbakhsh *et al*. with the closest laser intensity (3420 W/mm^2) to that used in this research produced parts with 18 % porosity suggesting that this intensity is still insufficient to fully consolidate the powder.

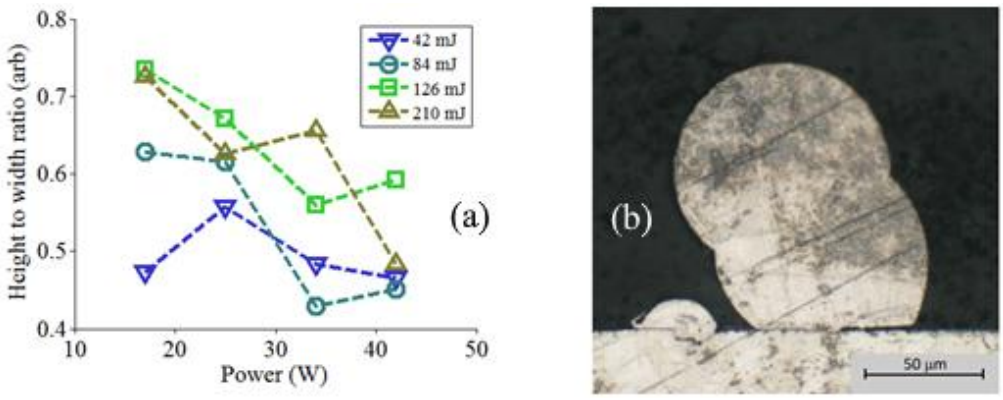

Figure 89 (a) Height to width aspect ratio of lines as a function of power. (b) Section of melt bead created with 42 mJ exposures to 25 W power illustrating how building with low power can create high features.

Table 15 Laser specifications from other research using stainless steel powders.

Material	Powder size (µm)	Layer thickness (µm)	Power (W)	Spot size (µm)	Intensity (W/mm^2)	Reference
316L	>5 <53	50-250	42	150	2400	This research
316L	50 (ave)	75	87	180	3420	[109]
316L	-	30	105	180	4130	[105]
904L	-	90	50	70	9740	[150]
316L	22 (d80)	100	80	100	10200	[78]
904L	<20	50	50	70	13000	[99]
316L	25 (d90)	50	50	70	13000	[152]
316L	17 (ave)	35	150	70	39000	[129]
316L	16 (ave)	100	75	30	106000	[94]

5.5 Summary

The creation of melt lines by the sequential placement of individual melt balls has been characterized by adjustment of the process variables (laser power, pulse energy, pulse shape, powder thickness, spot pitch, and process delay) and by quantifying their effect upon the mean height, mean width, Ra roughness, and line sharpness. In all cases the mean height and width of the line increased with increasing pulse energy as more powdered material is melted.

Increasing the powder thickness increased the mean height and width of the melt bead. It increased Ra roughness and decreased line sharpness for any given pulse energy. Ra roughness approximately scales with mean height suggesting that undulations within the line are amplified by powder thickness. The dimensions of the melt penetration into the substrate were observed to decrease with increasing powder thickness. It is therefore deemed preferable to use a thin powder layer to achieve an even melt line with good substrate penetration of the melt pool.

The spatial pitch of the spots within the melt line has been shown to affect the Ra roughness and the sharpness of the melt beads. Both sharpness and Ra are improved by the use of a smaller spot pitch and as the mean height decreases with spot pitch a small spot pitch is preferred.

A process delay between each sequent melt spot has been shown to affect the dimensions of the melt line and to improve the Ra and sharpness of the line. The optimum delay was found to be 400 ms added onto the minimum process time of 132ms. The insertion of any delay, especially one as large as this, will detrimentally affect build rate but to ameliorate this effect the scanning strategy could be altered to print elsewhere whilst waiting.

The effects of pulse shaping have been demonstrated for simple ramp up and ramp down profiles compared to the square pulse that has been used for the rest of this research. The Ra roughness and line sharpness of lines created by using a ramp up profile have been shown to be superior to those produced by a ramp down profile across all of the pulse energies used. However these improvements are pulse energy dependent when compared to the lines produced by a square pulse so there is no single best pulse shape for all processing conditions. However, the square pulse showed the flattest lines by having the lowest height-to- width ratio and is therefore the preferred profile.

The exposure power produced a significant effect upon the degree of melt penetration into the substrate with increasing power leading to increased depth and width of substrate melt. Line sharpness and Ra roughness are both improved by increasing power, and this accounted for the decrease in the aspect ratio of the melt bead. Therefore the maximum power of 42 W will be used for subsequent work.

The maximum feature height within all melt lines produced for this chapter is greater than the depth of the powder layer from which the lines were built except for those built with pulse energies of 210 mJ and above into powder depths of 200 μm and greater. However, using these settings means the resultant melt bead is inconsistent and has much flanking splatter. Working with the information presented in Table 12, the conclusion reached is that it may not be possible to build highly dense objects using the laser diodes incorporated into this research system.

Chapter 6

Multiple layer building

6.1 Introduction

This chapter will explore the creation of layers of melt balls from which planar objects or multiple layer 3D objects can be built. The layer creation process is regarded as the sequential placement of melt lines of particular length and orientation according to scanning strategy. The results of the previous chapter will be used to inform the choice of parameters for line building and the effect of scanning strategy will be evaluated on layer quality for layers built in a thin powder layer on a substrate, in deep powder, and for multiple layer objects.

In the following sections where reference is made to a scanning strategy number these correspond to the icons shown in Figure 90 which represent the strategies developed in Chapter 3

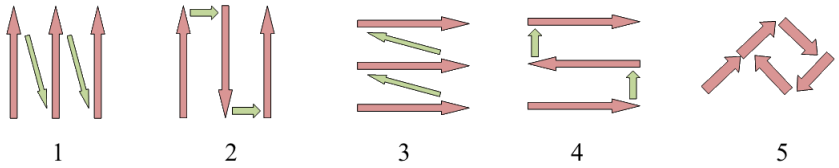

Figure 90 The five scanning strategies used for the placement of lines to create layers.

6.2 Single layer on substrate

To evaluate the effectiveness of the five scanning strategies developed for use with this technology, 15 rectangular arrays of melt spots were built in a thin layer of powder using 42 W and three pulse energies *per* scanning strategy. The grid pitch selected was 67 μm which is a ninth of the 600 μm pitch of the laser diodes' focal spots and so the size of the rectangular arrays

was chosen to be ten spots in the Y dimension. This means that when creating spots on the first row of the array with laser diode number one the spots on the tenth row can be simultaneously created with laser diode number two. This was desired so that the interaction between diodes would be present within the build. The length of the array in X was unimportant except for being long enough to show a representative melting pattern and was arbitrarily chosen to be 20 spots. The powder thickness was 75 μm and each melt spot was created by square pulses of 42 W. The three pulse energies used for the builds were 42, 210 and 420 mJ.

Figure 91 shows the height scans of 15 rectangular builds. It is noticeable that the denudation of powder whilst building has adversely affected the quality of the desired rectangular build. Scanning strategies one and two both have their primary line creation direction aligned with the Y axis and produce similar rectangular builds when using the higher pulse energies. The difference between the two strategies is more apparent when using the lowest pulse energy where horizontal features more prominent for scanning strategy one. When using scanning strategy one the balls are placed on the top and bottom rows first in each column when there is more powder available. Using scanning strategy two the balls in the top and bottom rows are placed first in odd numbered columns and last in the even numbered columns. When the balls are placed last there will have been more powder robbed by the preceding exposures and thus a smaller ball is created. Consequently, the continuity of the melt bead is broken.

Scanning strategies three and four are primarily X scanning with small jumps in the Y direction. This is noticeable for both strategies across all three pulse energies in the obvious horizontal features at the tops and bottoms of the builds. These features are created first when there is enough powder for their creation. After the initial horizontal features have been formed the remaining powder has been added partially to the lower horizontal feature (and thereby broadening it), but it has been consolidated mostly as low patches with random high spots.

The rectangles created by the diagonal scanning strategy (number five) show the first diagonal track as a strong feature. Then, as with the horizontal strategies, after the initial strong feature there is only sufficient powder to create low patches with the occasional random balling effect when there is enough powder available.

These rectangular patterns illustrate that the denudation of powder caused whilst building a line of melt spots adversely affects the ability to create another line of spots in close proximity to the first line.

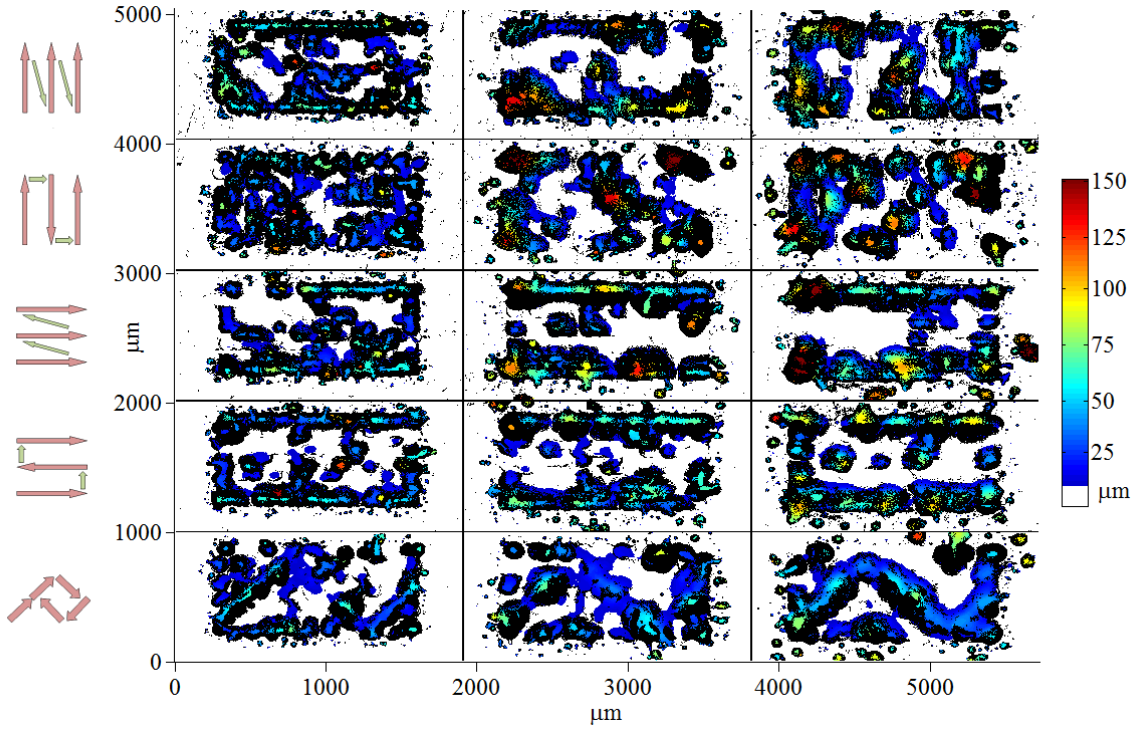

Figure 91 Height scans of rectangular builds in 75 µm of powder. Top to bottom: scanning strategies 1 to 5. Left to right: pulse energies of 42, 210 and 420 mJ. Points below 10 µm are coloured white to emphasise the low areas.

6.3 Multiple line building and powder refill strategy

In this section the effect of powder denudation is addressed by building parallel lines in order to establish the minimum spacing before the powder denudation, caused by the building of a previous line, adversely affects the building of the current line.

The lines for this study were built using 20 exposures of 42 mJ from 42 W on a 67 µm pitch in 75 µm of powder. The spacing of the lines was chosen so that the 600 µm pitch of the seven diode's focal spots was evenly divisible by the spacing. With reference to Figure 92, the top and bottom lines of each of the three rectangular shapes were built simultaneously by using diode number one for the bottom line and diode number two for the top line, therefore being 600 µm apart on account of the pitch of the focal spots. The other intermediate lines were built sequentially from bottom to top using diode number one only. The spacing of the lines within Figure 92 from left to right is 200, 150, and 120 µm.

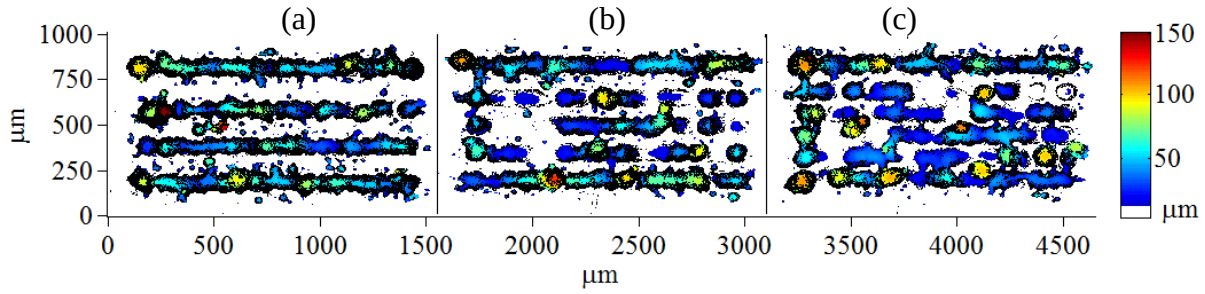

Figure 92 Evaluation of minimum line spacing, left to right: 200, 150 and 120 µm. All lines are built using 42 mJ exposures from 42 W on a 67 µm pitch in 75 µm of powder. All points below 10 µm are coloured white to emphasise the increasing low areas of melt caused by lack of material due to powder denudation.

The four lines built using a spacing of 200 µm are almost continuous and few low areas are visible. However when the spacing is 150 or 120 µm there are many low areas where powder has been incorporated into the previous line and there is insufficient material to create a continuous melt bead. It would therefore seem preferable when building a rectangular structure from lines to build lines with a spacing of 200 µm, then to refill with powder without changing the height of the build plate within the powder bed and finally place new lines interleaved with the previous. This refill and interleaf building strategy has been used to good effect by Morgan *et al* where densities of over 99 % for 316L were achieved [78].

To investigate the possibility of a refill and interleave strategy two rectangles were built using two interleaving distance offsets: 100 and 67 µm. The pulse energy used was 42 mJ and the initial power layer thickness was 75 µm. The first step, common to both rectangles, was to place four melt lines 200 µm apart as Figure 92 (a). Secondly a powder refill was attempted without changing the height of the build piston, which was impossible, and a drop of 100 µm was required to allow passage of the wiper. Thirdly, the first interleaving lines were added. In both cases at 200 µm spacing but in Figure 93 (a) with a 100 µm offset and in Figure 93 (b) with a 67 µm offset to the original set of four lines. The third interleaving set of lines for Figure 93 (b) required another powder refill and a 50 µm drop was required to allow passage of the wiper.

The white areas within the build of Figure 93 (a) indicate that the width of the melt lines is insufficient to cover the substrate effectively given the 100 µm spacing of the lines, whereas with regards to Figure 93 (b) the 67 µm spacing is sufficient to cover all of the substrate.

However, there are high horizontal features visible using a 67 µm spacing that are the result of the last three lines added which, when taken into consideration with the impossibility of a powder refill without height change, indicates that an interleaving strategy is difficult to implement.

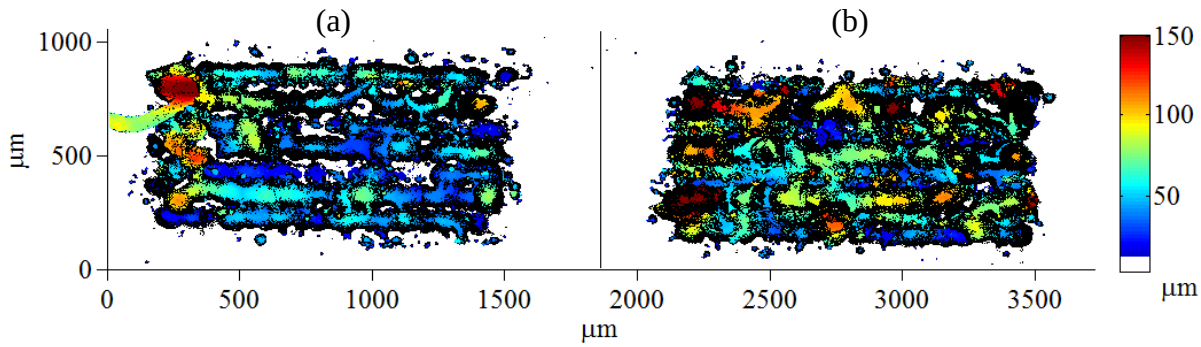

Figure 93 Interleaving of melt beads. First layer, 4 lines regularly spaced at 200 µm. First powder refill at 100 µm. (a) One interleaving operation at 50 % gap fill. (b) Two interleaving operations at 33 % gap fill.

6.4 Single layers in deep powder

When building a 3D object such as a cube the majority of a layer's melting will occur upon melted and re-solidified material within the previous layer but if the object is more elaborate than a cube, for example has overhangs or the layer is the first layer built upon anchor structures, then a percentage of the layer will be built over unconsolidated powder. A sequence of single-layer rectangles was built in deep powder with no support structures to judge the relative virtues of the five scanning strategies developed in Chapter 3.

For each of the five scanning strategies twenty rectangles were built by the use of five exposure times and four grid pitches. The overall dimensions of all the sample rectangles were kept constant at 4.2 by 8.4 mm so the number of individual exposures required to make the rectangle would increase as the grid pitch decreased. The differing grid pitches were chosen so that an integer amount of spots could be placed regularly within the 600 µm pitch of the individual laser diodes. The output power of the laser diodes was kept at maximum. The range of pulse energies used for the rectangles built with a 200 µm spot pitch was decreased for the other buildings in proportion to the spot pitches to create the smaller balls necessary.

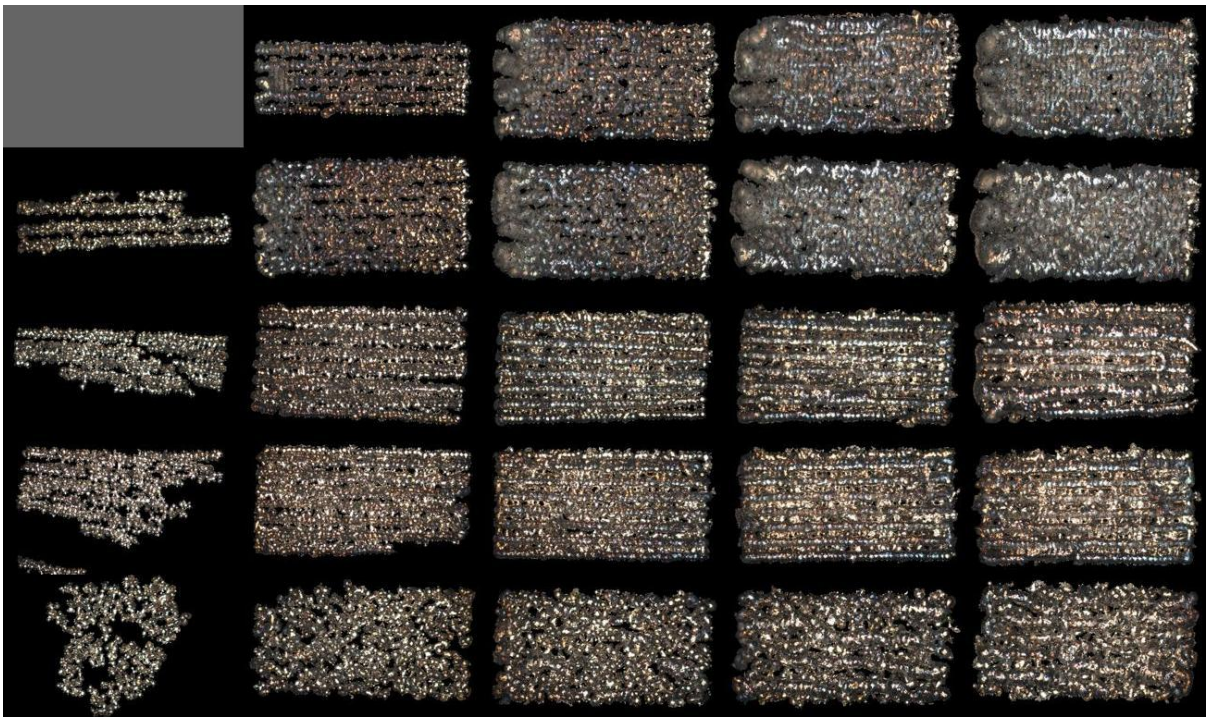

Figure 94 Grid pitch of 200 µm. Rows, top to bottom = Scanning strategy 1,2,3,4,5. Columns, left to right = pulse energies of 126, 252, 378, 504 and 630 mJ.

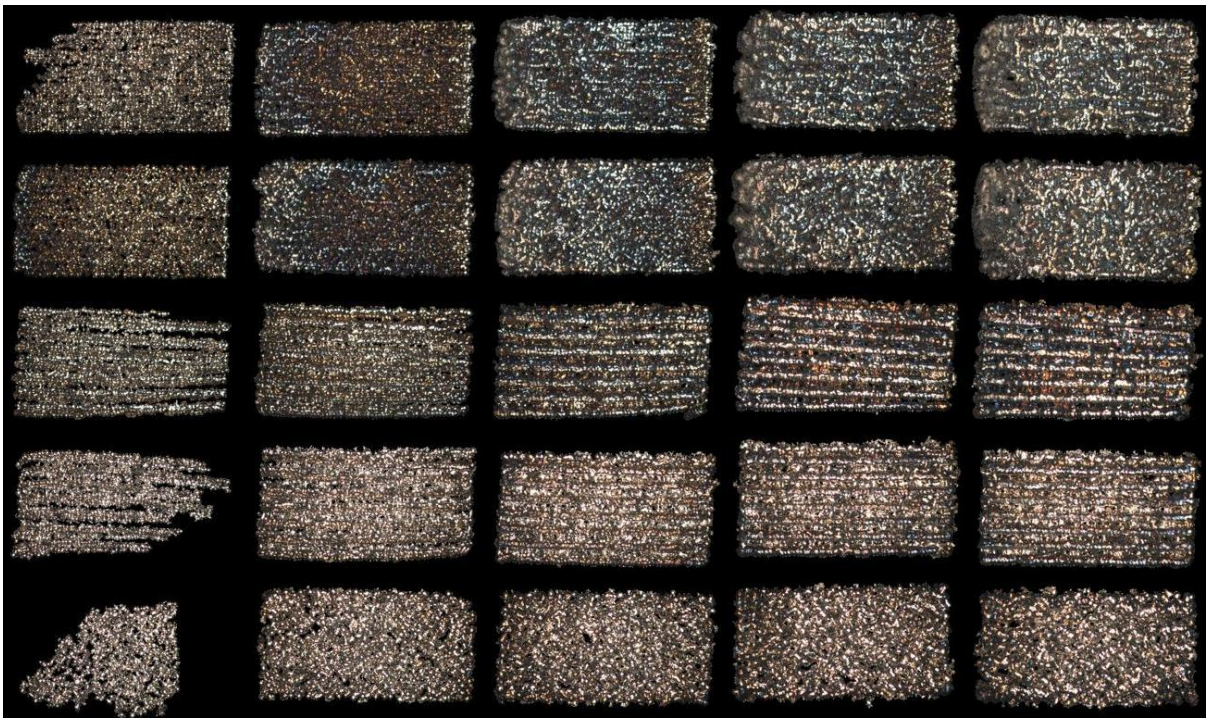

Figure 95 Grid pitch of 150 µm. Rows, top to bottom = Scanning strategy 1,2,3,4,5. Columns, left to right = pulse energies of 95, 189, 284, 378 and 473 mJ.

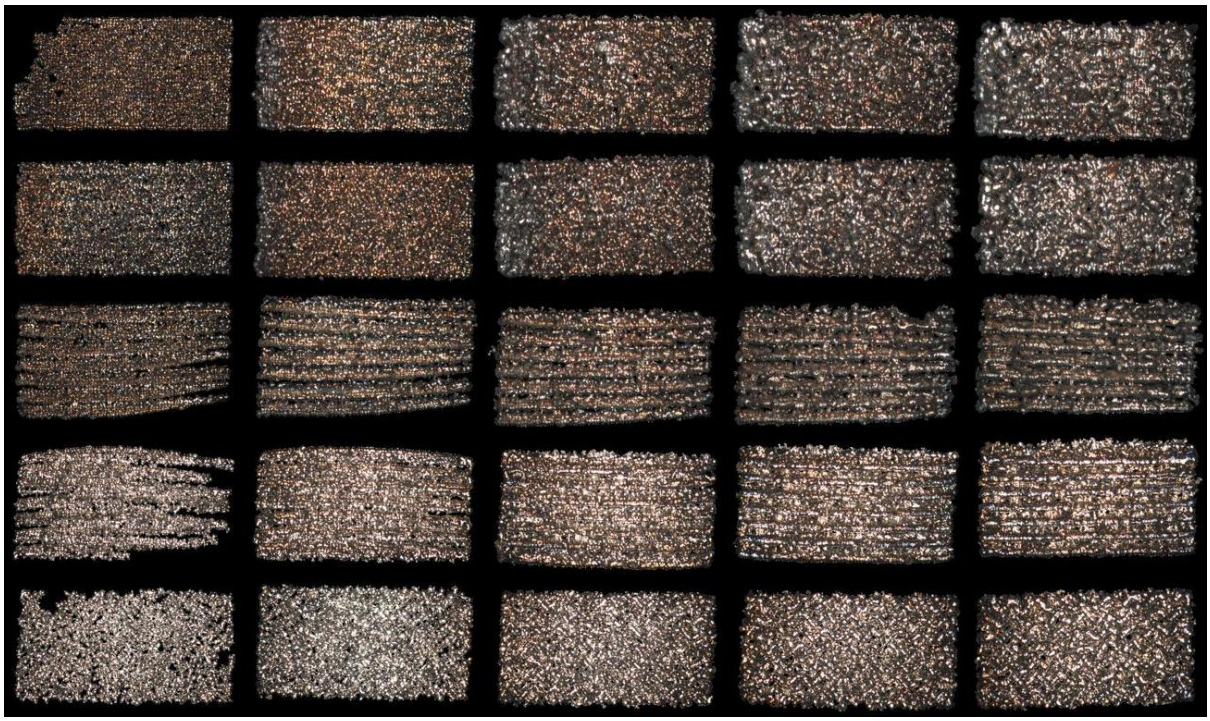

Figure 96 Grid pitch of 120 µm. Rows, top to bottom = Scanning strategy 1,2,3,4,5. Columns, left to right = pulse energies of 76, 151, 227, 302 and 378 mJ.

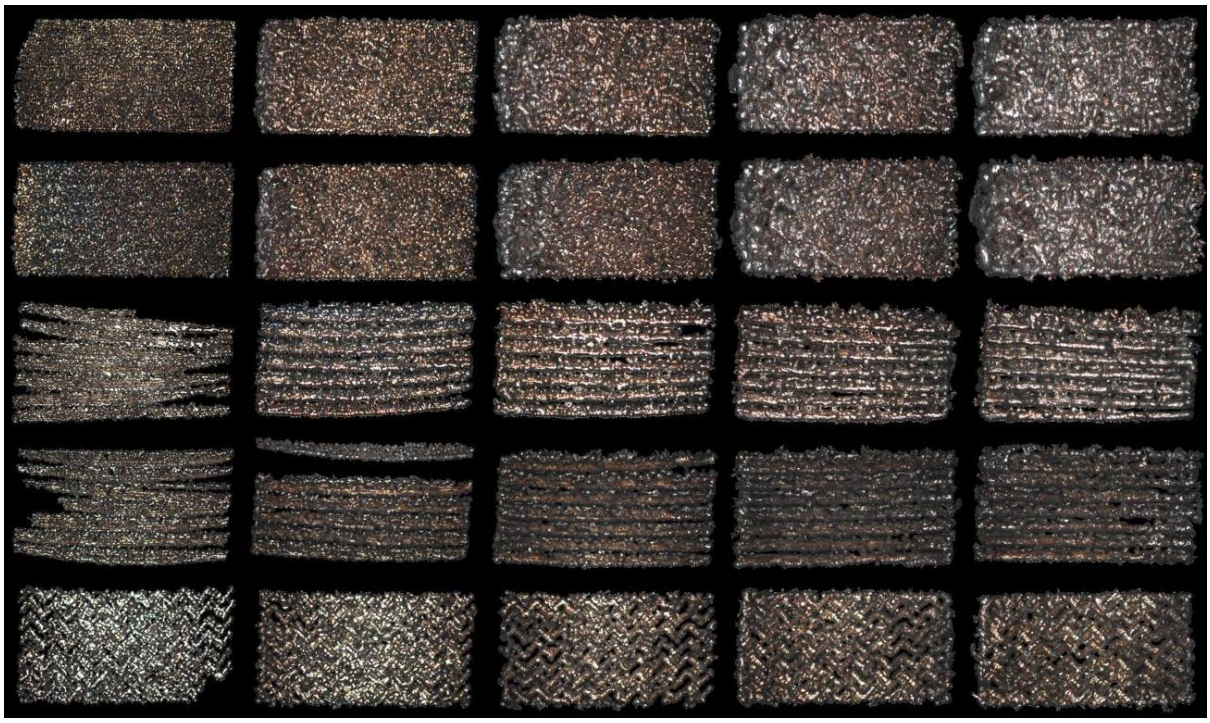

Figure 97 Grid pitch of 100 µm. Rows, top to bottom = Scanning strategy 1,2,3,4,5. Columns, left to right = pulse energies of 63, 126, 189, 252 and 315 mJ.

With regards to the top two rows of Figure 94, Figure 95,

Figure 96 and Figure 97 corresponding to scanning patterns one and two, there is an obvious macro melting effect that appears above a certain exposure time. This affects the beginning of the ribbon (the start point for each build is the bottom left) which decays leaving the individual balls visible with travel to the right. For the samples of Figure 94, built on a 200 μm grid pitch, the transition to the macro melting state happens even before full consolidation of the layer occurs as is evidenced by the holes through the ribbons created with 378 mJ pulse energy. This macro melting effect is a result of the laser diode array being oriented vertically and the primary scanning direction of these two scanning strategies also being vertical. Therefore the individual balls are placed in lines that are only 3 to 6 balls long before they link with the lines produced by another laser diode at which point the array moves horizontally one unit and the vertical scanning repeats. This has the effect of generating a localised region of high temperature that cools slowly allowing surface tension to create a smoother surface. It is most noticeable at the start of the ribbon because the surrounding powder has a low thermal conductivity, but as more of the ribbon is build the re-solidified consolidated material can conduct heat away more efficiently thereby reducing the cooling time.

With regards to the third and fourth rows of these ribbon figures, these samples are built with the predominantly horizontal scanning strategies and this is evident in their appearance. The first horizontal movement from the left hand edge to the right hand edge of the ribbon is the same for both strategies and produces seven long horizontal melt beads which stand out as the 'ribs' of the structure. For the second and subsequent passes the direction of the next added horizontal depends upon the strategy. However, regardless of direction the subsequent passes do little to affect the form of the initial seven lines of balls and serve to bridge the gaps between the 'ribs' with re-solidified material.

The samples shown in the bottom rows of the ribbon figures are built with the diagonal strategy, the form of which is most obvious in the samples built on the 100 μm grid pitch. These samples tend to be the least oxidised as a result of the heat energy being the least localised due to the scanning patterns' greater distance between successive melt balls.

Subsequent to building, each single layer rectangle was examined using a Wild M450 microscope and images were captured using a magnification of approximately 8X. Images were also taken of a calibration object to be able to calculate the millimetres *per* pixel scale for the

images. The thickness of each sample was measured three times at different places by the use of digital callipers with a readout precision of ±0.01 mm and an average value obtained. Also the weights of the samples were recorded using a Sartorious Analytic A210P which had a quoted standard deviation of ±0.0001 g. These measurements were used to generate other metrics and are used in the graphs and observations that follow.

6.4.1 Thickness

There is a trend for the thickness of the ribbons to increase with pulse energy irrespective of which scanning pattern was used Figure 99. This is consistent with higher energy pulses melting more material and thus creating larger constituent balls. However, the layer thicknesses far exceed the diameters of the individual melt balls created in deep powder detailed in chapter 3 where a 5 ms exposure (pulse energy 220 mJ) produced melt balls with an average diameter of ~270 μm. The thickness of the ribbons produced with that pulse energy here are up to three times this value dependent upon scanning pattern and grid pitch. The reason for this extra thickness is due to the change in density between the powder and the re-solidified melt balls. When a single melt ball is created by pulsed exposure to a laser beam an amount of powder melts then solidifies and the resultant ball, caused by surface tension effects, sits within a crater in the powder layer resulting from densification. The next application of the laser beam at a distance from the first has enough energy to melt the same amount of powder as the first but some of the energy goes to heating the previous ball and some goes to melting powder. The new melt will adhere to the previous ball and if the previous ball is heated to over-melt temperature then surface tension forces will draw the new melt into the previous ball rather than creating another similar sized ball at that location. This results in the next position of the laser beam overlapping the previous melt ball less than before thereby melting more powder and creating a crater that is deeper because it is formed over the previous crater. The new melt ball then sits deeper in the powder bed and will not be pulled into the old melt ball so much because the latter will be less heated. The placement of the subsequent balls will continue this effect until an equilibrium depth is arrived at whereby the melt balls are created at approximately the same depth in the powder bed. However, if the sunken line of melt balls joins with the start of another line of balls created by another one of the seven laser beams then a zig-zag depth profile can occur which increases layer thickness Figure 98. The depth of the zig-zag effect is expected to increase with a smaller grid pitch because

decreasing the grid pitch is analogous to decreasing the scanning speed in a conventional galvo-scanning mirror system. This increases the energy density and thus the depth of powder incorporated within the melt pool. This trend is present for all scanning strategies except for the ribbons produced by using scanning pattern five where the spot pitch has little influence on the thickness and the thickness increases approximately linearly with pulse energy.

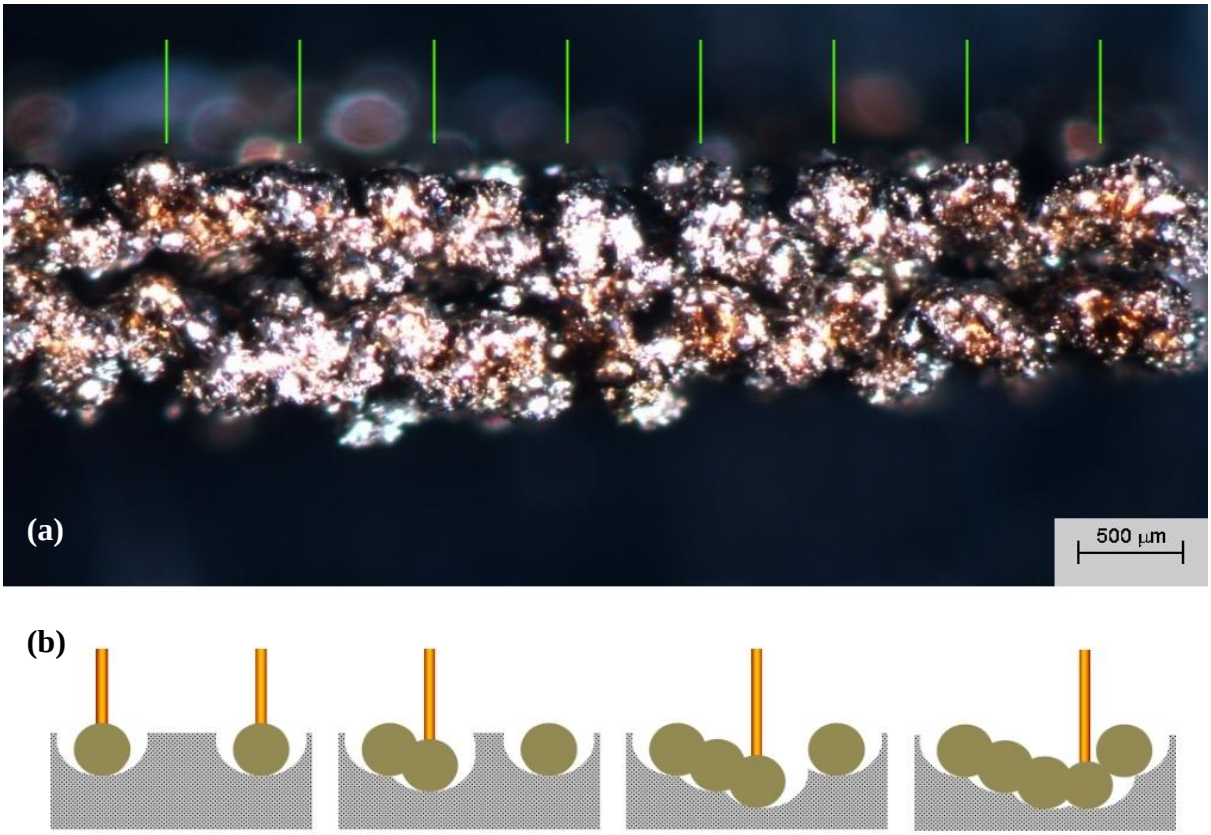

Figure 98 (a) Edge view of two layers created using scanning strategy one showing zigzag effect. Green lines indicate starting points of laser diodes. (b) The successive addition of melt balls creating the zigzag effect by increased penetration due to powder robbing by previous balls.

To verify that the relationship between scanning pattern and thickness is based upon energy density the data have been re-plotted with energy normalised by area Figure 100. In these graphs the trend for increasing layer thickness with decreasing spot pitch has disappeared and in the case of scanning pattern 5 the trend has been reversed. Except for scanning pattern 5 the

minimum ribbon thickness is observed for a spot pitch of 150 µm over a wide range of energy densities.

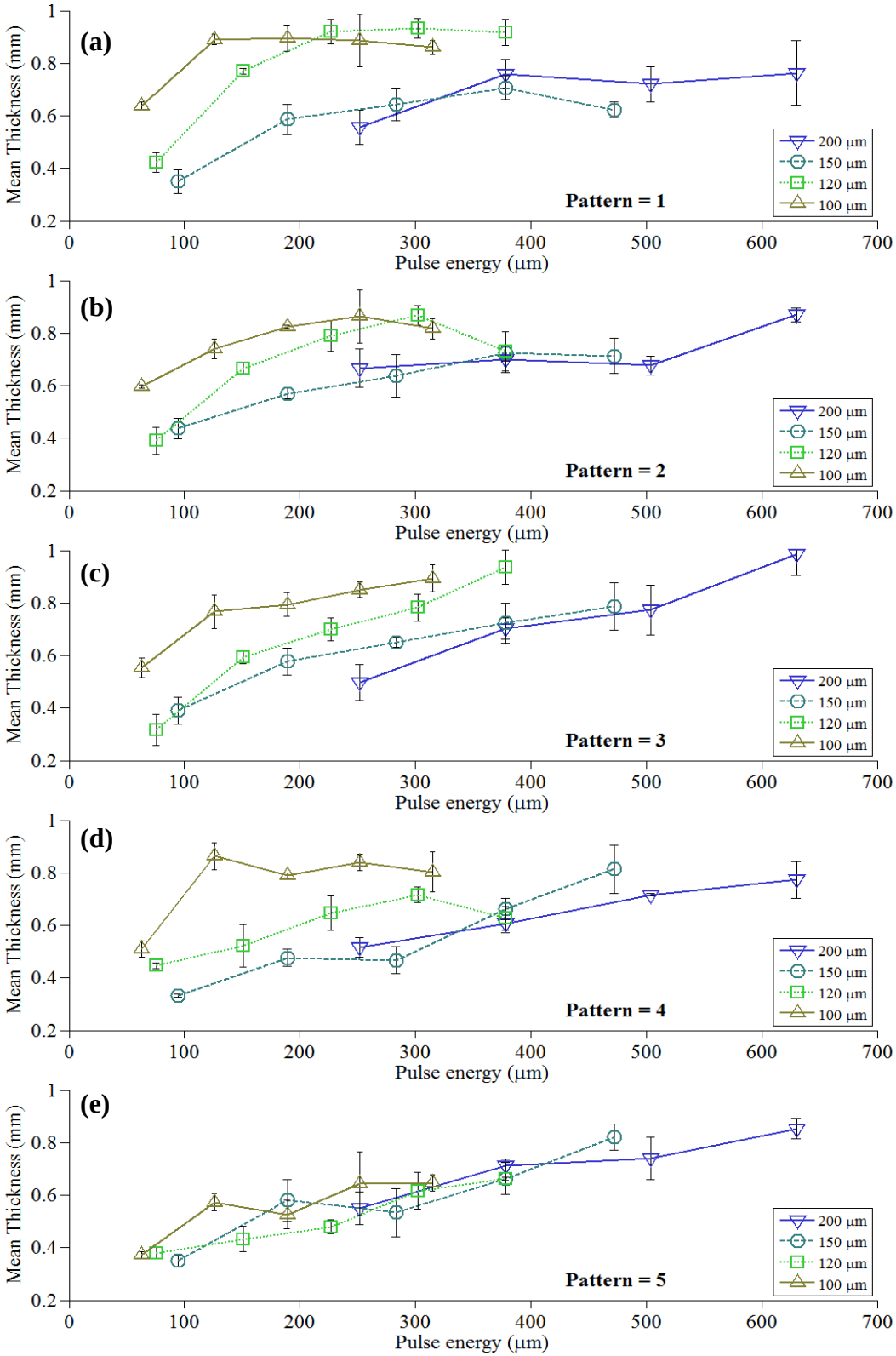

Figure 99 Mean thickness of the single layer ribbons as a function of pulse energy for four grid pitches and each of the five scanning patterns.

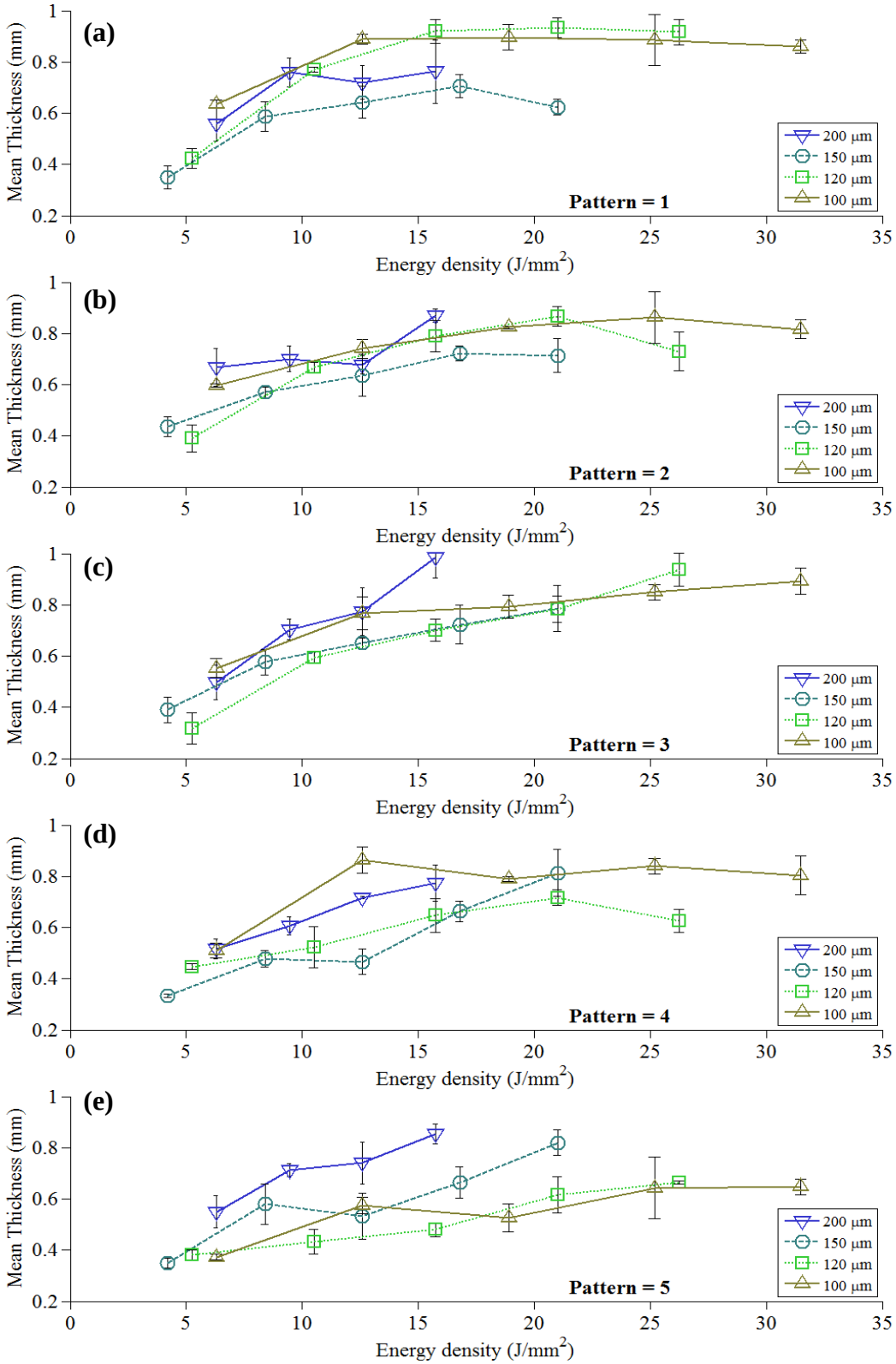

Figure 100 Mean thickness of the single layer ribbons as a function of area energy density for four grid pitches and each of the five scanning patterns.

6.4.2 Consolidation

The degree of consolidation of the samples could have been measured by the density of the objects. However, as these samples are single-layer objects with pores but no trapped air then the density of the objects is likely to be very close to that of the bulk material. In light of this another metric was created that would give some useful measure of consolidation based on the amount and/or size of holes within the sample. This was done by means of image-processing the microscope images of the samples. The aim was to measure the area and perimeter of the sample and this was achieved by taking two images of each sample: one with a dark background and one with a light background but each with the same exposure setting. Having obtained the two images, the dark image was subtracted from the light image and the resulting difference image converted to black and white by thresholding. It was inverted to obtain the sample as white pixels rather than black. The inversion was performed to make the areas easily obtained by summing the logical array of ones and zeros. The reason for creating a difference image was to make the thresholding process more reliable. If only the image with the black background had been used it would have been difficult to find a threshold level that would exclude all the background but include the darker areas within the undulations of the sample. Similarly, by using only the image with the white background the bright reflections from the tops of the rounded features would be difficult to differentiate from the background. The difference image produced a dark sample and a light background. This removed the image-specific dependence on the threshold value which made an automated process possible.

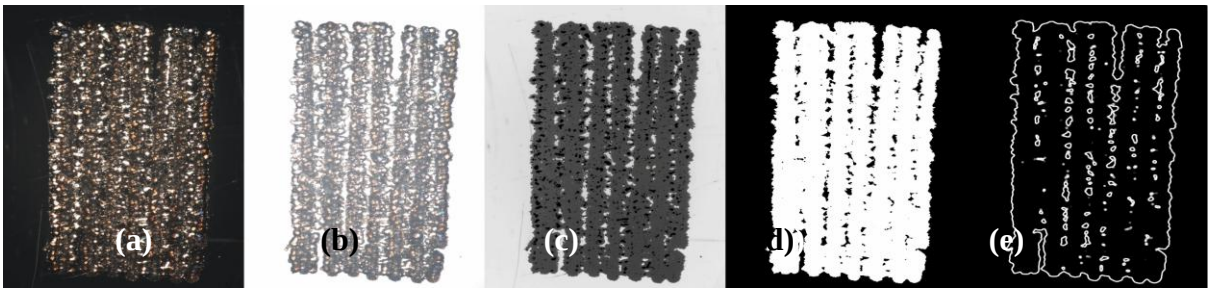

Figure 101 Steps showing area and perimeter extraction. (a) Sample on black background, (b) sample on white background, (c) difference image, (d) binary image, (e) perimeter.

A consolidation metric was desired such that the presence of holes within the sample would be detrimental to the quality of the sample. However, just counting the amount or total area of the holes within the sample was considered insufficient as unconsolidated areas appearing on the edge of the sample created inlets into the perimeter which would not appear as holes. Consequently, a dimensionless metric was designed that was based upon the area, number of white pixels Figure 101 (d), and perimeter, number of edge pixels Figure 101 (e) and defined as

$$Consolidation\ factor\ = \frac{\sqrt{area}}{perimeter}$$

The ribbons of this study were designed as rectangles with a 2:1 aspect ratio so the maximum possible consolidation value for the samples was

$$Consolidation\ factor = \frac{\sqrt{2l^2}}{6l} = 0.236$$

A value less than 0.236 would indicate the presence of holes and/or an uneven perimeter and thus a lack of consolidation.

The graphs of Figure 102 illustrate the effects of scanning strategy and energy density upon this consolidation metric. The maximum degree of consolidation occurs with scanning patterns one and two. These scanning patterns are the vertically based patterns whereby the lines of melt balls produced by each of the laser beams join with the lines produced by the other beams in the shortest time. This helps to keep the temperature of the re-solidified material high at the edge where the new melting is occurring. As a result, each new pulse of energy can more easily wet the newly melted powder to the previously consolidated material reducing the tendency for balling and for holes or pores to occur within the structure of the ribbon.

For the vertically based scanning patterns one and two the consolidation improves with increasing energy density until approximately 10-15 J/mm^2 after which the consolidation plateaus. The plateau is a result of there being few if any holes within the ribbons and the consolidation values being determined by the evenness of the perimeter. Below the plateau point there is a trend towards increased consolidation with decreasing grid pitch for a given energy density Therefore there are fewer holes within the ribbons built with a small grid pitch. This arises because energy delivered at a greater number of positions within a given area becomes delocalised, thereby creating smaller temperature gradients and finer features as a result of the reduced energy in each pulse.

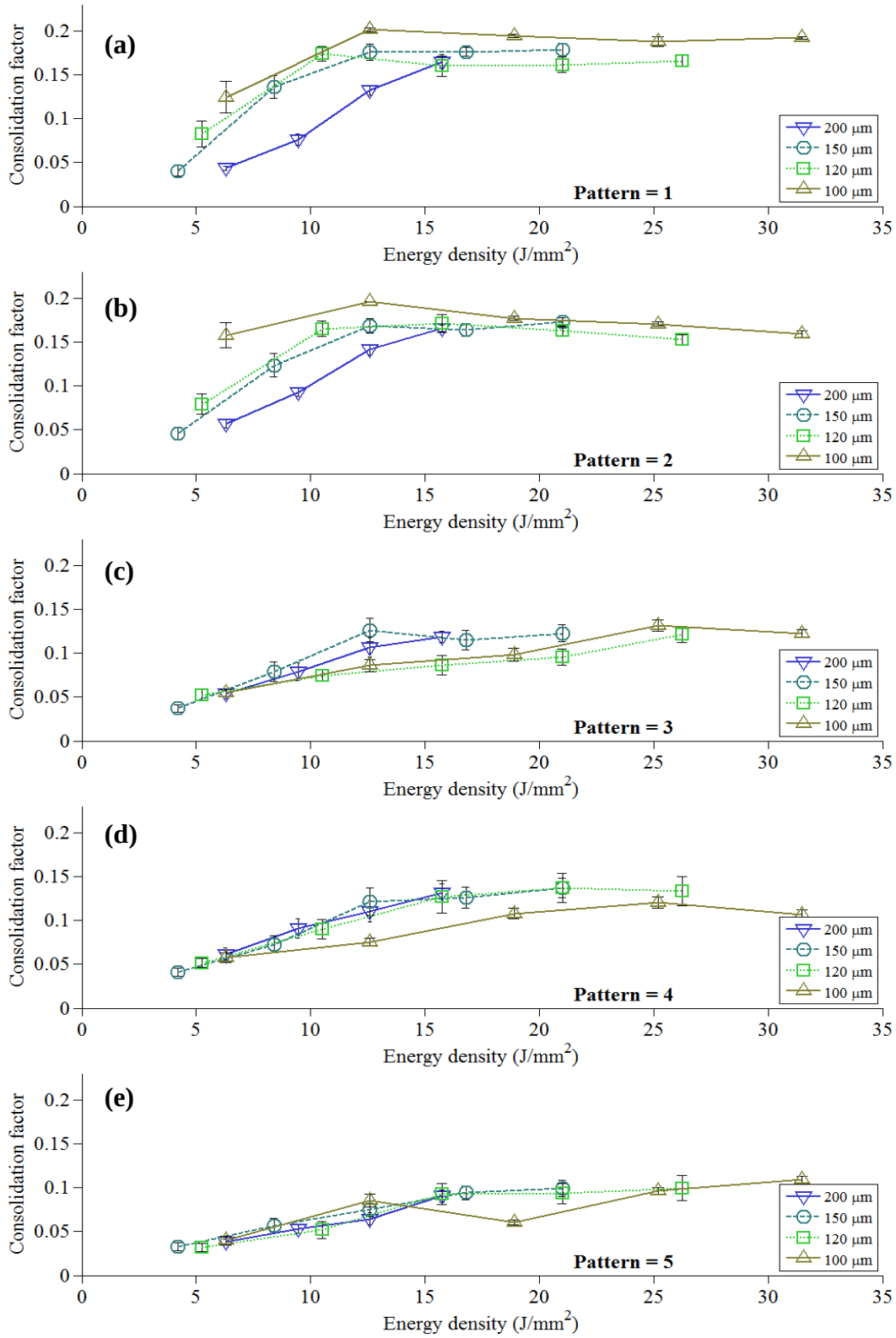

Figure 102 Consolidation factor of the single layer ribbons as a function of area energy density for four grid pitches and each of the five scanning patterns.

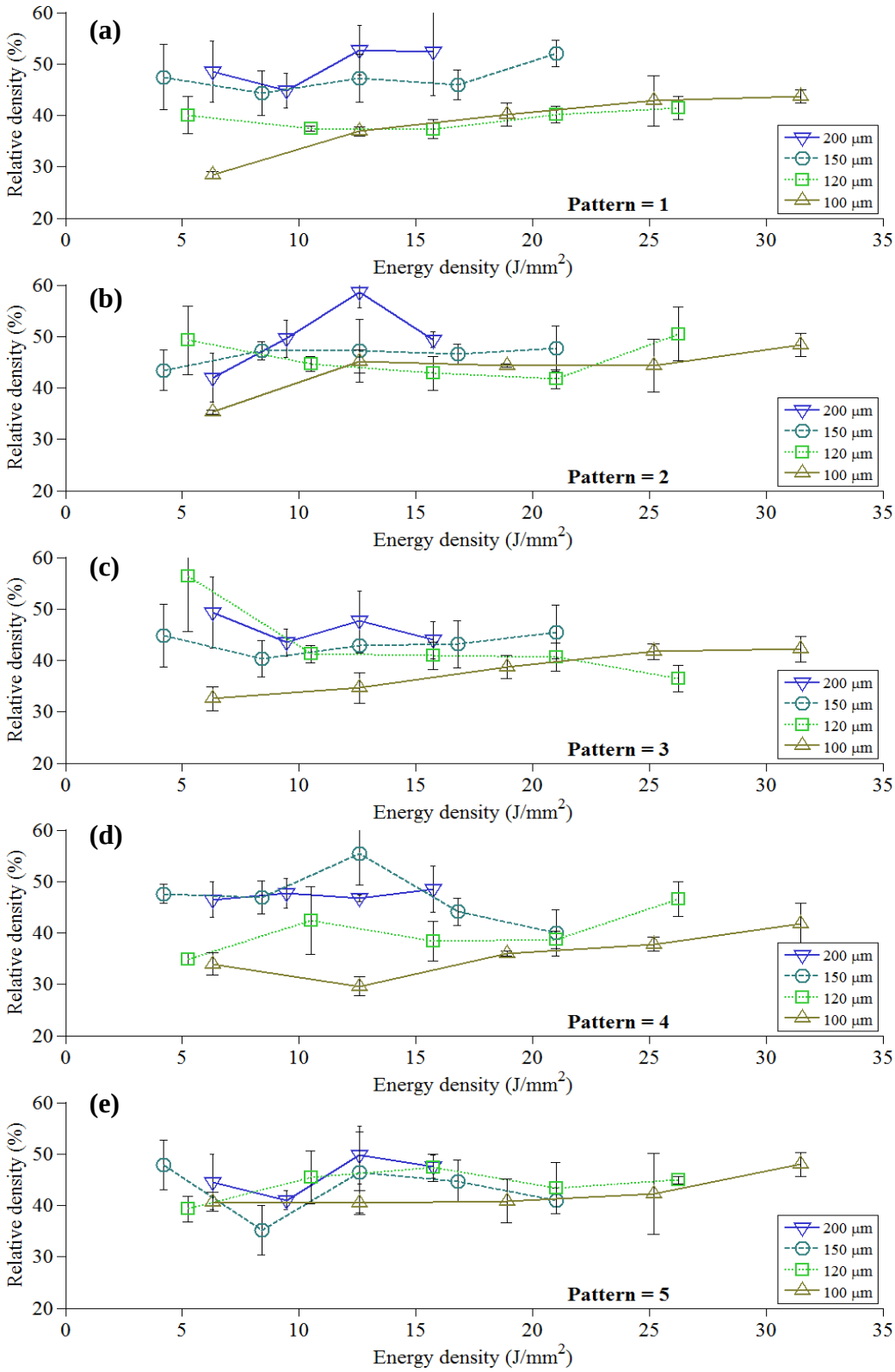

Figure 103 Relative density of the single layer ribbons as a function of area energy density for four grid pitches and each of the five scanning pattern.

The ribbons built using scanning patterns three, four, and five also show increasing consolidation with increasing energy density but are less consolidated than those built with the vertically-based patterns. Pattern five yields the lowest consolidation because it places the melt balls at $\sqrt{2}$ times the grid pitch which increases the chances of the melt bead being discontinuous. There is a slight tendency for the consolidation to decrease with grid pitch for patterns three and four which is in opposition to the trend displayed by the ribbons built using patterns one and two. This is likely because without the high local temperature at the build edge the lower energy pulses concomitant with a small grid pitch for a given energy density re-melt the re-solidified material less easily.

6.4.3 Compactness

As previously explained in 6.4.2 the density of all the ribbons of this trial are expected to be approximately that of the bulk material, but a density-like metric was created that would give an indication of compactness of the sample. This was defined as

$$Relative\ density = \frac{Weight}{Thickness \times Area} \times \frac{100\%}{Density\ of\ bulk}$$

The thickness and area within this equation are those used in the last two sections. The volume produced by multiplying the projected area by mean thickness will be larger than the true volume of the sample but it is an indication of the space that the sample occupies and when used to normalise the weight gives an indication of how compact the sample is.

The graphs of Figure 103 show that there is a small increase in relative density with increasing energy density for the samples built on a 100 μm grid pitch, but that for the larger grid pitches the relative density of the ribbon samples is mostly independent of the energy density. However, there is a tendency for the relative density to increase with grid pitch for a given energy density. Given the plateau in consolidation, indicating the existence of few through holes, and the relative independence of thickness to grid pitch observed in the previous two sections this means that using a large grid pitch results in less interstitial air than using a small grid pitch.

6.5 Cuboids

The rectangles built in section 6.2 demonstrate that the five scanning strategies used produce uneven layers from a thin layer of 316L powder on a planar substrate. The rectangles built in section 6.4 with the same scanning strategies show that consolidated structures can be

built in deep powder. Therefore cuboids were created to establish the degree of consolidation possible for a multiple layer object.

Four sets of cuboids were built, each using pulse energies of 42, 210, 210 and 420 mJ respectively. Each set comprised five cuboids, Figure 104, built using the five scanning strategies shown in Figure 90. In all cases the grid pitch was 100 μm and the layer size was 42 x 126 spots which equates to 4.2 x 12.6 mm. The layer thickness used for each set of five cuboids was the smallest that would allow passage of the powder wiper over the build, albeit scraping on the previous layer. For the 42 mJ exposures this was 150 μm, for the 210 mJ exposures this was 300 μm and 400 μm for the 420 mJ exposures.

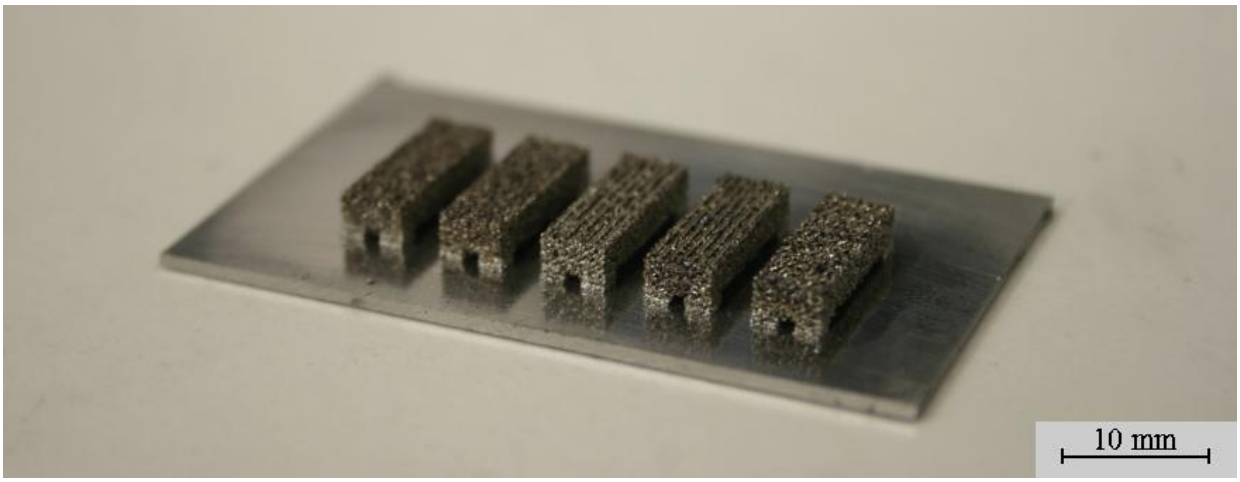

Figure 104 Ten layer cuboids built on corner support pillars using 210 mJ exposures on a 100 μm grid pitch. Left to right scanning strategies 1 to 5. Sections are shown in Figure 105.

With respect to the top two rows of Figure 105 it is evident that using the higher pulse energy produces a denser cuboid despite the minimum layer thickness increasing by the use of a higher pulse energy. The sections produced with 42 mJ exposures have no obvious structure to the melt balls and the positions of the melt balls appear random except at the left hand side edge of the cuboid made by scanning strategy one. In this case there is a line of ten melt balls up the edge of the image that would equate to the vertical edge of the build and indicate the starting position on each layer. The middle two rows of Figure 105 produced with 210 mJ exposures do have some structure, particularly within the cuboids built using scanning strategies three and four and to a lesser degree using number five. This structure is that of seven horizontal bands of melt

balls that would have been vertical during the build. These bands are the result of a structure within each layer that is common in all layers and is created by the strong initial lines produced by those scanning strategies demonstrated in Figure 91.

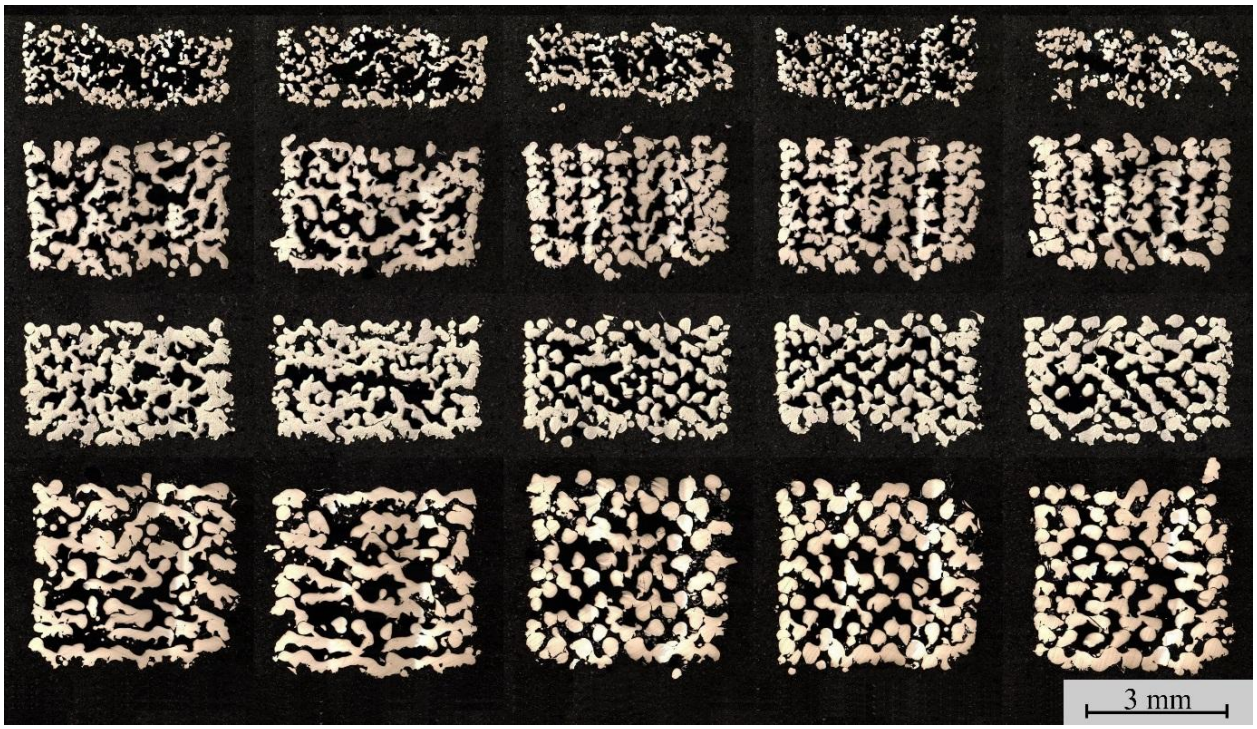

Figure 105 Sections of 10 layer cuboids built using exposures to 42 W. Left to right: scanning strategies 1 to 5. Top to bottom: pulse energies of 42, 210, 210 and 420 mJ respectively. Layer thickness of 150, 300, 300 and 400 μm respectively. Grid pitches of 67, 100, 100 and 100 μm respectively. Alternate layer offset none, none, 100 and 100 μm respectively.

The bottom two rows of Figure 105 show the cuboids built using an offset to the starting point in each layer. For the cuboids built using scanning strategies three, four and five the effect has been to break the vertical structures seen in the second row and replace them with a diagonal arrangement of spots. For the cuboids built using scanning strategies one and two the effects are less obvious due to the offset being in the primary scanning direction. However, there is an increase in density for the cuboids built using 210 mJ exposures with layer offset alternation over those built using 210 mJ exposures without layer offset alternation.

Table 16 gives the densities of the aforementioned cuboids calculated from the section images by image processing. It can be seen that the cuboids built using a pulse energy of 42 mJ

have the lowest densities despite being built using the lowest layer thickness. The density of the cuboids increases when the pulse energy is increased to 210 mJ and falls off when increasing the pulse energy to 420 mJ. This suggests that the optimum value for pulse energy is between 42 and 420 mJ.

Table 16 Densities of cuboids.

Pulse energy	Layer offset	Layer thickness	Density (%)				
			SS1	SS2	SS3	SS4	SS5
42 mJ	Constant	150 µm	**36.6**	**37.4**	**38.7**	**39.9**	**36**
210 mJ	Constant	300 µm	**55.9**	**57.3**	**59.5**	**59.8**	**58.5**
210 mJ	Alternate	300 µm	**61.9**	**62.2**	**52.8**	**54.4**	**54.6**
420 mJ	Alternate	400 µm	**53.4**	**51.3**	**52.8**	**52.4**	**55.2**

The interleaving strategy explored in section 6.3 was used in the building of a cuboid employing the same parameters as derived in that section (42 mJ exposures on 67 µm pitch). The interleaving process only works with parallel lines and so was attempted using a variant of scanning strategy number three. This was implemented by creating a layer of parallel melt lines 200 µm apart, refilling with powder after a minimum build chamber drop, adding the first set of interleaved lines at 67 µm offset, re-filling another minimum thickness layer and finally adding the third set of interleaved lines at 133 µm offset. This build could not be done on support pillars as the first lines were too fragile without the support of their neighbouring lines to stand up to a minimum height wiper pass and so it was built directly upon the substrate Figure 106. The density of this cuboid is 32.2 % which is comparable to the other cuboids built using 42 mJ exposures but slightly less than those built using the five scanning strategies of Figure 91.

The densities of the cuboids built using the technology developed within this research are significantly less than that achievable using commercially available technology. Figure 107 shows the plan view and cross sections through a cuboid built from Inconel 625 in a PM100 from Phenix Systems [156]. This cuboid has a density of >99 % and many commercial AM machines are capable of producing parts with comparable densities. These densities are achieved by the use of higher intensities, 9740 W/mm^2 for the PM100 compared to 2400 W/mm^2 for this work and by the use of CW laser exposure as opposed to a pulsed ‘expose-move-expose’ strategy

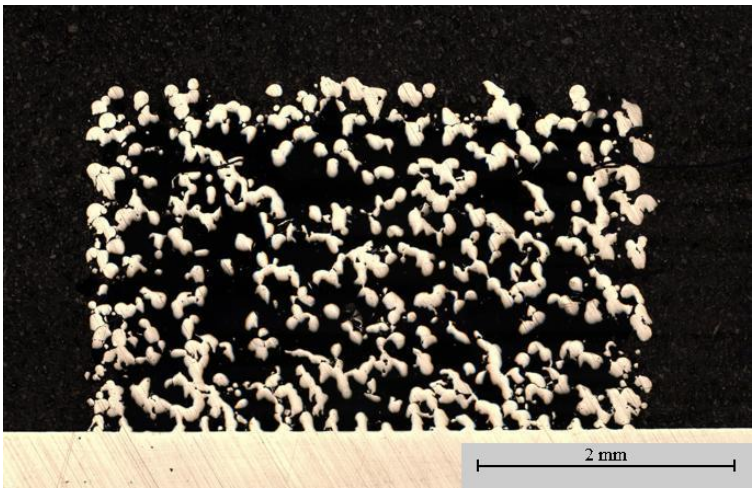

Figure 106 Section of a 30 layer cuboid built directly upon a substrate using pulse energies of 42 mW from 42 W power.

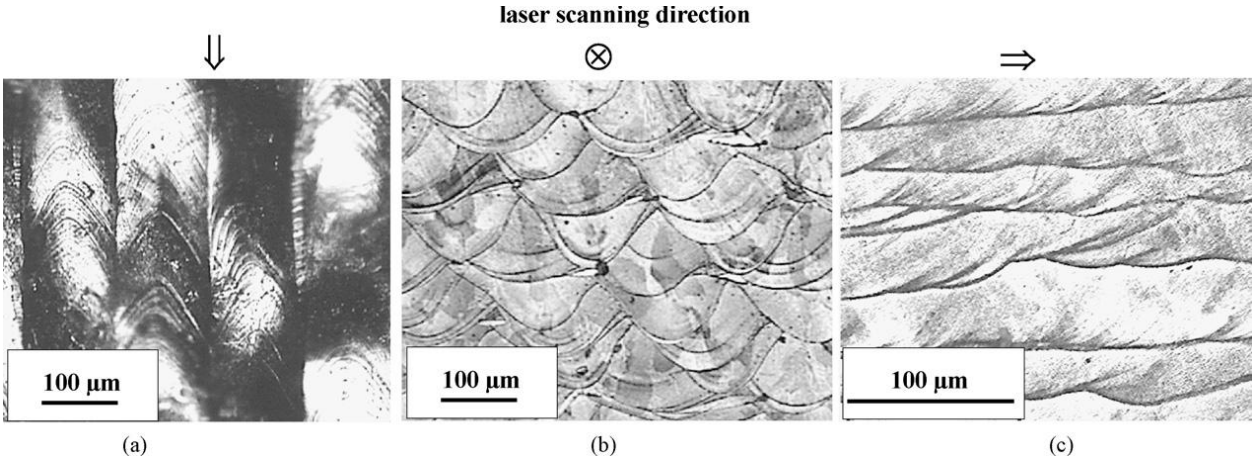

Figure 107 Cuboid built from Inconel 625 using a PM 100 by Phenix Systems with 99 % density. (a) plan view, (b) transverse cross section, (c) longitudinal cross section.

Figure 108 shows a nine-layer cuboid built using 420 mJ pulses on a 150 µm grid pitch. The building instructions for each layer were generated from a 261 by 64 pixel bitmap of an IPG logo where white pixels were printed and black pixels were not. A ribbon overlap of two pixels was used to join together the four ribbons necessary to span the 64 pixels and the mean minimum layer thickness was 560 µm. This resulted in an object ~5.5 mm thick. The large layer thickness resulted in de-lamination due to poor inter-layer consolidation.

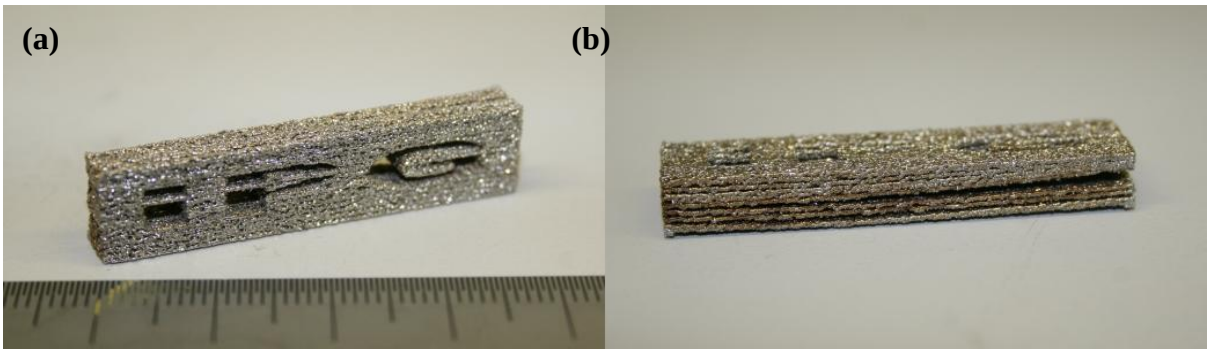

Figure 108 Nine layer prismatic object showing de-lamination as a result of poor interlayer consolidation.

6.6 Summary

This chapter has characterised the layer creation process using the five scanning strategies defined in Chapter 2. Single layer builds have been performed in a thin layer of powder on a substrate and in deep powder with no substrate, and have been characterised by thickness and level of consolidation. Cuboids have also been built and evaluated by density.

The rectangular builds in a thin layer of powder on a substrate demonstrated that the denudation of powder of the selective laser melting process causes many low areas and random high spots within the confines of the attempted rectangle if no consideration is given to the denudation process. The interleaving strategy for overcoming the denudation problem runs into difficulties because a re-layer action without height change of the building piston is impossible with the power available in this project.

The ribbon thickness has been seen to increase with pulse energy and to be inversely proportional to grid pitch for a given pulse energy. The consolidation metric introduced in this chapter demonstrates that consolidation plateaus after ~15 J/mm^2 and is greater for scanning strategies one and two. The relative density was found to be largely independent of energy density but was greater when using a larger grid pitch.

The building of cuboids using a least possible layer thickness has shown that scanning strategy makes little difference to the density of the build and that pulse energy has the greatest effect.

Chapter 7

Conclusions and future work

The aim of this work was to investigate the feasibility of using multiple-beam powder-bed fusion additive manufacturing system with metal powders. The multiple beams were provided by high power laser diodes which were fibre-coupled to an optical head. The head was scanned across the build chamber by a gantry mechanism operating in a similar manner to a dot matrix printer but operating on an expose – move – expose basis.

7.1 Conclusions

The following conclusions were drawn from chapters 4, 5 and 6.

7.1.1 Single spot processing

- Using 42 W into a ~150 μm diameter focal spot incident onto a substrate of stainless steel 304, the surface diameter of re-solidified material increases rapidly then levels off at ~160 μm within the range of pulse energies used. The depth of the re-melted material increases less rapidly but does not level off.
- For a given pulse energy the width and depth of the re-melted material were greater when using a higher power.
- The finite difference thermal conduction with phase change model developed within this work was able to match experimental results. It predicted that for a given pulse energy and power a smaller focal spot gives greater depth and smaller diameter of re-solidified material. Conversely, a larger focal spot was predicted to produce less depth and greater diameter of re-solidified material. However, for a 20 % variation in

focal spot size the total variation in depth was ~5 times the variation in diameter of the re-solidified material.

- For a given pulse energy melt balls created in a thin layer of powder on a substrate are larger when using a higher power level. This is due to less energy lost to conduction away from the interaction zone.
- The denudation of powder around exposure sites is independent of power and increases with pulse energy, at first rapidly but then at a decreasing rate with increasing pulse energy.
- For a given pulse energy the volume of melt balls created in deep powder is independent of power due to the low thermal conductivity and high absorptivity of powder.

7.1.2 Manufacture of lines

- The width and height of lines of melt balls increase with powder layer thickness within the experimental interval of 50-250 μm powder depth and 42-420 mJ pulse energies.
- With increasing powder layer thickness the Ra roughness increases and the line sharpness decreases.
- Line sharpness and Ra roughness are best when using a pulse energy of 210 mJ
- For a given pulse energy melt bead height is largely independent of laser power. However, both melt bead height and width grow with increasing pulse energy.
- Increasing laser power improves both the Ra roughness and the sharpness of the melt line
- The depth and width of melt penetration into the substrate both increase with increasing power or pulse energy.
- A spot pitch of 86 μm led to the highest Ra and lowest line sharpness for the three spot pitches used, whereas a spot pitch of 67 μm led to the lowest Ra roughness and highest line sharpness.
- A total time delay between individual exposures within the line building of ~530 ms improves the Ra roughness and line sharpness whilst decreasing the mean height and width of the melt bead.

- In the use of temporal pulse shapes, the square pulse used in all other cases gives the widest lines with the smallest height. However, the use of a ramp up pulse profile improves both the Ra roughness and the line sharpness for all pulse energies against the ramp down profile and for the 84 and 126 mJ pulse energies against the square pulse profile.

7.1.3 Multiple layer building

- The denudation of powder around the initial lines within a rectangular layer leads to uneven layer features.
- A spacing of 200 μm, as against a spacing of 150 μm between parallel melt lines is sufficient to avoid the adverse effects of denudation. For a given pulse energy, the thickness of single layers created in deep powder increases with decreasing grid pitch. The thickness also increases with pulse energy.
- For scanning strategies one and two the consolidation of the layer increases with decreasing grid pitch for energy densities of less than ~15 J/mm^2. Above this value the consolidation is independent of grid pitch. For scanning strategies three, four and five the consolidation is largely independent of grid pitch and lower than that produced by the application of scanning strategies one and two.
- The relative density of single layer builds in deep powder is independent of energy density but increases with grid pitch.
- The maximum density for a ten-layer cuboid was 62.2 % bulk value using 210 mJ pulse energy on a 100 μm grid pitch with a 50 % row offset on alternate layers.
- Minimum layer thickness to avoid fouling the wiper movement increases with pulse energy. The average density across all scanning strategies is 37.7, 58.2, 57.2 and 53 % for pulse energies of 42, 210, 210 and 420 mJ with the last two cases using a row offset on alternate layers. A pulse energy of 210 mJ gives the highest densities.

7.2 Summary

The research questions proposed at the beginning of this thesis are presented again and their solutions are addressed:

1) *How will the poor beam quality of laser diodes affect the PBF process?*

The minimum diameter of the focal spot achievable with a given optical system is affected by beam quality. Fibre lasers typically have very good beam qualities with M^2 values approaching 1 [157], this allows for a smaller focal spot than that achievable with the laser diodes used in this research with an M^2 of 18. The poor beam quality of the laser diodes meant that the minimum focal spot diameter achieved was 150 μm. Beam quality also determines how short a focal length lens is required to achieve the desired spot size. A galvo-scanning PBF system requires that the beam quality is high enough so that the beam can be focussed over hundreds of millimetres, laser diodes could not be used in this case. However for a gantry scanning system the focal length can be short and laser diodes can be used. Thus the effect of the poor beam quality is to reduce the intensity of the beam for a given beam source power.

2) *How much power is required of the laser diodes given the poor beam quality?*

The conclusions illustrate that, whilst a given exposure energy can be achieved by balancing exposure time with exposure power, the effects of an exposure are dependent upon the power of the source. Specifically, the depth of melt penetration into the substrate or the previously consolidated layers of powder is particularly sensitive to the power *per* unit area of the incident radiation. The 40 W available for this research focussed into a 150 μm diameter focal spot was found to be sufficient to create melt balls in a range of layer thicknesses and to produce up to 20 μm penetration of melt pool into the substrate using a 50 μm powder layer. However, this power density is not enough to produce good wetting of the melt balls and sufficient melt penetration into the previous layer for building multiple layer cuboids. With reference to the laser parameters used by other researchers working within the same field (Table 15) an increase of four or five times the power needed to achieve an average focal spot intensity of ~10,000 W/mm^2. This estimate of 150-200 W is based upon a core diameter of 100 μm for the fibres coupling the laser diodes to the optical head and the fact that the poor beam quality will only allow a minimum focal spot equal to the fibre core diameter.

3) *How do multiple beams interact and how does this affect the effectiveness of a multiple beam scanning strategy?*

The pitch of the laser diode beams when in focus was 600 μm and the focal diameter was found to be 150 μm therefore there was no overlapping of focal spots and thus no direct interaction between the individual beams in the particular experimental system used. The extent

of powder denudation in a 100 μm thick powder layer was found to be ~400 μm across a range of pulse energies which it is smaller than the spot spacing and thus no indirect interaction was present for a single multiple beam exposure. However the thermal history of a given point within the build can be adjusted by the choice of scanning strategy; the time between successive passes of a beam at a given point is dependent upon the paths of the beams. Thus an effective scanning strategy will utilise this control of thermal history.

4) *How do scanning strategies applicable to a multiple beam system affect the final part density?*

The scanning strategies developed and used within this research were based upon a pulsed 'expose - move – expose' strategy. This allowed for five scanning strategies to be developed that were used to explore the effects of melt ball placement order. In the context of single layers the scanning strategies that kept the local temperature higher in the area of melting were the ones with greater consolidation. These were the vertically based strategies where each line of melt balls was short and had the next line placed relatively quickly when compared to the horizontally based strategies where the lines were longer. In the context of multiple layer cuboid builds there was no significant correlation between density and scanning strategy. This lack of correlation, despite it being apparent in single layer builds, is due to the high surface roughness of the layers which required large layer thicknesses to allow passage of the wiper. It is thought that the effect of scanning strategy will be more obvious if higher intensity sources were used for the melting therefore allowing thinner power layers and greater overall densities.

7.3 Recommendations

The research objective was defined as:

Develop a multiple beam gantry scanned PBF AM system and establish the advantages, disadvantages and limitations of such a system.

The main advantage of a multiple beam system is the increase in build rate conferred by the use of greater power in a manner that doesn't exceed a given material's maximum useful intensity. This is a great motivation for all multiple beam system research and needs no further recommendation.

A significant disadvantage of the particular system developed for this research was the speed of communication between the sub-components. This had several effects: notably upon the

exposure strategy used and upon the pulse profile given that a static exposure strategy was employed. If faster communication were possible the laser diodes could be used in CW mode. However this would introduce a building constraint to the system if the orientation of the linear array were fixed as it were for this work. To avoid the problems attendant with single direction scanning it is recommended that the array of laser diodes be rotatable or be oriented at 45 degrees to the main axis of scanning so that alternate layers could be scanned at 90 degrees to each other; this would also have the effect of decreasing the pitch of the laser diodes within the array.

The pulse shaping used within this work proved that there is some advantage to using pulse shapes other than square pulses for improving the Ra roughness of the melt lines. However the response of the diode control electronics to a pulse profile produced undesirable artefacts in the outputs of the laser diodes. Further study of the effects of temporal pulse profile with better electronics is recommended.

The scalability of a multiple beam system is attractive but the ease of which this is possible is limited by the optics used. In this particular system the seven beams were focussed by a multi-element optic 35 mm in diameter that maintained a flat field of focus over the 3.6 mm length of the array. To focus an array that is tens or even hundreds of millimetres long will require optics that may limit the maximum packing density of the array.

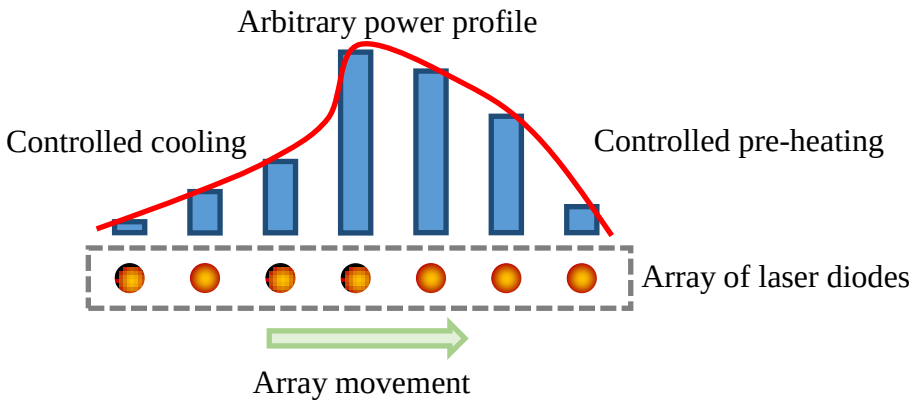

Figure 109 Serial processing with a multi-diode array to allow a thermal profile to be applied to the melted material.

The suggested increase in optical power in the previous section was based upon work that was conducted using a powder bed at room temperature. If the powder bed could be pre-heated by de-focussed beams, infra-red heaters, induction coils then the energy required to melt the material would be less. Therefore low powers could be used more effectively whilst simultaneously decreasing the thermal gradients and thus reducing residual stresses. A potentially useful pre-heating method could be implemented by using a linear array of laser diodes aligned to the direction of scanning with a power profile set across the array to exercise control of the pre-heating and post-cooling during processing Figure 109.

References

[1] T. Wohlers and T. Gornet, “The history of additive manufacturing.” Wohlers Associates, 2013.

[2] C. W. Hull, “Method for production of three-dimensional objects by stereolithography,” 4,929,402, Mar-1986.

[3] A. Gebhardt, *Rapid Prototyping*. Hanser Publishers, 2003.

[4] D. Zhang, Q. Cai, and J. Liu, “Formation of Nanocrystalline Tungsten by Selective Laser Melting of Tungsten Powder,” *Mater. Manuf. Process.*, vol. 27, no. 12, pp. 1267–1270, Dec. 2012.

[5] R. Wauthle *et al.*, “Additively manufactured porous tantalum implants,” *Acta Biomater.*, vol. 14, pp. 217–225, Mar. 2015.

[6] T. Wohlers, “Wohlers Report 2013: Additive Manufacturing and 3D Printing State of the Industry Annual Worldwide Progress Report.” Wohlers Associates, 2013.

[7] “3-Axis and high power scanning.” Cambridge Technology, 2016.

[8] “Xline 2000r datasheet.” Concept Laser, 2016.

[9] “Tips for 3D Printing with Plastic: Part 1 - Sculpteo Blog,” *3D Printing Blog: Tutorials, News, Trends and Resources | Sculpteo*. [Online]. Available: https://www.sculpteo.com/blog/2014/05/13/right-plastic-production-method/. [Accessed: 16-Nov-2017].

[10] “ISO/ASTM52900-15 Standard Terminology for Additive Manufacturing - General Principals - Terminology,” ASTM International West Conshohocken, PA, 2015.

[11] T. Mueller, “Comparing Cost and Quality of a Complex Pump Impeller Casting Made from Wax and QuickCast Patterns.” 3D Systems, 2013.

[12] C. G. Sandström, “The non-disruptive emergence of an ecosystem for 3D Printing — Insights from the hearing aid industry’s transition 1989–2008,” *Technol. Forecast. Soc. Change*, vol. 102, pp. 160–168, Jan. 2016.

[13] “Standard Terminology for Additive Manufacturing Technologies,” *ASTM Stand. F2792*, 2009.

[14] A. P. West, S. P. Sambu, and D. W. Rosen, “A process planning method for improving build performance in stereolithography,” *Comput.-Aided Des.*, vol. 33, no. 1, pp. 65–79, Jan. 2001.

[15] “SLA Production Series PDF.” 3D Systems Corporation, 2013.

[16] “Perfactory 4 Digital Shell Printer Series Data Sheet.” EnvisionTec GmbH.

[17] “Rapid Prototyping - Stereolithography (SLA).” [Online]. Available: http://www.custompartnet.com/wu/stereolithography. [Accessed: 16-Nov-2017].

[18] Rapid Shape, “S 30 technical specification,” Aug-2014. [Online]. Available: http://www.rapidshape.de/s30.html.

[19] A. Ambrosio *et al.*, “Two-photon patterning of a polymer containing Y-shaped azochromophores,” *Appl. Phys. Lett.*, vol. 94, no. 1, p. 011115, Jan. 2009.

[20] “SLA material selection guide.” 3D Systems, Aug-2013.

[21] A. Gebhardt, *Understanding Additive Manufacturing: Rapid Prototyping, Rapid Tooling, Rapid Manufacturing*. Hanser Gardner Publications, 2012.

[22] “Carbon: Process.” [Online]. Available: http://carbon3d.com/clip-process. [Accessed: 28-Sep-2016].

[23] R. Noorani, *Rapid Prototyping: Principles and Applications*. Wiley, 2006.

[24] “voxeljet VX500 datasheet.” 3D Systems, Jun-2012.

[25] “projet-4500 datasheet.” 3D Systems, 2014.

[26] “Rapid Prototyping - Three Dimensional Printing.” [Online]. Available: http://www.custompartnet.com/wu/3d-printing. [Accessed: 16-Nov-2017].
[27] “SMaxFuran datasheet.” ExOne, 23-Jan-2014.
[28] “Objet500 Connex3 datasheet.” Stratasys, 2014.
[29] “Max2 Datasheet 2016.pdf.” Solidscape, 2016.
[30] “Colour jet printers spec sheet.” 3D Systems, Apr-2016.
[31] “Inkjet Printing Process.” [Online]. Available: http://www.custompartnet.com/wu/ink-jet-printing. [Accessed: 16-Nov-2017].
[32] W. M. Johnson, M. Rowell, B. Deason, and M. Eubanks, “Comparative evaluation of an open-source FDM system,” *Rapid Prototyp. J.*, vol. 20, no. 3, pp. 205–214, Apr. 2014.
[33] “invent one| desktop 3d printer| italiana.” [Online]. Available: http://www.makerdreams.net/#!inventone-stampante-3dprinter/ceon. [Accessed: 22-Aug-2014].
[34] “Simple Maker’s Kit | Printrbot.” [Online]. Available: http://printrbot.com/shop/simple-makers-kit/. [Accessed: 22-Aug-2014].
[35] “3DP-Workbench-Datasheet-v2.pdf.” 3DPlatform, 2016.
[36] “Q3 3D Printers - Quality | Reliability | Speed | Always Open Source.” [Online]. Available: http://q3dprinter.com/. [Accessed: 28-Sep-2016].
[37] “Dimension 1200 datasheet.” Stratasys, May-2016.
[38] “Fused Deposition Modeling (FDM).” [Online]. Available: http://www.custompartnet.com/wu/fused-deposition-modeling. [Accessed: 16-Nov-2017].
[39] J. Park, M. J. Tari, and H. T. Hahn, “Characterization of the laminated object manufacturing (LOM) process,” *Rapid Prototyp. J.*, vol. 6, no. 1, pp. 36–50, 2000.
[40] “How paper based 3D printing works.” MCOR, 2013.
[41] “helysys_lom_1015.pdf,” *ned-manufacturing.com*. [Online]. Available: http://www.ned-manufacturing.com/doc/helysys_lom_1015.pdf.
[42] “Fabrisonic : Solid State Additive Manufacturer of Metals.” [Online]. Available: http://www.fabrisonic.com/. [Accessed: 26-May-2014].
[43] “Applications: Dissimilar metals,” 2014. [Online]. Available: http://www.fabrisonic.com/dissimilar_metals.html.
[44] “MCOR-PrinterBrochure.” Mcor, 2014.
[45] “Laminated Object Manufacturing (LOM).” [Online]. Available: http://www.custompartnet.com/wu/laminated-object-manufacturing. [Accessed: 16-Nov-2017].
[46] T. Shinbara, “Additive Manufacturing: enabling advanced manufacturing.” AMT, Apr-2013.
[47] “Sciaky-EBAM-Technology.pdf.” Sciaky, Dec-2015.
[48] “LENS_MR-7_Datasheet.” Optomec, Jan-2016.
[49] “The EFESTO 557 Is an Enormous Metal Printing Phenomenon,” *3D Printer World*, 20-Jun-2014. [Online]. Available: http://www.3dprinterworld.com/article/efesto-557-enormous-metal-printing-phenomenon. [Accessed: 16-Nov-2017].
[50] C. Atwood *et al.*, “Laser engineered net shaping (LENS): a tool for direct fabrication of metal parts,” presented at the Proceedings of ICALEO, 1998, vol. 98, pp. 16–19.
[51] J. M. Amado, M. J. Tobar, J. C. Alvarez, J. Lamas, and A. Yáñez, “Laser cladding of tungsten carbides (Spherotene®) hardfacing alloys for the mining and mineral industry,” *Appl. Surf. Sci.*, vol. 255, no. 10, pp. 5553–5556, Mar. 2009.
[52] A. J. Pinkerton, W. Wang, and L. Li, “Component repair using laser direct metal deposition,” *Proc. Inst. Mech. Eng. Part B J. Eng. Manuf.*, vol. 222, no. 7, pp. 827–836, Jul. 2008.

[53] C. Hauser, T. H. C. Childs, and K. W. Dalgarno, “Selective laser sintering of stainless steel 314S HC processed using room temperature powder beds,” in *Proceedings of the SFF Symposium 1999*, 1999, pp. 273–280.
[54] A. Franco and L. Romoli, “Characterization of laser energy consumption in sintering of polymer based powders,” *J. Mater. Process. Technol.*, vol. 212, no. 4, pp. 917–926, Apr. 2012.
[55] M. Huang *et al.*, “Comparison study of fabrication of ceramic rotor using various manufacturing methods,” *Ceram. Int.*, vol. 40, no. 8, Part A, pp. 12493–12502, Sep. 2014.
[56] A. Simchi and H. Pohl, “Effects of laser sintering processing parameters on the microstructure and densification of iron powder,” *Mater. Sci. Eng. A*, vol. 359, no. 1–2, pp. 119–128, Oct. 2003.
[57] “DMLS - Direct Metal Laser Sintering.” [Online]. Available: http://www.custompartnet.com/wu/direct-metal-laser-sintering. [Accessed: 16-Nov-2017].
[58] M. M. A. Dewidar, “Direct and indirect laser sintering of metals,” PhD Thesis, University of Leeds, 2002.
[59] “Additive manufacturing with EBM.” Arcam, 10-Apr-2012.
[60] S. Rengers, “EBM vs DMLS.” Nov-2012.
[61] “Renishaw_RenAM_500Q_Datasheet.” Renishaw, 2017.
[62] “EOS M400-4 Datasheet.” EOS, Aug-2016.
[63] T. Wohlers, “Wohlers Report 2013: Additive Manufacturing and 3D Printing State of the Industry Annual Worldwide Progress Report.” Wohlers Associates, 2013.
[64] “Additive Fabrication (Rapid prototyping, tooling).” [Online]. Available: http://www.custompartnet.com/wu/additive-fabrication. [Accessed: 22-Feb-2018].
[65] J. W. Lee, I. H. Lee, and D.-W. Cho, “Development of micro-stereolithography technology using metal powder,” *Microelectron. Eng.*, vol. 83, no. 4–9, pp. 1253–1256, Apr. 2006.
[66] C. Ladd, J.-H. So, J. Muth, and M. D. Dickey, “3D Printing of Free Standing Liquid Metal Microstructures,” *Adv. Mater.*, vol. 25, no. 36, pp. 5081–5085, Sep. 2013.
[67] N. Lass, L. Riegger, R. Zengerle, and P. Koltay, “Enhanced Liquid Metal Micro Droplet Generation by Pneumatic Actuation Based on the StarJet Method,” *Micromachines*, vol. 4, no. 1, pp. 49–66, Mar. 2013.
[68] S. X. Cheng, T. Li, and S. Chandra, “Producing molten metal droplets with a pneumatic droplet-on-demand generator,” *J. Mater. Process. Technol.*, vol. 159, no. 3, pp. 295–302, Feb. 2005.
[69] M. Orme and R. F. Smith, “Enhanced Aluminum Properties by Means of Precise Droplet Deposition,” *J. Manuf. Sci. Eng.*, vol. 122, no. 3, pp. 484–493, Sep. 1999.
[70] I. Yadroitsev and I. Smurov, “Selective laser melting technology: From the single laser melted track stability to 3D parts of complex shape,” *Phys. Procedia*, vol. 5, Part B, pp. 551–560, 2010.
[71] R. Li, J. Liu, Y. Shi, L. Wang, and W. Jiang, “Balling behavior of stainless steel and nickel powder during selective laser melting process,” *Int. J. Adv. Manuf. Technol.*, vol. 59, no. 9–12, pp. 1025–1035, 2012.
[72] J.-P. Kruth, G. Levy, F. Klocke, and T. H. C. Childs, “Consolidation phenomena in laser and powder-bed based layered manufacturing,” *CIRP Ann. - Manuf. Technol.*, vol. 56, no. 2, pp. 730–759, 2007.
[73] J.-P. Kruth, P. Mercelis, J. V. Vaerenbergh, L. Froyen, and M. Rombouts, “Binding mechanisms in selective laser sintering and selective laser melting,” *Rapid Prototyp. J.*, vol. 11, no. 1, pp. 26–36, 2005.

[74] N. K. Tolochko, S. E. Mozzharov, I. A. Yadroitsev, T. Laoui, and et al, “Balling processes during selective laser treatment of powders,” *Rapid Prototyp. J.*, vol. 10, no. 2, pp. 78–87, 2004.
[75] W. Wu, Y. Yang, and Y. Huang, “Direct manufacturing of Cu-based alloy parts by selective laser melting,” *Chin. Opt. Lett.*, vol. 5, no. 1, pp. 37–40, 2007.
[76] M. Rombouts, J. P. Kruth, L. Froyen, and P. Mercelis, “Fundamentals of Selective Laser Melting of alloyed steel powders,” *CIRP Ann. - Manuf. Technol.*, vol. 55, no. 1, pp. 187–192, 2006.
[77] J. P. Kruth, L. Froyen, J. Van Vaerenbergh, P. Mercelis, M. Rombouts, and B. Lauwers, “Selective laser melting of iron-based powder,” *J. Mater. Process. Technol.*, vol. 149, no. 1–3, pp. 616–622, Jun. 2004.
[78] R. H. Morgan, A. J. Papworth, C. Sutcliffe, P. Fox, and W. O’neill, “High density net shape components by direct laser re-melting of single-phase powders,” *J. Mater. Sci.*, vol. 37, no. 15, pp. 3093–3100, Aug. 2002.
[79] B. Xiao and Y. Zhang, “Marangoni and Buoyancy effects on direct metal laser sintering with a moving laser beam,” *Numer. Heat Transf. Part Appl.*, vol. 51, no. 8, pp. 715–733, 2007.
[80] “Marangoni effects in welding,” *Philos. Trans. R. Soc. Lond. Ser. Math. Phys. Eng. Sci.*, vol. 356, no. 1739, pp. 911–925, Apr. 1998.
[81] H. J. Niu and I. T. H. Chang, “Instability of scan tracks of selective laser sintering of high speed steel powder,” *Scr. Mater.*, vol. 41, no. 11, pp. 1229–1234, Nov. 1999.
[82] S. J. Rock and W. Z. Misiolek, “Distortion control for P/M-based rapid prototyping of advanced material components,” *Adv. Powder Metall. Part. Mater.*, vol. 2, p. 7, 1996.
[83] J. P. Kruth, L. Froyen, J. Van Vaerenbergh, P. Mercelis, M. Rombouts, and B. Lauwers, “Selective laser melting of iron-based powder,” *J. Mater. Process. Technol.*, vol. 149, no. 1–3, pp. 616–622, Jun. 2004.
[84] S. P. Soe, “Quantitative analysis on SLS part curling using EOS P700 machine,” *J. Mater. Process. Technol.*, vol. 212, no. 11, pp. 2433–2442, Nov. 2012.
[85] M. Shiomi, K. Osakada, K. Nakamura, T. Yamashita, and F. Abe, “Residual Stress within Metallic Model Made by Selective Laser Melting Process,” *CIRP Ann. - Manuf. Technol.*, vol. 53, no. 1, pp. 195–198, 2004.
[86] M. Fateri, J.-S. Hötter, and A. Gebhardt, “Experimental and Theoretical Investigation of Buckling Deformation of Fabricated Objects by Selective Laser Melting,” *Phys. Procedia*, vol. 39, pp. 464–470, 2012.
[87] K. Osakada and M. Shiomi, “Flexible manufacturing of metallic products by selective laser melting of powder,” *Int. J. Mach. Tools Manuf.*, vol. 46, no. 11, pp. 1188–1193, Sep. 2006.
[88] D. Manfredi, F. Calignano, M. Krishnan, R. Canali, E. Ambrosio, and E. Atzeni, “From Powders to Dense Metal Parts: Characterization of a Commercial AlSiMg Alloy Processed through Direct Metal Laser Sintering,” *Materials*, vol. 6, no. 3, pp. 856–869, Mar. 2013.
[89] S. Das, “Physical Aspects of Process Control in Selective Laser Sintering of Metals,” *Adv. Eng. Mater.*, vol. 5, no. 10, pp. 701–711, Oct. 2003.
[90] P. Gu, X. Zhang, Y. Zeng, and B. Ferguson, “Quality analysis and optimization of Solid Ground Curing process,” *J. Manuf. Syst.*, vol. 20, no. 4, pp. 250–263, 2001.
[91] “LCOS SLM Applications and features.” Hamamatsu, 2017.
[92] John F. Ready, D.F. Farson, and T. Feeley, Eds., *LIA Handbook of Laser Materials Processing*. Springer-Verlag Berlin Heidelberg New York, 2001.

[93] F. Calignano, D. Manfredi, E. P. Ambrosio, L. Iuliano, and P. Fino, “Influence of process parameters on surface roughness of aluminum parts produced by DMLS,” *Int. J. Adv. Manuf. Technol.*, vol. 67, no. 9–12, pp. 2743–2751, Aug. 2013.
[94] Q. Bo, S. Yu-sheng, W. Qing-song, and W. Hai-bo, “The helix scan strategy applied to the selective laser melting,” *Int. J. Adv. Manuf. Technol.*, vol. 63, no. 5–8, pp. 631–640, Nov. 2012.
[95] L. N. Carter, M. M. Attallah, and R. C. Reed, “Laser Powder Bed Fabrication of Nickel-Base Superalloys: Influence of Parameters; Characterisation, Quantification and Mitigation of Cracking,” in *Superalloys 2012*, E. S. Huron, R. C. Reed, rk C. Hardy, M. J. Mills, R. E. Montero, P. D. Portella, and J. Telesman, Eds. John Wiley & Sons, Inc., 2012, pp. 577–586.
[96] Q. Jia and D. Gu, “Selective laser melting additive manufacturing of Inconel 718 superalloy parts: Densification, microstructure and properties,” *J. Alloys Compd.*, vol. 585, pp. 713–721, Feb. 2014.
[97] I. Yadroitsev, L. Thivillon, P. Bertrand, and I. Smurov, “Strategy of manufacturing components with designed internal structure by selective laser melting of metallic powder,” *Appl. Surf. Sci.*, vol. 254, no. 4, pp. 980–983, Dec. 2007.
[98] D. Gu and Y. Shen, “Effects of processing parameters on consolidation and microstructure of W–Cu components by DMLS,” *J. Alloys Compd.*, vol. 473, no. 1–2, pp. 107–115, Apr. 2009.
[99] I. Yadroitsev, P. Bertrand, and I. Smurov, “Parametric analysis of the selective laser melting process,” *Appl. Surf. Sci.*, vol. 253, no. 19, pp. 8064–8069, Jul. 2007.
[100] H. J. Niu and I. T. H. Chang, “Liquid phase sintering of M3/2 high speed steel by selective laser sintering,” *Scr. Mater.*, vol. 39, no. 1, pp. 67–72, Jun. 1998.
[101] K. Maeda and T. H. C. Childs, “Laser sintering (SLS) of hard metal powders for abrasion resistant coatings,” *J. Mater. Process. Technol.*, vol. 149, no. 1–3, pp. 609–615, Jun. 2004.
[102] J. P. Kruth, L. Froyen, M. Rombouts, J. Van Vaerenbergh, and P. Mercells, “New Ferro Powder for Selective Laser Sintering of Dense Parts,” *CIRP Ann. - Manuf. Technol.*, vol. 52, no. 1, pp. 139–142, 2003.
[103] L. Thijs, F. Verhaeghe, T. Craeghs, J. V. Humbeeck, and J.-P. Kruth, “A study of the microstructural evolution during selective laser melting of Ti–6Al–4V,” *Acta Mater.*, vol. 58, no. 9, pp. 3303–3312, May 2010.
[104] B. Vandenbroucke and J.-P. Kruth, “Selective laser melting of biocompatible metals for rapid manufacturing of medical parts,” *Rapid Prototyp. J.*, vol. 13, no. 4, p. 196, 2007.
[105] E. Yasa, J. Deckers, T. Craeghs, M. Badrossamay, and J.-P. Kruth, “Investigation on occurrence of elevated edges in selective laser melting,” in *International Solid Freeform Fabrication Symposium, Austin, TX, USA*, 2009, pp. 673–85.
[106] J.-P. Kruth, M. Badrossamay, E. Yasa, J. Deckers, L. Thijs, and J. Van Humbeeck, “Part and material properties in selective laser melting of metals,” in *Proceedings of the 16th International Symposium on Electromachining*, Shanghai, 2010.
[107] K. Dai and L. Shaw, “Distortion minimization of laser-processed components through control of laser scanning patterns,” *Rapid Prototyp. J.*, vol. 8, no. 5, pp. 270–276, 2002.
[108] A. H. Nickel, D. M. Barnett, and F. B. Prinz, “Thermal stresses and deposition patterns in layered manufacturing,” *Mater. Sci. Eng. A*, vol. 317, no. 1–2, pp. 59–64, Oct. 2001.
[109] S. Dadbakhsh, L. Hao, and N. Sewell, “Effect of selective laser melting layout on the quality of stainless steel parts,” *Rapid Prototyp. J.*, vol. 18, no. 3, pp. 241–249, 2012.

[110] F. C. Herzog, “Production of sintered workpieces involves heating individual areas of material irradiation so that they fuse together, where individual areas are separated by distance at least their diameter,” DE10042134 (A1), 28-Mar-2002.
[111] K. Abd-Elghany and D. L. Bourell, “Property evaluation of 304L stainless steel fabricated by selective laser melting,” *Rapid Prototyp. J.*, vol. 18, no. 5, pp. 420–428, 2012.
[112] L. N. Carter, C. Martin, P. J. Withers, and M. M. Attallah, “The influence of the laser scan strategy on grain structure and cracking behaviour in SLM powder-bed fabricated nickel superalloy,” *J. Alloys Compd.*, vol. 615, pp. 338–347, Dec. 2014.
[113] “SLM 500 Datasheet.” SLM Solutions, Mar-2015.
[114] “Arcam-A2 datasheet.” Arcam.
[115] “Arcam-A2 datasheet.” Arcam.
[116] Y. Marutani and T. Kamitani, “Stereolithography system using multiple spot exposure,” in *Proc. Solid Freeform Fabrication Symposium*, 1996, pp. 321–326.
[117] M. Arai, T. Niino, and T. Nakagawa, “Optical Formation Device and Method,” EP0958912 (A1), 24-Nov-1999.
[118] K. Loose, T. Niino, and T. Nakagawa, “Effective Mechanisms of Multiple LED Photographic Curing,” 1998.
[119] K. Loose Toshiki Niino and T. Nakagawa, “Multiple LED photographic curing of models for design verification,” *Rapid Prototyp. J.*, vol. 5, no. 1, pp. 6–11, 1999.
[120] “Lunavast XG2 - RepRapWiki.” [Online]. Available: http://reprap.org/wiki/Lunavast_XG2. [Accessed: 15-Mar-2017].
[121] “Arcam EBM brochure.” Arcam, 2017.
[122] “the_power_of_additive_manufacturing.pdf.” Renishaw, 2015.
[123] “DILAS: The diode laser company - Single Emitters for Cinema Projection and Medical Applications.” [Online]. Available: http://www.dilas.com/pages/products.php?category=9&series=66. [Accessed: 21-Aug-2015].
[124] “Jenoptik.” [Online]. Available: http://www.jenoptik.com/en-semiconductor-laser-construction. [Accessed: 21-Aug-2015].
[125] D. Bergström, “The absorption of laser light by rough metal surfaces,” Division of Manufacturing Systems Engineering, Department of Applied Physics and Machanical Engineering, Lule\aa University of Technology, 2008.
[126] M. Zavala-Arredondo *et al.*, “Laser diode area melting for high speed additive manufacturing of metallic components,” *Mater. Des.*, vol. 117, pp. 305–315, Mar. 2017.
[127] L. Griffiths, “Fraunhofer Institute for Laser Technology to present SLM concept at EuroMold,” *TCT Magazine*, 18-Nov-2014. [Online]. Available: http://www.tctmagazine.com/api/content/295dda46-6f17-11e4-abaf-22000a4f82a6/. [Accessed: 28-Jul-2017].
[128] R. Rumpf, “Lecture 19 -- Interfacing MATLAB with CAD.pdf.” University of Texas at El Paso, 2016.
[129] D. Wang, Y. Yang, R. Liu, D. Xiao, and J. Sun, “Study on the designing rules and processability of porous structure based on selective laser melting (SLM),” *J. Mater. Process. Technol.*, vol. 213, no. 10, pp. 1734–1742, Oct. 2013.
[130] “EOS - e-Manufacturing Solutions.” [Online]. Available: http://www.eos.info/en. [Accessed: 27-May-2014].
[131] “974 nm PLD 60 series datasheet.” IPG Photonics.
[132] Y. Niu, Y. Wang, X. Liu, C. Zhang, and S. Zhu, “Laser beam quality factor M2 and its measurement,” 1998, vol. 3550, pp. 378–382.

[133] T. F. Johnston, “Beam propagation (M 2) measurement made as easy as it gets: the four-cuts method,” *Appl. Opt.*, vol. 37, no. 21, pp. 4840–4850, 1998.
[134] A. E. Siegman, “New developments in laser resonators,” in *OE/LASE’90, 14-19 Jan., Los Angeles, CA*, 1990, pp. 2–14.
[135] B. T. Kelley and V. K. Madisetti, “The fast discrete Radon transform. I. Theory,” *IEEE Trans. Image Process.*, vol. 2, no. 3, pp. 382–400, Jul. 1993.
[136] B. Steen and J. Mazumder, *Laser Materials Processing*, 4th ed. Springer-Verlag London, 2010.
[137] J. C. Ion, “Chapter 5 - Engineering Materials,” in *Laser Processing of Engineering Materials*, J. C. Ion, Ed. Oxford: Butterworth-Heinemann, 2005, pp. 139–177.
[138] P. W. Fuerschbach and G. R. Eisler, “Effect of laser spot weld energy and duration on melting and absorption,” *Sci. Technol. Weld. Join.*, vol. 7, no. 4, pp. 241–246, 2002.
[139] H. S. Carslaw and J. C. Jaeger, *Conduction of heat in solids*, 2nd ed. Oxford: Clarendon Press, 1959.
[140] C. T. Lynch, *CRC Handbook of Materials Science, Volume II: Material Composites and Refractory Materials*. CRC Press, 1975.
[141] R. Prapainop and K. Maneeratana, “Simulation of ice formation by the finite volume method,” *Simulation*, vol. 26, no. 1, p. 56, 2004.
[142] I. Yadroitsev and I. Smurov, “Selective laser melting technology: From the single laser melted track stability to 3D parts of complex shape,” *Phys. Procedia*, vol. 5, Part B, pp. 551–560, 2010.
[143] M. J. Matthews, G. Guss, S. A. Khairallah, A. M. Rubenchik, P. J. Depond, and W. E. King, “Denudation of metal powder layers in laser powder bed fusion processes,” *Acta Mater.*, vol. 114, pp. 33–42, Aug. 2016.
[144] M. Simonelli *et al.*, “A Study on the Laser Spatter and the Oxidation Reactions During Selective Laser Melting of 316L Stainless Steel, Al-Si10-Mg, and Ti-6Al-4V,” *Metall. Mater. Trans. A*, vol. 46, no. 9, pp. 3842–3851, Sep. 2015.
[145] A. Streek, P. Regenfuss, and H. Exner, “Fundamentals of Energy Conversion and Dissipation in Powder Layers during Laser Micro Sintering,” *Phys. Procedia*, vol. 41, pp. 858–869, 2013.
[146] J. H. Liu, W. J. Xie, S. B. Xiao, W. L. Zhao, and J. Zhang, “On Formation and Estimation of Pores during Selective Laser Melting of Single-Phase Metal Powders,” *Adv. Mater. Res.*, vol. 338, pp. 94–101, 2011.
[147] A. V. Gusarov, I. Yadroitsev, P. Bertrand, and I. Smurov, “Heat transfer modelling and stability analysis of selective laser melting,” *Appl. Surf. Sci.*, vol. 254, no. 4, pp. 975–979, Dec. 2007.
[148] M. Rombouts, L. Froyen, A. V. Gusarov, E. H. Bentefour, and C. Glorieux, “Photopyroelectric measurement of thermal conductivity of metallic powders,” *J. Appl. Phys.*, vol. 97, no. 2, p. 024905, Jan. 2005.
[149] D. Swift-Hook and A. Gick, “Penetration welding with lasers,” *Weld. J.*, vol. 52, no. 11, p. 492s–499s, 1973.
[150] I. Yadroitsev, I. Yadroitsava, P. Bertrand, and I. Smurov, “Factor analysis of selective laser melting process parameters and geometrical characteristics of synthesized single tracks,” *Rapid Prototyp. J.*, vol. 18, no. 3, pp. 201–208, 2012.
[151] I. Yadroitsev, A. Gusarov, I. Yadroitsava, and I. Smurov, “Single track formation in selective laser melting of metal powders,” *J. Mater. Process. Technol.*, vol. 210, no. 12, pp. 1624–1631, Sep. 2010.
[152] I. Yadroitsev, A. Gusarov, I. Yadroitsava, and I. Smurov, “Single track formation in selective laser melting of metal powders,” *J. Mater. Process. Technol.*, vol. 210, no. 12, pp. 1624–1631, Sep. 2010.

[153] E. O. Olakanmi, “Selective laser sintering/melting (SLS/SLM) of pure Al, Al–Mg, and Al–Si powders: Effect of processing conditions and powder properties,” *J. Mater. Process. Technol.*, vol. 213, no. 8, pp. 1387–1405, Aug. 2013.
[154] K. Mumtaz and N. Hopkinson, “Selective laser melting of Inconel 625 using pulse shaping,” *Rapid Prototyp. J.*, vol. 16, no. 4, pp. 248–257, 2010.
[155] T. H. C. Childs, C. Hauser, and M. Badrossamay, “Selective laser sintering (melting) of stainless and tool steel powders: Experiments and modelling,” *Proc. Inst. Mech. Eng. Part B J. Eng. Manuf.*, vol. 219, no. 4, pp. 339–357, Apr. 2005.
[156] I. Yadroitsev, L. Thivillon, P. Bertrand, and I. Smurov, “Strategy of manufacturing components with designed internal structure by selective laser melting of metallic powder,” *Appl. Surf. Sci.*, vol. 254, no. 4, pp. 980–983, Dec. 2007.
[157] “TruFiber datasheet.” Trumpf, 2017.
[158] V. Bobkov, L. Fokin, E. Petrov, V. Popov, V. Rumiantsev, and A. Savvatimsky, “Thermophysical Properties of Materials for Nuclear Engineering: A Tutorial and Collection of Data,” *IAEA Vienna*, 2008.
[159] “Properties: Stainless Steel - Grade 304 (UNS S30400),” *AZoM.com*. [Online]. Available: http://www.azom.com/properties.aspx?ArticleID=965. [Accessed: 06-Oct-2016].
[160] C. Kittel, *Introduction to solid state physics*, 5th ed. John Wiley & Sons, 1976.
[161] A. Goldsmith, *Handbook of thermophysical properties of solid materials*, vol. 2. Macmillan, 1961.
[162] G. R. Stewart, “Measurement of low-temperature specific heat,” *Rev. Sci. Instrum.*, vol. 54, no. 1, pp. 1–11, Jan. 1983.

Appendix A

Build instruction file processing

A.1 Build instruction file format

The file format used for the build instructions is a text file employing comma-separated variables and carriage returns to indicate end of line. Each line is 16 entries long and corresponds to one command. The first two lines of the file are reserved for system use and do not contain build commands. The first line of the file is a special file header line that contains signature values that are looked for by the G code file reader program running on the PC. The second line of the build file contains version and configuration data so that the behaviour of the G code file reader program can be altered. All subsequent lines are individual build commands.

Table 17 File format for the build instructions. Two example instruction lines are shown in red.

Position			Laser diodes							Exposure			Re-layer		
X	Y	Z	1	2	3	4	5	6	7	Time	Power	Wave	Yes	Down	Up
10	20	8	1	1	1	1	0	1	1	614	4095	100	0	0	0
0	0	0	0	0	0	0	0	0	0	0	0	0	1	4	6
1	2	3	4	5	6	7	8	9	10	11	12	13	14	15	16
Element number															

With reference to the two example lines shown in Table 17 the first is an exposure command and the second is a re-layer command. The exposure will take place at coordinates

X=10, Y=20, Z=8, using all seven laser diodes except number five, and using the given time, power and waveform exposure parameters. The re-layering involves dropping the build piston down by four steps (1 step = 25 μm) and lifting the supply piston by six steps.

A.2 Instruction file processing

The software that reads the build instruction files was written in G code and was run on proprietary Aerotech software running on the lab PC. After opening a build instruction file the build file reader program checks the validity of the proposed build file. The first line is read and checked for length and signature contents. If neither matches the expected values then the program ends here and displays an appropriate error message. The second line contains configuration bits for the build file reader program and is also not transmitted to the microcontroller. The first configuration bit defines how many configuration bits there are so that the system can be flexibly expanded if necessary. The second and only other used configuration bit, so far, is a version bit that must match the reader program version. This is to ensure that an old file with different order of contents is not used by a newer program or *vice versa*. After this the lines of build commands are then read and processed sequentially until the end of the file is reached

In parsing the build commands the program checks element 14 (the re-layer element) for each line and according to this element branches to either an exposure mode or a re-layer.

- An exposure entails sending the required exposure time, exposure power, and the pulse shape number to the microcontroller, moving the Aerotech stages to the required position then setting the required laser diode bits and sending the ‘fire’ signal that initiates the exposure.
- A re-layer entails sending the required number of piston up/down steps to the microcontroller then sending the re-layer signal and waiting for acknowledgment from the microcontroller that the re-layering has finished. Elements 1 to 13 are ignored when re-layering.

A.3 Transmission of data to microcontroller

The microcontroller used was a 16-bit dsPIC30F6010, manufactured by Microchip Inc. It was clocked at 8 MHz and had pulse width modulation (PWM) motor control and analogue to digital conversion capability. The purpose of the microcontroller was to handle

the sub-millisecond timing of the laser diode exposures and to provide the control logic for the system.

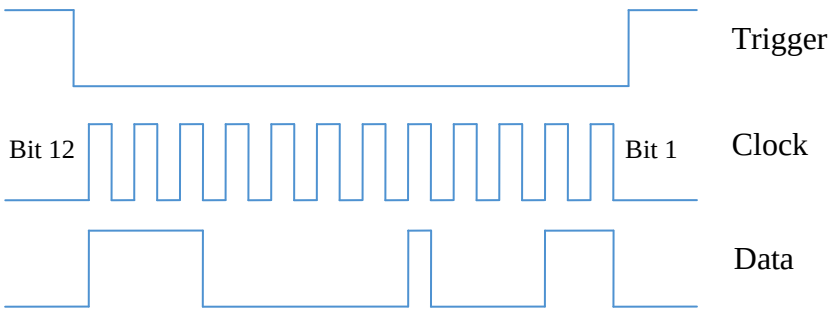

Figure 110 Communication signals for transferring data between software platforms. Communication is initiated by the trigger changing state from high to low and the clock signal is used to synchronise the data transfer. Words are 12 bits long and the most significant bit is transferred first. In this example the number transmitted is 2048+1024+512+16+2+1=3603.

Various data had to be sent between the G code program running on the lab PC and the firmware running on the Microcontroller. The majority of this traffic was from the PC to the microcontroller but one signal was sent back, which was the 'Re-layering finished' signal the G code needed before moving on to the first exposure command in the new layer. All communication was digital and achieved by setting a voltage on a dedicated line, either high or low. Eleven lines were used in all, one for the 'Re-layering finished' signal from the microcontroller to the PC and ten the other way. Of the ten lines, seven were used for the individual states of the laser diodes or communication data, one was used to initiate exposure, one initiated re-layering and one initiated a more complex mode of communication used to transfer numbers such as exposure time and exposure power rather than just states. In order to transfer numbers a communication protocol based upon Microchip's Serial Peripheral Interface (SPI) was implemented. This protocol uses three lines to transfer a single number: trigger, clock, and data. The trigger is used to initiate the transmission by changing state from high to low; the clock is started after the trigger is set and is used to time the data transfer; and the data is sent synchronous to the clock. The word length was chosen to be 12 bits with the most significant bit being sent first. In the example shown in Figure 110 the number 3603 (2048+1024+512+16+2+1) is being sent. Using this protocol and adding one more line *per* extra data stream, several data streams can be sent simultaneously using the same trigger and clock. In the current implementation five numbers - the exposure time, exposure power,

exposure waveform, piston steps up, and piston steps down - are sent simultaneously by the use of seven data lines. The data lines used were the same as those which communicated the desired laser diode on/off states.

Appendix B

Temperature dependent properties of 316L

B.1 Thermal conductivity:

Thermal conductivity is a measure of how well heat energy can be transported through a material and is defined as:

$$\lambda = -k\frac{dT}{dz} \tag{B.1}$$

where λ is the heat flux, k is the thermal conductivity, T is temperature and z is the direction of the energy flow. Phonons and free electrons are both the vehicles for conductivity in metals and each has a conductivity associated with them, the sum of which is the material conductivity.

$$k = k_l + k_e \tag{B.2}$$

The thermal conductivity data for Figure 111 are taken from 'Thermophysical properties of materials for nuclear engineering'[158]. The best fit line applied to the 304 data is a polynomial of degree two fitted between 293 and 1473 K by least squares method yielding

$$k = 4.63 \times 10^{-6} \times T^2 + 0.0022 \times T + 15.7 \qquad 250 \leq T \leq 1473$$

Whereas the 316 data is generated from the given relationship

$$k = 0.01571 \times T + 9.248 \qquad 250 \leq T \leq 1703$$

Above 1473 K the conductivity is not given for 304 but the extrapolated trend to melting point (1673-1723 K [159]) does not seem unreasonable when compared with the 316 data so this extrapolated data will be used within the finite difference model for temperatures

above 1473 K. The observed trend of thermal conductivity rising with temperature is because as the temperature of a material increases the average particle velocity increases and consequently the energy transferred between collisions also increases.

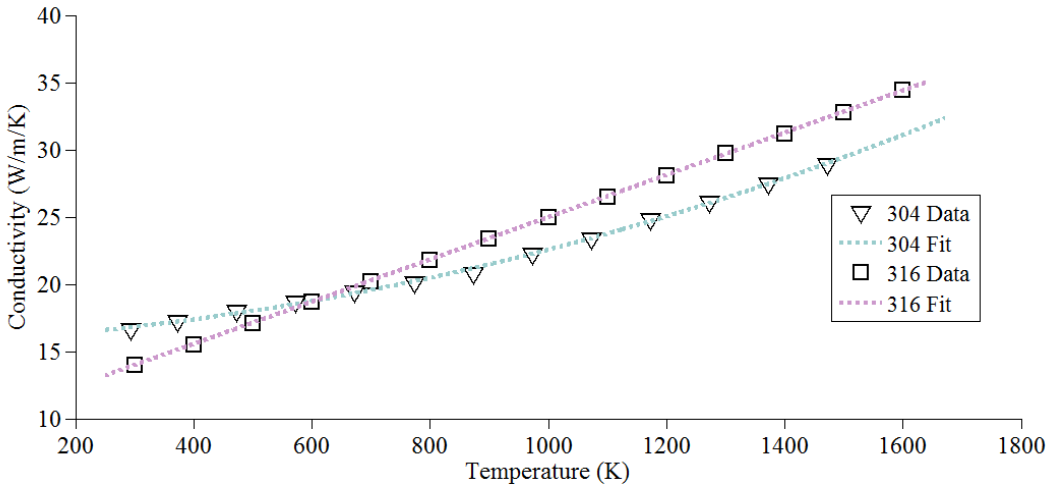

Figure 111 Thermal conductivity for stainless steels 304 and 316 [158].

B.2 Thermal diffusivity:

Thermal diffusivity is related to conductivity by:

$$thermal\ diffusivity = \alpha = \frac{k}{\rho C_p} \tag{B.3}$$

where ρ is bulk density and C_p is the molar heat capacity. Thermal diffusivity can be regarded as how quickly a material will conduct heat and absorb the energy. It determines how far into a material energy will travel in a given time. A useful approximation [137] of penetration as a function of time is given by:

$$z = \sqrt{4at} \tag{B.4}$$

The thermal diffusivity data for Figure 112 are taken from 'Thermophysical properties of materials for nuclear engineering'[158]. Two trends appear within the 304 data and so two straight line fits were applied to the data for use within the finite difference model: the first from 293 K to 873 K and the second from 873 K to 1473 K.

$$\alpha = \begin{cases} 2.26 \times 10^{-10} \times T + 4.34 \times 10^{-6} & 293 \leq T \leq 873 \\ 1.50 \times 10^{-9} \times T + 3.20 \times 10^{-9} & 873 < T < 1703 \end{cases}$$

The 316 data has been calculated using equation B.3 and the temperature dependent data for thermal conductivity, density, and specific heat.

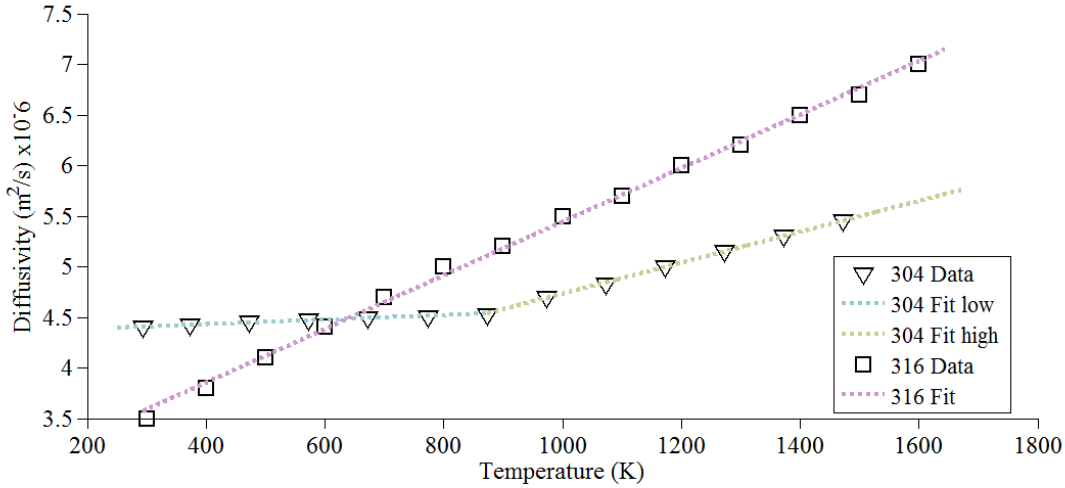

Figure 112 Temperature dependence of thermal diffusivity for stainless steel 304 and 316. The 304 data has had two linear fit lines applied meeting at 873 K data point.

B.3 Heat capacity:

This is defined as the amount of energy required to raise the temperature of a given mass of material by one degree Celsius. It can be expressed as:

$$C = \frac{dQ}{dT} \tag{B.5}$$

Normally heat capacity is defined *per* mole of substance but it can be defined *per* mass, in which case it is denoted by a lower case c. Heat capacity can be calculated or given at constant pressure (C_p) or at constant volume (C_v), the difference being related to the thermal expansion and compressibility of the substance. The relevant value in this work is that of C_p as the volume is not constrained during heating.

The specific heat data for Figure 113 are taken from 'Thermophysical properties of materials for nuclear engineering'[158]. The best fit line applied to the 304 data is a polynomial of degree one fitted between 293 and 1473 K by least squares method yielding

$$C_p = 0.211 \times T + 416 \qquad 250 \leq T \leq 1473$$

Whereas the 316 data is generated from the given relationship

$$C_p = 0.134 \times T + 462 \qquad 250 \leq T \leq 1703$$

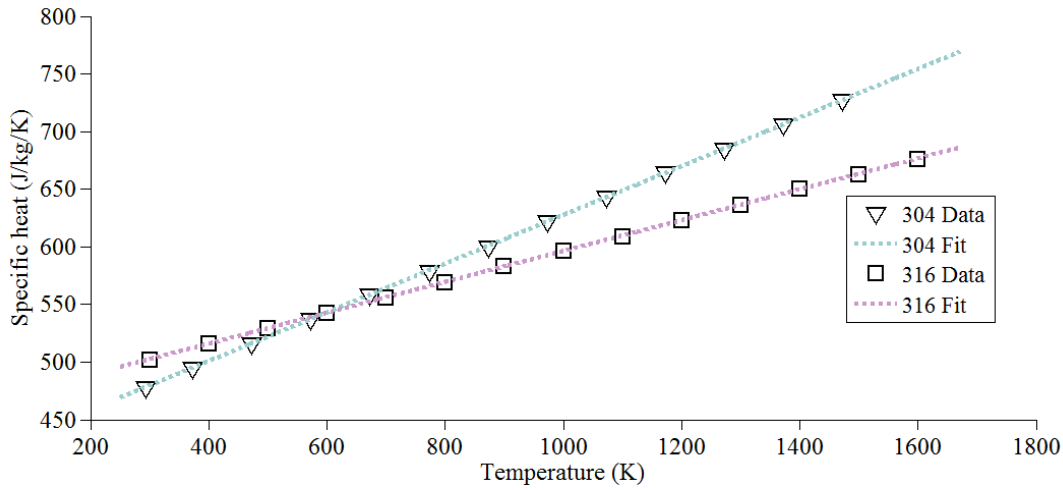

Figure 113 Temperature dependence of specific heat capacity for stainless steel 304 and 316.

According to the Debeye model C_V converges towards a value of 25 J/K/Mol for most solids above the Debeye temperature [160, p. 137]. The atomic mass of Iron is 58.8 g and stainless 316L is ~65 % iron [161] so C_V for stainless 316L will converge to approximately that of iron, ~425 J/K/Kg above the Debeye temperature, 477 K [162]. The reason that the C_P values in Figure 113 exceed 450 J/K/kg and continue to increase with temperature is that at constant pressure work is done expanding the volume of the material thus lowering the temperature rise for a given energy input.

B.4 Latent heat of melting/vaporisation and transformation temperatures:

These are material specific values that represent the amount of energy required to disassociate enough molecular bonds to enable the phase changes from solid to liquid (melting) or liquid to gas (vaporisation) without a change in temperature and the temperatures at which these phase changes occur.

Table 18 Phase change properties of stainless steels 304 and 316.

Property	Symbol	SS 316	SS 304	Units	Ref.
Latent heat of fusion	Lf	270	260-285	kJ/kg	[158] [159]
Freezing point	T_s	1703	1673-1723	K	[158] [159]
Boiling point	T_g	3090	-	K	[158]

Appendix C

Industrial significance

This research produced no journal papers as its findings were industrially sensitive however it did underpin the filing of two patents. In both cases the applicant was IPG photonics corporation and the inventors were Joseph Dallarosa (IPG), Bill O'Neill (my supervisor), Martin Sparkes (the group's senior research associate) and myself. An image of the first page of each patent follows for reference.

(12) INTERNATIONAL APPLICATION PUBLISHED UNDER THE PATENT COOPERATION TREATY (PCT)

(19) World Intellectual Property Organization
International Bureau

(43) International Publication Date
15 December 2016 (15.12.2016)

WIPO | PCT

(10) International Publication Number
WO 2016/201309 A1

(51) International Patent Classification:
B29C 67/04 (2006.01) *B33Y 10/00* (2015.01)
B22F 3/105 (2006.01)

(21) International Application Number:
PCT/US2016/036999

(22) International Filing Date:
10 June 2016 (10.06.2016)

(25) Filing Language: English

(26) Publication Language: English

(30) Priority Data:
62/173,541 10 June 2015 (10.06.2015) US

(71) Applicant: **IPG PHOTONICS CORPORATION** [US/US]; 50 Old Webster Road, Oxford, Massachusetts 01540 (US).

(72) Inventors: **DALLAROSA, Joseph,**; 574 Elmwood Ave., Uxbridge, Massachusetts 01569 (US). **O'NEILL, William**; 14 Riverside, Cambridge CB58HL (GB). **SPARKES, Martin**; Penquite, Flecks Lane, Shingay Cum Wendy, Herts SG8 0HT (GB). **PAYNE, Andrew,**; 84 Consort Avenue, Trumpington, Cambridge CB2 9AF (GB).

(74) Agents: **CARROLL, Kevin J.,** et al.; Grossman Tucker Perreault & Pfleger, PLLC, 55 South Commercial Street, Manchester, New Hampshire 03101 (US).

(81) Designated States *(unless otherwise indicated, for every kind of national protection available)*: AE, AG, AL, AM, AO, AT, AU, AZ, BA, BB, BG, BH, BN, BR, BW, BY, BZ, CA, CH, CL, CN, CO, CR, CU, CZ, DE, DK, DM, DO, DZ, EC, EE, EG, ES, FI, GB, GD, GE, GH, GM, GT, HN, HR, HU, ID, IL, IN, IR, IS, JP, KE, KG, KN, KP, KR, KZ, LA, LC, LK, LR, LS, LU, LY, MA, MD, ME, MG, MK, MN, MW, MX, MY, MZ, NA, NG, NI, NO, NZ, OM, PA, PE, PG, PH, PL, PT, QA, RO, RS, RU, RW, SA, SC, SD, SE, SG, SK, SL, SM, ST, SV, SY, TH, TJ, TM, TN, TR, TT, TZ, UA, UG, US, UZ, VC, VN, ZA, ZM, ZW.

(84) Designated States *(unless otherwise indicated, for every kind of regional protection available)*: ARIPO (BW, GH, GM, KE, LR, LS, MW, MZ, NA, RW, SD, SL, ST, SZ, TZ, UG, ZM, ZW), Eurasian (AM, AZ, BY, KG, KZ, RU, TJ, TM), European (AL, AT, BE, BG, CH, CY, CZ, DE, DK, EE, ES, FI, FR, GB, GR, HR, HU, IE, IS, IT, LT, LU, LV, MC, MK, MT, NL, NO, PL, PT, RO, RS, SE, SI, SK, SM, TR), OAPI (BF, BJ, CF, CG, CI, CM, GA, GN, GQ, GW, KM, ML, MR, NE, SN, TD, TG).

Published:

— *with international search report (Art. 21(3))*

(54) Title: MULTIPLE BEAM ADDITIVE MANUFACTURING

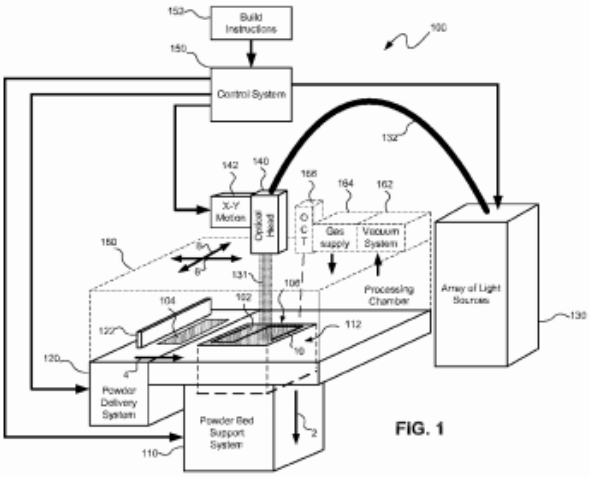

FIG. 1

(57) Abstract: Systems and methods for multiple beam additive manufacturing use multiple beams of light (e.g., laser light) simultaneously to expose layers of powder material in selected regions until the powder material fuses to form voxels, which form build layers of a three-dimensional structure. The light may be generated from selected light sources and coupled into an array of optical fibers having output ends arranged in an optical head such that the multiple beams are directed by the optical head to different locations on each of the powder layers. The multiple beams may provide distributed exposures forming a distributed exposure pattern including beam spots that are spaced sufficiently to separate the fused regions formed by each exposure. The multiple beams may be moved using various techniques (e.g., by moving the optical head) and according to various scan patterns such that a plurality of multiple beam distributed exposures form each build layer.

WO 2016/201309 A1

(12) INTERNATIONAL APPLICATION PUBLISHED UNDER THE PATENT COOPERATION TREATY (PCT)

(19) World Intellectual Property Organization
International Bureau

(43) International Publication Date
15 December 2016 (15.12.2016)

WIPO | PCT

(10) International Publication Number
WO 2016/201326 A1

(51) International Patent Classification: *B29C 67/00* (2006.01)

(21) International Application Number: PCT/US2016/037021

(22) International Filing Date: 10 June 2016 (10.06.2016)

(25) Filing Language: English

(26) Publication Language: English

(30) Priority Data:
62/173,541 10 June 2015 (10.06.2015) US

(71) Applicant: **IPG PHOTONICS CORPORATION** [US/US]; 50 Old Webster Road, Oxford, Massachusetts 01540 (US).

(72) Inventors: **DALLAROSA, Joseph,**; 574 Elmwood Ave., Uxbridge, Massachusetts 01569 (US). **O'NEILL, William**; 14 Riverside, Cambridge CB58HL (GB). **SPARKES, Martin**; Penquite, Flecks Lane, Shingay Cum Wendy, Herts SG8 0HT (GB). **PAYNE, Andrew,**; 84 Consort Avenue, Trumpington, Cambridge CB2 9AF (GB).

(74) Agents: **CARROLL, Kevin J.,** et al.; Grossman Tucker Perreault & Pfleger, PLLC, 55 South Commercial Street, Manchester, New Hampshire 03101 (US).

(81) Designated States *(unless otherwise indicated, for every kind of national protection available)*: AE, AG, AL, AM, AO, AT, AU, AZ, BA, BB, BG, BH, BN, BR, BW, BY, BZ, CA, CH, CL, CN, CO, CR, CU, CZ, DE, DK, DM, DO, DZ, EC, EE, EG, ES, FI, GB, GD, GE, GH, GM, GT, HN, HR, HU, ID, IL, IN, IR, IS, JP, KE, KG, KN, KP, KR, KZ, LA, LC, LK, LR, LS, LU, LY, MA, MD, ME, MG, MK, MN, MW, MX, MY, MZ, NA, NG, NI, NO, NZ, OM, PA, PE, PG, PH, PL, PT, QA, RO, RS, RU, RW, SA, SC, SD, SE, SG, SK, SL, SM, ST, SV, SY, TH, TJ, TM, TN, TR, TT, TZ, UA, UG, US, UZ, VC, VN, ZA, ZM, ZW.

(84) Designated States *(unless otherwise indicated, for every kind of regional protection available)*: ARIPO (BW, GH, GM, KE, LR, LS, MW, MZ, NA, RW, SD, SL, ST, SZ, TZ, UG, ZM, ZW), Eurasian (AM, AZ, BY, KG, KZ, RU, TJ, TM), European (AL, AT, BE, BG, CH, CY, CZ, DE, DK, EE, ES, FI, FR, GB, GR, HR, HU, IE, IS, IT, LT, LU, LV, MC, MK, MT, NL, NO, PL, PT, RO, RS, SE, SI, SK, SM, TR), OAPI (BF, BJ, CF, CG, CI, CM, GA, GN, GQ, GW, KM, ML, MR, NE, SN, TD, TG).

Published:

— *with international search report (Art. 21(3))*

(54) **Title**: MULTIPLE BEAM ADDITIVE MANUFACTURING

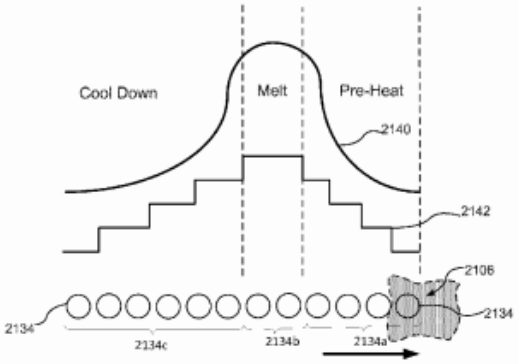

FIG. 21

(57) **Abstract**: Systems and methods for multiple beam additive manufacturing use multiple beams of light (e.g., laser light) to expose layers of powder material in selected regions until the powder material fuses to form voxels, which form build layers of a three-dimensional structure. The light may be generated from selected light sources and coupled into an array of optical fibers having output ends arranged in an optical head in at least one line such that multiple beams are sequentially directed by the optical head to the same powder region providing multiple beam sequential exposures (e.g., with pre-heating, melting and controlled cool down) to fuse the powder region. The multiple sequential beams may be moved using various techniques (e.g., by moving the optical head) and according to various scan patterns such that a plurality of fused regions form each build layer.

WO 2016/201326 A1